

國立臺灣大學工學院化學工程學研究所



博士論文

Department of Chemical Engineering

College of Engineering

National Taiwan University

Doctoral Dissertation

不同維度鈣鈦礦材料於發光二極體之應用

Applications of Perovskite Materials with Different  
Dimensionalities in Light-Emitting Diodes

陳炯翰

Chiung-Han Chen

指導教授：闕居振 博士

Advisor: Chu-Chen Chueh, Ph.D.

中華民國 114 年 7 月

July, 2025

國立臺灣大學博士學位論文

口試委員會審定書

DOCTORAL DISSERTATION ACCEPTANCE CERTIFICATE  
NATIONAL TAIWAN UNIVERSITY

不同維度鈣鈦礦材料於發光二極體之應用

Applications of Perovskite Materials

with Different Dimensionalities in Light-Emitting Diodes

本論文係 陳炯翰 (姓名) F08524012 (學號) 在國立臺灣大學  
化工 (系/所/學位學程) 完成之博士學位論文，於民國 114 年  
7 月 7 日承下列考試委員審查通過及口試及格，特此證明。

The undersigned, appointed by the Department / Graduate Institute of Chemical Engineering on 7 (date) 7 (month) 2025 (year) have examined a Doctoral Dissertation entitled above presented by Chiung-Han Chen (name) F08524012 (student ID) candidate and hereby certify that it is worthy of acceptance.

口試委員 Oral examination committee:

閻居振                      郭宗灼                      趙宇強

(指導教授 Advisor)

呂育蓉                      黃裕清                      蔣英志

林皓訓                      陳嘉聖

系(所、學位學程) 主管 Director: 蔣英志

## 誌謝




還記得在 2017 年的暑假，我選擇加入了闕居振老師的實驗室做專題，成為了闕老師的第一屆專題生，開啟了我對於鈣鈦礦材料的研究，還記得當時是實驗室的草創時期，我們在工綜與陳文章老師共用實驗室，在當時沒有自己的辦公室和實驗，在實驗條件很嚴峻的情況下，很感謝有陳文章老師的實驗室設備，讓我能無顧慮的嘗試一些想做的研究，也讓我慢慢對於鈣鈦礦有了很深的認識，除此之外，也很感謝在當時闕老師元件組的學長姐們，長紘、佳蓁、佳欣、芷儀、柏辰和蘇博以及當時和我一起加入實驗的同屆好友明筠，在我實驗有遇到一些困難時都給了我很多的建議和幫助，也非常感謝合成組的學長姐們，建瑋、聖淵、飛豪、宇昊、之後在西北給了我很多幫助的彥文以及後來也一起跟我簽博的吳哥，還記得在那個時期為了合成東西和聊天跑去舊數的美好時光。也非常感謝陳老師實驗室各位厲害的博班大學長姐們，彥丞、健忠、蕙璟、楷婷、濼甄、立哲、志鍵、Ender 以及未來要一起在台積同部門當同事的耘洁學長，感謝你們在當時儀器和設備方面給予我們闕家很大的幫助。

在與鈣鈦礦有著一些認識後，闕老師也決定開發鈣鈦礦發光二極體這個全新的研究方向，也在當時開啟了我們與北科郭霽慶老師實驗室的合作，還記得當時在懵懵懂懂的時期，我與明義學長一起進行摸索，永遠還記得當時光蒸鍍就要花四~六小時，卻一次只能做九片，而且還很常都不能 work 的可怕時光，也開啟了做 Device 的這條血汗不歸路。開始踏進了 Perovskite LED (PeLED) 領域之後，也很感謝闕老師在 2018 年當時連續兩年送我到在當時是在華南理工大學而現在是在香港城市大學的葉軒立老師實驗室學習 PeLED 的製備技術也讓我大開了眼界，一次可以蒸鍍 64 片的全自動蒸鍍機以及非常多不同用途的手套箱，讓我了解到這領域要在世界上生存非常不容易，很感謝當時帶我的振超師兄以及我兩次去的室友藥坤和天啟師兄，在實驗上和生活中都給了我很大的幫助，我也在回來後成功地建立起了 PeLED 小組，成為了組長，除了自己要建立 baseline 之外、想自己的題目當然更重要的是幫助小組的學弟妹們，也讓我學習到了不少，感謝 LED 小組歷年來的各位學弟妹們，彥宏、巧欣、芳榕、昱寬、音醍、宇翔、李濤和家榆，有了大家

的努力，這個組才能慢慢的成長起來，相信在大家繼續的努力下，我們在台灣的 PeLED 領域仍然有我們的一席之地。

而在當時我也選擇了繼續在闕老師實驗室念博士班，也成為了老師的第一屆博士班學生，也在當時鄭江樓終於正式落成啟用，闕家也有了自己的辦公室和實驗室，隨著上面的學長姐慢慢畢業，也突然意識到自己成為了在實驗室的大學長，在博士班期間除了要搞好自己的研究，還要處理和統籌規劃實驗室大大小小的事情，特別感謝明軒和我處理不知道多少雜事之外，也常和我討論實驗，在我博士班最後一年去國外的時間也幫助我帶 LED 組的學弟妹們，除此之外也很感謝同為博班的宇呈、嘉富和吳哥，大家都一起扛了不少事情。在博班的最後一年多，也很感謝闕老師的支持，讓我前後前往了日本九州大學和美國西北大學做研究。還記得當時一直有個想去日本生活做研究的夢想，於是我就鼓起勇氣親自寄 Email 給了九州大學 Adachi Chihaya 老師，最後也很幸運地成功地加入了 Adachi 老師的實驗室，終於了解到 OLED 是怎麼製作以及 TADF 材料的工作原理，在這期間很感謝土屋老師的指導，艷梅師姐、佐々木さん、水越さん、安部さん在實驗上和生活上給的幫助。

最後，我在順利地拿到博士班千里馬計畫後，我也決定前往我夢想中的西北大學 Edward Sargent 老師的實驗室開啟了我鈣鈦礦材料的另一個篇章，在交流的這一年主要是做鈣鈦礦疊層太陽能電池，對於之前沒做過太陽能電池的我，很感謝我的 mentor 劉源以及崇文師兄，在我加入後手把手的教我怎麼做錫鉛和寬帶隙的太陽能電池，我也成為了 ALD 的 super user，有了這些基礎後，我也開啟了沒日沒夜的地獄調 tandem baseline 過程，歷經快一年的時間最後終於成功疊起來，也在這期間成功地建立起 Perovskite/OPV tandem 的新研究方向，真的非常有成就感。在這期間非常感謝我的調 baseline 好夥伴吳越，我調 SnO<sub>2</sub> 你調 IZO，我們真的被分配到最地獄的兩個工作，除此之外，非常聰明的你時常在我遇到不懂的時候，跟我解釋一些量測上和機制上的問題和原理，不愧是北大物理系的高材生。也很感謝玉瑞師兄，雖然我們才共事兩三個月但你挾帶潭海仁老師那邊所有的經驗和技術讓我建的 baseline 有了跳躍式的進展。感謝斌哥以及 Ted 的指導，感謝 group leader 們劉成、楊熠、Deokjae、Donghoon 給的 support 和建議，感謝 PV group 的大家，桂香、楚瑩、林瑞、先付、鵬舉、李楚、侯晉、家樂、可夫、Sami、Pronoy、Abdul



以及我的 mentee, Palm, 這一年來很高興能認識如此厲害的各位, 讓我成長不少。還有感謝實驗室的其他好麻吉們, 斌斌、越老闆、楚姐、Erick 哥、颯哥、永祥、花姐等等, 讓我在做實驗之餘, 也跟你們一起快樂地度過很多時光。還有我的西北的台灣朋友們, 帶我認識大家的彥文、晨瑋、于庭、常棣、明修、比爾、我的 mentor 怡平、惠卿, 因為有你們讓我在美國這一年過得很精采, 一起度過好多美好的假日就像回到家一樣, 有你們真好。

這個誌謝記錄了我在闕 Lab 從 2017~2025 年這八年來的所遇到的一切, 也是我這八年來的鈣鈦礦研究生涯, 這一路上非常感謝所得到的幫助包含各位教授們及各位學長姐們, 以及所有曾經加入闕 Lab 的各位, 建賢、淳皓學長、杰勵、誌元、世峰、奕翔、稟翔、媿婷、彥涵、丁力、筑雁、旭孜等等, 因為有你們讓我這八年的研究過的十分精彩, 也成就了這本博士論文, 也感謝在研究做得很疲憊的時候新一代的闕 Lab 博班三本柱浩維陪我打魔物獵人教我狩獵、聶哥陪我打 PTCG 和大老二、冠霖還有陳老師家的阿豪陪我打牌和吃晚餐, 豐富了我很多無聊的時光, 希望闕 Lab 現役的大家能繼續保有研究的熱忱, 不論大家是否要投入學術界或是前往業界, 希望在闕 Lab 所進行的磨練都能為各位帶來更美好的未來, 也祝在閱讀這本博論的你或妳, 研究一切順利, 未來前程似錦。

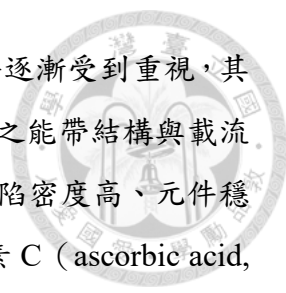
## 中文摘要



金屬鹵化物鈣鈦礦發光二極體 (Perovskite light-emitting diodes, PeLEDs) 因具備高螢光量子產率 (photoluminescence quantum yield, PLQY)、窄半高寬 (FWHM) 發光、能階可調控性，以及可利用低溫溶液製程等優勢，成為次世代高效率顯示與照明應用的重要候選材料。不同維度的鈣鈦礦材料在光電特性與結構穩定性上展現出顯著差異，進一步決定其在元件應用中的潛力與挑戰。本論文針對三維 (3D)、準二維 (quasi-2D) 以及二維錫基 (2D Sn-based) 無鉛鈣鈦礦等三種系統，分別發展出具針對性的材料設計與元件工程策略，期以提升 PeLEDs 在效率、穩定性與實用性上的綜合表現。

在 3D 全無機 PeLED 方面，因其具備高載流子遷移率與優異的載子傳輸特性，曾為早期研究之重點，但卻易受濕氣與熱的影響而導致結構崩解與效率衰退。本研究導入具共軛主鏈與極性橋接官能基的高分子中間層，應用於 PEDOT:PSS 與 CsPbBr<sub>3</sub> 之間，以改善能階對齊、提升界面浸潤性並優化鈣鈦礦薄膜之結晶品質。實驗結果顯示，在最佳化條件下，此設計可將元件之最高亮度提升六倍，外部量子效率 (external quantum efficiency, EQE) 亦提高至原始裝置的 3.6 倍，證實高分子中間層於界面修飾之成效。

進一步也針對準二維鈣鈦礦之挑戰來提出解決方法，本研究聚焦於其相位分佈控制與電子注入界面之工程優化。quasi-2D 材料內部同時存在多個不同  $n$  值的相 ( $n=1$  至  $\infty$ )，彼此間之能量傳遞與載子注入效率對元件性能影響深遠。透過引入天然環狀分子添加劑  $\alpha$ -與  $\beta$ -環糊精 (cyclodextrin) 成功調控不同  $n$  相之相對含量，其中  $\alpha$ -CD 可抑制低  $n$  相形成、而  $\beta$ -CD 有助於穩定中  $n$  相並促進能量傳遞效率。此外，利用具有籠狀結構的 cryptand 分子進一步強化配位能力與晶體均勻性，有效壓抑非輻射複合路徑。配合具導電性且具缺陷鈍化能力之磷氧化物 (PPT 與 PPF) 界面層設計，本研究成功製備出亮度達 73,897 cd/m<sup>2</sup>、EQE 超過 10% 的 quasi-2D PeLED 元件，並顯著抑制高電流密度下的效率衰退 (efficiency roll-off)，展現跨尺度相位與界面工程之協同優勢。



而在面對鉛毒性所帶來之環境與健康疑慮，無鉛鈣鈦礦材料逐漸受到重視，其中以錫（Sn）為 B 位金屬的二維鈣鈦礦材料具備可比擬鉛材料之能帶結構與載流子特性。然而， $\text{Sn}^{2+}$  易氧化為  $\text{Sn}^{4+}$  且晶化速率過快，導致薄膜缺陷密度高、元件穩定性差。為克服此一挑戰，本研究提出結合天然抗氧化劑維生素 C（ascorbic acid, VitC）與螯合劑 18-Crown-6 之雙添加劑策略，兩者可分別抑制氧化反應與捕捉過量離子，有效降低缺陷密度與提升薄膜緻密性與均勻性。實驗結果顯示，優化後元件之 EQE 由原始的 0.21% 提升至 1.87%，亮度提升近四倍，並展現良好之操作穩定性，證明此策略於無鉛紅光 PeLED 具高度潛力。

綜合以上，本研究針對不同維度鈣鈦礦材料發展出具系統性與針對性的設計策略，涵蓋高分子界面修飾、環狀分子相位調控、無鉛系統穩定化與多功能界面層應用，成功實現具高效率與高穩定性之 PeLED 元件，為推動鈣鈦礦光電材料實用化與環境友善化之重要里程碑。

# ABSTRACT

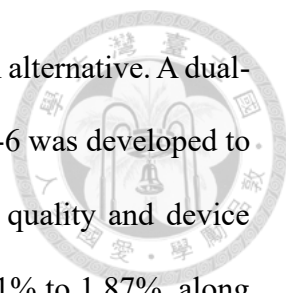


Metal halide perovskite light-emitting diodes (PeLEDs) have emerged as promising candidates for next-generation display and lighting applications due to their high photoluminescence quantum yield (PLQY), narrow emission bandwidths, and low-temperature solution processability. However, PeLEDs based on different perovskite dimensionalities—three-dimensional (3D), quasi-two-dimensional (quasi-2D), and two-dimensional (2D) lead-free tin-based systems—each face distinct challenges related to efficiency, stability, and material control. This dissertation presents a series of dimension-specific material and device engineering strategies aimed at overcoming these bottlenecks and improving the performance of PeLEDs.

In the 3D PeLED system, we introduce conjugated polymeric interlayers bearing polar-bridged side groups to tailor the energy-level alignment and crystallization behavior between PEDOT:PSS and CsPbBr<sub>3</sub>. This interfacial modification significantly enhances hole injection and film morphology, yielding a sixfold increase in luminance and a 3.6-fold improvement in external quantum efficiency (EQE) compared to the control device.

For quasi-2D perovskites, phase control and interfacial optimization are crucial. We employed cyclic molecular additives such as  $\alpha$ -/ $\beta$ -cyclodextrins and cryptands to regulate the distribution of different n-phases, enhance energy transfer, and suppress nonradiative losses. Furthermore, we introduced multifunctional phosphine oxide additives (PPT and PPF) at the electron transport interface to facilitate electron injection and defect passivation. This comprehensive approach enabled quasi-2D PeLEDs to achieve an EQE exceeding 10% and luminance over 73,000 cd/m<sup>2</sup>, while effectively mitigating efficiency roll-off under high bias conditions.





To address lead toxicity, we explored 2D Sn-based PeLEDs as an alternative. A dual-additive strategy combining ascorbic acid (Vitamin C) and 18-crown-6 was developed to prevent Sn<sup>2+</sup> oxidation and trap formation, thereby improving film quality and device stability. The resulting devices exhibited an enhanced EQE from 0.21% to 1.87%, along with improved operational stability, validating this approach for efficient red-emitting, lead-free PeLEDs.

In summary, this study provides a comprehensive framework for dimension-dependent optimization of perovskite optoelectronic materials, integrating additive engineering, phase control, and interfacial design. The results demonstrate significant advances in efficiency, stability, and structural tunability, paving the way toward practical and environmentally friendly PeLED technologies.

Overall, this work presents a unified framework for optimizing perovskite LEDs across varying structural dimensionalities, offering practical solutions to enhance efficiency, phase purity, and operational robustness for future commercial applications.

# CONTENTS



口試委員會審定書 .....	#
誌謝 .....	i
中文摘要 .....	iv
ABSTRACT .....	vi
CONTENTS .....	viii
LIST OF FIGURES .....	xii
LIST OF TABLES .....	xxiv
<b>Chapter 1 Introduction .....</b>	<b>1</b>
1.1 Introduction of Perovskites .....	1
1.2 Introduction of Perovskite Light-Emitting Diodes (PeLEDs) .....	5
1.3 Research Objectives for Dimension-Specific Strategies to Enhance the Performance of Perovskite Light-Emitting Diodes .....	7
1.4 Tables and Figures .....	9
<b>Chapter 2 3D All-inorganic Perovskite Light-Emitting Diodes .....</b>	<b>14</b>
2.1 Engineering of 3D All-inorganic Perovskite Light-Emitting Diodes by Interlayer Modification .....	14
2.1.1 Background .....	14
2.1.2 Experimental Section .....	16
2.1.3 Results and Discussion .....	21
2.1.4 Summary .....	31
2.1.5 Tables and Figures .....	32
<b>Chapter 3 Quasi-2D Perovskite Light-Emitting Diodes .....</b>	<b>48</b>

3.1	Engineering of Perovskite Light-Emitting Diodes Based on Quasi-2D Perovskites Formed by Diamine Cations .....	48
3.1.1	Background .....	48
3.1.2	Experimental Section .....	52
3.1.3	Results and Discussion.....	55
3.1.4	Summary .....	62
3.1.5	Tables and Figures.....	63
3.2	Regulating the Phase Distribution of Quasi-2D Perovskites Using Cyclic Molecules Toward Improved Light-Emitting Performance.....	75
3.2.1	Background .....	75
3.2.2	Experimental Section .....	78
3.2.3	Results and Discussion.....	80
3.2.4	Summary .....	86
3.2.5	Tables and Figures.....	87
3.3	Realizing High Brightness Quasi-2D Perovskite Light-Emitting Diodes with Reduced Efficiency Roll-Off via Multifunctional Interface Engineering ..	100
3.3.1	Background .....	100
3.3.2	Experimental Section .....	103
3.3.3	Results and Discussion.....	105
3.3.4	Summary .....	117
3.3.5	Tables and Figures.....	118
<b>Chapter 4</b>	<b>2D Lead-Free Perovskite Light-Emitting Diodes.....</b>	<b>130</b>
4.1	Improving Performance of Lead-Free Two-Dimensional Pure Red Perovskite Light Emitting Diodes via Natural Antioxidants Additive .....	130
4.1.1	Background .....	130



4.1.2	Experimental Section .....	133
4.1.3	Results and Discussion.....	135
4.1.4	Summary .....	145
4.1.5	Tables and Figures.....	147
<b>Chapter 5</b>	<b>Conclusion and Future Works .....</b>	<b>160</b>
5.1	Conclusion .....	160
5.2	Future Works.....	161
5.2.1	Stability of PeLEDs.....	162
5.2.2	Full-Color and White PeLED Integration .....	163
5.2.3	Exploration of Environment-Friendly Materials for PeLEDs.....	165
5.2.4	Integration with Flexible and Large-Area Substrates .....	166
<b>Chapter 6</b>	<b>(Appendix) Perovskite Tandem Solar Cells .....</b>	<b>168</b>
6.1	Optimization of ALD SnO <sub>2</sub> in All-Perovskite Tandem Solar Cells.....	168
6.1.1	Introduction .....	168
6.1.2	Experimental Section .....	171
6.1.3	Results and Discussion.....	175
6.1.4	Summary and Future works .....	179
6.1.5	Tables and Figures.....	181
6.2	Improving the Performance of Perovskite/Organic Tandem Solar Cells....	188
6.2.1	Introduction .....	188
6.2.2	Experimental Section .....	191
6.2.3	Results and Discussion.....	195
6.2.4	Summary and Future works .....	200
6.2.5	Tables and Figures.....	201
REFERENCE	.....	207

**PUBLICATION LIST .....226**



# LIST OF FIGURES

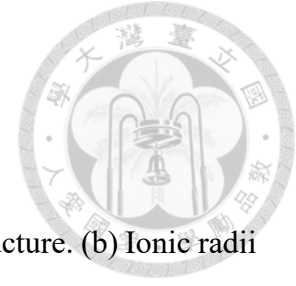


**Fig. 1.1** (a) Schematic illustration of the  $ABX_3$  perovskite crystal structure. (b) Ionic radii of various A-site cations and X-site anions, along with the resulting tolerance factor variations in perovskites upon cation substitution.<sup>[82]</sup> (c) Dependence of the Goldschmidt Tolerance Factor (GTF) on the A-site cation radius in  $APbI_3$  perovskites, where the shaded region ( $0.8 < t < 1$ ) indicates the range for a structurally stable cubic phase.<sup>[41]</sup> (d) Energy band alignment of  $MASnI_3$  and  $MAPbI_3$  perovskites, highlighting differences in bandgap and electronic structure.<sup>[82]</sup> (e) Roles of the A-site cation in influencing the structural stability, phase behavior, and optoelectronic properties of halide perovskites.<sup>[15]</sup> .....9

**Fig. 1.2** (a) Schematic illustration of perovskite materials with varying dimensionalities, including 3D, 2D, 1D, and 0D structures.<sup>[34]</sup> (b) Conceptual depiction of the formation mechanism, crystal structure of quasi-2D perovskites.<sup>[83]</sup> (c) Structural and compositional comparison between Dion–Jacobson (DJ) and Ruddlesden–Popper (RP) phases in both oxide and halide perovskites, emphasizing differences in spacer configuration.<sup>[46]</sup> .....10

**Fig. 1.3** (a) Annual number of publications and (b) citations related to perovskite light-emitting diodes (PeLEDs) from 2014 to 2024, as indexed by the Web of Science (data retrieved on December 31, 2024). (c) Chronological progression of the peak external quantum efficiency (EQE) in PeLEDs over the same period, excluding enhancements from out-coupling structures.<sup>[42]</sup>11

**Fig. 1.4** (a) Working mechanism of PeLEDs.<sup>[84]</sup> (b) Schematic illustration of quasi-2D perovskites and the energy transfer process.<sup>[26]</sup> .....12

<b>Fig. 1.5</b> Objectives for dimension-specific strategies to enhance the performance of perovskite light-emitting diodes. <sup>[76, 77, 80, 85, 86]</sup> .....	13
<b>Fig. 2.1</b> <sup>1</sup> H NMR spectra of (a) 1-vinylpyrene and (b) 4-(pyren-1-yl)butyl methacrylate in CDCl <sub>3</sub> . .....	33
<b>Fig. 2.2</b> <sup>1</sup> H NMR spectrum of <b>P4a</b> in CDCl <sub>3</sub> .....	34
<b>Fig. 2.3</b> <sup>1</sup> H NMR spectrum of <b>P4b</b> in CDCl <sub>3</sub> .....	35
<b>Fig. 2.4</b> <sup>1</sup> H NMR spectrum of <b>P4c</b> in CDCl <sub>3</sub> . .....	36
<b>Fig. 2.5</b> (a) Structures of the fabricated PeLED and P4a-c along with their energy levels and schematic of the distinct aggregation behaviors between P4a-c. (b) PES measurement and (c) UV-vis absorption spectra of the films of P4a-c. ....	37
<b>Fig. 2.6</b> Solubility test of <b>P4a-c</b> in DMSO and DMF.....	38
<b>Fig. 2.7</b> Temperature-dependent UV-vis absorption spectra of (a) P4a, (b) P4b, and (c) P4c solutions from 20–70 °C. (d) The calculated intensity ratio of the 0–0 and 0–1 characteristic absorption peaks of P4a, P4b, and P4c. ....	38
<b>Fig. 2.8</b> Tauc plots of the films of P4a–c. ....	39
<b>Fig. 2.9</b> 2D and 3D AFM topographies of the films of (a) PEDOT:PSS, (b) PEDOT:PSS/ <b>P4a</b> , (c) PEDOT:PSS/ <b>P4b</b> , and (c) PEDOT:PSS/ <b>P4c</b> . The surface roughness of the films is labeled on the images.....	39
<b>Fig. 2.10</b> (a) UV-vis absorption and (b) PL spectra of the films of PEDOT:PSS/CsPbBr <sub>3</sub> and PEDOT:PSS/P4a-c/CsPbBr <sub>3</sub> .....	40
<b>Fig. 2.11</b> Contact angle measurement of (a,d) P4a, (b,e) P4b, (c,f) and P4c films using (a-c) water and (d-f) glycerol. The respective contact angle values for P4a, P4b, and P4c are presented below and the surface energy was calculated using Wu model. ....	40

<b>Fig. 2.12</b> SEM images of CsPbBr <sub>3</sub> films grown on (a) PEDOT:PSS, (b) PEDOT:PSS/P4a, (c) PEDOT:PSS/P4b, and (c) PEDOT:PSS/P4c. ....	41
<b>Fig. 2.13</b> (a) XRD characteristics of the perovskite films grown on different layers as indicated, where pure means the pristine PEDOT:PSS. GIWAXS patterns of the films of (b) PEDOT:PSS/CsPbBr <sub>3</sub> and (c) PEDOT:PSS/P4c/CsPbBr <sub>3</sub> , and (d) their corresponding 1-D characteristics extracted from the GIWAXS patterns shown in (b, c).....	42
<b>Fig. 2.14</b> GIWAXS patterns of the samples of (a) PEDOT:PSS/P4a/CsPbBr <sub>3</sub> and (b) PEDOT:PSS/P4b/CsPbBr <sub>3</sub> . (c) The corresponding normalized 1-D incident characteristics of CsPbBr <sub>3</sub> films grown on the pristine and P4a-c-modified HTLs.....	43
<b>Fig. 2.15</b> UPS measurements of the films of (a) PEDOT:PSS/P4a, (b) PEDOT:PSS/P4b, and (c) PEDOT:PSS/P4c. ....	44
<b>Fig. 2.16</b> (a) The energy-level diagram of PEDOT:PSS and PEDOT:PSS/P4a-c. J-V curves of (b) the hole-only device and (c) the electron-only device using pristine PEDOT:PSS or PEDOT:PSS/P4a-c as the HTL.....	45
<b>Fig. 2.17</b> (a) Energy-level diagram of the studied PeLEDs. (b) J-V-L, (c) current efficiency-voltage, and (d) EQE curves of the studied PeLEDs. ....	46
<b>Fig. 2.18</b> (a) EL curves of Device III under different operation voltages and (b) the corresponding contour plot. ....	46
<b>Fig. 2.19</b> J-V-L curves of the PeLEDs made from P4a solutions with different concentration for optimization.....	47
<b>Fig. 2.20</b> Contour plots of EL spectra of (a) control device, (b) Device I, and (c) Device II.....	47



<b>Fig. 3.1</b> Illustration of the studied DJ phase quasi-2D EDBE(MAPbBr <sub>3</sub> ) <sub>n-1</sub> PbBr <sub>4</sub> in this work.....	65
<b>Fig. 3.2</b> The SEM images of the prepared quasi-2D EDBE(MAPbBr <sub>3</sub> ) <sub>n-1</sub> PbBr <sub>4</sub> perovskite films.....	66
<b>Fig. 3.3</b> (a) 1D XRD patterns of the prepared quasi-2D EDBE(MAPbBr <sub>3</sub> ) <sub>n-1</sub> PbBr <sub>4</sub> perovskite films and their corresponding (b) normalized UV-vis spectra, (c) normalized PL spectra, and (d) energy levels.....	67
<b>Fig. 3.4</b> Tauc plots of the studied quasi-2D EDBE(MAPbBr <sub>3</sub> ) <sub>n-1</sub> PbBr <sub>4</sub> perovskite films.....	68
<b>Fig. 3.5</b> The relative PL intensity of the studied quasi-2D EDBE(MAPbBr <sub>3</sub> ) <sub>n-1</sub> PbBr <sub>4</sub> perovskite films.....	69
<b>Fig. 3.6</b> (a) Device configuration of our studied PeLED and the corresponding energy-level diagram. (b) TRPL of the studied quasi-2D EDBE(MAPbBr <sub>3</sub> ) <sub>n-1</sub> PbBr <sub>4</sub> perovskite films and the fitted curves. (c) TRPL of the EDBE(MAPbBr <sub>3</sub> ) <sub>n-1</sub> PbBr <sub>4</sub> film with or without TPBi passivation and the fitted curves.....	70
<b>Fig. 3.7</b> (a) The J-V-L characteristics of the top-performing device. The inset is the real picture of the device operated under a voltage of 5 V. (b) The EQE curve and (c) the EL curves of the champion device.....	71
<b>Fig. 3.8</b> The surface AFM image of the PEDOT:PSS films with different conductivity on ITO glass. (a) AL 4083 (b) CH 8000 (c) CH 8000 with methanol post-treatment.....	72
<b>Fig. 3.9</b> The (a, c, e) J-V-L and (b, d, f) EQE curves of the studied PeLEDs processed with different optimized conditions as noted.....	73
<b>Fig. 3.10</b> (a) The J-V-L and (b) EQE curves of the studied PeLEDs with and without using TPBi as a protecting layer. The device configuration is ITO/PEDOT:PSS (AL	

4083)/EDBE(MAPbBr<sub>3</sub>)<sub>2</sub>PbBr<sub>4</sub>/TPBi (spin-coated)/TPBi (vacuum-deposited, 40 nm)/LiF/Al.....74

**Fig. 3.11** The J-V-L curves of the studied PeLEDs using a vacuum-deposited TPBi ETL with different thickness. The device configuration is ITO/PEDOT:PSS (CH8000)/ EDBE(MAPbBr<sub>3</sub>)<sub>2</sub>PbBr<sub>4</sub>/TPBi (spin-coated)/TPBi (vacuum-deposited, with different thickness)/LiF/Al.....74

**Fig. 3.12** (a,b) UV-vis absorption and (c,d) PL emission spectra of the hybrid quasi-2D perovskite films with different doping ratios of (a,c)  $\alpha$ -CD and (b,d)  $\beta$ -CD. ....88

**Fig. 3.13** (a) TRPL curves of the hybrid  $\alpha$ -CD/quasi-2D perovskite and  $\beta$ -CD/quasi-2D perovskite films. Temperature-dependent PL measurement of the (b) pristine perovskite, (c)  $\alpha$ -CD/PVSK, and (d)  $\beta$ -CD/PVSK films.....89

**Fig. 3.14** (a) XRD characteristics of the hybrid  $\alpha$ -CD/quasi-2D perovskite (with a ratio of 0.1:1) and  $\beta$ -CD/quasi-2D perovskite (with a ratio of 0.07:1) films. SEM images of the (b) pristine perovskite, (c)  $\alpha$ -CD/PVSK, and (d)  $\beta$ -CD/PVSK films.....90

**Fig. 3.15** FTIR spectroscopy of  $\alpha$ -CD/PVSK,  $\beta$ -CD/PVSK,  $\alpha$ -CD, and  $\beta$ -CD. ....91

**Fig. 3.16** XPS spectra of (a) Pb 4f signal, (b) O 1s signal for the pristine quasi-2D,  $\alpha$ -CD/PVSK, and  $\beta$ -CD/PVSK films. XPS spectra of (c) Cs 3d signal for the pure CsBr,  $\alpha$ -CD/CsBr, and  $\beta$ -CD/CsBr films and (d) N 1s signal for the pure PEABr,  $\alpha$ -CD/PEABr, and  $\beta$ -CD/PEABr films.....92

**Fig. 3.17** UV-vis absorption measurement of quasi-2D perovskite films with (a) different doping ratios of Cryptand and (b) with different doping ratios of 18-Crown-6 added. (c) PL emission spectra, (d)TRPL curves of quasi-2D perovskite films with different doping ratios of Cryptand. ....93

<b>Fig. 3.18</b> PLQY of quasi-2D perovskite films with different doping ratios of Cryptand.	94
<b>Fig. 3.19</b> Temperature-dependent PL of (a) the pristine quasi-2D perovskite film, and the film with (b) 0.025 doping ratio (c) 0.05 doping ratio (d) 0.075 doping ratio of the cryptand.	95
<b>Fig. 3.20</b> (a-d) The XRD measurement and (e-h) SEM images of the quasi-2D perovskite films with different added doping ratios of the cryptand.	96
<b>Fig. 3.21</b> (a) The NMR spectra of the cryptand without and with different perovskite precursors as noted and (b) NMR spectra of the cryptand, PEABr, and their mixture in the range of 7.4 to 8.2 ppm.	97
<b>Fig. 3.22</b> XPS measurement of O 1s spectra of the cryptand without and with different perovskite precursors as noted.	97
<b>Fig. 3.23</b> (a) Structure and (b,c) the energy-level diagram of the fabricated PeLEDs.	98
<b>Fig. 3.24</b> (a-c) J-V-L, and (d-f) EQE-voltage curves of the fabricated devices.	99
<b>Fig. 3.25</b> (a) Chemical structures of PPT and PPF and schematic representation of the post-treatment process and illustration of the interfacial engineering. (b) PL emission spectra, (c) PLQYs, and (d) TRPL curves of pristine, PPT-treated and PPF-treated perovskite films, where the PLQYs were measured by a 368 nm laser.	120
<b>Fig. 3.26</b> (a) XRD characteristics and (b) UV-vis absorption spectra of the pristine, PPT-modified and PPF-modified perovskite films.	120
<b>Fig. 3.27</b> SEM images of the (a) pristine, (b) CB-treated, (c) PPT-modified and (d) PPF-modified perovskite films	121
<b>Fig. 3.28</b> <sup>31</sup> P NMR spectra of (a) PPT and (b) PPF and their mixtures with different perovskite precursor components. (c) ESP map of PPT molecule. (d) XPS	

<p>spectra of Pb 4f signal for the pristine, PPT-modified and PPF-modified perovskite films. (e) Schematic illustration of the passivation function of PPT on a perovskite surface. ....</p>	121
<b>Fig. 3.29</b> ESP map of PPF molecule .....	122
<b>Fig. 3.30</b> XPS spectra of P 2p signal for the pristine, PPT-modified and PPF-modified perovskite films. ....	122
<b>Fig. 3.31</b> (a) Structure and (b) the energy-level diagram of the fabricated PeLEDs. (c) J–V–L characteristics, (d) normalized EQE-voltage curves, (e) normalized EQE-current density curves and (f) EQE-luminance curves of the fabricated devices. ....	123
<b>Fig. 3.32</b> J-V characteristics of the studied (a) hole-only devices (b) electron-only devices. ....	124
<b>Fig. 3.33</b> EL curves of the fabricated PeLEDs measured at 4V. ....	124
<b>Fig. 3.34</b> Color plot for transient absorption (TA) in the visible regions for (a) pristine, (b) PPT-modified, and (c) PPF-modified perovskite films. Ultrafast time-resolved TA spectra of (d) pristine, (e) PPT-modified, and (f) PPF-modified perovskite films. ....	125
<b>Fig. 3.35</b> Power-dependent carrier dynamics at the probe wavelength of 505 nm for (g) pristine, (h) PPT-modified, and (i) PPF-modified perovskite films. ....	126
<b>Fig. 3.36</b> Femtosecond time-resolved TA spectra of (a) pristine, (b) PPT-modified and (c) PPF-modified perovskite films. ....	127
<b>Fig. 3.37</b> (a) EIS analyses and (b) capacitance-voltage curves of control, PPT-modified and PPF-modified devices. (c) Energy levels of the pristine, PPT-modified, PPF-modified perovskite films and TPBi. (d) Schematic representation of the better carrier dynamics in the modified device.....	128

<b>Fig. 3.38</b>	UPS results of the (a,b) pristine, (c,d) PPT-modified and (e,f) PPF-modified perovskite films. ....	129
<b>Fig. 4.1</b>	UV irradiated PEA <sub>2</sub> SnI <sub>4</sub> films containing 25% molar ratio of (a) Vit C, (b) Caffeic acid, (c) Ferulic acid, and (d) p-Coumaric acid. ....	148
<b>Fig. 4.2</b>	(a) Photoluminescence quantum yield (PLQY) of PEA <sub>2</sub> SnI <sub>4</sub> films with varying molar ratios of ascorbic acid (VitC), with and without the addition of 18-Crown-6. (b) UV-vis absorption spectra, (c) photoluminescence (PL) emission spectra, (d) time-resolved PL (TRPL) decay curves, and (e) X-ray diffraction (XRD) patterns of pristine, 25C (25% VitC), and 25CC (25% VitC + 18-Crown-6) PEA <sub>2</sub> SnI <sub>4</sub> films. (f) Grazing-incidence wide-angle X-ray scattering (GIWAXS) pattern of the 25CC PEA <sub>2</sub> SnI <sub>4</sub> film. (g-i) Scanning electron microscopy (SEM) images of (g) pristine, (h) 25C, and (i) 25CC PEA <sub>2</sub> SnI <sub>4</sub> films. ....	149
<b>Fig. 4.3</b>	(a) UV-vis absorption and (b) PL emission spectra as well as (c) TRPL measurements of Pure, 25C, and 25CC PEA <sub>2</sub> SnI <sub>4</sub> films. ....	150
<b>Fig. 4.4</b>	GIWAX patterns of (a) pristine and (b) 25CC PEA <sub>2</sub> SnI <sub>4</sub> films. ....	150
<b>Fig. 4.5</b>	The AFM images of Pure, 25C, and 25CC PEA <sub>2</sub> SnI <sub>4</sub> films. ....	151
<b>Fig. 4.6</b>	Temperature-dependent PL measurements from 50 K to 300 K and the corresponding 2D contour plots of (a, d) pristine, (b, e) 25C, and (c, f) 25CC PEA <sub>2</sub> SnI <sub>4</sub> films. ....	151
<b>Fig. 4.7</b>	Pseudocolor plots of transient absorption spectra (TAS) of (a, d) pristine, (b, e) 25C and (c,f) 25CC PEA <sub>2</sub> SnI <sub>4</sub> films excited at 400 nm with different scanning delay times. Kinetic traces of (g) pristine, (h) 25C and (i) 25CC PEA <sub>2</sub> SnI <sub>4</sub> films at the probe wavelength of 610 nm. ....	152

<b>Fig. 4.8</b>	Kinetic traces of pristine, 25C and 25CC PEA <sub>2</sub> SnI <sub>4</sub> films at 610 nm probe wavelength.....	153
<b>Fig. 4.9</b>	(a–c) X-ray photoelectron spectroscopy (XPS) spectra of the Sn 3d core levels for (a) pristine, (b) 25C (25% VitC), and (c) 25CC (25% VitC + 18-Crown-6) PEA <sub>2</sub> SnI <sub>4</sub> films. (d) <sup>1</sup> H NMR spectra of VitC, VitC + PEAI, and VitC + SnI <sub>2</sub> , and (e) <sup>13</sup> C NMR spectra of VitC and VitC + SnI <sub>2</sub> in DMSO- d <sub>6</sub> solution. (f) Fourier-transform infrared (FTIR) spectra of pristine, 25C, and 25CC PEA <sub>2</sub> SnI <sub>4</sub> films. (g) <sup>1</sup> H NMR spectra of 18-Crown-6, 18-Crown-6 + PEAI, and 18-Crown-6 + SnI <sub>2</sub> in DMSO-d <sub>6</sub> . (h) Schematic illustration of the proposed interactions between VitC, 18-Crown-6, and the PEA <sub>2</sub> SnI <sub>4</sub> perovskite structure.....	154
<b>Fig. 4.10</b>	ESP map of VitC molecule. ....	155
<b>Fig. 4.11</b>	SCLC measurements of devices based on (a) pristine, (b) 25C and (c) 25CC PEA <sub>2</sub> SnI <sub>4</sub> films. (d) EIS measurements, (e) C-V measurements, and (f) transient EL measurements of the devices based on pristine, 25C and 25CC PEA <sub>2</sub> SnI <sub>4</sub> films.....	155
<b>Fig. 4.12</b>	Transient EL results of the devices based on pristine, 25C and 25CC PEA <sub>2</sub> SnI <sub>4</sub> films. ....	156
<b>Fig. 4.13</b>	(a) Schematic illustration of the device architecture and (b) corresponding energy-level diagrams for pristine, 25C (25% VitC), and 25CC (25% VitC + 18-Crown-6) PEA <sub>2</sub> SnI <sub>4</sub> films and their respective PeLEDs. (c) Current density–voltage–luminance (J–V–L) characteristics and (d) external quantum efficiency (EQE) versus current density curves of devices based on the three film types. (e) CIE 1931 chromaticity coordinates of the 25CC device under various applied voltages; inset: photograph of the 25CC device in operation.	

	Electroluminescence (EL) intensity contour plots for devices incorporating (f) pristine, (g) 25C, and (h) 25CC PEA <sub>2</sub> SnI <sub>4</sub> emissive layers.....	157
<b>Fig. 4.14</b>	UPS results of (a, d) Pure, (b, e) 25C and (c, f) 25CC PEA <sub>2</sub> SnI <sub>4</sub> films. ....	158
<b>Fig. 4.15</b>	CIE coordinates for (a) Pure and (b) 25C devices when operating at the biases from 2.4 V to 3.6 V. ....	158
<b>Fig. 4.16</b>	EL results of devices based on (a) Pure, (b) 25C and (c) 25CC PEA <sub>2</sub> SnI <sub>4</sub> films when operating at different bias voltages. EL results and the calculated FWHM values of devices based on (d) Pure, (e) 25C and (f) 25CC PEA <sub>2</sub> SnI <sub>4</sub> films when operating at 3.6 V. ....	159
<b>Fig. 5.1</b>	Future research directions for commercialized PeLEDs.....	162
<b>Fig. 6.1</b>	The detailed ALD mechanism for SnO <sub>2</sub> formation. <sup>[304]</sup> .....	182
<b>Fig. 6.2</b>	The operating panel of ALD machine for SnO <sub>2</sub> formation. ....	182
<b>Fig. 6.3</b>	Performance variation of single-junction PbSn perovskite solar cells with the device structure ITO/PEDOT:PSS/PbSn perovskite/C <sub>60</sub> /SnO <sub>2</sub> /Ag under different ALD SnO <sub>2</sub> deposition temperatures. ....	183
<b>Fig. 6.4</b>	ALD optimization process based on different bandgaps of perovskites. ....	183
<b>Fig. 6.5</b>	The base pressure changes after using a powerful pump. ....	184
<b>Fig. 6.6</b>	(a) The device structure of all-perovskite tandem solar cells. (b) J-V curves of all-perovskite tandem solar cells under different purging time. ....	184
<b>Fig. 6.7</b>	J-V curves of all-perovskite tandem solar cells under different cycles of ALD SnO <sub>2</sub> . ....	184
<b>Fig. 6.8</b>	(a) The device structure of 1.78eV WBG perovskite solar cells. (b) J-V curves of the champion device and the box chart of the performance of 1.78eV WBG perovskite solar cells.....	185

**Fig. 6.9** The baseline of all-perovskite tandem solar cells developed in the Sargent group (indicated by the yellow star) is shown in comparison with previously published results worldwide, as well as with devices fabricated by our group at the University of Toronto.....185

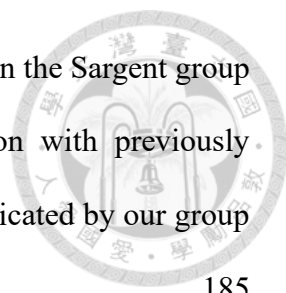


**Fig. 6.10** (a) Device architecture of PbSn NBG solar cells integrated with ITO nanoparticles. (b) Schematic diagram of bonding between 2PACz and ITO or ITO NCs.<sup>[303]</sup> (c-f) Box charts of the PV parameter of PbSn NBG perovskite solar cells by using different conditions of hole transporting layer.....186

**Fig. 6.11** Comparison of EQE curves with different device configuration by using different HTL.....186

**Fig. 6.12** Box charts of the PV parameter of PbSn NBG perovskite solar cells by using different concentration of ITO nanoparticles.....187

**Fig. 6.13** EQE curves with different device configuration by using different concentration of ITO nanoparticles. ....187

**Fig. 6.14** The device architecture of (a) all-perovskite tandem solar cells and (b) perovskite/organic tandem solar cells (PO-TSCs).....202

**Fig. 6.15** NFA chemical structures and their optoelectronic and thermal properties. (a) Chemical structures of the benchmark NFA Y6 and the CF<sub>3</sub>-functionalized series Y<sub>n</sub>CF<sub>3</sub> (n = 1, 2, 3). (b) Normalized UV–vis absorption spectra of Y6 and Y<sub>n</sub>CF<sub>3</sub>s measured in chloroform solution (dashed lines) and as thin films (solid lines). (c) Energy level diagram illustrating the HOMO and LUMO positions of Y6 and Y<sub>n</sub>CF<sub>3</sub>s as determined by cyclic voltammetry (CV).<sup>[309]</sup> .....202

**Fig. 6.16** (a) Y<sub>n</sub>CF<sub>3</sub> series shows a 2D mesh-like structure from single crystal XRD. (b) GIWAXS line-cut profiles of Y<sub>n</sub>CF<sub>3</sub> neat films. (c) Comparison of the d-



spacing and CCL values of Y6 and YnCF3 neat films from GIWAXS analyses.<sup>[309]</sup> .....203

**Fig. 6.17** (a) DFT-calculated ESP distribution and dipole moment of YnCF3. Photovoltaic performance of (a) J-V characteristics of D18:Y6 and D18:YnCF3 OSCs and (b) statistical distribution of PCEs with 15 individual devices. (c) Corresponding EQE spectra (scattered line) and integrated current densities (dashed line).<sup>[309]</sup> .....204

**Fig. 6.18** (a) Device architecture of 1.88eV WBG single junction perovskite solar cells. (b) J-V characteristics and (b) statistical distribution of Vocs, PCEs, Jscs and FFs with several individual devices. (d) The champion device and average performance of 1.88eV WBG single junction perovskite solar cells. ....204

**Fig. 6.19** (a) Device architecture of PO-TSCs. (b) J-V characteristics of different subcells (c) EQE of PO-TSCs. (d) Reverse and forward J-V characteristics of champion device. (e) 5min of SPO measurement of PO-TSCs.....205

**Fig. 6.20** (a) Molecule structure and design strategy of YCF3-BF and YCF3-NF. (b) Normalized UV-vis absorption spectra of YCF3-BF and YCF3-NF measured in chloroform solution (dashed lines) and as thin films (solid lines). (c) Molecular structure of PM6, Y6 and L8BO. (d) Energy level of PM6, YCF3-NF, YCF3-BF, Y6 and L8BO. ....205

**Fig. 6.21** Four potential research directions for future development of PO-TSCs. ....206

# LIST OF TABLES



<b>Table 2.1</b> Device performance of fabricated PeLEDs.....	32
<b>Table 3.1</b> The relationship between the prepared quasi-2D (EDBE)(MA) <sub>n-1</sub> Pb <sub>n</sub> Br <sub>3n+1</sub> perovskites and the precursor ratios. The ratio in the columns are molar ratio. .....	63
<b>Table 3.2</b> TRPL lifetime of the studied quasi-2D EDBE(MAPbBr <sub>3</sub> ) <sub>n-1</sub> PbBr <sub>4</sub> perovskite films deposited on ITO glass. ....	64
<b>Table 3.3</b> The luminescence characteristics of the studied PeLEDs using a vacuum-deposited TPBi ETL with different thickness. The device configuration is ITO/PEDOT:PSS (CH8000 treated with methanol)/EDBE(MAPbBr <sub>3</sub> ) <sub>2</sub> PbBr <sub>4</sub> /TPBi (spin-coated)/TPBi (vacuum-deposited, with different thickness)/LiF/Al. ....	64
<b>Table 3.4</b> The fitting parameters for the TRPL results of pristine, hybrid $\alpha$ -CD/quasi-2D perovskite and $\beta$ -CD/quasi-2D. ....	87
<b>Table 3.5</b> The fitting parameters for the TRPL results of quasi-2D perovskite films with different added doping ratios of the cryptand. ....	87
<b>Table 3.6</b> PLQY of quasi-2D perovskite films with different added doping ratios of the cryptand. ....	87
<b>Table 3.7</b> Performance of fabricated PeLEDs.....	88
<b>Table 3.8</b> Bi-exponential fitting parameters for the TRPL results. ....	118
<b>Table 3.9</b> Performance of the fabricated PeLEDs.....	118
<b>Table 3.10</b> Recombination decay constants of the control, PPT-modified and PPF-modified perovskite films. ....	119

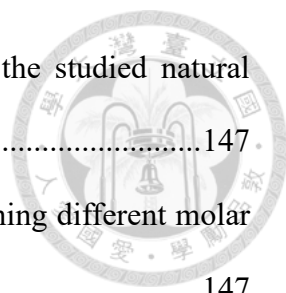


**Table 4.1** PLQY of PEA<sub>2</sub>SnI<sub>4</sub> film containing different ratios of the studied natural antioxidants.....147

**Table 4.2** PLQY of PEA<sub>2</sub>SnI<sub>4</sub> films with or w/o 18-Crown-6 containing different molar ratios of VitC.....147

**Table 4.3** TRPL fitting parameters and the radiative and nonradiative recombination rates of pristine, 25C and 25CC PEA<sub>2</sub>SnI<sub>4</sub> films. ....147

**Table 4.4** The carrier lifetime calculated from transient absorption measurement of different 2D Sn-based perovskite. ....147

**Table 4.5** Device performance of the fabricated PeLEDs.....148

**Table 6.1** Performance of NBG perovskite solar cells with different chamber temperatures but in same batch. ....181

**Table 6.2** Performance of 1.78eV WBG perovskite solar cells with optimized ALD conditions.....181

**Table 6.3** Performance of all-perovskite tandem solar cells with optimized ALD conditions.....181

**Table 6.4** Device performance of perovskite and OPV single junction and PO-TSCs.201

**Table 6.5** The summarized results of UV-vis absorption and CV measurement. ....201

# Chapter 1 Introduction



## 1.1 Introduction of Perovskites

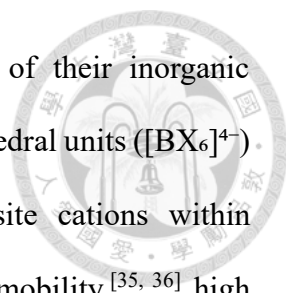
Metal halide perovskites have garnered significant attention in recent years as promising candidates for optoelectronic applications due to their exceptional properties, including tunable bandgap, high photoluminescence quantum yield (PLQY), and solution processability. Perovskites are materials characterized by the general chemical formula  $ABX_3$ , where “A” represents a monovalent organic (typically methylammonium ( $MA^+$ ) and formamidinium ( $FA^+$ )) or inorganic cation (typically  $Cs^+$ ,  $Rb^+$ ,  $K^+$ ),<sup>[1, 2]</sup> “B” is typically a divalent metal cation such as lead ( $Pb^{2+}$ ) or tin ( $Sn^{2+}$ ),<sup>[3, 4]</sup> and “X” is a halide anion ( $Cl^-$ ,  $Br^-$ , or  $I^-$ ).<sup>[5, 6]</sup>

The formation and phase stability of perovskite crystal structures can be preliminarily predicted using the Goldschmidt tolerance factor (GTF), defined as  $t = (r_A + r_X) / \sqrt{2}(r_B + r_X)$ , where  $r_A$ ,  $r_B$  and  $r_X$  represent the ionic radii of the A-site cation, B-site metal cation, and halide anion, respectively.<sup>[7]</sup> It is generally observed that perovskite structures with GTF values in the range of  $0.8 < t < 1.0$  tend to form stable three-dimensional (3D) phases (**Fig. 1.1b**).<sup>[8, 9]</sup> Within this window, the corner-sharing  $[BX_6]^{4-}$  octahedral network can be maintained, supporting a perovskite-type crystal lattice. However, significant deviations from this range often lead to the formation of non-perovskite structures such as hexagonal or layered phases, particularly when the A-site cation is either too small (e.g.,  $Na^+$ ,  $K^+$ ,  $Rb^+$ ,  $Cs^+$ ) or too large (e.g.,  $FA^+$ ), resulting in edge- or face-sharing octahedra instead of the desired corner-sharing framework.<sup>[8-10]</sup> While the GTF provides a useful guideline, numerous exceptions exist, prompting the

development of refined structural predictors that more accurately describe perovskite phase formation across diverse compositions.<sup>[9-11]</sup>

The optoelectronic properties of halide perovskites are primarily governed by the inorganic metal-halide framework,  $[BX_6]^{4-}$ . As illustrated in the electronic band structure (**Fig. 1.1c**), the valence band originates from the hybridization of  $Pb^{2+}$  6s or  $Sn^{2+}$  5s orbitals with halide p orbitals (3p for  $Cl^-$ , 4p for  $Br^-$ , and 5p for  $I^-$ ), forming bonding and antibonding states (**Fig. 1.1d**). Meanwhile, the conduction band minimum is primarily formed by antibonding interactions between the  $Pb^{2+}$  6p orbitals and halide p orbitals.<sup>[12]</sup> Some studies also suggest that halide s orbitals may interact with Pb orbitals, introducing minor s-character into the conduction band.<sup>[13, 14]</sup> Although the A-site cation does not directly contribute to states near the band edges due to its ionic bonding nature, it plays an indirect but crucial role in determining the structural stability, bandgap, and electronic structure of the perovskite lattice. Specifically, the size and steric effects of the A-site cation influence octahedral tilting, B-X-B bond angles, and B-X bond lengths, thereby modulating the band structure and optical properties.<sup>[15, 16]</sup> For instance, the bandgap tends to decrease as the A-site cation size increases from  $Cs^+$  to  $MA^+$  to  $FA^+$ , due to reduced octahedral tilting. Therefore, the physical characteristics of the A-site cation including size, shape, and charge distribution play an essential role in tuning the structural and optoelectronic behavior of halide perovskites (**Fig. 1.1e**). The structural flexibility and compositional versatility of perovskites enable precise tuning of their optoelectronic properties, thereby allowing their integration into various kinds of opto-electronic devices, including solar cells,<sup>[17-21]</sup> light-emitting diodes (LEDs),<sup>[22-27]</sup> photodetectors,<sup>[28-31]</sup> and so on.

Perovskite materials exhibit dimensional versatility, categorized primarily into three-dimensional (3D), quasi-two-dimensional (quasi-2D), one-dimensional (1D), and

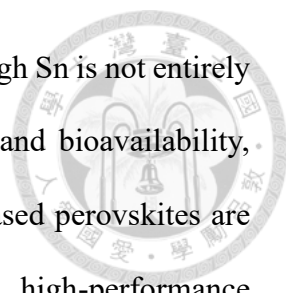


zero-dimensional (0D) configurations based on the connectivity of their inorganic frameworks (**Fig. 1.2a**).<sup>[32-34]</sup> In 3D perovskites, corner-sharing octahedral units ( $[BX_6]^{4-}$ ) form a continuous lattice structure accommodating smaller A-site cations within interstitial sites. The resulting 3D perovskites enable high carrier mobility,<sup>[35, 36]</sup> high absorption coefficients,<sup>[18, 37]</sup> direct bandgaps,<sup>[38, 39]</sup> low trap density and high photoluminescence quantum yield (PLQY)<sup>[35, 40]</sup> which together facilitate charge injection and transport and reduced nonradiative losses. The optoelectronic performance of these materials is further influenced by structural parameters such as octahedral tilting and tolerance factors, which are sensitive to A-site cation size and chemistry.<sup>[41]</sup> Ongoing research continues to explore compositional engineering, including A-site mixing, to enhance phase stability and enable commercialization of perovskite-based devices. Two-dimensional (2D) perovskites represent structurally layered metal halide perovskites that integrate organic and inorganic components in defined architectures. In classical 2D perovskites, large organic spacer cations (A') are intercalated between single layers of corner-sharing metal-halide octahedra, resulting in well-defined layered structures. The two most common structural types are the Ruddlesden–Popper (RP) and Dion–Jacobson (DJ) phases. These are typically represented by the formulas  $(A')_2BX_4$  for RP and  $(A')BX_4$  for DJ perovskites. The formation of these distinct phases is primarily governed by the nature of the organic spacer cation. Monofunctional ammonium cations (bearing a single amine group) tend to yield RP phases, whereas bifunctional diammonium cations promote the formation of DJ phases due to their ability to bridge adjacent inorganic layers more effectively.<sup>[42-46]</sup> The insulating nature of the bulky organic spacers and the strong quantum and dielectric confinement effects contribute to high exciton binding energies, strong photoluminescence, and superior stability against moisture and heat.<sup>[33, 45, 47, 48]</sup>

However, the limited charge transport across the organic layers presents challenges for electronic applications.<sup>[33, 49]</sup>

Quasi-2D perovskites, often described as layered perovskites with mixed dimensional phases, represent a more disordered yet highly tunable variant of ideal 2D structures. These materials consist of a distribution of multiple n-phase domains (e.g., n = 1, 2, 3, ...), which coexist within a single film as a result of kinetic effects during crystallization. They are generally represented by the formulas  $(A')_2(A)_{n-1}B_nX_{3n+1}$  for Ruddlesden–Popper (RP) and  $(A')(A)_{n-1}B_nX_{3n+1}$  for Dion–Jacobson (DJ) perovskites (**Fig. 1.2b-c**).<sup>[43]</sup> The resulting phase heterogeneity creates an energetic cascade, enabling excitons and charge carriers to funnel from wider-bandgap, low-n domains to narrower-bandgap, high-n domains, thereby enhancing radiative recombination in the latter.<sup>[49-51]</sup> This unique architecture allows quasi-2D perovskites to strike a balance between the structural stability of 2D perovskites and the efficient charge transport of 3D counterparts. Their tunable dimensionality, coupled with favorable energy alignment, makes them particularly attractive for light-emitting applications such as PeLEDs, where they demonstrate high photoluminescence quantum yield (PLQY) and improved operational stability.<sup>[50, 52]</sup>

Considering the environmental and health concerns associated with lead toxicity, lead-free perovskites have emerged as a promising alternative to conventional lead-based counterparts. Among various B-site substitutes, tin ( $\text{Sn}^{2+}$ ) is considered the most suitable candidate due to its similar valence electron configuration and comparable ionic radius to lead. Tin halide perovskites (THPs), such as  $\text{MASnI}_3$  and  $\text{CsSnI}_3$ , exhibit desirable optoelectronic properties including narrow bandgaps (1.3–1.4 eV), high charge carrier mobility, and long diffusion lengths which are favorable for efficient photovoltaic and light-emitting applications.<sup>[4]</sup> From an environmental standpoint, Sn-based perovskites



offer a lower toxicity profile compared to lead-based systems. Although Sn is not entirely non-toxic, its compounds generally exhibit lower water solubility and bioavailability, thereby posing a reduced ecological and health risk. As such, Sn-based perovskites are considered an essential direction in the development of sustainable, high-performance optoelectronic devices.<sup>[53]</sup>

## **1.2 Introduction of Perovskite Light-Emitting Diodes (PeLEDs)**

Since the first observation of electroluminescence in perovskite materials in 1994, perovskite light-emitting diodes (PeLEDs) have undergone rapid development.<sup>[54]</sup> Initial studies reported electroluminescence only at low temperatures, limiting practical applications. It was not until 2014 that significant breakthroughs occurred, when researchers successfully demonstrated room-temperature PeLEDs with modest external quantum efficiencies (EQEs). In 2014,  $\text{CH}_3\text{NH}_3\text{PbBr}_3$  films were sandwiched between  $\text{TiO}_2$  and F8 layers to achieve green and near-infrared EL with EQEs of 0.1% and 0.76%, respectively, as published by Tan et al.<sup>[35]</sup> This early breakthrough marked the beginning of a new era in display and lighting technologies. In less than a decade, EQEs for red and green PeLEDs have surpassed 20% due to improvements in defect passivation, phase engineering, and emissive layer design. Milestones include Friend's group pushing room-temperature PeLEDs into practical use and multiple teams independently achieving EQEs >20% in the green and red regions by 2018. However, blue-emitting PeLEDs remain a challenge due to issues such as wider bandgaps, less stable emission, and poorer carrier confinement, particularly in quasi-2D systems. Over the past eleven years, significant progress has been made in the development of PeLEDs, with green, red, and blue devices



achieving peak external quantum efficiencies (EQEs) of 32.1%,<sup>[55]</sup> 29.04%,<sup>[56]</sup> and 26.4%,<sup>[57]</sup> respectively. These advancements, primarily driven by organic additive engineering, represent an unprecedented rate of improvement in the history of light-emitting diode technologies. Despite these remarkable advances, PeLEDs continue to face several critical challenges, including efficiency roll-off at high current densities and limited operational stability (**Fig. 1.3**).

The working mechanism of a PeLED generally follows a typical p-i-n structure. Electrons and holes are injected from the cathode and anode into the perovskite emissive layer through electron transport layers (ETLs) and hole transport layers (HTLs), respectively. Upon recombination of these carriers in the emissive layer, radiative decay produces photons, resulting in light emission (**Fig. 1.4a**).<sup>[58, 59]</sup> The high PLQY of perovskite materials and their balanced charge transport capabilities facilitate efficient radiative recombination. However, non-radiative losses due to traps, imbalanced carrier injection, or poor phase distribution can limit the efficiency. Effective PeLEDs rely on minimizing these losses through optimized materials and interfaces. In quasi-2D perovskites, the natural quantum-well structure comprising alternating organic and inorganic layers enhances carrier confinement and energy funneling from small-n to large-n domains, facilitating efficient emission (**Fig. 1.4b**). However, challenges such as phase impurity, random n-phase distribution, and inefficient carrier transport across organic spacers still hinder the overall performance in PeLEDs. Ongoing efforts aim to optimize domain distribution, reduce trap densities, and improve outcoupling efficiencies through compositional tuning, additive engineering, and interfacial modification.<sup>[59-61]</sup> These strategies collectively drive the PeLEDs closer to their theoretical performance limits and enhance their competitiveness with OLEDs and QLEDs in next-generation display and lighting applications.<sup>[62, 63]</sup>

### 1.3 Research Objectives for Dimension-Specific Strategies to Enhance the Performance of Perovskite Light-Emitting Diodes



To optimize the performance of PeLEDs across various perovskite dimensionalities, distinct strategies have been developed to address their respective limitations. In 3D perovskites, various strategies such as additive engineering,<sup>[64-69]</sup> interface modification,<sup>[70-73]</sup> and low-dimensional structural engineering<sup>[74]</sup> have been extensively explored to address critical issues including poor film morphology, low exciton binding energy, and inefficient charge injection, all of which contribute to nonradiative recombination losses. Among these, additive engineering involving organic compounds,<sup>[68, 69]</sup> inorganic compounds,<sup>[67]</sup> and polymers<sup>[65, 75]</sup> has proven effective in modulating the crystallization kinetics, leading to smoother films with enhanced photoluminescence quantum yield (PLQY). Additionally, surface engineering approaches have been employed to effectively passivate surface defects and further suppress nonradiative recombination pathways.<sup>[70-73]</sup>

For quasi-2D perovskites, where random phase distribution and inefficient energy transfer hinder performance, strategies such as phase regulation using cyclic molecules (e.g., cyclodextrins, cryptands, 18-Crown-6) or organic molecules have been shown to selectively suppress low-n phases and enhance exciton funneling, leading to improved photoluminescence quantum yield (PLQY), color purity, and external quantum efficiency (EQE).<sup>[22, 76-79]</sup> Additionally, multifunctional interfacial layers like conductive phosphine oxides (PPT, PPF) serve to passivate defects and facilitate electron injection, significantly reducing efficiency roll-off under high bias conditions.<sup>[80, 81]</sup> For 2D lead-free systems, especially Sn-based PeLEDs, a major challenge lies in the oxidative instability of Sn<sup>2+</sup>. Here, dual-additive strategies, combining antioxidants (e.g., ascorbic acid) and cyclic

molecules (e.g., 18-crown-6) have proven effective in inhibiting Sn oxidation, slowing crystallization, and passivating trap states, thereby greatly enhancing film quality, emission intensity, and device stability Together, these targeted approaches highlight a multi-faceted framework for overcoming dimension-specific bottlenecks and advancing PeLED technologies toward practical applications (**Fig. 1.5**).

## 1.4 Tables and Figures

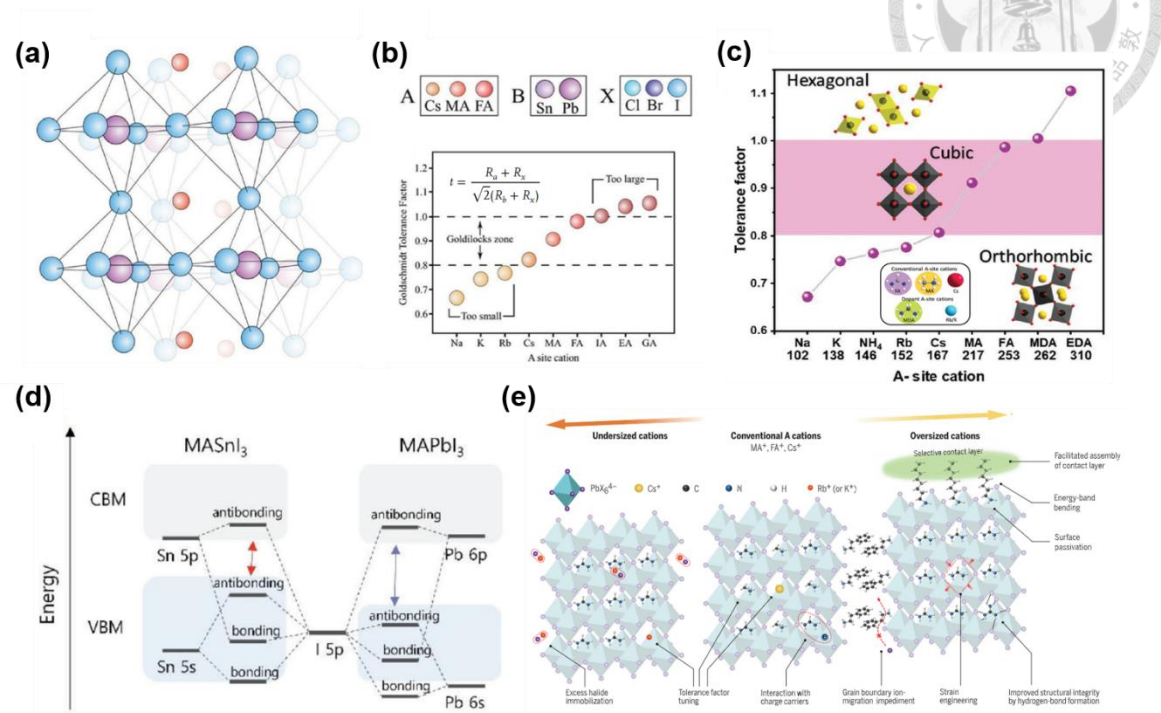


**Fig. 1.1** (a) Schematic illustration of the ABX<sub>3</sub> perovskite crystal structure. (b) Ionic radii of various A-site cations and X-site anions, along with the resulting tolerance factor variations in perovskites upon cation substitution.<sup>[82]</sup> (c) Dependence of the Goldschmidt Tolerance Factor (GTF) on the A-site cation radius in APbI<sub>3</sub> perovskites, where the shaded region (0.8 < t < 1) indicates the range for a structurally stable cubic phase.<sup>[41]</sup> (d) Energy band alignment of MASnI<sub>3</sub> and MAPbI<sub>3</sub> perovskites, highlighting differences in bandgap and electronic structure.<sup>[82]</sup> (e) Roles of the A-site cation in influencing the structural stability, phase behavior, and optoelectronic properties of halide perovskites.<sup>[15]</sup>

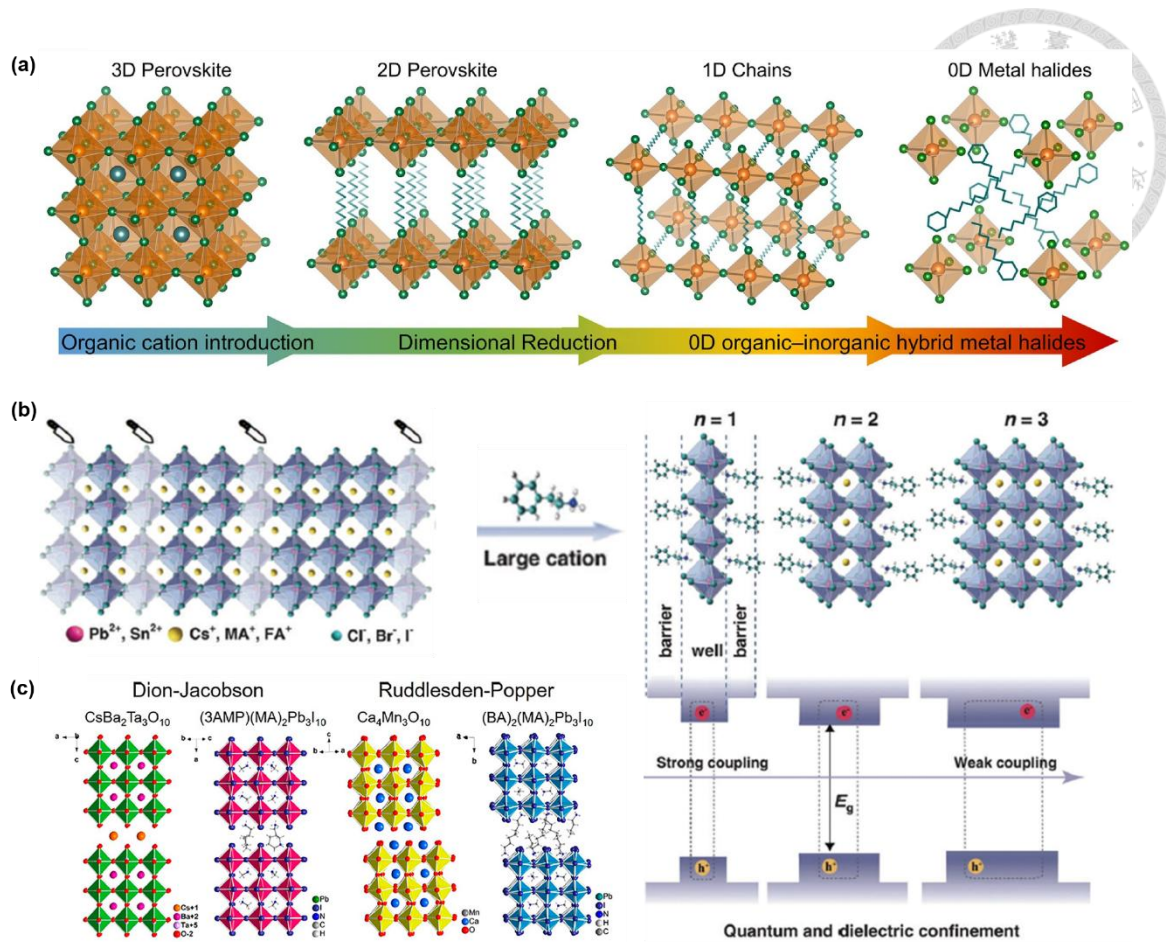
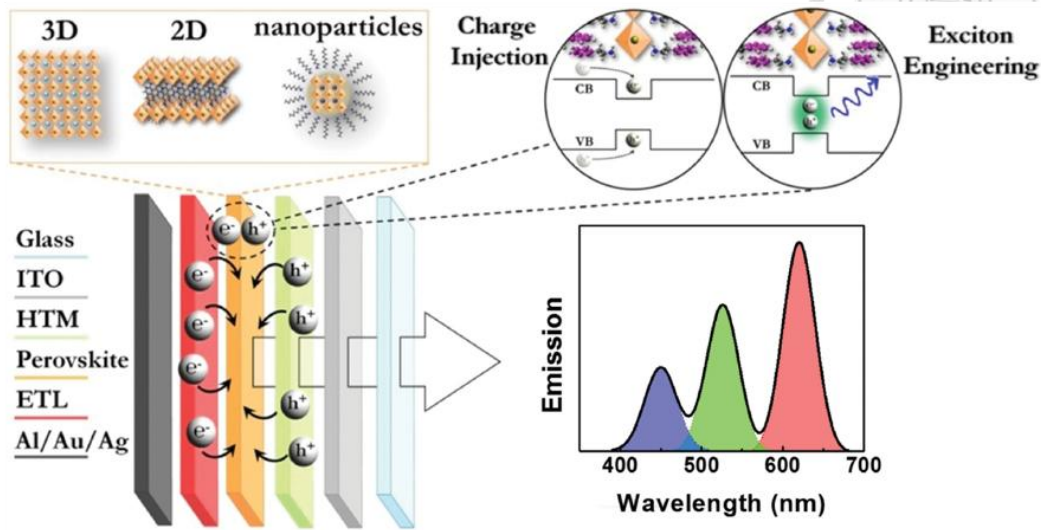


**Fig. 1.2** (a) Schematic illustration of perovskite materials with varying dimensionalities, including 3D, 2D, 1D, and 0D structures.<sup>[34]</sup> (b) Conceptual depiction of the formation mechanism, crystal structure of quasi-2D perovskites.<sup>[83]</sup> (c) Structural and compositional comparison between Dion–Jacobson (DJ) and Ruddlesden–Popper (RP) phases in both oxide and halide perovskites, emphasizing differences in spacer configuration.<sup>[46]</sup>



(a)



(b)

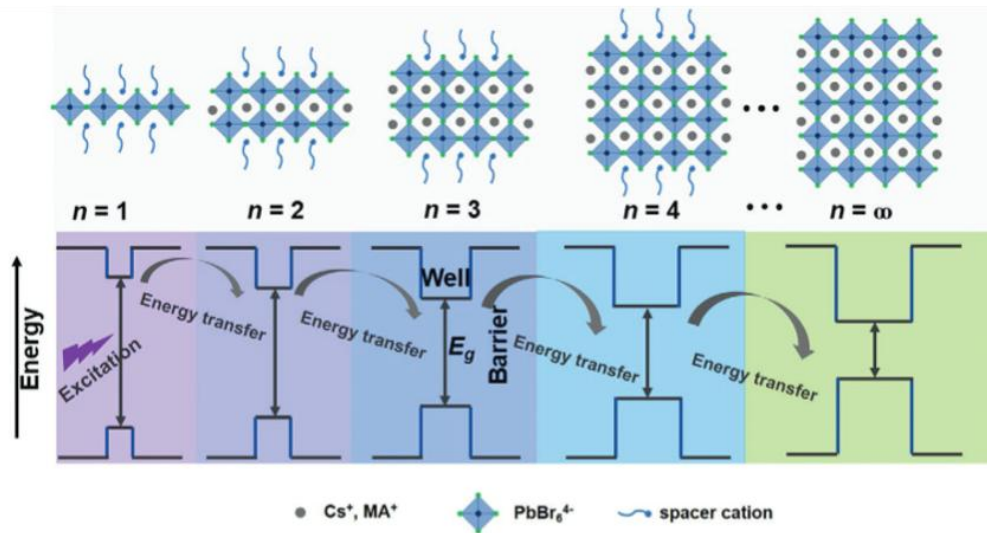


**Fig. 1.4** (a) Working mechanism of PeLEDs.<sup>[84]</sup> (b) Schematic illustration of quasi-2D perovskites and the energy transfer process.<sup>[26]</sup>

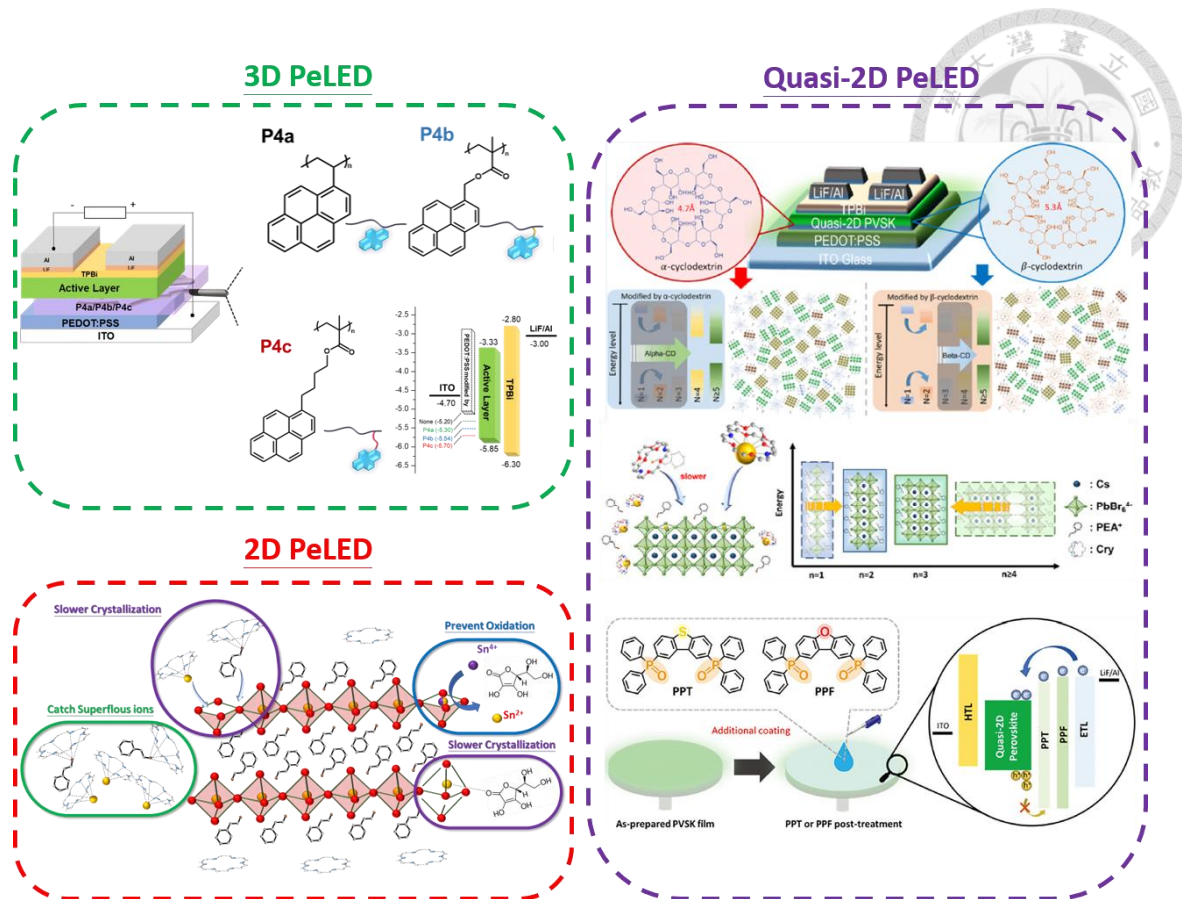


**Fig. 1.5** Objectives for dimension-specific strategies to enhance the performance of perovskite light-emitting diodes.<sup>[76, 77, 80, 85, 86]</sup>



# Chapter 2 3D All-inorganic Perovskite Light-Emitting Diodes



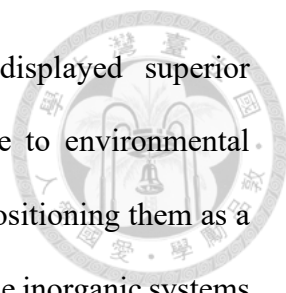
## 2.1 Engineering of 3D All-inorganic Perovskite Light-Emitting Diodes by Interlayer Modification

The text and figures in this section are reproduced with permission from:

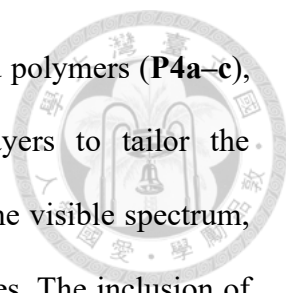
**C. H. Chen**, Y. C. Lin, Y. F. Yang, Y. C. Chiang, Z. Li, H. L. Yip, W. C. Chen\*, C. C. Chueh\*, “Improving the Performance of All-Inorganic Perovskite Light-Emitting Diodes Through Using Polymeric Interlayers with a Pendant Design”, *Mater. Chem. Front.*, 5, 7199-7207 (2021).

### 2.1.1 Background

Owing to their adjustable bandgap, high luminous efficacy, and sharp emission spectra, metal halide perovskites have rapidly become a central focus in the field of light emission and are increasingly acknowledged as a viable material for light-emitting diodes (LEDs). Initial development of perovskite LEDs (PeLEDs) primarily involved hybrid organic-inorganic compositions such as methylammonium lead bromide (MAPbBr<sub>3</sub>), which served as the emissive layer in early prototypes.<sup>[35, 74, 75, 87-89]</sup> Although these early devices exhibited modest efficiency, their demonstration marked a pivotal moment in the pursuit of solution-processable emissive materials. Within a short timeframe, the performance of MAPbBr<sub>3</sub>-based PeLEDs was significantly enhanced through methods such as additive modification<sup>[64-69]</sup> and interfacial engineering.<sup>[70-73]</sup> A notable leap in efficiency was achieved via compositional engineering. Specifically, all-inorganic



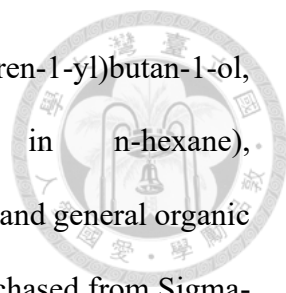
variants like CsPbX<sub>3</sub> (X = Cl<sup>-</sup>, Br<sup>-</sup>, I<sup>-</sup>, or mixed halides) displayed superior photoluminescence quantum yields (PLQYs) and greater resilience to environmental degradation and operational stress when compared with MAPbX<sub>3</sub>, positioning them as a more robust platform for PeLED development.<sup>[90-92]</sup> Nonetheless, these inorganic systems often suffer from suboptimal film morphology and interfacial charge transport due to limited solubility,<sup>[93]</sup> presenting a barrier to further progress. To address this, researchers have employed a range of approaches, such as the use of tailored molecular additives,<sup>[94-97]</sup> nanocrystal pinning strategies (NCP),<sup>[98]</sup> and incorporation of engineered interfacial layers.<sup>[99, 100]</sup> Among these tactics, interface modification, particularly at the junction between the charge-transporting layers (CTLs) and perovskite, has gained substantial traction for its simplicity and efficacy. For instance, Paul et al. reported improved device metrics by introducing a thin film of two-dimensional black phosphorus (BP) between the hole transport layer (HTL) and the perovskite.<sup>[101]</sup> The deeper HOMO level of BP relative to PEDOT:PSS enhanced hole injection across the interface. Similarly, Zheng et al. demonstrated performance gains by embedding a thin polymeric layer, either polyvinylidene fluoride (PVDF) or poly(methyl methacrylate) (PMMA), at the same interface. These interlayers not only improved surface compatibility for perovskite growth but also provided charge-blocking functions via their wide bandgaps, promoting more efficient recombination within the emissive layer.<sup>[102]</sup> On the electron-transport side, Huang et al. utilized polyethyleneimine (PEI) as an interfacial modifier at the ETL/perovskite boundary, which improved film quality and facilitated electron injection by lowering the associated energy barrier.<sup>[70]</sup> These examples collectively highlight the crucial role of interfacial engineering in modulating CTL surface properties, thereby enhancing film formation and charge transfer dynamics.



In this work, we developed a series of conjugated pyrene-based polymers (**P4a–c**), each functionalized with distinct side groups, as interfacial layers to tailor the HTL/CsPbBr<sub>3</sub> boundary. Designed for optical transparency within the visible spectrum, these polymers are well-suited for application in PeLED architectures. The inclusion of pyrene units supports favorable alignment of the HOMO level, bridging the energy offset between PEDOT:PSS and the perovskite. Our investigation revealed that the deeper HOMO levels of **P4a–c** effectively lower the work function of PEDOT:PSS, enhancing hole injection, while their broad optical bandgaps serve to suppress electron leakage. Notably, we identified the chemical nature of the pendant bridge group as a key factor influencing device performance: structures incorporating polar bridges improved the crystallinity of CsPbBr<sub>3</sub> films and facilitated more optimal energy alignment. As a result, the device incorporating P4c achieved a sixfold enhancement in peak luminance (~36,000 cd/m<sup>2</sup>) and a 3.6× boost in external quantum efficiency (EQE: 2.16%) relative to the control device (~6,000 cd/m<sup>2</sup>, 0.60%). These findings establish a promising interlayer design strategy for next-generation all-inorganic PeLEDs.

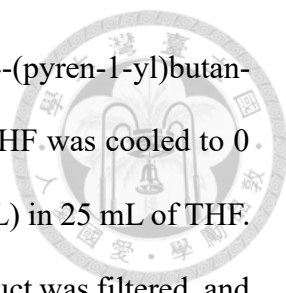
### 2.1.2 Experimental Section

**Materials.** Lead(II) bromide (PbBr<sub>2</sub>, >99.9%) and methyltriphenylphosphonium bromide were obtained from Tokyo Chemical Industry Co., Ltd. Cesium bromide (CsBr, >99.9%), lithium fluoride (LiF, >99.99%), and solvents such as dimethylformamide (DMF, 99.8%) and dimethyl sulfoxide (DMSO, ≥99.9%) were supplied by Sigma-Aldrich and used without further purification. The electron transport material 2,2',2''-(1,3,5-benzenetriyl)-tris(1-phenyl-1H-benzimidazole) (TPBi) was sourced from Ultra Fine Chemical Technology Corp., and the hole transport material PEDOT:PSS (Clevios™ P Al 4083) was purchased from Uniregion Bio-tech; both materials were used as received.



Additional reagents, including pyrene-1-carbaldehyde, 4-(pyren-1-yl)butan-1-ol, pyren-1-ylmethyl methacrylate, *n*-butyllithium (1.6 M in *n*-hexane), azobisisobutyronitrile (AIBN), methacryloyl chloride, triethylamine, and general organic solvents such as dichloromethane (DCM) and toluene, were also purchased from Sigma-Aldrich. Among these, AIBN was recrystallized from methanol before use, while the remaining chemicals were employed without additional treatment. The synthetic protocols for 1-vinylpyrene, 4-(pyren-1-yl)butyl methacrylate, and the polymer series (P4a–c) are described below. The corresponding <sup>1</sup>H NMR spectra (400 MHz, CDCl<sub>3</sub>) for these compounds are shown in **Fig. 2.1-4**.

**Synthesis of 1-vinylpyrene.** A solution of methyltriphenylphosphonium bromide (6.97 g, 19.5 mmol) in 20 mL of THF was cooled to 0 °C and dropwisely added with *n*-butyllithium (12.2 mL, 1.6 M in *n*-hexane). After stirring for 10 min at room temperature, the solution was slowly added with a solution of pyrene-1-carbaldehyde (3.00 g, 13.0 mmol) in 45 mL of THF. Afterwards, the reaction proceeded at room temperature for 16 h. The crude product was filtered, and the filtrate was diluted with DCM and extracted with water and brine sequentially. The organic phase was then dried by MgSO<sub>4</sub>, filtered, and the solvent was removed under reduced pressure. Finally, the crude product was purified by column chromatography with hexane, and the pure fractions are combined and dried to give 2.09 g (70 % yield, yellow solids). <sup>1</sup>H-NMR (**Fig. 2.1a**, 400 MHz, CDCl<sub>3</sub>),  $\delta$  (ppm): 8.36-8.39 (m, Ar-H, 1H), 8.08-8.20 (m, Ar-H, 5H), 7.96-8.03 (m, Ar-H, 3H), 7.74-7.81 (m, Ar-CH, 1H), 5.95-6.00 (dd, CH-CH<sub>2</sub>, 1H), 5.58-5.61 (dd, CH-CH<sub>2</sub>, 1H).

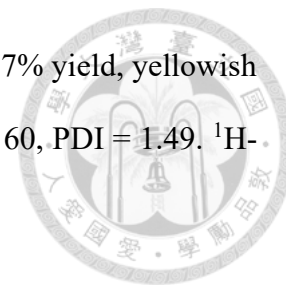


**Synthesis of 4-(pyren-1-yl)butyl methacrylate.** A solution of 4-(pyren-1-yl)butan-1-ol (1.00 g, 3.64 mmol) and 0.6 mL of triethylamine in 25 mL of THF was cooled to 0 °C and slowly added with a solution of methacryloyl chloride (0.4 mL) in 25 mL of THF. The reaction proceeded at room temperature for 16 h. The crude product was filtered, and the filtrate was diluted with DCM and extracted with water and brine sequentially. The organic phase was then dried by MgSO<sub>4</sub>, filtered, and the solvent was removed under reduced pressure. Finally, the crude product was purified by column chromatography with hexane/ethyl acetate, and the pure fractions were combined and dried to give 0.66 g (53% yield, yellow oil). <sup>1</sup>H-NMR (**Fig. 2.1b**, 400 MHz, CDCl<sub>3</sub>), δ (ppm): 8.23-8.26 (m, Ar-H, 1H), 8.07-8.16 (m, Ar-H, 4H), 7.97-8.01 (m, Ar-H, 3H), 7.84-7.86 (m, Ar-CH, 1H), 5.52-6.08 (d, C-CH<sub>2</sub>, 2H), 4.20-4.23 (t, O-CH<sub>2</sub>-CH<sub>2</sub>, 2H), 3.36-3.40 (t, Ar-CH<sub>2</sub>-CH<sub>2</sub>, 2H), 1.83-1.99 (br, CH<sub>2</sub>-CH<sub>2</sub>-CH<sub>2</sub>, -CH<sub>3</sub>, 7H).

**Synthesis of poly(1-vinylpyrene) (P4a).** 1-Vinylpyrene (2.00 g, 8.8 mmol) was dissolved in 18 mL of toluene and the solution was degassed with three freeze-pump cycles. Afterwards, AIBN (14 mg, 1 mol% respect to 1-vinylpyrene) was added and the polymerization proceeded at 80 °C for 24 h. Crude polymers were precipitated in MeOH to afford 0.89 g (44% yield, yellowish solids). Molecular weight evaluated by size exclusion chromatography (SEC): Mn = 8150, Mw = 13850, PDI = 1.70. <sup>1</sup>H-NMR (400 MHz, CDCl<sub>3</sub>) of **P4a** is presented in **Fig. 2.2**.

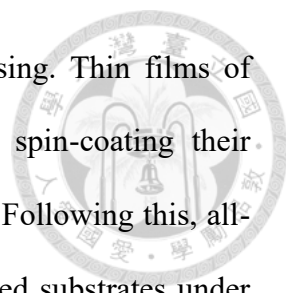
**Synthesis of poly(pyren-1-ylmethyl methacrylate) (P4b).** Pyren-1-ylmethyl methacrylate (2.00 g, 6.7 mmol) was dissolved in 13 mL of toluene and the solution was degassed with three freeze-pump cycles. Afterwards, AIBN (47 mg, 5 mol% respect to pyren-1-ylmethyl methacrylate) was added and the polymerization proceeded at 80 °C for

24 h. Crude polymers were precipitated in MeOH to afford 1.73 g (77% yield, yellowish solids). Molecular weight evaluated by SEC:  $M_n = 8810$ ,  $M_w = 13160$ ,  $PDI = 1.49$ .  $^1H$ -NMR (400 MHz,  $CDCl_3$ ) of **P4b** is presented in **Fig. 2.3**.



**Synthesis of poly(4-(pyren-1-yl)butyl methacrylate) (P4c).** 4-(Pyren-1-yl)butyl methacrylate (0.66 g, 2.0 mmol) was dissolved in 5 mL of toluene and the solution was degassed with three freeze-pump cycles. Afterwards, AIBN (10 mg, 3 mol% respect to 4-(pyren-1-yl)butyl methacrylate) was added and the polymerization proceeded at 80 °C for 24 h. Crude polymers were precipitated in MeOH to afford 0.55 g (83% yield, yellowish solids). Molecular weight evaluated by SEC:  $M_n = 6670$ ,  $M_w = 13140$ ,  $PDI = 1.97$ .  $^1H$ -NMR (400 MHz,  $CDCl_3$ ) of **P4c** is presented in **Fig. 2.4**.

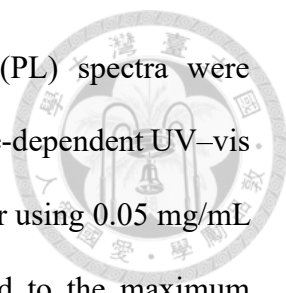
**Device fabrication.** The preparation of the perovskite precursor solution involves dissolving CsBr and  $PbBr_2$  in 1ml of DMSO with a molar ratio of 1.5:1, followed by stirring at room temperature overnight. Prior to film deposition, the ITO-coated glass substrates were thoroughly cleaned, beginning with a detergent wash, followed by sequential ultrasonication in deionized water, acetone, and isopropyl alcohol for 15 minutes each. After cleaning, the substrates were dried using a nitrogen gun and further dehydrated in an oven at 60°C to eliminate residual solvents. Finally, the cleaned substrates were subjected to plasma treatment to render their surfaces hydrophilic. For material characterization, perovskite films were prepared by spin-coating the precursor solutions at 4000 rpm for 60 seconds. In the device fabrication process, a hole-transport layer (HTL) of PEDOT:PSS was first deposited onto pre-cleaned substrates via spin-coating at 3500 rpm for 40 seconds, followed by thermal annealing at 150 °C for 15 minutes under ambient conditions. The PEDOT:PSS-coated substrates were then



transferred into a nitrogen-filled glove box for subsequent processing. Thin films of polymers P4a–c were deposited onto the PEDOT:PSS layer by spin-coating their precursor solutions (0.5 mg/mL in DMF) at 4000 rpm for 1 minute. Following this, all-inorganic CsPbBr<sub>3</sub> films were spin-coated onto the polymer-modified substrates under the same conditions (4000 rpm for 60 seconds), and then annealed at 70 °C for 10 minutes. The PeLED device architecture was finalized by sequential thermal evaporation of TPBi (30 nm), LiF (1 nm), and aluminum (120 nm) under high vacuum ( $<10^{-6}$  Torr).

**SCLC measurement.** For the hole-only device, the PEDOT:PSS HTL is deposited onto the ITO substrate by spin coating at 3500 rpm for 40 seconds, followed by annealing at 150°C for 15 minutes in air. Subsequently, the PEDOT:PSS-coated substrates were transferred into a nitrogen-filled glove box, where films of P4a-c and the all-inorganic CsPbBr<sub>3</sub> layer were deposited following the methods described previously. Finally, MoO<sub>3</sub> (8 nm) and Ag (100 nm) layers were sequentially deposited via thermal evaporation under high vacuum conditions ( $<10^{-6}$  Torr). For the electron-only devices, ZnO layers were prepared by spin-coating a precursor solution—consisting of 0.1 g zinc acetate dissolved in 1 mL of 2-methoxyethanol, with 28  $\mu$ L ethanolamine added as a stabilizer—onto ITO substrates, followed by annealing at 200°C for 30 minutes in ambient air. Afterward, these ZnO-coated substrates were transferred into a nitrogen-filled glove box, where films of P4a-c and all-inorganic CsPbBr<sub>3</sub> were deposited using the aforementioned procedures. Device fabrication was finalized by sequential thermal evaporation of TPBi (30 nm), LiF (1 nm), and Al (120 nm) layers under high vacuum conditions ( $<10^{-6}$  Torr).

**Characterization.** <sup>1</sup>H-NMR spectra were recorded on a Bruker AVIII HD 400 spectrometer operating at 400 MHz. UV–visible absorption spectra were measured using

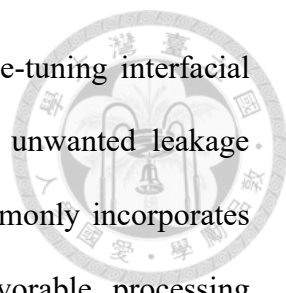


a Hitachi U-4100 spectrophotometer, while photoluminescence (PL) spectra were obtained using a Horiba Fluorolog-3 spectrofluorometer. Temperature-dependent UV-vis measurements were conducted with a Jasco V-650 spectrophotometer using 0.05 mg/mL solutions of the P4a-c polymers, and the spectra were normalized to the maximum absorption peak. Surface morphology and roughness were analyzed by atomic force microscopy (AFM) in tapping mode using a MultiMode system with a Nanoscope 3D controller (Digital Instruments). Contact angles were measured using a CAM 110 contact angle goniometer (Creating Nano Technologies, Inc.). Scanning electron microscopy (SEM) images were acquired with a Nova™ NanoSEM 230 instrument. HOMO energy levels were determined using a photoelectron spectrometer (model AC-2, Riken Keiki). Optical bandgaps ( $E_g$ ) were estimated from Tauc plots, assuming a direct transition. Structural properties and phase identification were carried out via X-ray diffraction (XRD) using a Rigaku SmartLab SE diffractometer. Grazing-incidence wide-angle X-ray scattering (GIWAXS) patterns were collected at the TLS 17A1 beamline of the National Synchrotron Radiation Research Center (NSRRC), using an incidence angle of  $0.12^\circ$  and a sample-to-detector distance of approximately 234.4 mm. Electrical characterizations, including current density-voltage-luminance (J-V-L), external quantum efficiency (EQE), and electroluminescence (EL) measurements, were performed using an LQ-100 system (Enlitech Co., Ltd.) equipped with a 100 mm integrating sphere. All measurements were conducted in ambient air on encapsulated PeLED devices.

### 2.1.3 Results and Discussion

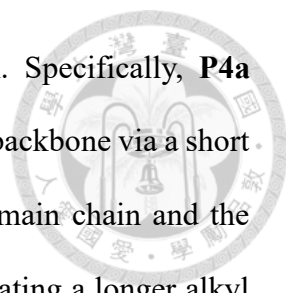
**Characterization of synthesized polymers.** Interface engineering has gained significant attention as an effective strategy for improving the performance of multilayered optoelectronic devices. By optimizing the interfaces between layers, this





method enhances film uniformity and compatibility while also fine-tuning interfacial energy levels to support efficient charge transport and minimize unwanted leakage currents. In the field of PeLEDs, the p-i-n device architecture commonly incorporates PEDOT:PSS as the hole transport layer (HTL) due to its favorable processing characteristics. However, PEDOT:PSS also presents several limitations, such as poor chemical stability and suboptimal energy level alignment that can hinder device efficiency if not properly addressed through surface modification techniques.<sup>[103]</sup> For instance, the energy level mismatch between PEDOT:PSS and the perovskite layer can result in increased leakage current and inefficient, uneven charge injection into the perovskite emitter.<sup>[104]</sup> Moreover, the surface properties of PEDOT:PSS can negatively impact the morphology and crystallinity of the overlying perovskite film,<sup>[68]</sup> potentially leading to suboptimal film quality. In addition, its acidic nature poses risks of etching the underlying ITO electrode or degrading the perovskite layer during extended device operation.<sup>[105]</sup> As a result, numerous surface modification strategies for PEDOT:PSS have been investigated to enhance the performance of PeLEDs. These include removing excess surface PSS to improve conductivity,<sup>[106, 107]</sup> introducing additional polymer interlayers<sup>[102]</sup>, and tuning the film thickness to control the charge recombination zone.<sup>[108]</sup> Despite their varied approaches, these strategies share a common goal to tailor the surface and electronic properties of PEDOT:PSS for improved interfacial quality and device efficiency.

Based on the aforementioned design strategy, we synthesized a series of polymers, designated as **P4a–c**, each containing a common pendant pyrene moiety but differing in their bridge group structures. This molecular design was intended to achieve deep-lying HOMO energy levels while retaining high optical transparency across the visible spectrum. The molecular structures of **P4a–c** are illustrated in **Fig. 2.5a**, and detailed



synthetic procedures can be found in the Supporting Information. Specifically, **P4a** features a minimal design, with the pyrene unit linked directly to the backbone via a short alkyl chain. **P4b** introduces an ester linkage between the polymer main chain and the pyrene pendant, while **P4c** extends this structure further by incorporating a longer alkyl spacer between the ester group and the pyrene unit. The successful synthesis of these polymers is confirmed by the  $^1\text{H}$  NMR spectra of both the monomers and the resulting polymers, shown in **Fig. 2.1–Fig. 2.4**. Solubility tests (**Fig. 2.6**) reveal that all three polymers are readily soluble in DMF but insoluble in DMSO. This behavior can be attributed to the relatively low polarity of **P4a–c**, which contrasts with the higher polarity of DMSO. Consequently, their incompatibility with DMSO makes them ideal candidates for interfacial modification in perovskite devices, as they remain chemically stable when deposited atop perovskite layers processed from DMSO-based solvents, such as in typical perovskite fabrication protocols.

As previously discussed, a notable energy offset exists at the interface between PEDOT:PSS (HOMO: -5.2 eV) and  $\text{CsPbBr}_3$  (valence band maximum: -5.85 eV),<sup>[109]</sup> which can hinder efficient hole injection. To address this interfacial mismatch, a thin interlayer with a deeper HOMO level than PEDOT:PSS is proposed to improve band alignment and facilitate charge transfer. Accordingly, the energy levels of the synthesized polymers **P4a–c** were determined using photoelectron spectroscopy (PES). As shown in **Fig. 2.5b**, **P4a** displays a HOMO level of -5.76 eV, which is significantly deeper than that of PEDOT:PSS, owing to its pendant pyrene structure. To further tailor the electronic properties and improve solubility, an ester functionality was introduced between the pyrene and alkyl chain, yielding **P4b** with a methacrylate group. This modification resulted in a slightly deeper HOMO level of -5.82 eV. In the case of **P4c**, a four-carbon alkyl spacer was inserted between the ester linkage and the pyrene unit. This structural

insulation of the conjugated pyrene moiety broadened the optical bandgap ( $E_g$ ), leading to a higher LUMO level (-2.81 eV) while maintaining a deep HOMO level of -5.86 eV. These results confirm that all three polymers possess deeper HOMO levels than PEDOT:PSS, highlighting their suitability as interfacial modifiers to enhance hole transport at the PEDOT:PSS/CsPbBr<sub>3</sub> junction.

The UV-vis absorption spectra of **P4a–c** films are shown in **Fig. 2.5c**, revealing comparable overall absorption profiles among the three polymers, yet with noticeable differences in aggregation behavior attributable to their distinct pendant group structures. Each polymer exhibits two characteristic absorption bands: a high-energy band in the 260–310 nm range, corresponding to the intrinsic absorption of the pyrene moiety, and a broader band between 320–400 nm, ascribed to intramolecular vibrational coupling along the polymer backbone. The inset of **Fig. 2.5c** provides a magnified view of the second absorption band, highlighting the vibronic transitions (0–0 and 0–1). The intensity ratios of the 0–0 to 0–1 peaks were calculated to be 1.088 for **P4a**, 1.145 for **P4b**, and 1.176 for **P4c**. These increasing ratios suggest enhanced molecular aggregation from **P4a** to **P4c**. In particular, the incorporation of a methacrylate unit in **P4b** appears to promote closer packing, while the additional alkyl spacer in **P4c** further amplifies aggregation of the pyrene side groups rather than causing their segregation. To further investigate the aggregation behavior, temperature-dependent UV-vis absorption spectra of **P4a–c** in solution were recorded (**Fig. 2.7a–c**), with the results summarized in **Fig. 2.7d**. Both **P4b** and **P4c** displayed minimal spectral changes from 20 to 60 °C, with slight increases in the 0–0/0–1 intensity ratio, indicative of stable and persistent aggregation across the temperature range. In contrast, **P4a** showed a noticeable decrease in absorption intensity with rising temperature, suggesting a tendency toward disaggregation or weaker intermolecular interactions. Collectively, these observations indicate that structural

modifications to the pendant group significantly influence the aggregation tendencies of **P4a–c**. These differences may, in turn, affect their performance as interfacial layers in PeLEDs by modulating film morphology and intermolecular packing.

**Fig. 2.8** presents the Tauc plots derived from the UV-vis absorption spectra of **P4a–c**. Thanks to their pendant design, all of these polymers exhibit wide energy bandgaps ( $E_g$ ) and high transparency in the visible light region, making them suitable candidates for interlayers in devices, thereby avoiding parasitic absorption of the emitting light from CsPbBr<sub>3</sub>. The estimated  $E_g$  values for **P4a**, **P4b**, and **P4c** are 2.7, 2.8, and 3.05 eV, respectively. Combining these results with the PES data, their lowest unoccupied molecular orbital (LUMO) energy levels can be calculated and summarized in **Fig. 2.5a**. Notably, **P4c** demonstrates the deepest HOMO level at -5.86 eV, along with the highest LUMO level at -2.81 eV. When serving as an interlayer, its deep HOMO level can better adjust the interfacial band alignment across the PEDOT:PSS/CsPbBr<sub>3</sub> interface, while its high LUMO level presents a significant potential barrier for electron blocking, enhancing charge combination in the CsPbBr<sub>3</sub> film. Further details will be discussed in subsequent sections. In summary, **P4a–c** exhibit promising potential for modifying the PEDOT:PSS/CsPbBr<sub>3</sub> interface to enhance hole injection and reduce leakage current in derived PeLEDs.

**Polymeric interlayer's effect on the CsPbBr<sub>3</sub> film.** The effect of **P4a–c** on the CsPbBr<sub>3</sub> film grown atop them was investigated and compared to films grown on pristine PEDOT:PSS HTL. It is worth noting that, due to their insulating nature, the thickness of these polymeric interlayers (**P4a–c**) should be minimized when incorporated into the device, with an optimized thickness of approximately 5 nm in our experiments (further optimization details will be discussed later). **Fig. 2.9** displays atomic force microscope

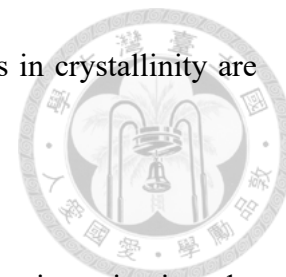
(AFM) images of films comprising pristine PEDOT:PSS and PEDOT:PSS/**P4a-c** (5 nm). The images reveal that the surface texture of PEDOT:PSS undergoes a homogeneous change after **P4a-c** coating, indicating uniform film formation. The root mean square ( $R_q$ ) values for PEDOT:PSS, PEDOT:PSS/**P4a**, PEDOT:PSS/**P4b**, and PEDOT:PSS/**P4c** films are 1.17, 2.19, 2.52, and 2.76 nm, respectively. This discrepancy in  $R_q$  can be attributed to their distinct aggregation behaviors, as discussed earlier. Specifically, **P4b** and **P4c**, exhibiting a higher propensity for aggregation, resulted in a rougher surface compared to **P4a**.

**Fig. 2.10a** illustrates the UV-vis absorption spectra of the PEDOT:PSS/CsPbBr<sub>3</sub> and PEDOT:PSS/**P4a-c** (5 nm)/CsPbBr<sub>3</sub> films. The main absorption peak of CsPbBr<sub>3</sub> at ~520 nm is clearly observed, while the absorption of **P4a-c** is not prominent due to its extremely thin thickness. In **Fig. 2.10b**, only one emission peak at 525 nm attributed to CsPbBr<sub>3</sub> is observed in the photoluminescence (PL) spectra. Although the emission peak of CsPbBr<sub>3</sub> shows no clear shift when grown on the **P4a-c**-modified PEDOT:PSS HTL, its PL intensity changes. Compared to pristine PEDOT:PSS, the PL intensity of CsPbBr<sub>3</sub> increases when grown on **P4a-c**, with the intensity gradually increasing from **P4a** to **P4c**. This enhanced PL intensity likely indicates improved film quality and enhanced radiative recombination for the CsPbBr<sub>3</sub> film grown on the polymer-modified PEDOT:PSS HTL. Additionally, the polymer structure appears to play a significant role in the degree of PL enhancement, suggesting distinct interactions between the perovskite precursor solution and the polymeric interlayers. To investigate this further, the surface energy of **P4a-c** films was characterized by contact angle measurement using water and glycerol. According to the Wu model, the calculated surface energy for **P4a**, **P4b**, and **P4c** is 43.8, 54.9, and 61.3 mN/m, respectively (**Fig. 2.11**). The varying surface polarity among **P4a-c** suggests differences in their surface texture, which likely correlates with their different

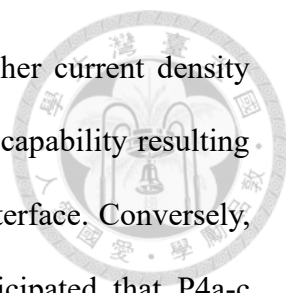
aggregation behaviors discussed earlier. Notably, **P4c** exhibited the most hydrophilic surface with the highest surface energy. This characteristic could promote the formation of smaller perovskite crystals,<sup>[110]</sup> which is advantageous for enhancing the quantum confinement effect. This may explain the observed increase in PL intensity.<sup>[111]</sup> The reduction in crystal size of CsPbBr<sub>3</sub> was validated through scanning electron microscope (SEM) imaging, as depicted in **Fig. 2.12**. Although all CsPbBr<sub>3</sub> films exhibited similar surface morphology, those grown on **P4a-c** appeared to have slightly smaller crystals.

The enhanced crystallinity of the CsPbBr<sub>3</sub> film deposited on the **P4a-c**-modified PEDOT:PSS HTLs is evident in the X-ray diffraction (XRD) analysis. In **Fig. 2.13a**, diffraction peaks at approximately 15°, 21°, and 30°, corresponding to the (100), (110), and (200) planes, respectively, are observed for the CsPbBr<sub>3</sub> film grown on pristine PEDOT:PSS HTL.<sup>[112, 113]</sup> When deposited on **P4a-c**, these diffraction peaks retain their positions but exhibit increased intensity, particularly notable in the case of **P4c**, consistent with the photoluminescence intensity enhancements observed (**Fig. 2.10b**). Subsequently, grazing incidence wide angle X-ray diffraction (GIWAX) patterns were obtained for these CsPbBr<sub>3</sub> films. **Fig. 2.13b** and **c** compare the GIWAXS patterns of PEDOT:PSS/CsPbBr<sub>3</sub> and PEDOT:PSS/**P4c**/CsPbBr<sub>3</sub>, respectively, while **Fig. 2.14a** and **b** depict the patterns of PEDOT:PSS/**P4a**/CsPbBr<sub>3</sub> and PEDOT:PSS/**P4b**/CsPbBr<sub>3</sub>. Enhanced crystallization in the CsPbBr<sub>3</sub> films grown on the **P4a-c**-modified PEDOT:PSS HTLs is clearly evident. Taking **P4c** as an example, the CsPbBr<sub>3</sub> film deposited on it exhibits a more prominent ring at ~1.53 Å compared to the film grown on PEDOT:PSS, alongside a clearer peak at ~0.92 Å. Moreover, as depicted in the corresponding 1D profiles (**Fig. 2.13d**), the intensities of characteristic peaks at ~0.92 Å, ~1.08 Å, and ~1.53 Å are higher for CsPbBr<sub>3</sub> films grown on **P4c** than on PEDOT:PSS. These findings strongly indicate the improved

crystallinity of CsPbBr<sub>3</sub> films grown on **P4c**. Similar enhancements in crystallinity are observed for **P4a** and **P4b** (Fig. 2.14c) but with a lower degree.



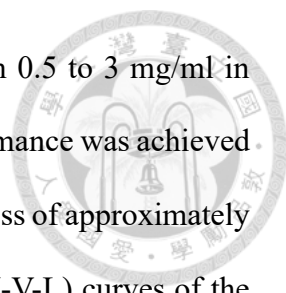
**Characterizations of interfacial electrical properties.** After investigating the impacts of **P4a-c** on the morphology and crystallinity of the CsPbBr<sub>3</sub> films, their effects on the interfacial electrical properties at the PEDOT:PSS/perovskite interface were examined. As discussed earlier, it was anticipated that **P4a-c** could improve energy-level alignment across this interface due to their deeper-lying HOMO levels compared to PEDOT:PSS. To verify this, we measured the work function (WF) values and the HOMO levels of the PEDOT:PSS/**P4a-c** films using ultraviolet photoelectron spectroscopy (UPS) (Fig. 2.15). Taking Fig. 2.15a as an example, the WF and the onset of the PEDOT:PSS/**P4a** film were at 16.53 and 0.663 eV (binding energy), respectively. With the UPS UV source providing 21.2 eV incident power, the WF value and HOMO level were estimated to be 4.67 and 5.33 eV, respectively. Similarly, the HOMO levels for the PEDOT:PSS/**P4b** and PEDOT:PSS/**P4c** films were calculated to be 5.54 and 5.70 eV, respectively (Fig. 2.15b,c). As illustrated in Fig. 2.16a, **P4a-c** interlayers effectively shifted down the energy level of PEDOT:PSS to better align with the HOMO level of the CsPbBr<sub>3</sub> film, with the degree of downshift correlating well with the HOMO levels of **P4a-c**. These downshifted energy levels consequently reduced the potential barrier across the interface, facilitating hole transport. To understand how **P4a-c** affect the charge dynamics across the PEDOT:PSS/CsPbBr<sub>3</sub> interface, space charge limited current (SCLC) measurements were conducted. Initially, hole-only devices were fabricated with a device configuration of ITO/PEDOT:PSS/**P4a-c**/CsPbBr<sub>3</sub>/MoO<sub>3</sub>/Ag, and the results were compared with those of the control device (ITO/PEDOT:PSS/CsPbBr<sub>3</sub>/MoO<sub>3</sub>/Ag). The resulting current density-voltage (J-V) curves of these devices are displayed in Fig. 2.16b.



It is evident that the devices using **P4a-c** interlayers exhibited higher current density compared to the control device, indicating improved hole transport capability resulting from a reduced potential barrier across the PEDOT:PSS/CsPbBr<sub>3</sub> interface. Conversely, considering the energy-level diagram (**Fig. 2.16a**), it can be anticipated that P4a-c interlayers better block electrons due to their shallower LUMO levels. Subsequently, electron-only devices were fabricated with a device structure of ITO/ZnO/**P4a-c**/CsPbBr<sub>3</sub>/TPBi/LiF/Al, and their performance was compared with that of the control device (ITO/ZnO/CsPbBr<sub>3</sub>/TPBi/LiF/Al). **Fig. 2.16c** presents the resulting current density-voltage curves of these devices. As observed, the control device exhibited higher current density compared to the devices incorporating **P4a-c** interlayers. This outcome unequivocally demonstrates the superior electron-blocking effect exerted by **P4a-c** during device operation.<sup>[102]</sup> It's worth noting that due to its deepest HOMO level and lowest LUMO level, **P4c** demonstrated the most effective capability to modulate the electrical properties at the PEDOT:PSS/perovskite interface, potentially leading to the highest device performance. This highlights the significant role of fine-tuning the structures of **P4a-c** for optimizing device performance.

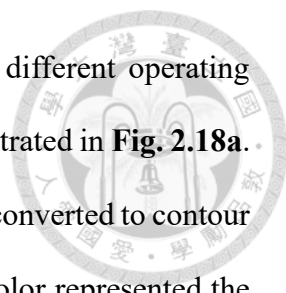
**Fabrication and characterization of PeLEDs.** We proceeded to fabricate PeLEDs using **P4a-c** to modify the PEDOT:PSS HTL. The device structure was ITO/PEDOT:PSS/**P4a-c**/CsPbBr<sub>3</sub>/TPBi/LiF/Al, with a control device (ITO/PEDOT:PSS/CsPbBr<sub>3</sub>/TPBi/LiF/Al) fabricated for comparison. Denoted as Device I, Device II, and Device III, the PeLEDs were made using **P4a**, **P4b**, and **P4c**, respectively. The energy-level diagram of the fabricated PeLEDs is presented in **Fig. 2.17a**. Considering the insulating nature of **P4a-c**, the thickness of these interlayers needed optimization. To achieve this, various concentrations of polymer solutions were utilized for device





fabrication. Taking **P4a** as an example, concentrations ranging from 0.5 to 3 mg/ml in DMF were tested, with the results shown in **Fig. 2.19**. Optimal performance was achieved with a solution concentration of 0.5 mg/ml, corresponding to a thickness of approximately 5 nm. **Fig. 2.17b** illustrates the current density-voltage-luminance (J-V-L) curves of the optimized devices for **P4a-c**, with relevant performance parameters summarized in **Table 2.1**. As demonstrated, Devices I-III exhibited significant improvements in both luminance and current density compared to the control device, highlighting the efficacy of **P4a-c** in enhancing the performance of all-inorganic CsPbBr<sub>3</sub> PeLEDs. Particularly noteworthy is Device III, which achieved the highest luminance ( $L_{\max}$ ) of 36,072.4 cd/m<sup>2</sup>, representing a six-fold enhancement compared to the control device's value of 5,979.0 cd/m<sup>2</sup>. Devices I and II achieved  $L_{\max}$  values of 28,788.6 cd/m<sup>2</sup> and 32,927.5 cd/m<sup>2</sup>, respectively. Despite having lower  $L_{\max}$  values than Device III, both devices still exhibited significantly improved performance compared to the control device. The variations in performance among Devices I-III can be attributed to their differential impacts on the morphology and crystallization of the CsPbBr<sub>3</sub> films, as well as their distinct energy levels.

The influence of **P4a-c** in enhancing the electrical properties across the PEDOT:PSS/perovskite interface was initially evidenced by the reduction in turn-on voltage ( $V_{\text{on}}$ ) of the device. Devices I-III exhibited a lower  $V_{\text{on}}$  of 2.5 V compared to the control device. Additionally, Devices I-III showed increased current efficiency (CE) and external quantum efficiency (EQE), as depicted in **Fig. 2.19c,d**, respectively. Among them, Device III demonstrated the highest  $CE_{\max}$  of 6.97 cd/A and the highest  $EQE_{\max}$  of 2.16%, representing 3-4 times higher values than those of the control device (2.35 cd/A and 0.60%, respectively). These enhancements validate the effectiveness of **P4a-c** interlayers in reducing the potential barrier across the PEDOT:PSS/perovskite interface, thereby facilitating improved hole injection.



The electroluminescence (EL) spectra of these devices under different operating voltages were then measured, and the spectrum of Device III was illustrated in **Fig. 2.18a**. To facilitate comparison, the EL spectrum of each device was further converted to contour plots, as presented in **Fig. 2.18b** and **Fig. 2.20a-c**, where the same color represented the same EL intensity. A significant difference between the control device and Devices I-III was clearly observed. The control device required a much higher operating voltage ( $> 3.75$  V) to reach the same EL intensity as Devices I-III. Additionally, a slight discrepancy was observed among Devices I-III. Device I required a higher operating voltage ( $> 3.25$  V) than Devices II and III ( $\sim 3.1$  V) to achieve the same EL intensity. Such discrepancies among them were again attributed to the different energy levels of **P4a-c**, which induced different degrees of energy-level shifting at the PEDOT:PSS interface. From the above results, the effectiveness of **P4a-c** in enhancing the performance of all-inorganic CsPbBr<sub>3</sub> PeLEDs was clearly demonstrated.

#### 2.1.4 Summary

To conclude, we developed a series of polymers (**P4a-c**), each incorporating a pyrene side group and distinct bridging units. This pendant-type molecular design enabled the polymers to achieve deep HOMO energy levels and strong optical transparency throughout the visible spectrum. When applied as interfacial modifiers between PEDOT:PSS and CsPbBr<sub>3</sub> in PeLED architectures, these polymers reduced the work function of PEDOT:PSS due to their deep HOMO levels, thereby promoting more efficient hole injection. Additionally, their wide bandgaps served as effective electron-blocking layers, helping to suppress leakage currents. The structural variations in the bridge moieties of **P4a-c** influenced both the energy-level alignment and aggregation behavior in the solid state, ultimately impacting device performance. Among all of them,

**P4c** bearing a polar bridging group exhibited the best device performance by optimizing interfacial energy alignment and assisting in controlled CsPbBr<sub>3</sub> crystallization. PeLEDs incorporating **P4c** achieved a sixfold increase in peak luminance (~36,000 cd/m<sup>2</sup>) and a 3.6-fold enhancement in external quantum efficiency (EQE, 2.16%) compared to the unmodified control (~6,000 cd/m<sup>2</sup>, 0.60%). Furthermore, devices with P4a–c interlayers demonstrated reduced turn-on voltages, underscoring their role in mitigating interfacial barriers and improving charge injection. These results highlight a promising strategy for designing functional organic interlayers tailored for enhancing the performance of all-inorganic perovskite LEDs.

### 2.1.5 Tables and Figures

**Table 2.1** Device performance of fabricated PeLEDs.

Device	V <sub>on</sub> (V)	CE <sub>max</sub> (cd/A)	Max. Lum. (cd m <sup>-2</sup> )	Max. EQE (%)
Control	3	2.35	5979.0	0.60
I (P4a)	2.5	5.10	28788.6	1.40
II (P4b)	2.5	6.32	32927.5	1.74
III (P4c)	2.5	6.97	36072.4	2.16

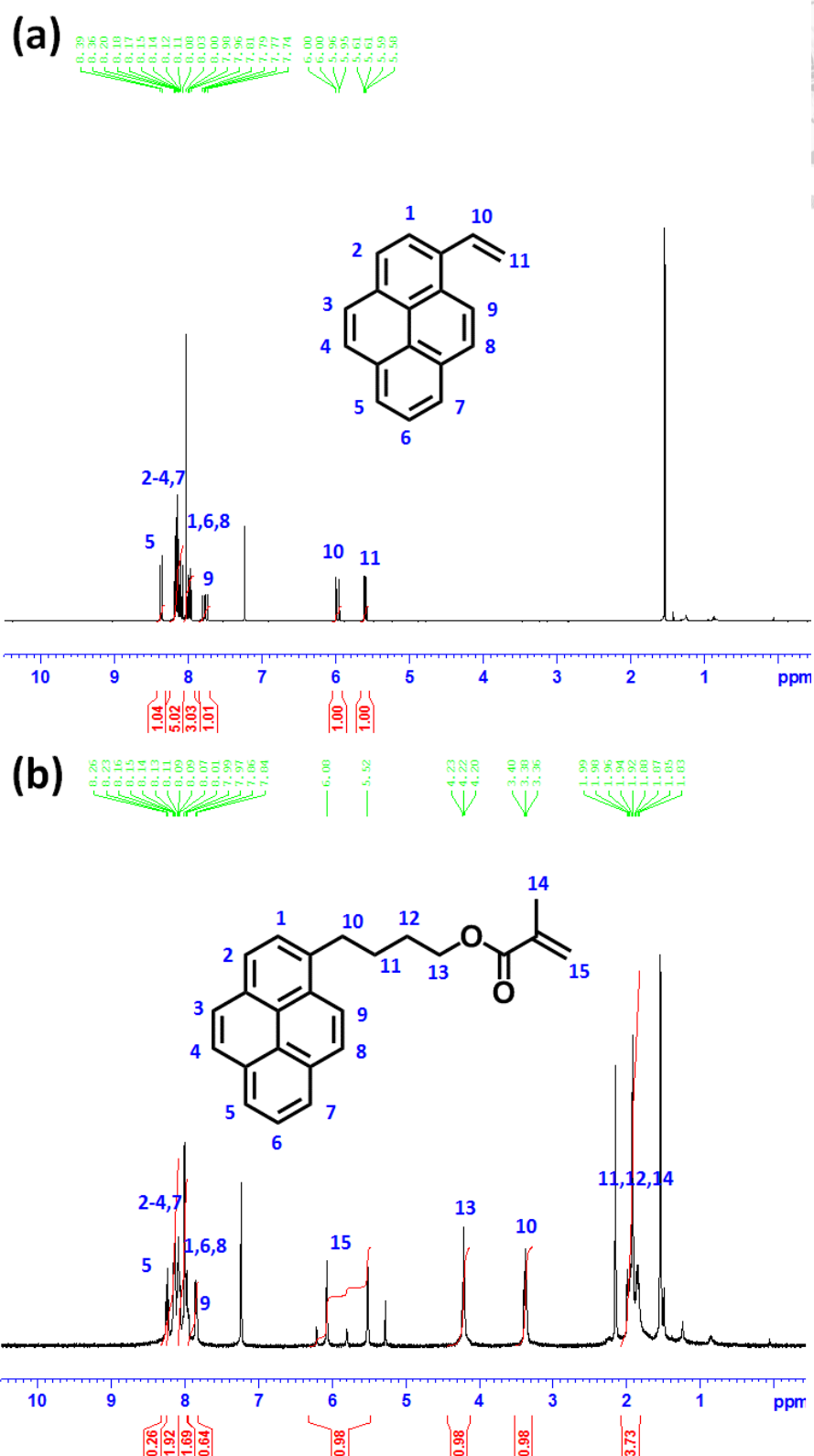


**Fig. 2.1**  $^1\text{H}$  NMR spectra of (a) 1-vinylpyrene and (b) 4-(pyren-1-yl)butyl methacrylate in  $\text{CDCl}_3$ .

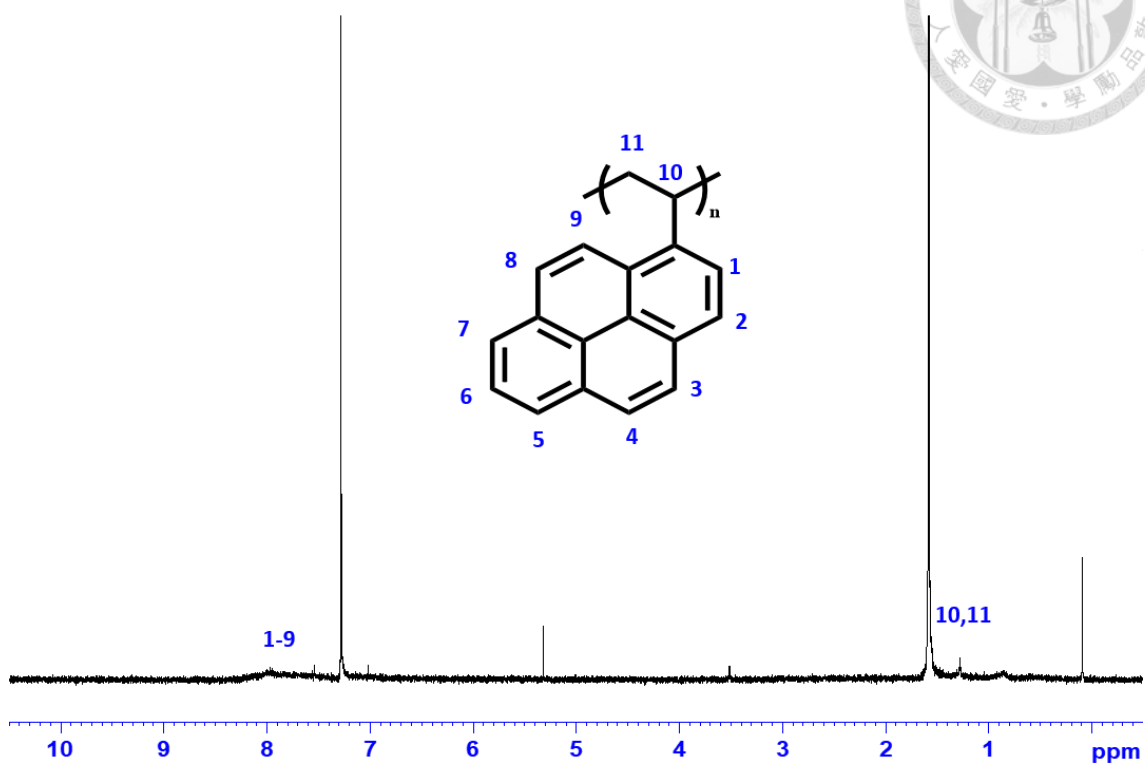


Fig. 2.2  $^1\text{H}$  NMR spectrum of **P4a** in  $\text{CDCl}_3$

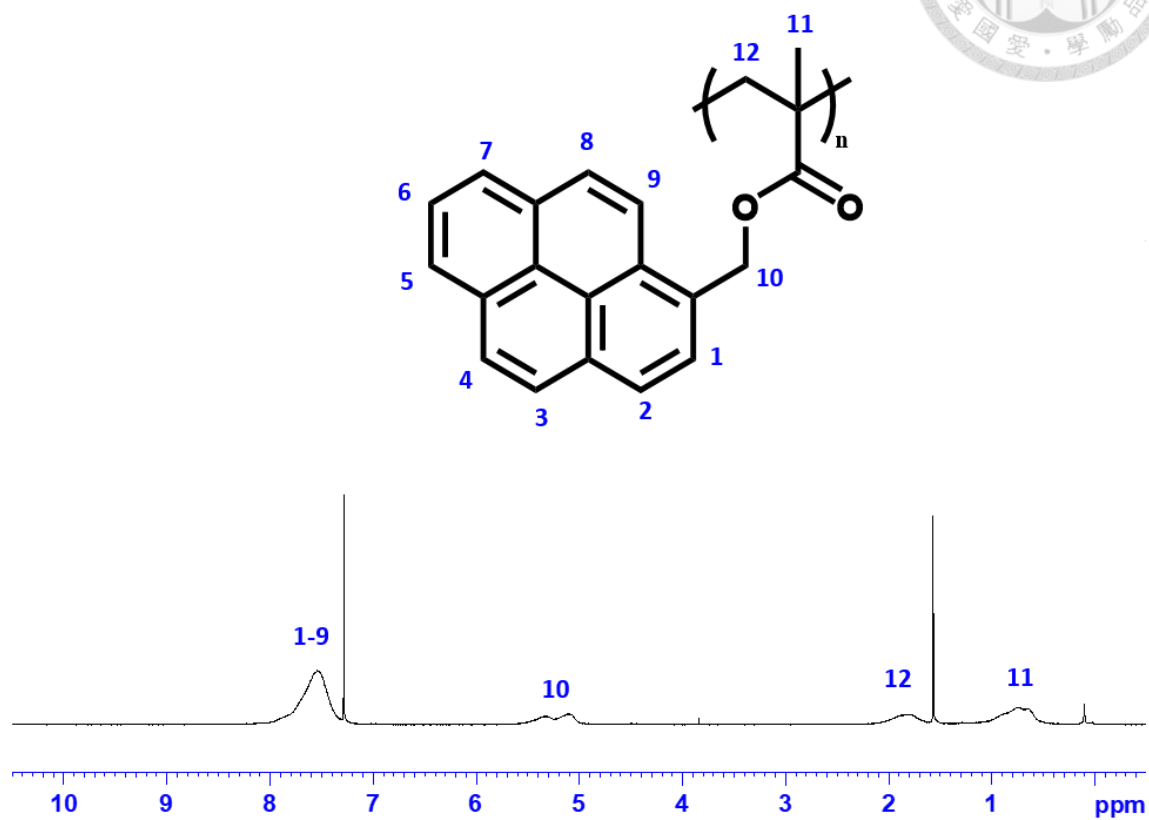


Fig. 2.3 <sup>1</sup>H NMR spectrum of P4b in CDCl<sub>3</sub>

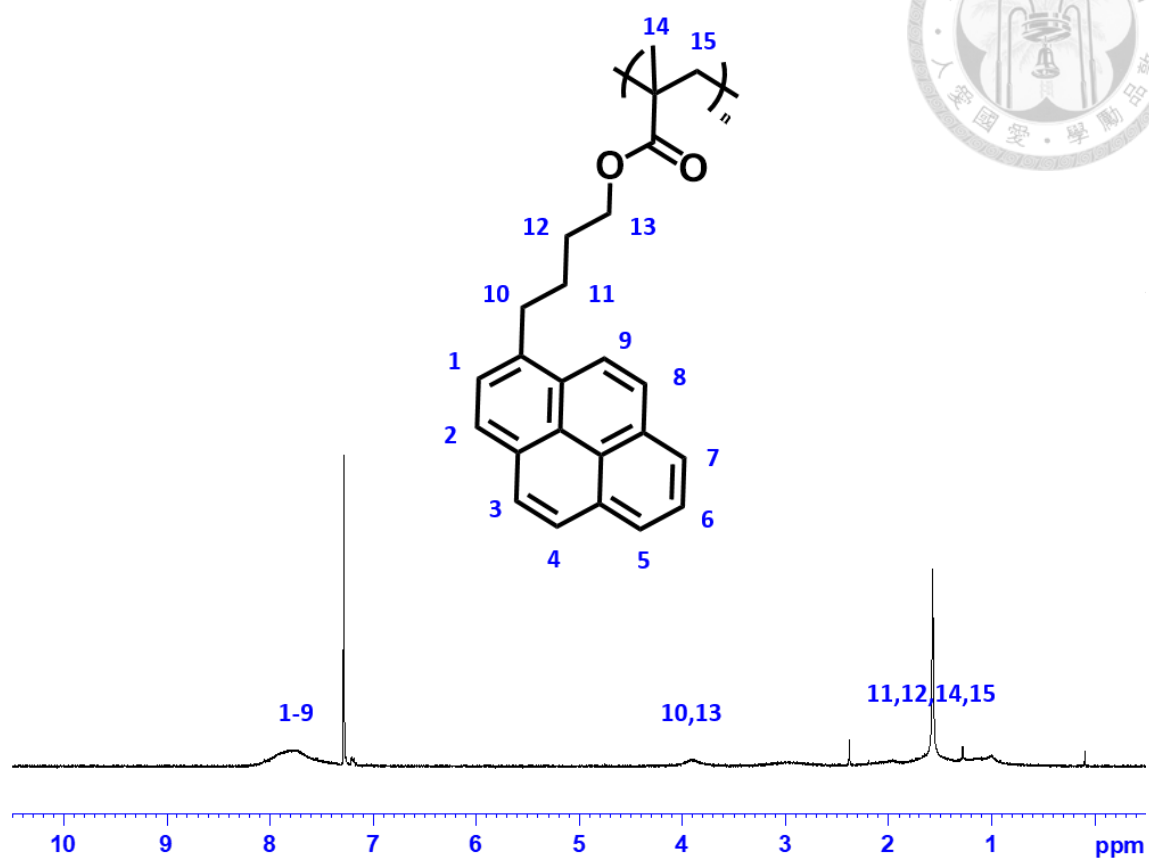
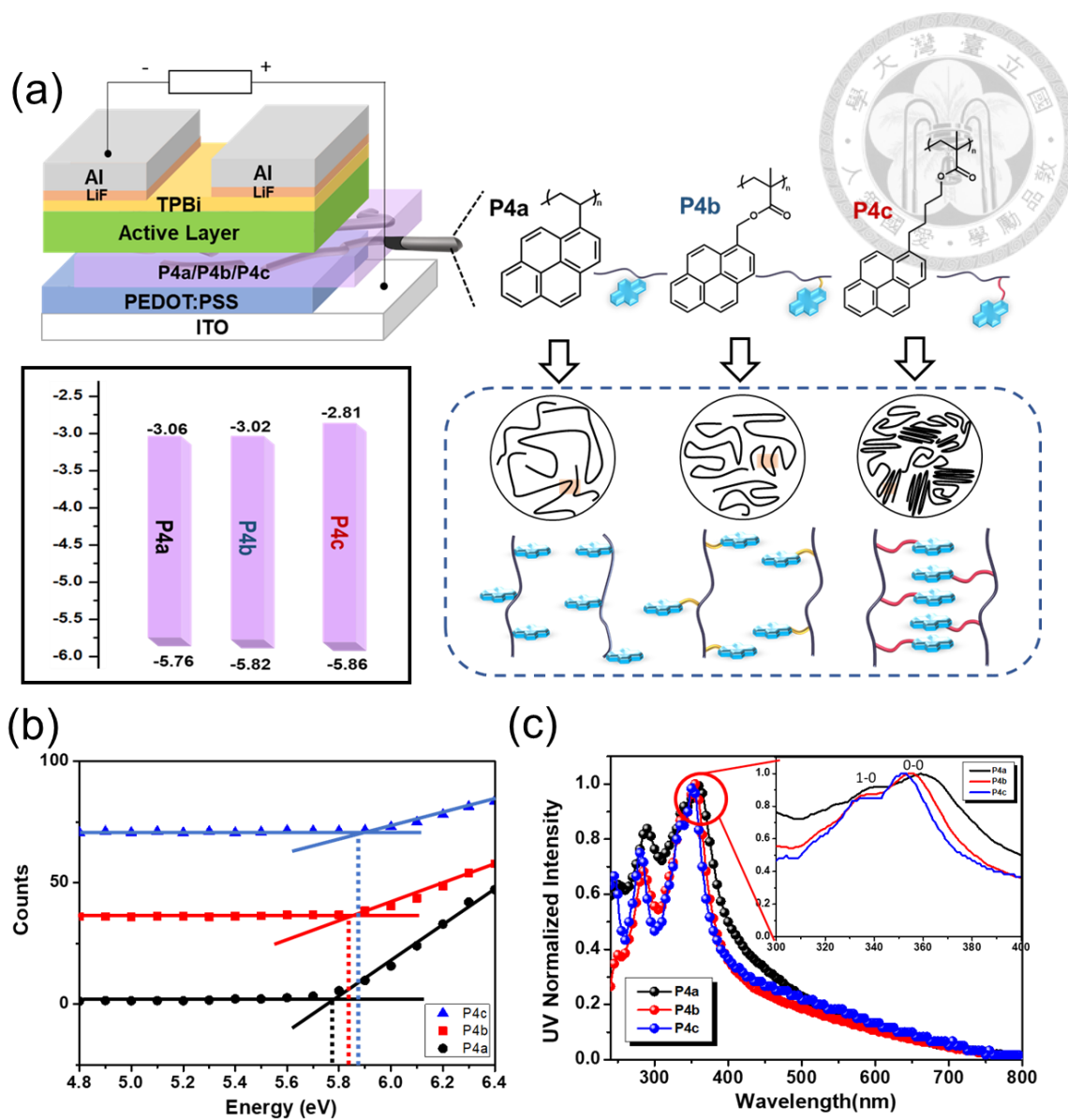


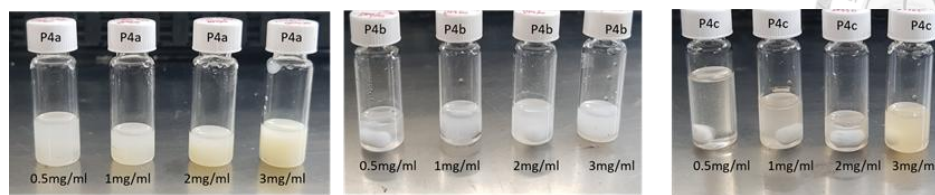
Fig. 2.4  $^1\text{H}$  NMR spectrum of P4c in  $\text{CDCl}_3$ .



**Fig. 2.5** (a) Structures of the fabricated PeLED and P4a-c along with their energy levels and schematic of the distinct aggregation behaviors between P4a-c. (b) PES measurement and (c) UV-vis absorption spectra of the films of P4a-c.



Solubility test of P4a-c in DMSO.



Solubility test of P4a-c in DMF.

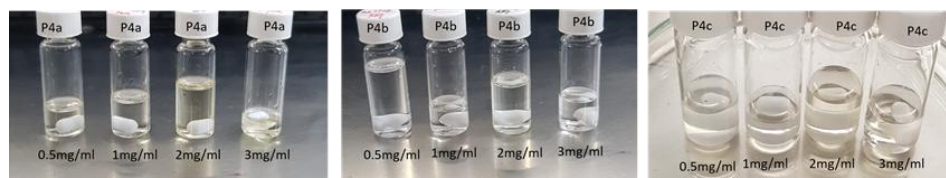


Fig. 2.6 Solubility test of P4a-c in DMSO and DMF.

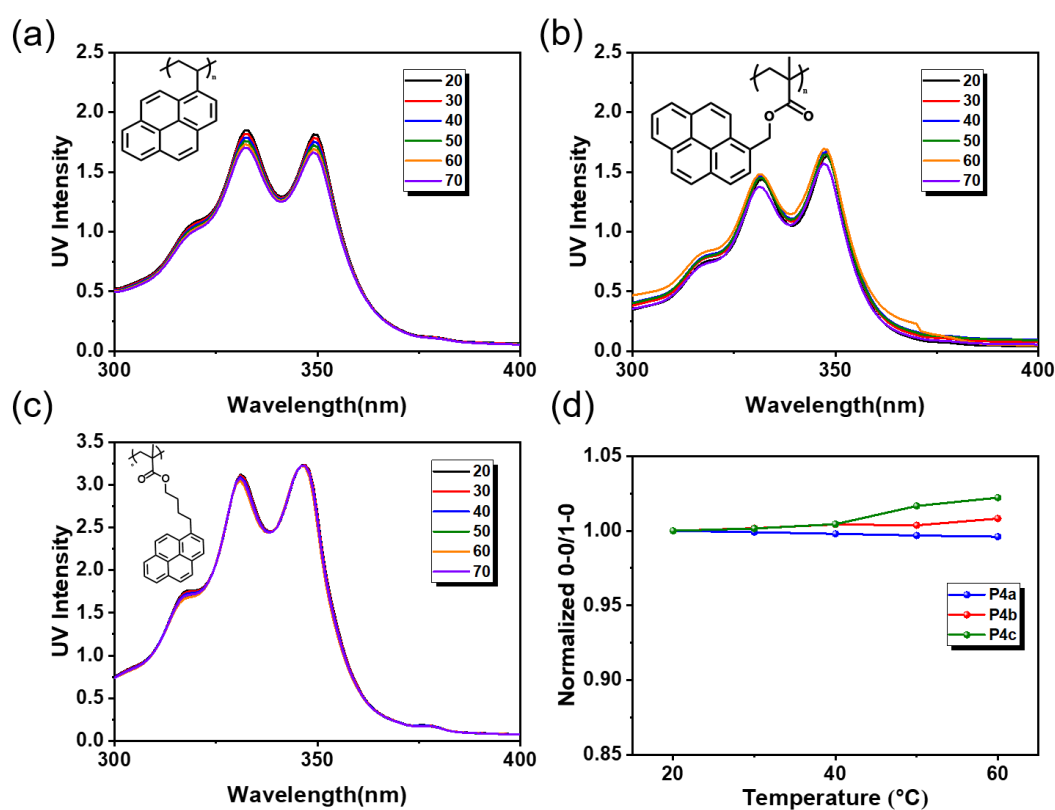


Fig. 2.7 Temperature-dependent UV-vis absorption spectra of (a) P4a, (b) P4b, and (c) P4c solutions from 20–70 °C. (d) The calculated intensity ratio of the 0–0 and 0–1 characteristic absorption peaks of P4a, P4b, and P4c.

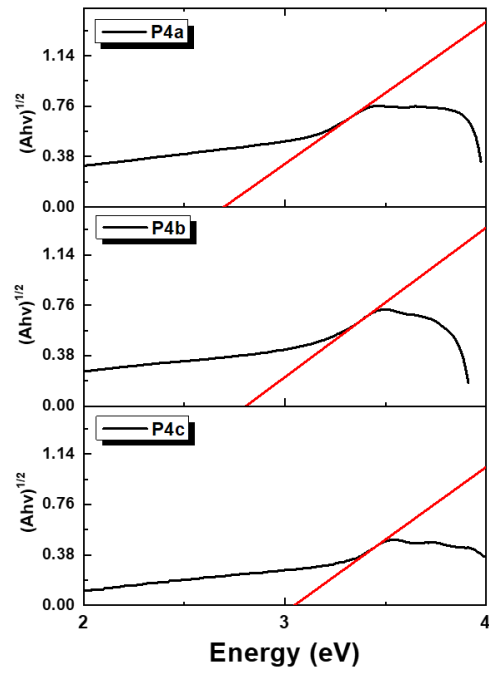


Fig. 2.8 Tauc plots of the films of P4a–c.

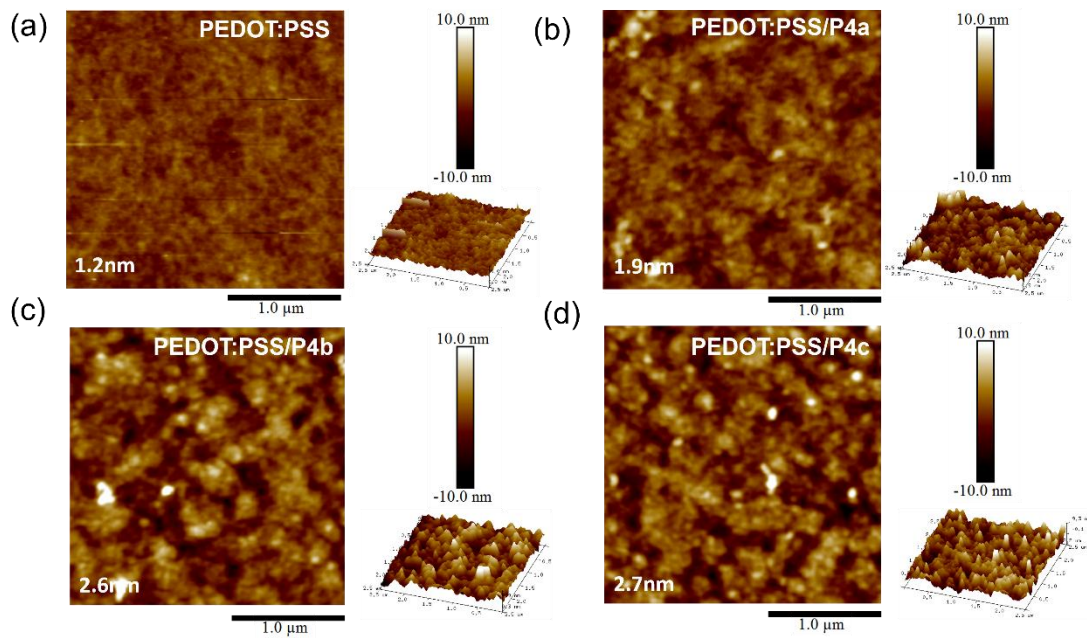
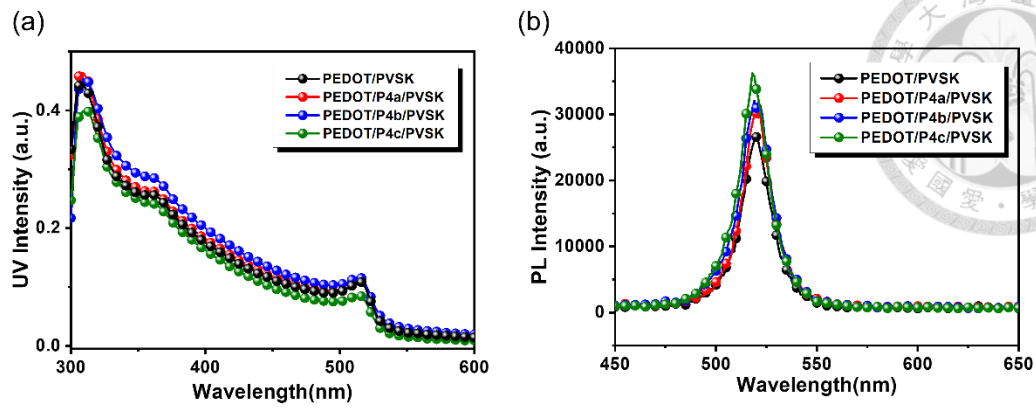
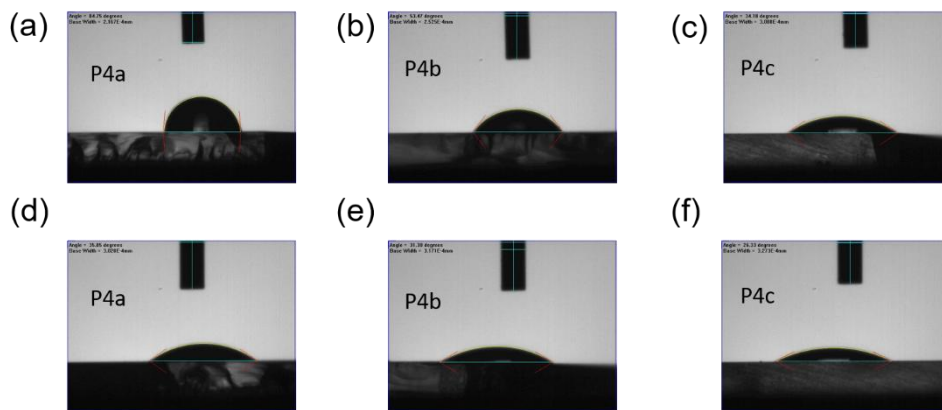


Fig. 2.9 2D and 3D AFM topographies of the films of (a) PEDOT:PSS, (b) PEDOT:PSS/P4a, (c) PEDOT:PSS/P4b, and (d) PEDOT:PSS/P4c. The surface roughness of the films is labeled on the images.



**Fig. 2.10** (a) UV-vis absorption and (b) PL spectra of the films of PEDOT:PSS/CsPbBr<sub>3</sub> and PEDOT:PSS/P4a-c/CsPbBr<sub>3</sub>.



	$\theta_{\text{water}}(^{\circ})^a$	$\theta_{\text{glycerol}}(^{\circ})^a$	$\sigma_s(\text{mN/m})^b$
P4a	84.75	35.85	43.8
P4b	53.47	31.30	54.9
P4c	34.18	26.33	61.3

<sup>a</sup> Contact angle between the film and water or glycerol. <sup>b</sup> Surface energy fitted by Wu method.

**Fig. 2.11** Contact angle measurement of (a,d) P4a, (b,e) P4b, (c,f) and P4c films using (a-c) water and (d-f) glycerol. The respective contact angle values for P4a, P4b, and P4c are presented below and the surface energy was calculated using Wu model.

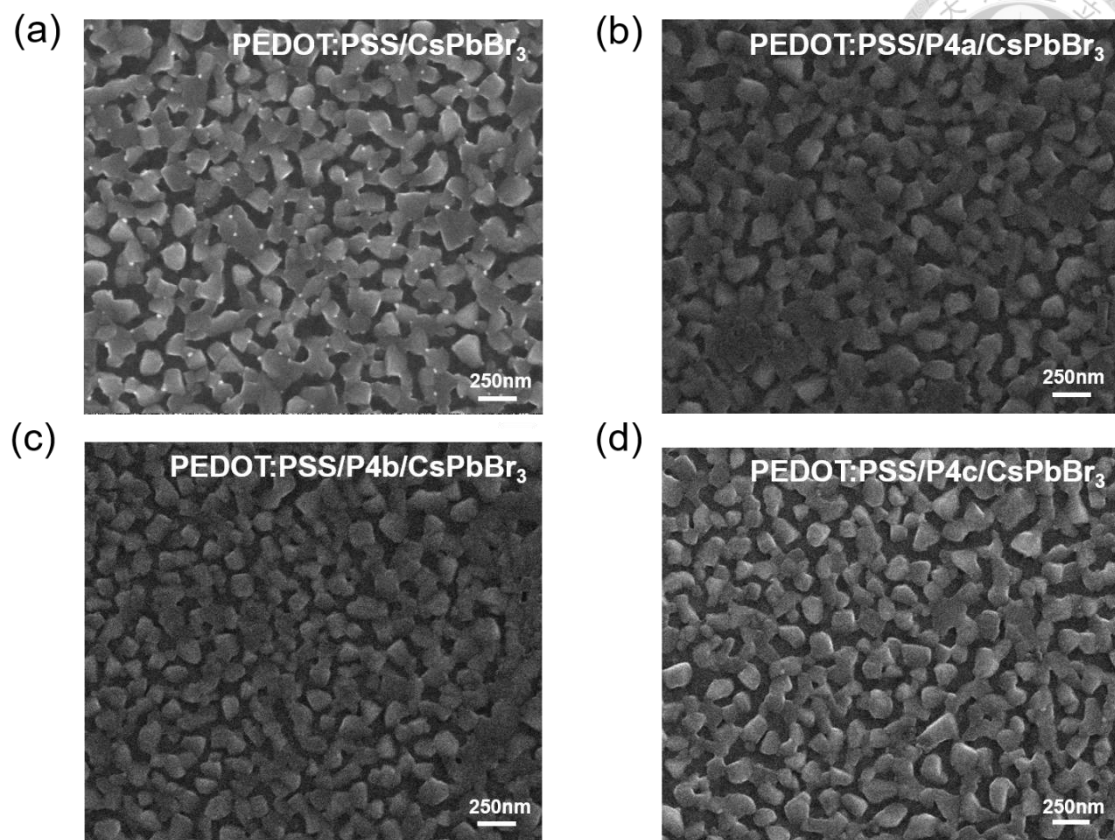


**Fig. 2.12** SEM images of CsPbBr<sub>3</sub> films grown on (a) PEDOT:PSS, (b) PEDOT:PSS/P4a, (c) PEDOT:PSS/P4b, and (d) PEDOT:PSS/P4c.

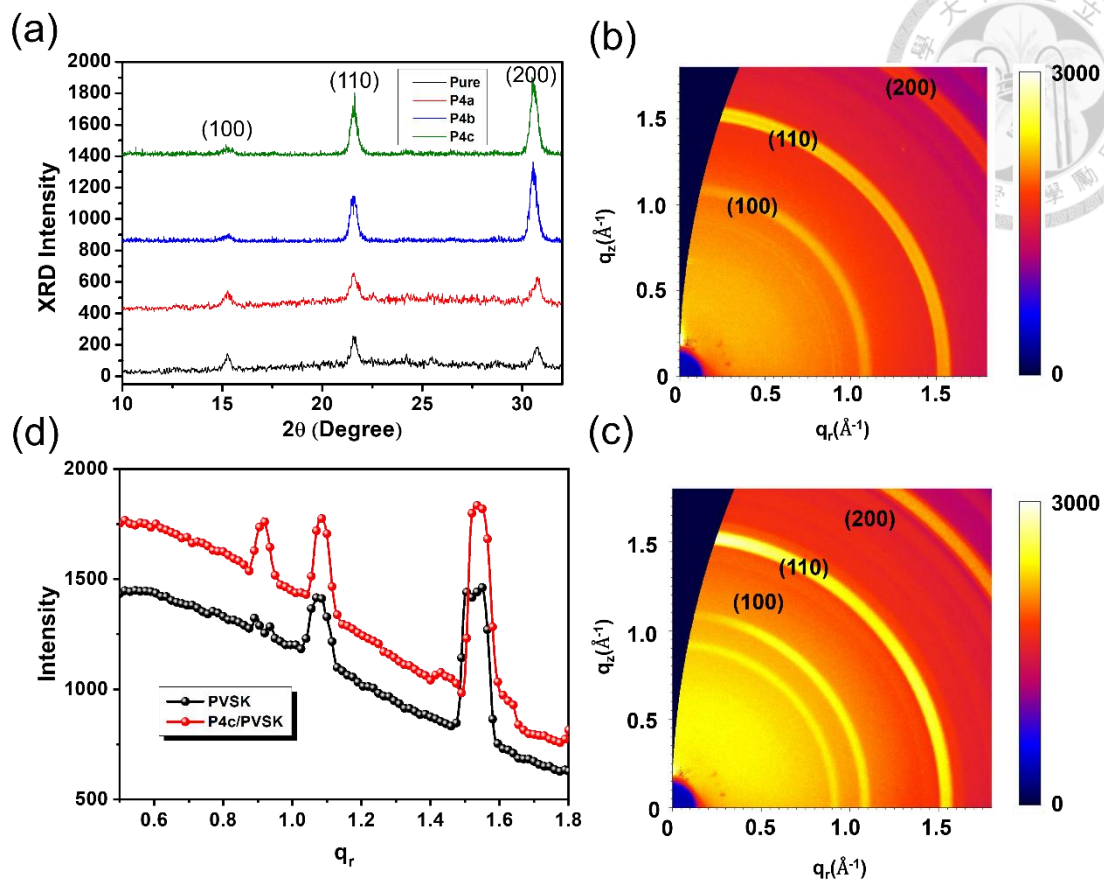


**Fig. 2.13** (a) XRD characteristics of the perovskite films grown on different layers as indicated, where pure means the pristine PEDOT:PSS. GIWAXS patterns of the films of (b) PEDOT:PSS/CsPbBr<sub>3</sub> and (c) PEDOT:PSS/P4c/CsPbBr<sub>3</sub>, and (d) their corresponding 1-D characteristics extracted from the GIWAXS patterns shown in (b, c).

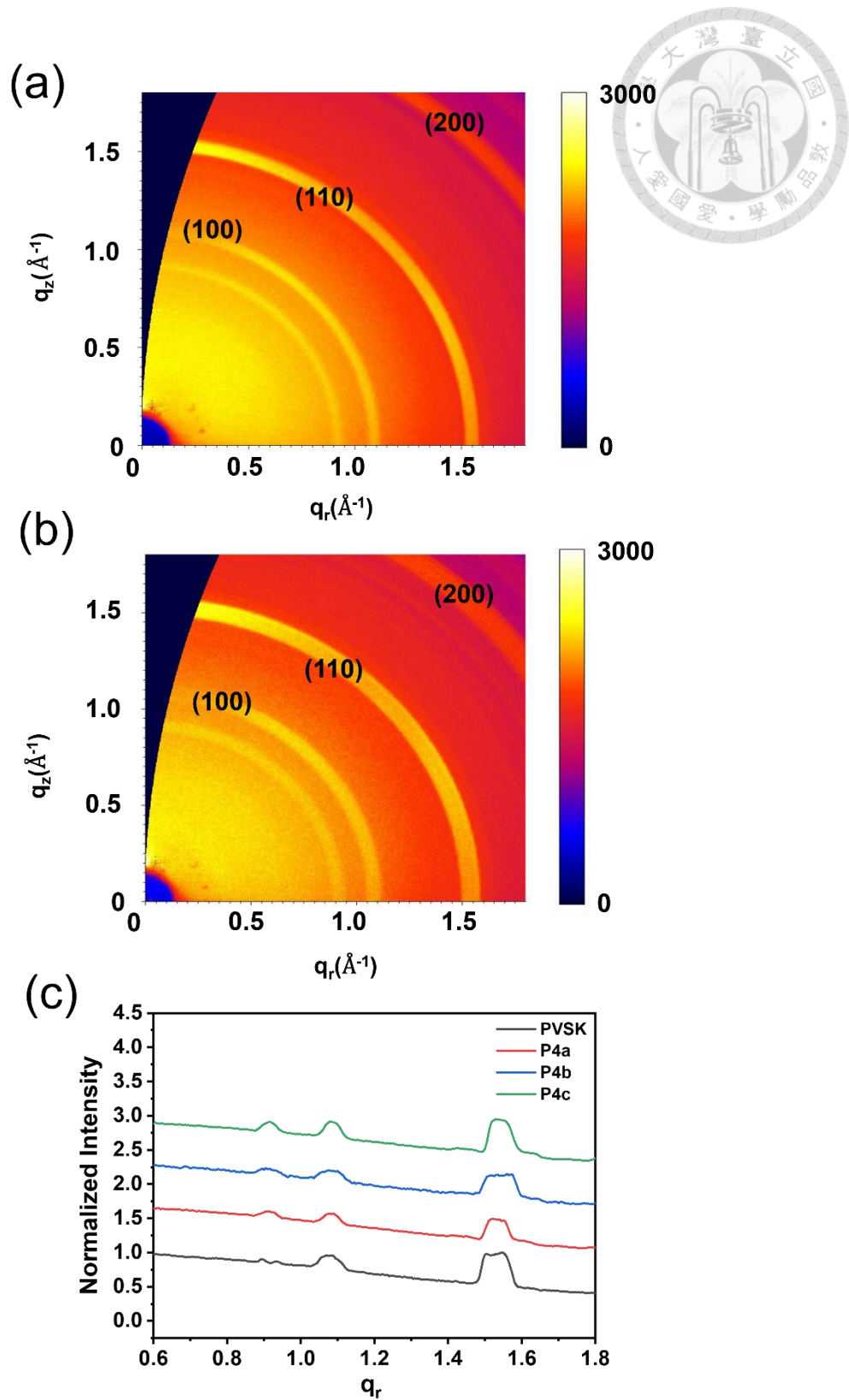


**Fig. 2.14** GIWAXS patterns of the samples of (a) PEDOT:PSS/P4a/CsPbBr<sub>3</sub> and (b) PEDOT:PSS/P4b/CsPbBr<sub>3</sub>. (c) The corresponding normalized 1-D incident characteristics of CsPbBr<sub>3</sub> films grown on the pristine and P4a-c-modified HTLs.

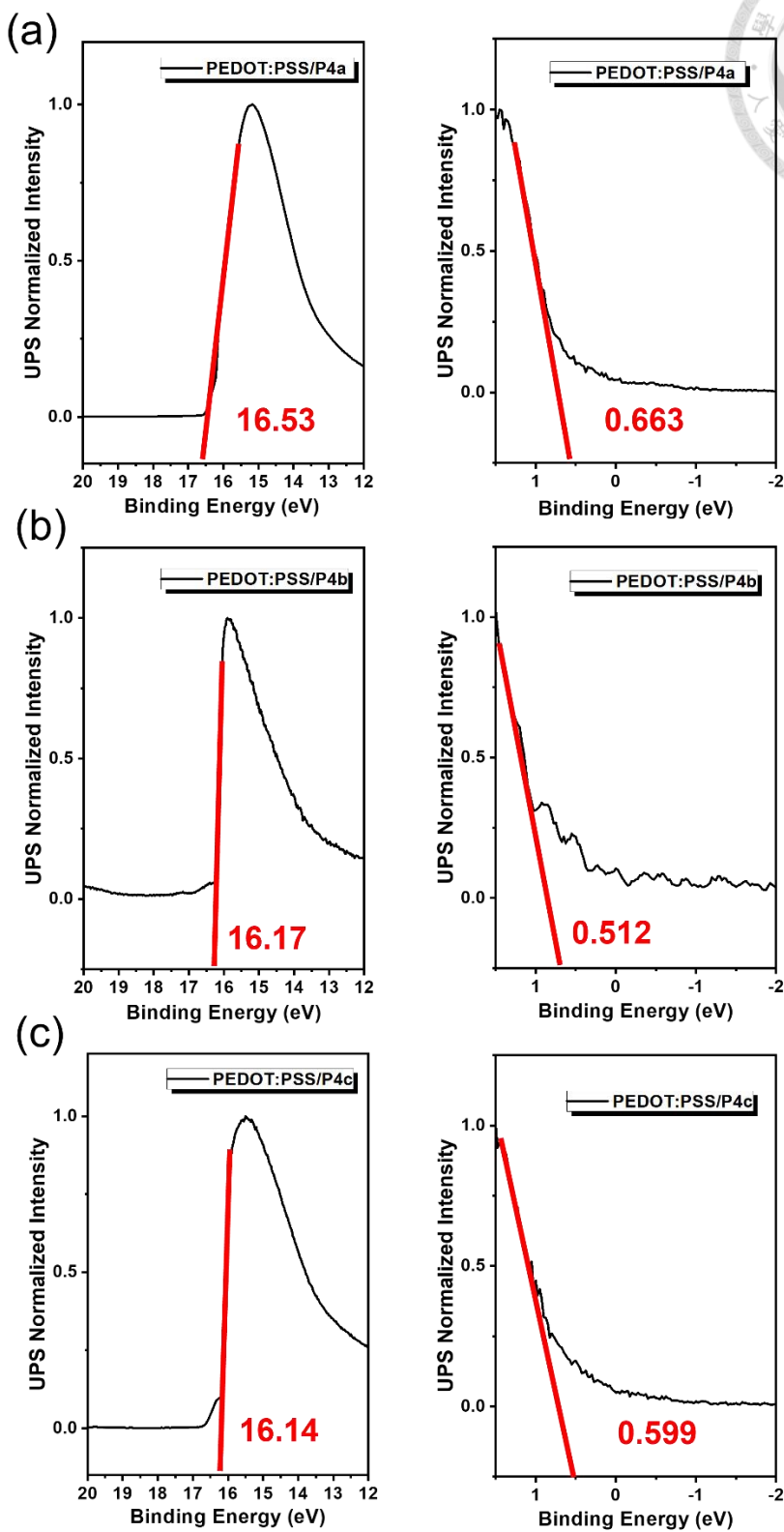


**Fig. 2.15** UPS measurements of the films of (a) PEDOT:PSS/P4a, (b) PEDOT:PSS/P4b, and (c) PEDOT:PSS/P4c.

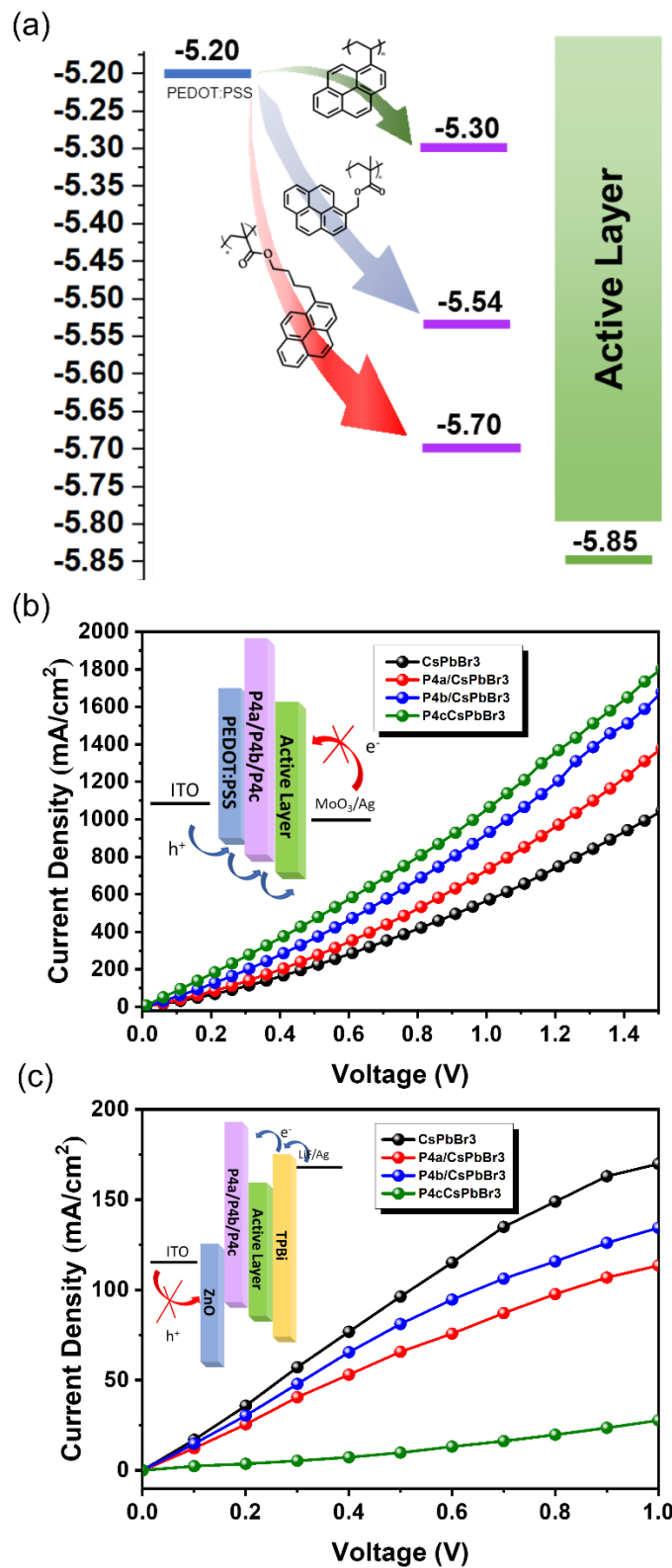


**Fig. 2.16** (a) The energy-level diagram of PEDOT:PSS and PEDOT:PSS/P4a-c. J-V curves of (b) the hole-only device and (c) the electron-only device using pristine PEDOT:PSS or PEDOT:PSS/P4a-c as the HTL.



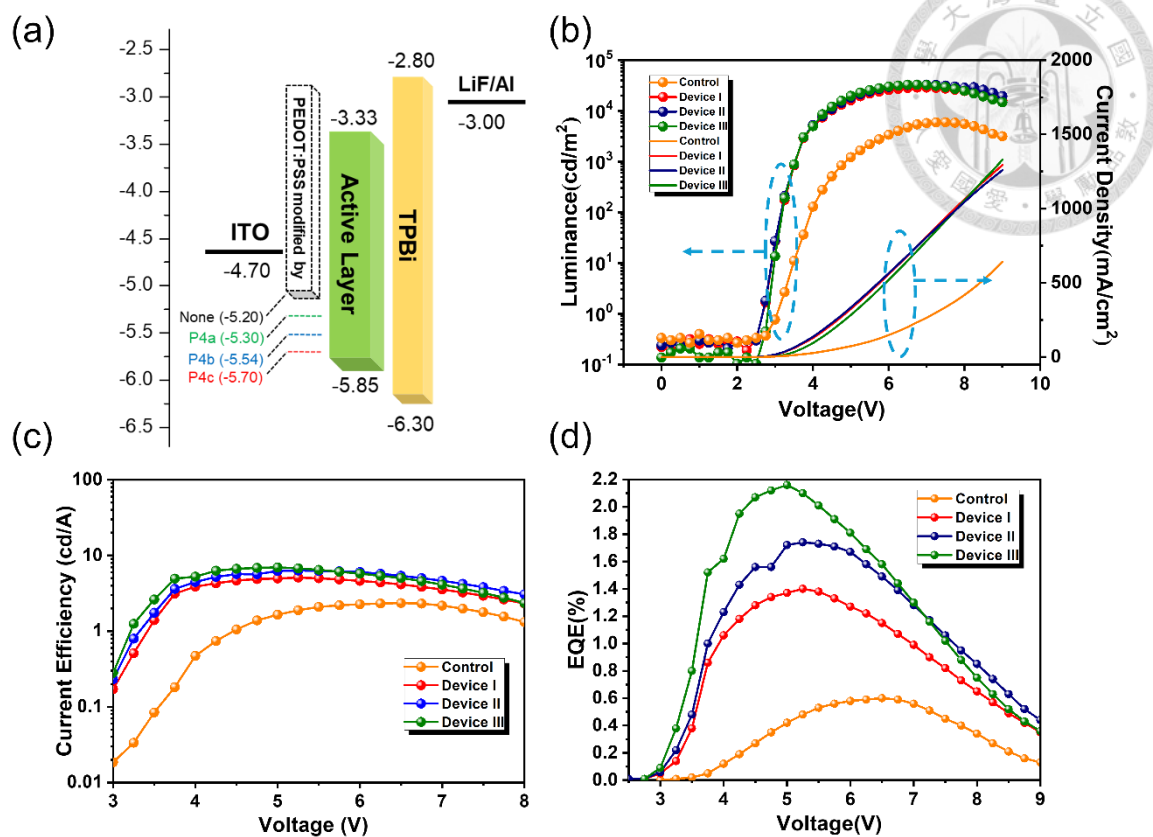


**Fig. 2.17** (a) Energy-level diagram of the studied PeLEDs. (b) J-V-L, (c) current efficiency-voltage, and (d) EQE curves of the studied PeLEDs.

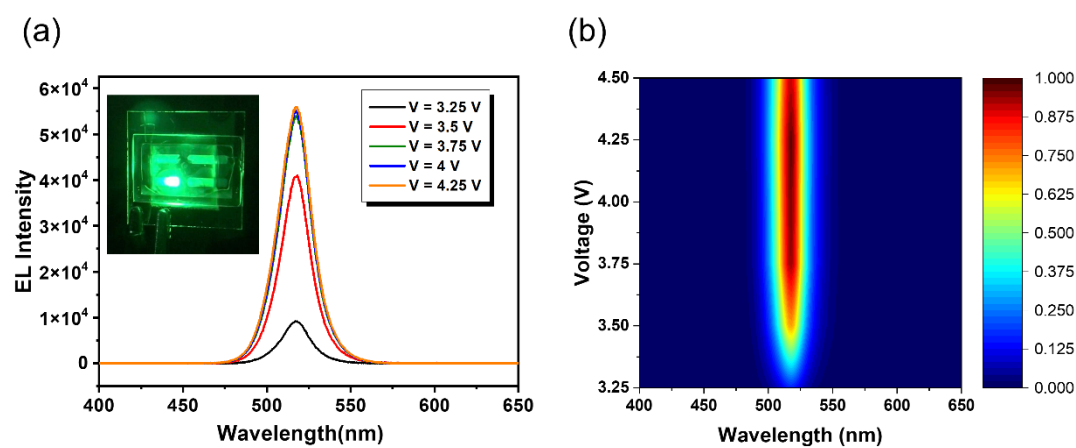


**Fig. 2.18** (a) EL curves of Device III under different operation voltages and (b) the corresponding contour plot.

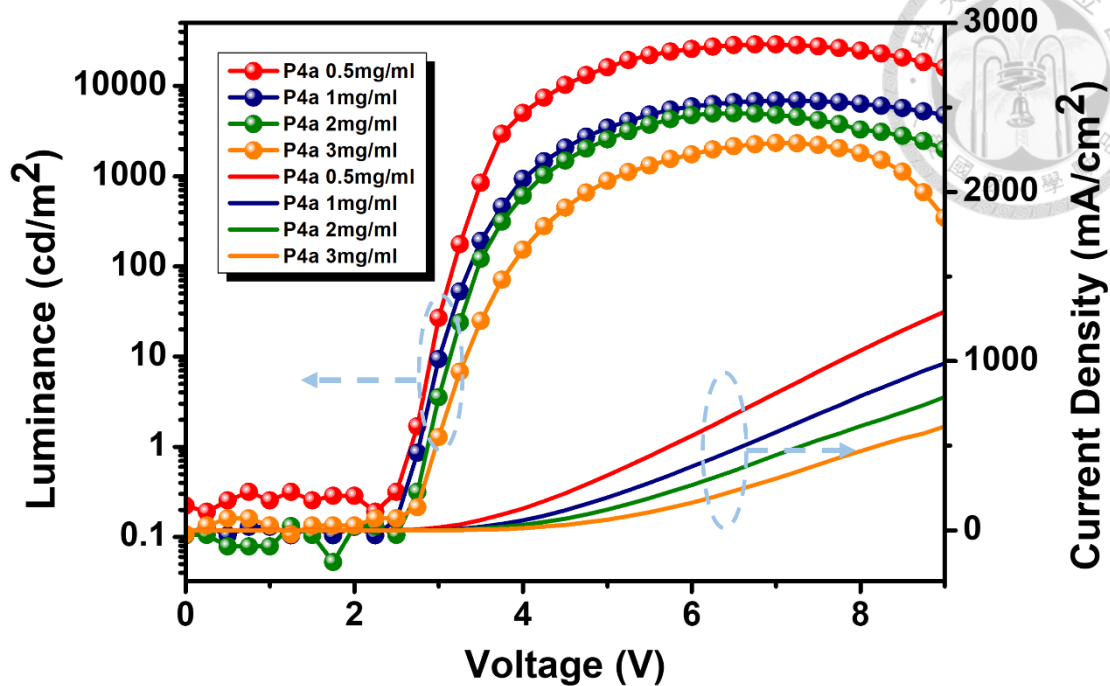


Fig. 2.19 J-V-L curves of the PeLEDs made from P4a solutions with different concentration for optimization.

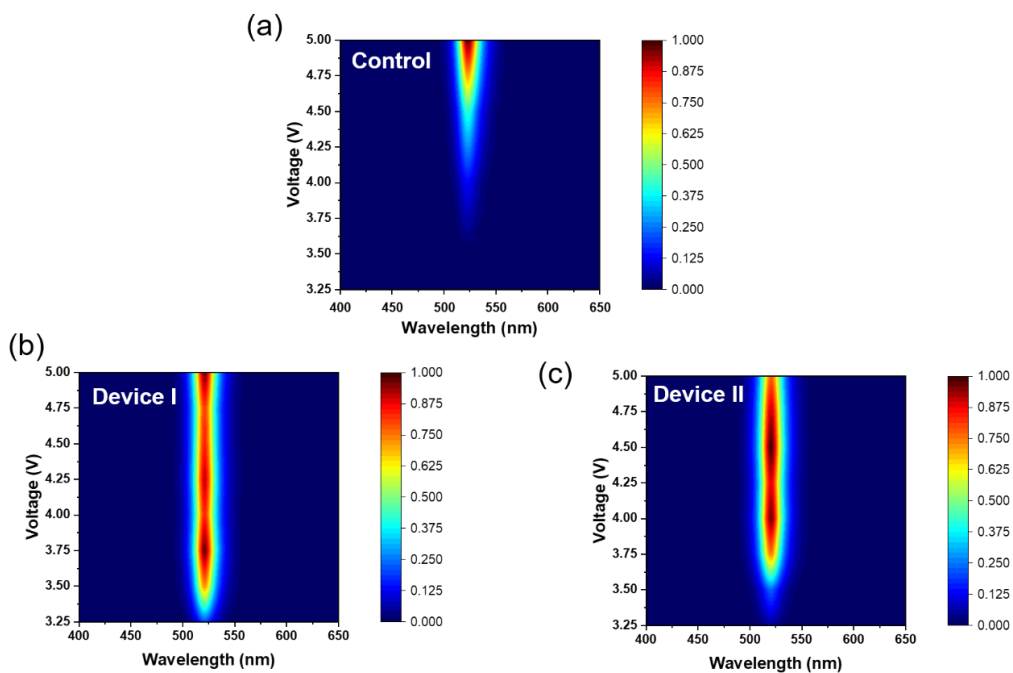


Fig. 2.20 Contour plots of EL spectra of (a) control device, (b) Device I, and (c) Device II.

II.

# Chapter 3 Quasi-2D Perovskite Light-Emitting Diodes



## 3.1 Engineering of Perovskite Light-Emitting Diodes Based on Quasi-2D Perovskites Formed by Diamine Cations

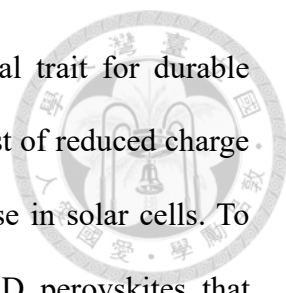
The text and figures in this section are reproduced with permission from:

**C. H. Chen**, Z. Li, Q. Xue\*, Y. A. Su, C. C. Lee, H. L. Yip\*, W. C. Chen, C. C. Chueh\*, “Engineering of Perovskite Light-Emitting Diodes Based on Quasi-2D Perovskites Formed by Diamine Cations”, *Org. Electronics.*, 75, 105400 (2019).

### 3.1.1 Background

Hybrid perovskites have recently emerged as influential materials in the optoelectronic landscape, owing to their impressive semiconductor properties and adaptable crystal structures.<sup>[84, 114-117]</sup> Their inherent structural tunability enables precise tailoring at the molecular level, which has driven extensive interest in material design. Across a range of dimensional configurations, functional perovskites have demonstrated substantial progress in applications involving both light absorption and emission.<sup>[115, 118-122]</sup>

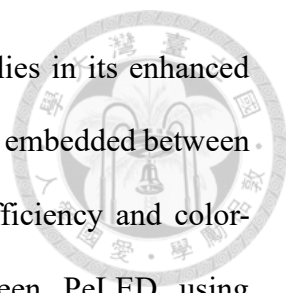
Perovskite materials are known for their diverse structural configurations, ranging from fully three-dimensional (3D) frameworks to quasi-two-dimensional (quasi-2D or layered 2D/3D hybrids), and even to strictly two-dimensional (2D) architectures.<sup>[115, 118-122]</sup> Among these, 3D perovskites have garnered attention for their outstanding power conversion efficiencies in photovoltaic devices.<sup>[123]</sup> In contrast, quasi-2D variants have



drawn interest due to their superior intrinsic stability—an essential trait for durable operation.<sup>[48]</sup> However, this improved stability often comes at the cost of reduced charge transport and electronic performance, posing challenges for their use in solar cells. To address this, ongoing research is focused on engineering quasi-2D perovskites that preserve their stability while regaining or enhancing their optoelectronic performance.<sup>[122, 124]</sup>

In addition to their success in photovoltaics, quasi-2D perovskite materials have attracted growing attention for light-emitting applications, largely due to their strong exciton confinement and tunable semiconductor properties.<sup>[115, 118-122]</sup> These features stem from the layered architecture of quasi-2D perovskites, where inorganic perovskite slabs alternate with organic spacer molecules. The contrast in energy levels and dielectric environments between the perovskite layers and organic interlayers gives rise to both quantum and dielectric confinement effects.<sup>[125, 126]</sup> These effects significantly boost exciton binding energies and localize charge carriers, making quasi-2D perovskites promising candidates for the development of high-efficiency light-emitting diodes (LEDs).<sup>[84, 116]</sup>

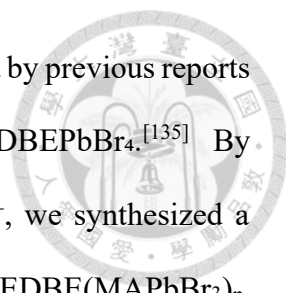
In quasi-2D perovskites, bulky organic cations serve as spacer molecules, their size exceeding the limits of the conventional 3D perovskite lattice and thereby inducing the formation of layered structures. These large cations separate the inorganic perovskite slabs, giving rise to low-dimensional phases. Much of the recent progress in perovskite light-emitting diodes (PeLEDs) has focused on such quasi-2D architectures, particularly those incorporating large monoamine cations.<sup>[51, 81, 127, 128]</sup> These monoamines form bilayer organic barriers between the inorganic layers, resulting in a Ruddlesden-Popper (RP) structure.<sup>[48, 129-131]</sup> This configuration features monoamine cations interacting with the perovskite lattice via van der Waals forces, establishing a single anchoring point and



stabilizing the layered assembly. A key advantage of this structure lies in its enhanced moisture resistance, attributed to the hydrophobic alkyl or aryl chains embedded between the perovskite sheets. Leveraging these features, numerous high-efficiency and color-tunable PeLEDs have been demonstrated. For example, a green PeLED using  $\text{PEA}_2(\text{FAPbBr}_3)_{n-1}\text{PbBr}_4$  (where PEA is phenylethylammonium) achieved a current efficiency of 62.4 cd/A and an external quantum efficiency (EQE) of 14.36%.<sup>[81]</sup> In another case, a red-emitting PeLED based on  $(\text{BA})_2(\text{Cs})_{n-1}\text{Pb}_n\text{I}_{3n+1}$  (with BA representing benzylammonium) reached a luminance of 1392 cd/m<sup>2</sup> and an EQE of 6.23%.<sup>[132]</sup> These results highlight the design flexibility and strong potential of quasi-2D perovskites in advancing next-generation emissive technologies.

It is also important to recognize that the organic spacer in layered perovskites can be formed using large diamine cations, which serve to separate the inorganic slabs and result in what is known as the Dion–Jacobson (DJ) phase structure.<sup>[46, 133, 134]</sup> In contrast to the Ruddlesden–Popper (RP) phase, DJ phase quasi-2D perovskites exhibit stronger interlayer connectivity due to the bidentate nature of diamine spacers, which form direct bonds with adjacent perovskite layers. This structural feature offers the potential for enhanced material stability compared to RP-type architectures. However, despite these promising attributes, the application of DJ phase quasi-2D perovskites in PeLEDs has been relatively underexplored. Motivated by this gap, we aim to investigate the viability of DJ-phase materials in light-emitting devices. Such studies may provide valuable insights and open new directions for the development of high-performance perovskite-based optoelectronic technologies.

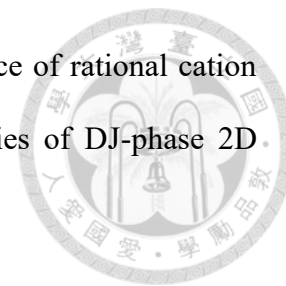
In this study, we employed the bulky diammonium cation 2,2'-(ethylenedioxy)bis(ethylammonium) ( $\text{EDBE}^{2+}$ ), in conjunction with the small monovalent methylammonium ( $\text{MA}^+$ ), to construct a series of Dion–Jacobson (DJ) phase



quasi-2D perovskite materials. The selection of EDBE<sup>2+</sup> was informed by previous reports highlighting its ability to form the stable 2D compound EDBEPbBr<sub>4</sub>.<sup>[135]</sup> By systematically adjusting the molar ratio between EDBE<sup>2+</sup> and MA<sup>+</sup>, we synthesized a range of DJ-phase quasi-2D perovskites with the general formula EDBE(MAPbBr<sub>3</sub>)<sub>n-1</sub>PbBr<sub>4</sub> ( $n = 1, 3, 5, \dots, \infty$ ), as illustrated in **Fig. 3.1** Interestingly, the pure 2D EDBEPbBr<sub>4</sub> film exhibited broad photoluminescence due to self-trapped excitons, whereas the quasi-2D variants displayed sharper emission profiles. This can be attributed to the incorporation of 3D-like perovskite domains, which reduce lattice distortion and help regulate trap-state distributions. Among the synthesized films, EDBE(MAPbBr<sub>3</sub>)<sub>2</sub>PbBr<sub>4</sub> showed the most intense photoluminescence, likely due to the preserved quantum confinement effect. We then evaluated this composition in a p-i-n structured PeLED and optimized the device performance through multiple strategies: fine-tuning the hole-transport layer (HTL), adjusting precursor concentration, additive-based passivation, thermal annealing, and optimizing the thickness of the electron transport layer (ETL). Notably, the integration of the n-type small molecule TPBi (2,2',2''-(1,3,5-benzenetriyl)-tris(1-phenyl-1H-benzimidazole)),<sup>[65]</sup> as a passivation agent during film formation led to the most substantial performance enhancement. The optimized green-emitting PeLED achieved a peak luminance of 1903 cd/m<sup>2</sup> and a maximum external quantum efficiency (EQE) of 1.06%, marking the first successful demonstration of a visible-light-emitting PeLED based on a DJ-phase quasi-2D perovskite.

However, despite this achievement, the device performance remained lower than that of comparable RP-phase quasi-2D PeLEDs. This shortfall may be due to the limited thermal stability of EDBE-based perovskites. Since the EDBE<sup>2+</sup> cation forms direct links between perovskite layers, any thermally induced conformational changes such as twisting or rotation can exert a greater influence on the structural integrity of the lattice

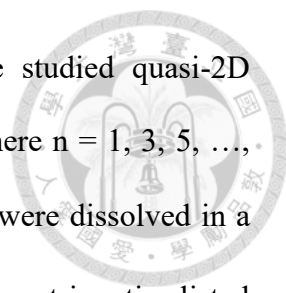
than in RP-phase systems. These findings underscore the importance of rational cation design to further improve the thermal and optoelectronic properties of DJ-phase 2D-perovskite emitters.



### 3.1.2 Experimental Section

**Materials.** All chemicals were used as received without further purification. 2,2'-(Ethylenedioxy)bis(ethylammonium) (EDBE, 98%), methylammonium bromide (MABr, 98%), lead(II) bromide ( $\text{PbBr}_2$ , 99.999%), and solvents including dimethylformamide (DMF, 99.8%) and dimethyl sulfoxide (DMSO,  $\geq 99.9\%$ ) were purchased from Sigma-Aldrich. The electron-transport material 2,2',2''-(1,3,5-benzenetriyl)-tris(1-phenyl-1H-benzimidazole) (TPBi) was obtained from Ultra Fine Chemical Technology Corp. PEDOT:PSS formulations (Clevios™ P AI 4083 and CH 8000) were supplied by Uniregion Bio-tech.

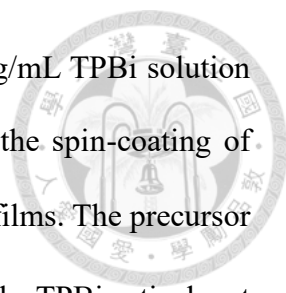
**Synthesis of EDBEBr<sub>2</sub>.** For a solution of 14.43 g (97.38 mmol) of 2,2'-(ethylenedioxy)bis(ethylamine) (EDBE) powder, 40 mL of 40% hydrobromic acid (HBr) was added dropwise under continuous stirring at low temperature, maintained using a water–liquid nitrogen cooling bath. The reaction mixture was stirred for an additional 30 minutes, during which a brown solution formed. The resulting mixture was then filtered, and the precipitated product was thoroughly washed multiple times with tetrahydrofuran (THF). The collected white solid was dried overnight in a vacuum oven at 50–60 °C, affording 25.90 g (84.07 mmol) of EDBEBr<sub>2</sub> as a white powder, corresponding to an isolated yield of 86.3%.



**Preparation of quasi-2D perovskite films.** To prepare the studied quasi-2D perovskites with the general formula  $\text{EDBE}(\text{MAPbBr}_3)_{n-1}\text{PbBr}_4$  (where  $n = 1, 3, 5, \dots$ , and  $\infty$ ), the organic salts  $\text{EDBEBr}_2$  and  $\text{MABr}$ , along with  $\text{PbBr}_2$ , were dissolved in a mixed solvent of DMF and DMSO (1:1 v/v) according to the stoichiometric ratios listed in **Table 3.1**. All precursor solutions were prepared at a total concentration of 0.16 M. For the pure 2D perovskite  $\text{EDBEPbBr}_4$  ( $n = 1$ ), equimolar amounts of  $\text{EDBEBr}_2$  and  $\text{PbBr}_2$  (0.08 mmol each) were dissolved in 0.5 mL of the mixed solvent. To synthesize the 3D perovskite  $\text{MAPbBr}_3$  ( $n = \infty$ ), 0.08 mmol of  $\text{MABr}$  and 0.08 mmol of  $\text{PbBr}_2$  were used in the same solvent volume. For intermediate quasi-2D compositions, the desired  $n$ -value was controlled by adjusting the  $\text{MABr}$  and  $\text{PbBr}_2$  content relative to  $\text{EDBEBr}_2$ . Specifically, for  $\text{EDBE}(\text{MAPbBr}_3)_2\text{PbBr}_4$  ( $n = 3$ ), 0.08 mmol of  $\text{EDBEBr}_2$ , 0.16 mmol of  $\text{MABr}$ , and 0.24 mmol of  $\text{PbBr}_2$  were combined in 0.5 mL of solvent, while the precursor for  $\text{EDBE}(\text{MAPbBr}_3)_4\text{PbBr}_4$  ( $n = 5$ ) consisted of 0.08 mmol of  $\text{EDBEBr}_2$ , 0.32 mmol of  $\text{MABr}$ , and 0.40 mmol of  $\text{PbBr}_2$  in the same solvent volume. All solutions were stirred until completely dissolved before use in film deposition.

**Fabrication of quasi-2D PeLEDs.** ITO substrates were thoroughly cleaned through a multi-step procedure beginning with detergent washing, followed by sequential ultrasonic treatment in deionized water, acetone, and isopropyl alcohol for 15 minutes each. After drying with a nitrogen stream, the substrates were treated with ultraviolet ozone to enhance surface wettability prior to HTL deposition. PEDOT:PSS aqueous solutions with varying conductivities were spin-coated at 3000 rpm for 30 seconds and then annealed at 150 °C for 15 minutes in ambient conditions. For substrates coated with PEDOT:PSS CH8000, a methanol surface treatment was applied by dispensing 60  $\mu\text{L}$  of methanol and spin-coating at 2000 rpm for 1 minute. Following surface preparation, the





substrates were transferred into a nitrogen-filled glove box. A 10 mg/mL TPBi solution in chlorobenzene was prepared and used as an antisolvent during the spin-coating of quasi-2D EDBe( $\text{MAPbBr}_3$ )<sub>n-1</sub>PbBr<sub>4</sub> ( $n = 1, 3, 5, \dots, \infty$ ) perovskite films. The precursor solutions were spin-coated at 4000 rpm for 2 minutes, with 120  $\mu\text{L}$  of the TPBi antisolvent dripped after 1 minute of spinning. When applicable, thermal annealing of the as-cast films was performed at 60–100 °C for 10 minutes. The PeLED devices were finalized by sequential thermal evaporation of TPBi, LiF, and aluminum under a high vacuum ( $<10^{-6}$  torr). The TPBi layer thickness was adjusted as described in the experimental section, while the thicknesses of LiF and Al were fixed at 1 nm and 120 nm, respectively.

**Characterizations.** The optical properties of the materials were characterized using a Hitachi U-4100 UV–visible spectrophotometer for absorption spectra and a Horiba Fluorolog-3 spectrofluorometer for photoluminescence (PL) emission spectra. Time-resolved PL decay measurements were performed using a Quantaaurus-Tau fluorescence lifetime system (C11367-03, Hamamatsu Photonics, Japan). The surface roughness of the hole-transport layer (HTL) was evaluated by atomic force microscopy (AFM) using a MultiMode system with a Nanoscope 3D controller (Digital Instruments) operating in tapping mode. The surface morphology of the perovskite films was examined via scanning electron microscopy (SEM) using a NOVA NANO SEM 450 instrument. The energy levels of the prepared films were determined by photoelectron spectroscopy using an AC-2 spectrometer (Riken Keiki). Crystallographic analysis was carried out using a Bruker D8 X-ray diffractometer equipped with Cu K $\alpha$  radiation. Electrical performance, including current density–voltage–luminance (J–V–L), external quantum efficiency (EQE), and electroluminescence (EL) characteristics, was measured using an XPQY-EQE-350-1100 system equipped with an integrating sphere (GPS-4P-SL, Labsphere) and

a photodetector array (S7031-1006, Hamamatsu Photonics), provided by Guangzhou Xi Pu Optoelectronics Technology Co., Ltd.



### 3.1.3 Results and Discussion

**Structural and phase characterization of novel quasi-2D perovskites.** As previously mentioned, the selection of the large-size diamine, EDBE, was influenced by recent research findings on the intriguing properties of 2D EDBEPbBr<sub>4</sub>, as reported in the literature.<sup>[135]</sup> Building upon this discovery, we proceeded to synthesize a series of quasi-2D perovskite materials by carefully controlling the stoichiometric ratios of EDBEBr<sub>2</sub>:MABr, as illustrated in **Fig. 3.1**. In this structural configuration, each phase unit consists of n-1 sheets of [PbBr<sub>6</sub>]<sup>4-</sup> octahedra intercalated with an EDBE chain. The specific relationships between the prepared quasi-2D EDBE(MAPbBr<sub>3</sub>)<sub>n-1</sub>PbBr<sub>4</sub> perovskites and the precursor ratios are detailed in **Table 3.1**.

To evaluate the structural properties of the synthesized quasi-2D perovskite films, X-ray diffraction analysis was performed. In contrast to the characteristic peaks observed in the reference 3D perovskite (n = infinite), the 2D EDBEPbBr<sub>4</sub> film displayed distinct peaks at approximately 6.1°, 12.3°, 18.5°, and 24.8°, resembling the patterns reported for the DJ phase perovskite analogue.<sup>[136]</sup> Upon increasing the n-phase to 3 and 5, the intensity of these peaks gradually diminished, accompanied by the emergence of a peak at 14.9° corresponding to the (110) plane of the 3D MAPbBr<sub>3</sub>, indicating the presence of a mixed phase of 3D perovskite in the quasi-2D perovskite films (n >3).<sup>[137]</sup> This phenomenon, observed in previous studies,<sup>[51, 81, 138]</sup> is advantageous for forming quantum wells within quasi-2D perovskites, facilitating more successful binding of electrons and photons. The morphology of the solution-processed films was further examined using scanning electron microscopy (SEM), as depicted in **Fig. 3.2**. It is evident that all the

prepared films exhibited a compact surface morphology. Interestingly, upon incorporation of EDBE<sup>2+</sup> in the composition, a noticeable reduction in grain size was observed in the quasi-2D films compared to the 3D MAPbBr<sub>3</sub> film. Moreover, relative to the 2D EDBEPbBr<sub>4</sub> film, these quasi-2D films also exhibited smaller grain sizes, which is advantageous for LED construction as it reduces carrier diffusion paths and enhances spatial confinement of excitons.<sup>[74, 128]</sup>

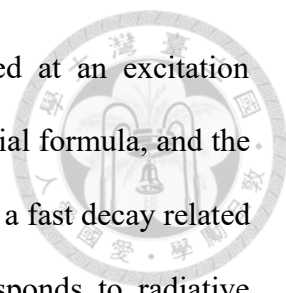
**Optical and Electronic Properties of quasi-2D perovskites.** Fig. 3.3b presents the UV-visible spectra of the prepared quasi-2D perovskite films. It is evident that the 2D EDBEPbBr<sub>4</sub> film displayed a distinct and intense absorption peak at around 380 nm, attributable to the exciton confinement effect.<sup>[135]</sup> Conversely, in films with increasing n-phase, the absorption peak at around 380 nm disappeared, indicating a weakened exciton confinement effect. Additionally, the absorption edge gradually red-shifted beyond 500 nm, with the degree of peak shifting proportional to the number of n-phase. The optical bandgap of these prepared films was estimated using their corresponding tau plots, as depicted in Fig. 3.4. The extracted bandgaps for EDBEPbBr<sub>4</sub> (n = 1), EDBE(MAPbBr<sub>3</sub>)<sub>2</sub>PbBr<sub>4</sub> (n = 3), EDBE(MAPbBr<sub>3</sub>)<sub>4</sub>PbBr<sub>4</sub> (n = 5), and MAPbBr<sub>3</sub> (n = ∞) were approximately 3.2 eV, 2.4 eV, 2.3 eV, and 2.2 eV, respectively. A clear trend of decreasing bandgap with increasing n-phase is observed, consistent with the trend reported for RP phase quasi-2D perovskite materials in the literature.<sup>[127]</sup>

Fig. 3.3c displays the normalized photoluminescence (PL) spectra of these films. Consistent with the observations in the UV-vis spectra (Fig. 3.3b), the PL emission gradually red-shifted as the n-phase increased, indicating a transition of the perovskite structure from 2D, 2D/3D, to bulk. Interestingly, the 2D EDBEPbBr<sub>4</sub> film exhibited a broad PL emission with a maximum peak at approximately 519 nm, resembling white-

light emission. This phenomenon stems from self-trapped carriers induced by intense electron-phonon coupling resulting from large lattice deformations.<sup>[135]</sup> However, this unique effect appears to diminish as the number of perovskite sheets increases. Both EDBE(MAPbBr<sub>3</sub>)<sub>2</sub>PbBr<sub>4</sub> (n = 3) and EDBE(MAPbBr<sub>3</sub>)<sub>4</sub>PbBr<sub>4</sub> (n = 5) films exhibit much narrower PL emissions, with slightly red-shifted maximum peaks at 529 nm and 533 nm, respectively. This suggests that the increasing presence of the perovskite phase in the DJ-phase 2D perovskite may effectively alleviate severe lattice torsion, thereby modulating the distribution of trap states. Consequently, unlike the white-light emission of the 2D EDBEPbBr<sub>4</sub> film, the quasi-2D perovskite and 3D MAPbBr<sub>3</sub> films emit green light.

The energy levels of the prepared films were assessed using a photoelectron spectrometer and are depicted in **Fig. 3.3d**. Among the films studied, the 2D EDBEPbBr<sub>4</sub> film exhibited the highest LUMO of -2.70 eV and the lowest HOMO of -5.86 eV, indicating its widest bandgap. However, with increasing n-phase, the bandgap gradually decreases, with the 3D MAPbBr<sub>3</sub> film showing the smallest bandgap at 2.18 eV. This reduction in bandgap can be attributed to the gradual decrease in LUMO level, as illustrated in the figure. Notably, the HOMO levels of the quasi-2D perovskite films show minimal changes as the n-phase increases.

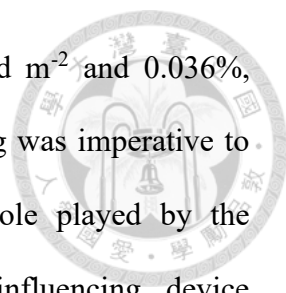
To better assess the potential of these films for light-emitting applications, we initially compared their relative photoluminescence (PL) intensities, as depicted in **Fig. 3.5**. It's apparent that the quasi-2D films exhibited stronger PL intensity compared to the pristine 2D film, EDBE(MAPbBr<sub>3</sub>)<sub>2</sub>PbBr<sub>4</sub> film shows the highest intensity. This enhancement can be ascribed to the reduced lattice torsion discussed earlier, which mitigates trap states to some extent. Additionally, even with a slight increase in the n-phase, appreciable quantum confinement effects are maintained, evidenced by the stronger PL intensity of the EDBE(MAPbBr<sub>3</sub>)<sub>2</sub>PbBr<sub>4</sub> film.<sup>[81]</sup> Subsequently, time-



resolved PL (TRPL) measurements of these films were conducted at an excitation wavelength of 365 nm. These curves were fitted using a bi-exponential formula, and the detailed parameters were summarized in **Table 3.2**. Here,  $\tau_1$  signifies a fast decay related to trap-assisted recombination, while the slower decay ( $\tau_2$ ) corresponds to radiative recombination. As illustrated, the PL lifetime increased as the n value decreased from  $\infty$  to 3, suggesting that EDBeBr<sub>2</sub> may offer certain surface passivation effects to reduce trap-assisted recombination. However, notably, the PL lifetime decreased as the n value further decreased to 1. This could be attributed to the increased exciton binding energy in the pure 2D film due to quantum and dielectric confinement effects.

**Fabrication and optimization of DJ phase quasi-2D PeLEDs.** Based on the above results, the EDBe(MAPbBr<sub>3</sub>)<sub>2</sub>PbBr<sub>4</sub> film demonstrates the most promising potential for light-emitting applications. Consequently, we proceeded to fabricate a p-i-n PeLED with a device configuration consisting of indium tin oxide (ITO)/PEDOT:PSS/EDBe(MAPbBr<sub>3</sub>)<sub>2</sub>PbBr<sub>4</sub>/TPBi (40 nm)/LiF (1 nm)/Al (120 nm), as illustrated in **Fig. 3.6a**. In this setup, LiF functions as the cathode buffer layer, facilitating charge transfer at the electron-transporting layer (ETL)/metal interface.<sup>[81, 127, 139, 140]</sup> The energy-level diagram of the fabricated device is presented in **Fig. 3.6b**. Notably, the EDBe(MAPbBr<sub>3</sub>)<sub>2</sub>PbBr<sub>4</sub> film exhibits a HOMO level of -5.53 eV and a LUMO level of -3.12 eV, which align well with the respective energy levels of the employed hole-transporting layer (HTL) (PEDOT:PSS, -5.20 eV) and ETL (TPBi, -2.80 eV). This alignment ensures efficient charge collection across the associated interfaces in the device and facilitates efficient recombination of injected holes and electrons in the emissive layer.

Despite the promising characteristics and appropriate energy levels, the performance of the EDBe(MAPbBr<sub>3</sub>)<sub>2</sub>PbBr<sub>4</sub> film falls short of expectations. As depicted in **Fig. 3.7**,



the luminance and EQE of the fabricated device are only 43.7 cd m<sup>-2</sup> and 0.036%, respectively. Thus, it became evident that proper device engineering was imperative to enhance performance. A recent study underscored the critical role played by the composition and conductivity of the PEDOT:PSS HTL in influencing device performance.<sup>[141]</sup> It was revealed that the surface chemistry and texture of PEDOT:PSS significantly impact interfacial interactions with the emissive layer, while its conductivity influences charge transport within the device. Therefore, PEDOT:PSS CH 8000, known for its higher resistivity ( $5 \times 10^4 - 3 \times 10^5$  ohm-cm) compared to PEDOT:PSS P Al 4083 (500 – 5000 ohm-cm), was selected. Furthermore, a methanol post-treatment was applied in line with previous findings.<sup>[107]</sup> This simple treatment effectively removes the reductant PSS from the film surface, thereby facilitating hole transfer across the corresponding interface.

As illustrated in **Fig. 3.7**, employing PEDOT:PSS CH 8000 as the HTL resulted in significantly improved device performance (luminance: 354.64 cd m<sup>-2</sup> and EQE: 0.75%) compared to the original control device. Beyond the impact of conductivity, we examined the surface texture and roughness of these two distinct PEDOT:PSS layers using atomic force microscopy (AFM), as depicted in **Fig. 3.8**. Notably, the CH8000 film exhibited a smoother surface compared to the 4083 film. After the methanol post-treatment, the surface of the CH8000 film became considerably rougher, indicating successful removal of insulating PSS from the surface.<sup>[107]</sup>

Since the overall luminance characteristics remain unsatisfactory, we conducted additional optimizations to enhance device performance. Sequential adjustments included modifying the concentration of the precursor solution, implementing passivation with TPBi, and performing thermal annealing. As depicted in **Fig. 3.9a** and **Fig. 3.9b**, we initially varied the concentration of the precursor solution, comparing solutions of 0.16

M and 0.18 M. It was observed that the PeLED fabricated from the 0.18 M precursor solution exhibited superior performance, likely due to improved film quality. However, increasing the concentration beyond 0.18 M resulted in an opaque film with reduced luminance, leading to decreased device performance.

Moreover, recent studies have emphasized the significant performance enhancements achievable through proper passivation of the emissive layer.<sup>[65, 141, 142]</sup> Various approaches have been explored, including incorporating polymers<sup>[143]</sup> or small molecules<sup>[52]</sup> into the precursor solution to provide effective passivation of the perovskite films. Another common method involves adding an additional layer on top of the emissive layer, facilitating surface recrystallization to refine the surface structure. Given the p-i-n architecture of our fabricated PeLED, we opted to utilize TPBi for passivating the perovskite emissive layer.<sup>[65, 141, 142]</sup> TPBi was introduced during the film evolution via a dripping process (10 mg/ml in chlorobenzene (CB)).

To evaluate the effectiveness of TPBi passivation, we initially assessed the photoluminescence quantum efficiency (PLQY) of the EDBE(MAPbBr<sub>3</sub>)<sub>2</sub>PbBr<sub>4</sub> film with and without TPBi treatment. The pristine EDBE(MAPbBr<sub>3</sub>)<sub>2</sub>PbBr<sub>4</sub> film exhibited a low PLQY of 0.3%; however, this was significantly enhanced to 14.3% after TPBi passivation. Furthermore, their time-resolved photoluminescence (TRPL) measurements (**Fig. 3.6c**) also indicated a prolonged lifetime of the TPBi-passivated film (see **Table 3.2**). These findings strongly suggest an improved performance of the derived PeLED. As depicted in **Fig. 3.9c** and **d**, the TPBi-passivated device exhibited a five-fold increase in luminance and EQE compared to the non-passivated device, with luminance improving from 455.88 cd/m<sup>2</sup> to 1431.81 cd/m<sup>2</sup>, and EQE increasing from 0.12% to 0.63%. Notably, the inset image in Fig. S6c depicts the films under a UV lamp, where the TPBi-passivated

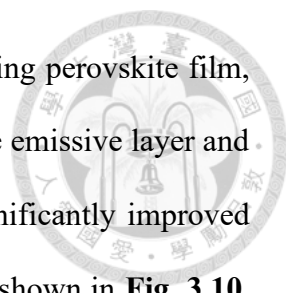
film emits noticeably brighter light than the pristine film, further confirming the efficacy of TPBi passivation.

Finally, thermal annealing was applied to the EDDBE(MAPbBr<sub>3</sub>)<sub>2</sub>PbBr<sub>4</sub> film under optimized conditions. Thermal annealing is widely recognized as a crucial step in enhancing the performance of PeLEDs, as it facilitates improved crystallinity of the perovskite layer, thereby enhancing its semiconducting properties.<sup>[144]</sup> However, it is worth noting that our investigated DJ phase quasi-2D perovskite exhibits inferior thermal stability. Typically, the as-cast film, post-spin coating, is transparent. However, upon annealing at 100°C for a brief period, the film becomes opaque, and its luminance characteristics vanish under UV illumination. Consequently, we opted for an optimized annealing temperature of 60°C for our system, significantly lower than temperatures typically applied in other perovskite systems.

**Fig. 3.9e&f** illustrate a comparison of the luminescence characteristics of the devices with and without annealing. Clearly, proper annealing led to improved luminescence characteristics of the device, with luminance increasing from 1431.81 cd/m<sup>2</sup> to 1651.75 cd/m<sup>2</sup>, and EQE rising from 0.63% to 0.72%. Despite the demonstrated improvement in device performance, this outcome highlights the inferior thermal stability of our studied DJ phase quasi-2D perovskite system as a limiting factor. We speculate that this limitation stems from the soft, long diamine chain between the perovskite sheets, which is sensitive to thermal energy. The direct linkage of the diamine cation between adjacent perovskite sheets renders it susceptible to twisting or rotating induced by thermal energy, profoundly affecting the overall lattice structure and resulting in inferior thermal stability.

Due to the inferior thermal stability of our studied quasi-2D film, we applied an additional TPBi layer as a protective coating by spin-coating it onto the film. This protective layer





serves multiple purposes: it enhances the passivation of the underlying perovskite film, smoothes the film surface, and facilitates charge transfer between the emissive layer and ETL.<sup>[145-147]</sup> The device utilizing this protective layer exhibited significantly improved luminance and EQE compared to the reference device without it, as shown in **Fig. 3.10**. Building upon these optimized conditions, we further adjusted the thickness of the TPBi ETL via thermal vacuum deposition. Previous studies have documented a negative correlation between TPBi thickness and the resulting turn-on voltage, with the commonly optimized thickness being around ~40 nm.<sup>[145, 148-151]</sup> However, due to the incorporation of an additional TPBi protective layer, we found that the optimized thickness of the vacuum-deposited TPBi ETL was reduced to 30 nm in our case, as depicted in **Fig. 3.11** and

**Table 3.3.** Finally, the top-performing PeLED based on the quasi-2D EDDBE(MAPbBr<sub>3</sub>)<sub>2</sub>PbBr<sub>4</sub> film achieved a maximum luminance of 1903 cd m<sup>-2</sup> with a maximum EQE of 1.06%, as presented in **Fig. 3.7a** and **b**. **Fig. 3.7c** displays its corresponding electroluminescence (EL) curves under different bias conditions. Notably, the peak position remained unchanged with bias, and a small full width at half maximum (FWHM) of ~26 nm was observed, indicating its stability and high color purity.

### 3.1.4 Summary

In conclusion, this work marks a pioneering step in the development of visible-light-emitting quasi-2D perovskite LEDs based on diamine-derived Dion–Jacobson (DJ) phase structures. By incorporating the bulky diammonium spacer 2,2'-(ethylenedioxy)bis(ethylammonium) (EDBE), we synthesized a series of DJ-phase EDDBE(MAPbBr<sub>3</sub>)<sub>n-1</sub>PbBr<sub>4</sub> (n = 1, 3, 5, ⋯, ∞). Notably, the quasi-2D films exhibited

significantly narrower photoluminescence compared to the broader emission profile of 2D EDBEPbBr<sub>4</sub>, which is dominated by self-trapped states. This improvement is attributed to the increased incorporation of 3D-like perovskite domains that alleviate lattice distortion and help modulate trap state distribution. With careful device optimization, we achieved a green-emitting PeLED based on the EDBE(MAPbBr<sub>3</sub>)<sub>2</sub>PbBr<sub>4</sub> composition, delivering a peak luminance of 1903 cd/m<sup>2</sup> and a maximum external quantum efficiency (EQE) of 1.06%. Nevertheless, thermal instability of the EDBE-based perovskites remains a key challenge, likely due to the flexibility and thermal sensitivity of the diamine spacer. Compared to RP-phase analogs, this limitation constrains device durability and performance. Future studies should prioritize the molecular design of more thermally robust diamine cations to further advance DJ-phase 2D perovskite emitters.

### 3.1.5 Tables and Figures

**Table 3.1** The relationship between the prepared quasi-2D (EDBE)(MA)<sub>n-1</sub>Pb<sub>n</sub>Br<sub>3n+1</sub> perovskites and the precursor ratios. The ratio in the columns are molar ratio.

	(EDBE)Br <sub>2</sub> : MABr : PbBr <sub>2</sub>
<b>n = 1</b>	1 : 0 : 1
<b>n = 3</b>	1 : 2 : 3
<b>n = 5</b>	1 : 4 : 5
<b>n = ∞</b>	0 : 1 : 1

**Table 3.2** TRPL lifetime of the studied quasi-2D EDDBE(MAPbBr<sub>3</sub>)<sub>n-1</sub>PbBr<sub>4</sub> perovskite films deposited on ITO glass.

	$\tau_1$ (ns)	Fraction 1(%)	$\tau_2$ (ns)	Fraction 2(%)
<b>n = 1</b>	2.14	39.6	6.58	60.3
<b>n = 3</b>	2.37	74.6	16.1	20.9
<b>n = 5</b>	0.90	95.1	10.6	4.88
<b>n = ∞</b>	0.83	75.6	3.38	24.4
<b>n =3 with TPBi Passivation</b>	5.66	70.7	47.1	24.5

**Table 3.3** The luminescence characteristics of the studied PeLEDs using a vacuum-deposited TPBi ETL with different thickness. The device configuration is ITO/PEDOT:PSS (CH8000 treated with methanol)/EDDBE(MAPbBr<sub>3</sub>)<sub>2</sub>PbBr<sub>4</sub>/TPBi (spin-coated)/TPBi (vacuum-deposited, with different thickness)/LiF/Al.

Thickness	Luminance (cd/m <sup>2</sup> )	EQE (%)
<b>50 nm</b>	55.26	0.23
<b>40 nm</b>	313.00	0.42
<b>35 nm</b>	1627.23	0.63
<b>30 nm</b>	1902.88	1.06

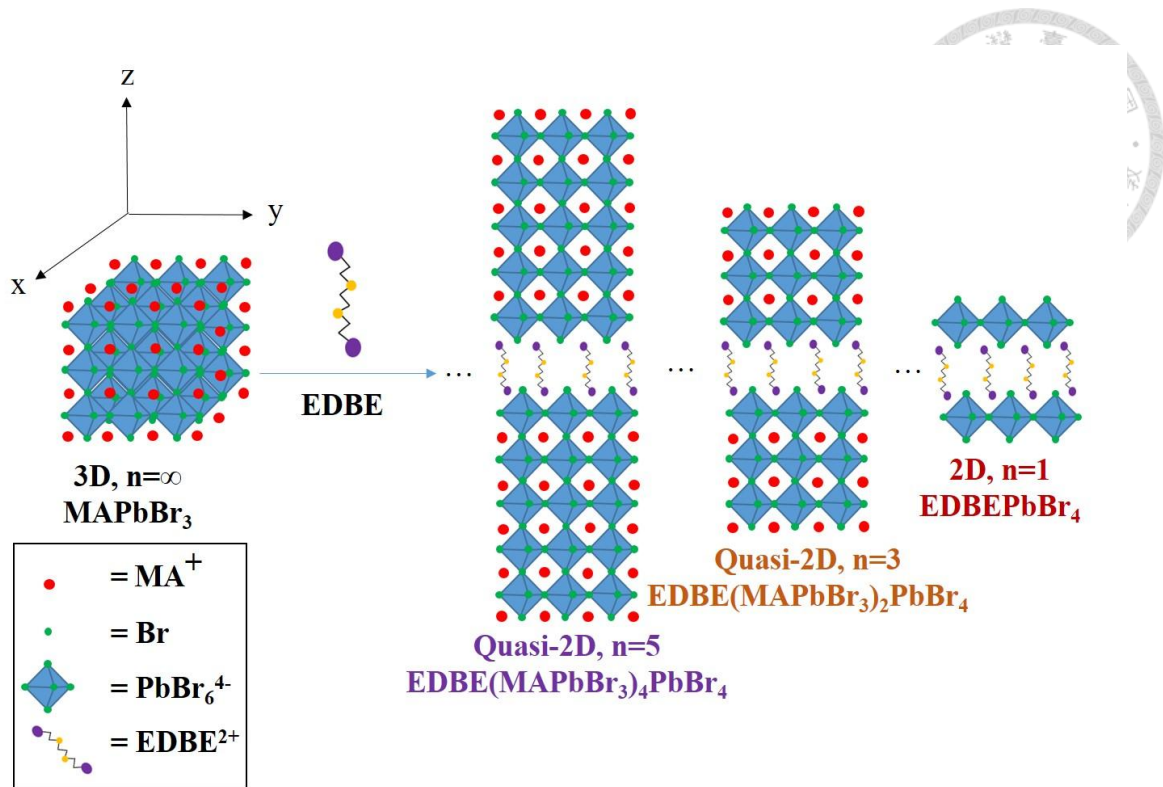


**Fig. 3.1** Illustration of the studied DJ phase quasi-2D ED BE(MAPbBr<sub>3</sub>)<sub>n-1</sub>PbBr<sub>4</sub> in this work.

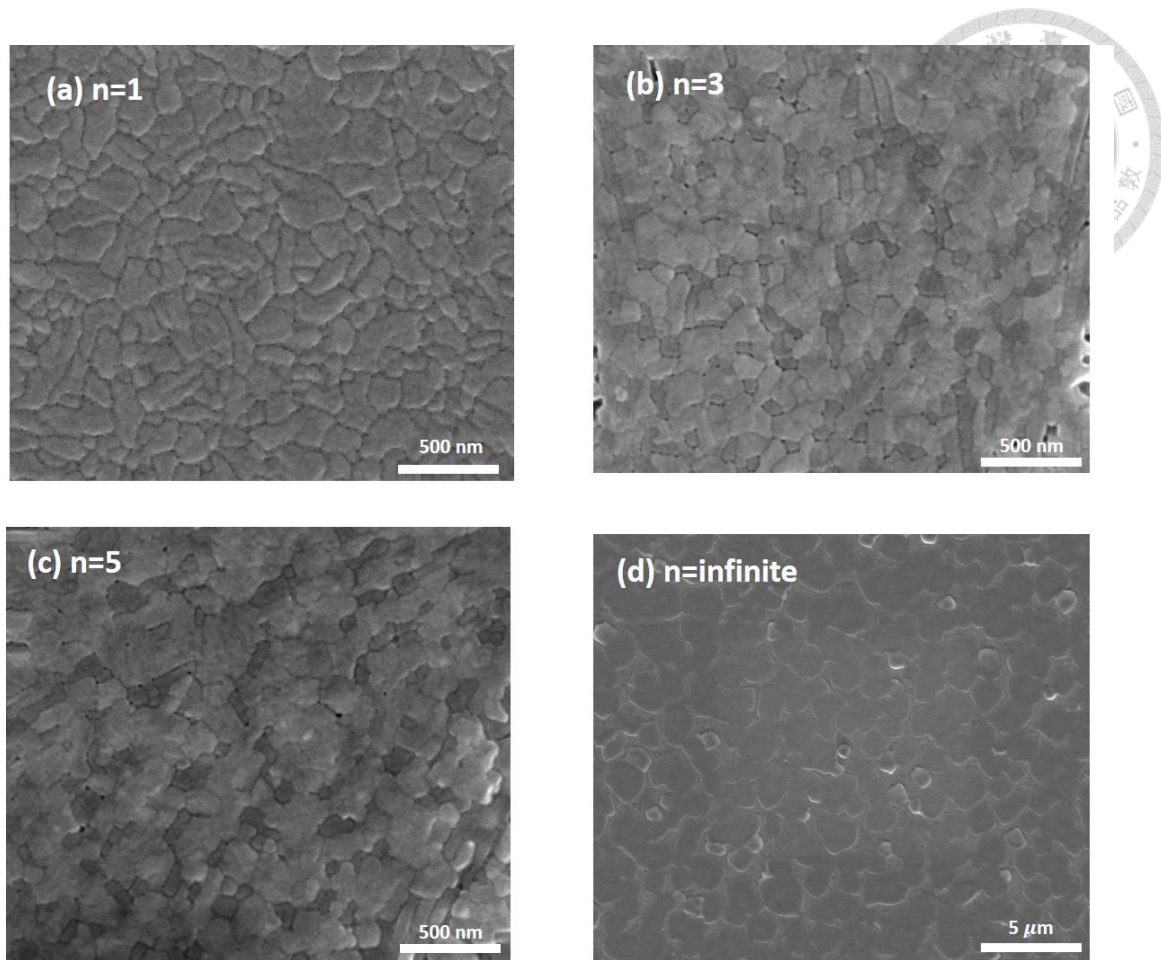


**Fig. 3.2** The SEM images of the prepared quasi-2D EDDBE(MAPbBr<sub>3</sub>)<sub>n-1</sub>PbBr<sub>4</sub> perovskite films.

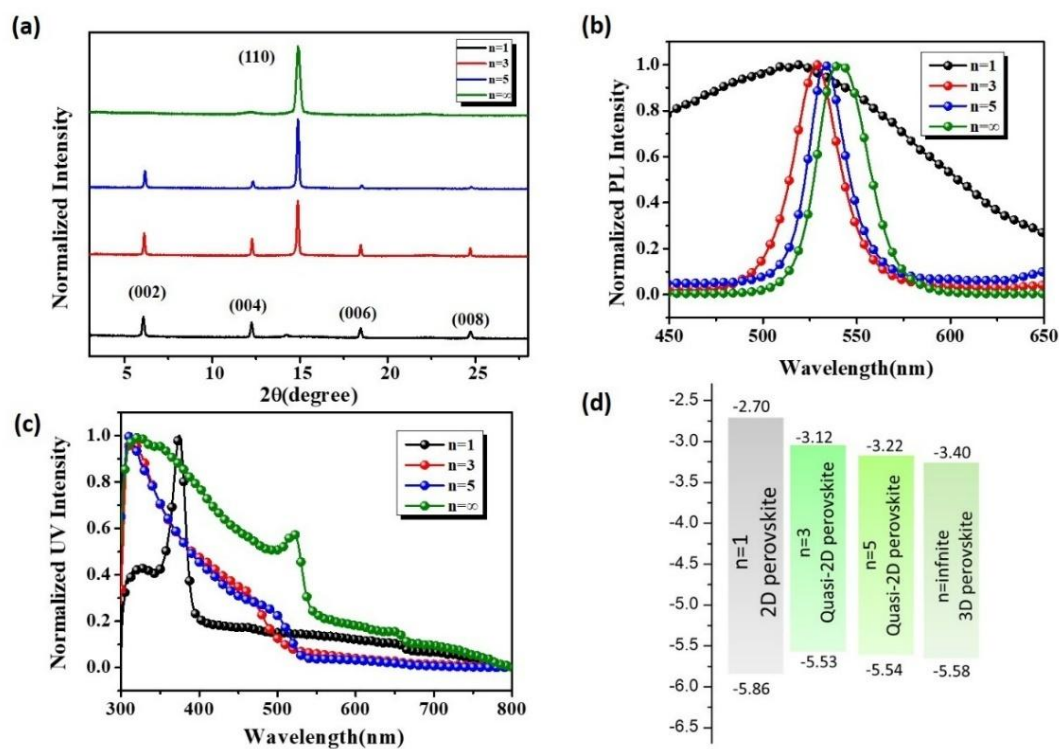


**Fig. 3.3** (a) 1D XRD patterns of the prepared quasi-2D EDPE(MAPbBr<sub>3</sub>)<sub>n-1</sub>PbBr<sub>4</sub> perovskite films and their corresponding (b) normalized UV-vis spectra, (c) normalized PL spectra, and (d) energy levels.

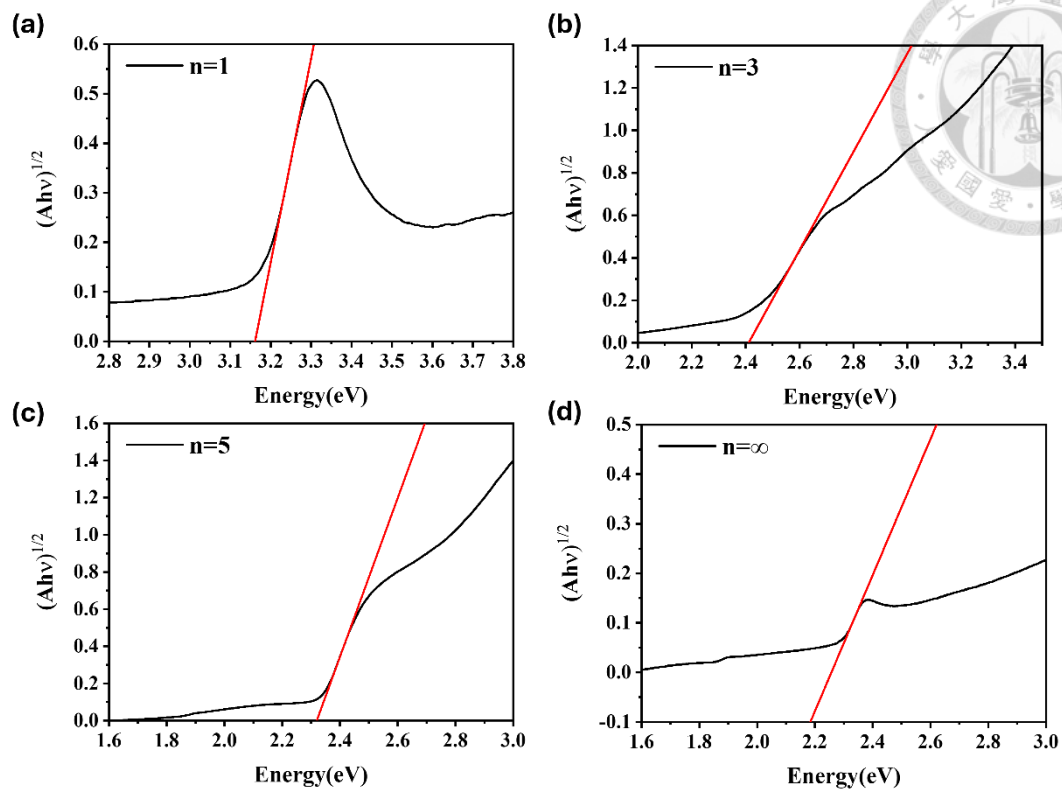


**Fig. 3.4** Tauc plots of the studied quasi-2D EDDBE(MAPbBr<sub>3</sub>)<sub>n-1</sub>PbBr<sub>4</sub> perovskite films.

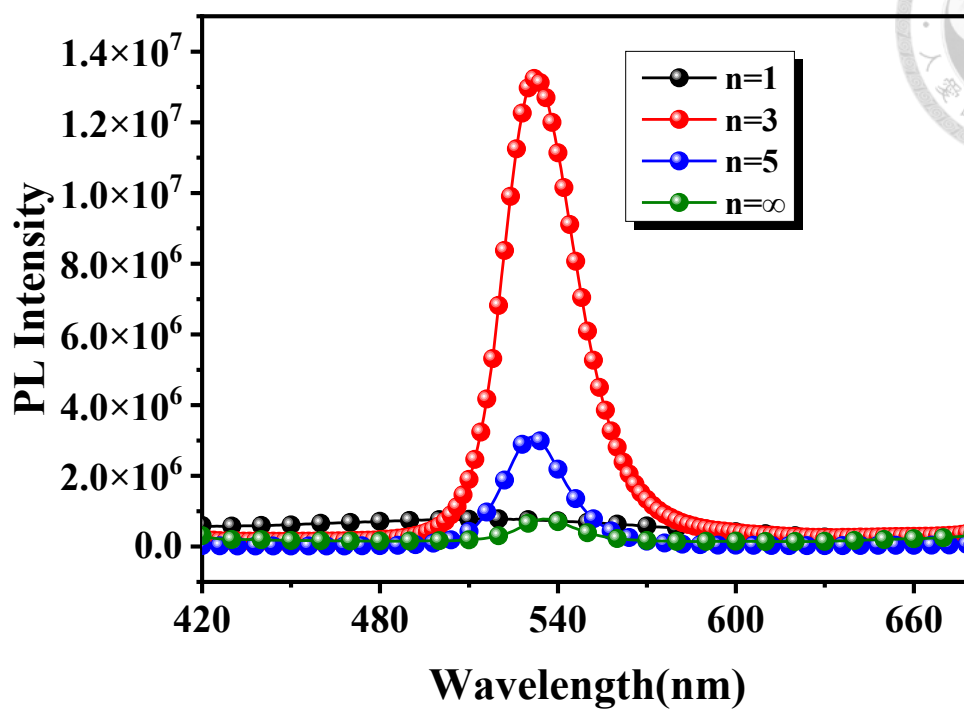


**Fig. 3.5** The relative PL intensity of the studied quasi-2D EDBe(MAPbBr<sub>3</sub>)<sub>n-1</sub>PbBr<sub>4</sub> perovskite films.



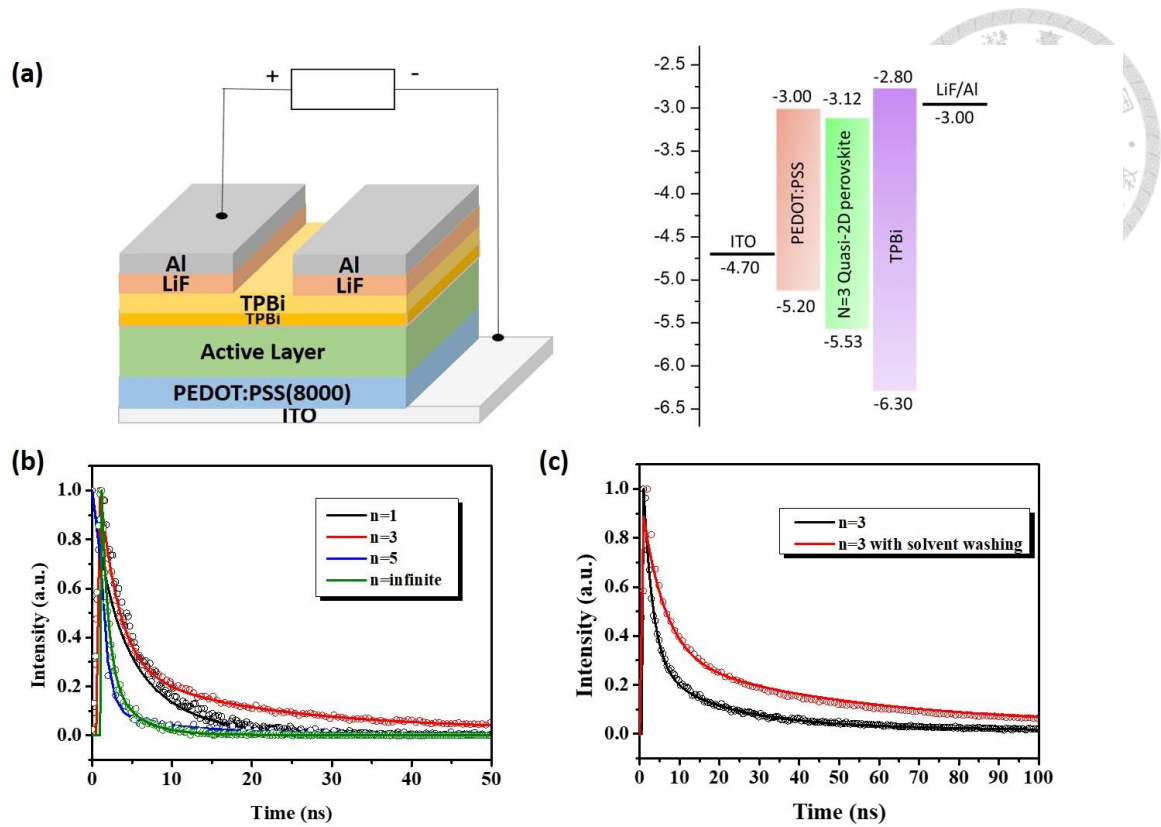


**Fig. 3.6** (a) Device configuration of our studied PeLED and the corresponding energy-level diagram. (b) TRPL of the studied quasi-2D EDPE(MAPbBr<sub>3</sub>)<sub>n-1</sub>PbBr<sub>4</sub> perovskite films and the fitted curves. (c) TRPL of the EDPE(MAPbBr<sub>3</sub>)<sub>n-1</sub>PbBr<sub>4</sub> film with or without TPBi passivation and the fitted curves.

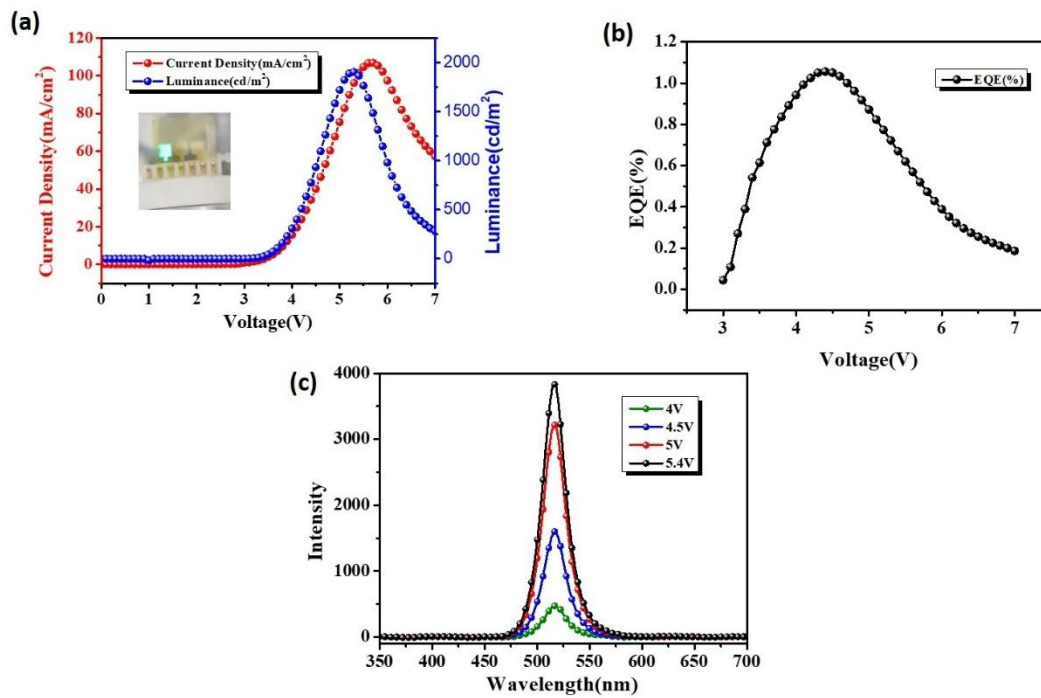


**Fig. 3.7** (a) The J-V-L characteristics of the top-performing device. The inset is the real picture of the device operated under a voltage of 5 V. (b) The EQE curve and (c) the EL curves of the champion device.

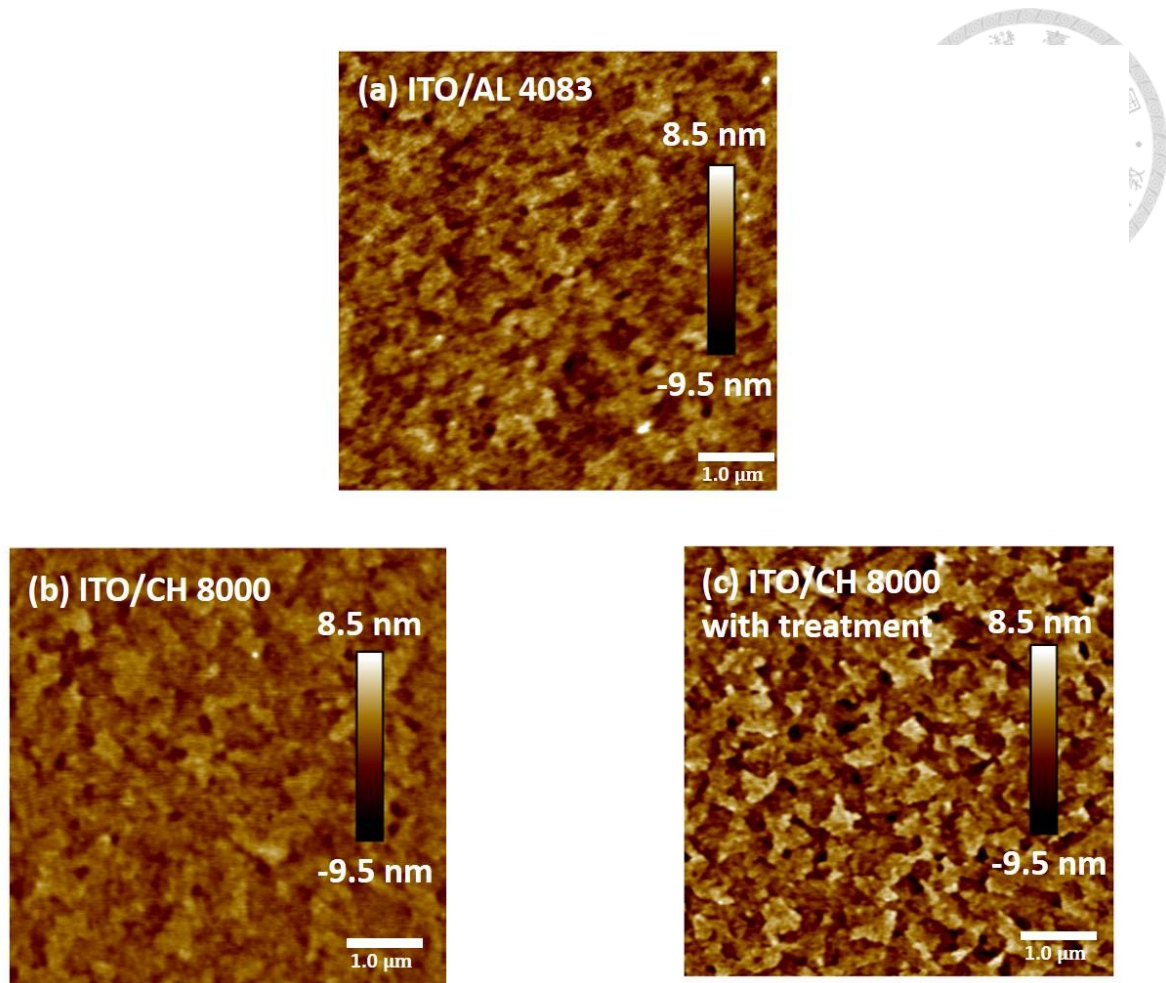


**Fig. 3.8** The surface AFM image of the PEDOT:PSS films with different conductivity on ITO glass. (a) AL 4083 (b) CH 8000 (c) CH 8000 with methanol post-treatment.

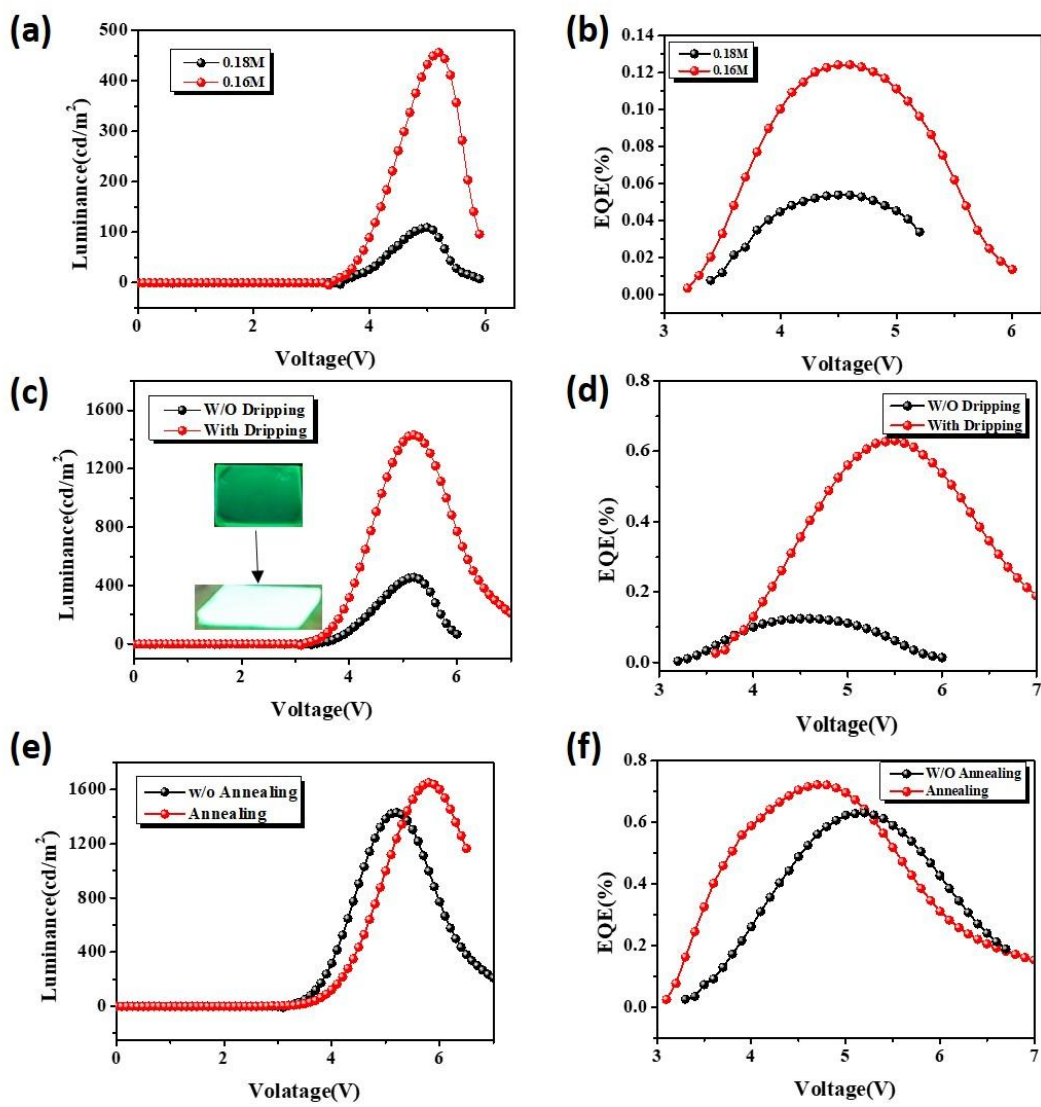


**Fig. 3.9** The (a, c, e) J-V-L and (b, d, f) EQE curves of the studied PeLEDs processed with different optimized conditions as noted.

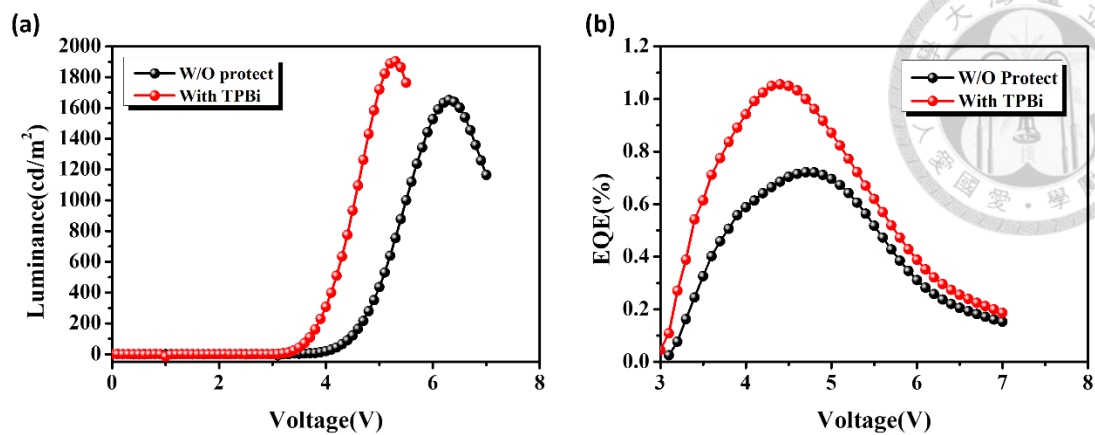


**Fig. 3.10** (a) The J-V-L and (b) EQE curves of the studied PeLEDs with and without using TPBi as a protecting layer. The device configuration is ITO/PEDOT:PSS (AL 4083)/EDBE(MAPbBr<sub>3</sub>)<sub>2</sub>PbBr<sub>4</sub>/TPBi (spin-coated)/TPBi (vacuum-deposited, 40 nm)/LiF/Al.

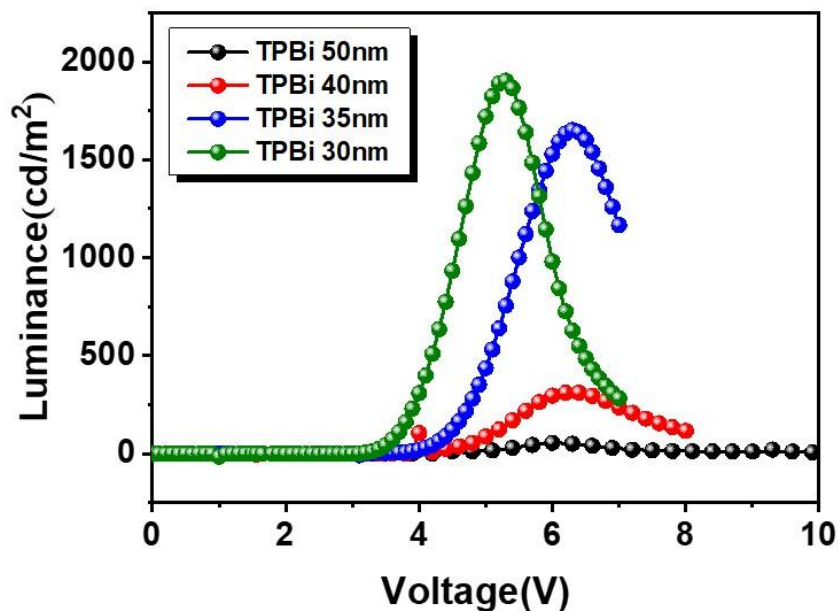


**Fig. 3.11** The J-V-L curves of the studied PeLEDs using a vacuum-deposited TPBi ETL with different thickness. The device configuration is ITO/PEDOT:PSS (CH8000)/EDBE(MAPbBr<sub>3</sub>)<sub>2</sub>PbBr<sub>4</sub>/TPBi (spin-coated)/TPBi (vacuum-deposited, with different thickness)/LiF/Al.

## 3.2 Regulating the Phase Distribution of Quasi-2D Perovskites Using Cyclic Molecules Toward Improved Light-Emitting Performance



The text and figures in this section are reproduced with permission from:

**C. H. Chen**<sup>†</sup>, Y. H. Kuo<sup>†</sup>, Y. K. Lin, I. C. Ni, B. H. Lin, C. I. Wu, H. L. Yip, C. C. Kuo\*, C. C. Chueh\*, “Enhancing the Performance of Quasi-2D Perovskite Light-Emitting Diodes Using Natural Cyclic Molecules with Distinct Phase Regulation Behaviors”, *ACS Appl. Mater. Inter.*, 14, 7, 9587–9596 (2022).

**C. H. Chen**<sup>†</sup>, C. H. Hsu<sup>†</sup>, I. C. Ni, B. H. Lin, C. I. Wu, C. C. Kuo\*, C. C. Chueh\*, “Regulating the Phase Distribution of Quasi-2D Perovskites Using a Three-Dimensional Cyclic Molecule Toward Improved Light-Emitting Performance”, *Nanoscale*, 14, 17409-17414 (2022).

### 3.2.1 Background

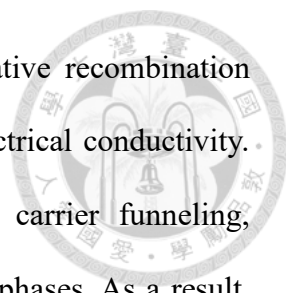
Metal halide perovskites have attracted considerable attention for their outstanding optoelectronic properties, including tunable emission wavelengths, high photoluminescence quantum efficiencies, and compatibility with solution processing methods.<sup>[51, 83, 152-154]</sup> Among various structural forms, quasi-two-dimensional (quasi-2D) perovskites, represented by the general formula  $(A_2)_2(A_1)_{n-1}B_nX_{3n+1}$ ;  $A_2$  = large organic cation ( $R^+$ , monoamine),  $A_1 = CH_3NH_3^+$ ,  $Cs^+$  or  $(A_2)(A_1)_{n-1}B_nX_{3n+1}$ ;  $A_2$  = large organic cation ( $R^{2+}$ , diamine), have emerged as a leading candidate for next-generation perovskite light-emitting diodes (PeLEDs). This structure combines the benefits of enhanced environmental stability imparted by hydrophobic organic spacers with intrinsic quantum-

well confinement effects that effectively boost exciton recombination rates and emission efficiency.

A defining characteristic of quasi-2D perovskites is the presence of multiple coexisting “phases,” distinguished by the number ( $n$ ) of stacked inorganic perovskite layers sandwiched between organic spacers. These phases range from pure two-dimensional structures ( $n = 1$ ), consisting of single-layer inorganic sheets isolated by bulky organic molecules, to quasi-2D structures (higher  $n$  values) that increasingly resemble three-dimensional perovskites.<sup>[42-46]</sup> Each of these phases has distinct electronic and optical properties due to varying degrees of quantum confinement and excitonic interactions, resulting in a gradient of bandgaps across different  $n$  values. Typically, lower- $n$  phases possess wider bandgaps and higher exciton binding energies, whereas higher- $n$  phases exhibit narrower bandgaps with lower exciton binding energies, approaching the behavior of bulk perovskites.

During solution-processed crystallization of quasi-2D perovskite films, multiple  $n$ -phases spontaneously form due to differences in thermodynamic stability and crystallization kinetics. Specifically, phases with lower  $n$  (e.g.,  $n = 1$  or  $2$ ) exhibit lower formation energies and faster nucleation rates, causing them to readily precipitate and dominate the initial crystallization stage. In contrast, higher- $n$  phases ( $n \geq 4$ ), possessing higher formation energies and more complex crystallization pathways, typically form later during solvent evaporation or annealing steps. Ideally, in a PeLED configuration, electrically injected carriers generated in these quasi-2D films would transfer efficiently from low- $n$  phases toward higher- $n$  phases, which is the phenomenon named “energy funneling effect”.<sup>[59-61]</sup>

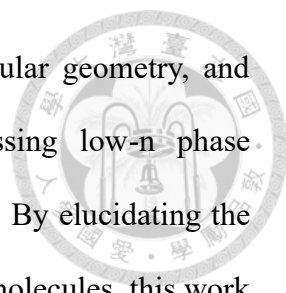
However, the uncontrolled, random formation of low- $n$  phases (especially  $n = 1$ ) can be detrimental to device performance. The presence of excessively low- $n$  phases



introduces defects, increases trap density, and promotes non-radiative recombination pathways due to their strong exciton binding energies and poor electrical conductivity. Furthermore, excessively low-n phases impede efficient charge carrier funneling, trapping excitons before they can reach the emission-active high-n phases. As a result, films containing significant amounts of low-n phases exhibit lower emission intensities, broader emission spectra, decreased color purity, and compromised overall device performance. To overcome the critical influence of random phase distribution on the performance of quasi-2D PeLEDs, considerable research has focused on controlling phase purity by employing various strategies, such as adjusting precursor ratios, tuning solvents, and adding functional additives. Among these methods, additive engineering has emerged as a particularly effective strategy, leveraging molecules capable of selectively interacting with specific perovskite precursor components to control phase formation kinetics.

Building on this concept, cyclic molecular additives have been investigated as promising candidates due to their ability to form stable complexes or interactions with both inorganic and organic perovskite precursors. These interactions can selectively suppress the rapid formation of undesirable low-n phases while promoting the controlled growth of favorable high-n phases. In this section, two published studies are combined and compared to gain deeper insight into the phase regulation mechanisms in quasi-2D perovskites. The first study explores the use of natural cyclic molecules, cyclodextrins, with two distinct cavity sizes:  $\alpha$ -cyclodextrin ( $\alpha$ -CD) and  $\beta$ -cyclodextrin ( $\beta$ -CD). This work examines how varying pore sizes influence phase distribution during film formation. The second study investigates a three-dimensional cage-like cyclic molecule, cryptand, which exhibits strong interactions with perovskite precursors due to its rigid 3D structure.



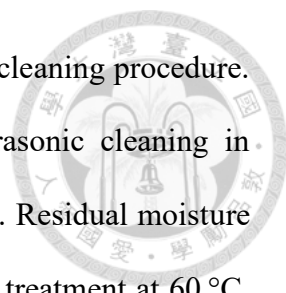


Each additive, characterized by its unique cavity size, molecular geometry, and chemical functionality, demonstrates distinct effects in suppressing low-*n* phase nucleation and facilitating the formation of desired higher-*n* phases. By elucidating the specific interactions and phase-regulating behaviors of these cyclic molecules, this work aims to deepen the understanding of molecular structure–property relationships and establish design principles for high-performance quasi-2D PeLED materials.

### 3.2.2 Experimental Section

**Materials.** Lead bromide (PbBr<sub>2</sub>, >99.9%) was purchased from Tokyo Chemical Industry Co., Ltd. Phenethylammonium bromide (PEABr, ≥98%) was purchased from Greatcell Solar Materias. Cesium bromide (CsBr, >99.9%), α-CD (≥98%), β-CD (≥97%), Kryptofix® 222 (cryptand, 98%), lithium fluoride (LiF, >99.99%) and solvents such as dimethylformamide (DMF, 99.8%) and dimethyl sulfoxide (DMSO, ≥99.9%), all purchased from Sigma-Aldrich and used as received without further purification. TPBi (2,2',2''-(1,3,5-benzenetriyl)-tris(1-phenyl-1H-benzimidazole)) was sourced from Ultra Fine Chemical Technology Corp., and PEDOT:PSS (Clevios™ P AI 4083) was obtained from Uniregion Bio-Tech, both also used without additional purification.

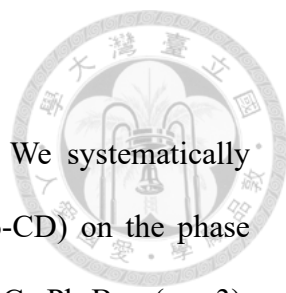
**Device fabrication.** To prepare the quasi-2D perovskite (PEA<sub>2</sub>Cs<sub>2</sub>Pb<sub>3</sub>Br<sub>10</sub>), a solution was formulated by mixing PEABr, CsBr, and PbBr<sub>2</sub> in dimethyl sulfoxide (DMSO) at a 1:1:1.5 molar ratio. This mixture was stirred at room temperature overnight to ensure complete dissolution. For additive engineering, α-cyclodextrin (α-CD), β-cyclodextrin (β-CD), and cryptand were introduced into the precursor solution in varying amounts, using PbBr<sub>2</sub> as the reference. The molar ratios employed were 1:0.02, 1:0.04, 1:0.07, and 1:1 for the cyclodextrins, and 1:0.025, 1:0.05, and 1:0.075 for cryptand. The



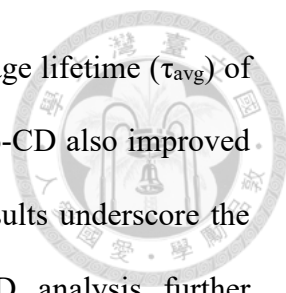
substrates, consisting of ITO and plain glass, underwent a multistep cleaning procedure. Initially washed with detergent, they were then subjected to ultrasonic cleaning in deionized water, acetone, and isopropyl alcohol for 15 minutes each. Residual moisture and solvents were removed by nitrogen drying followed by thermal treatment at 60 °C. Plasma treatment was subsequently applied to render the substrate surfaces more hydrophilic. PEDOT:PSS was used as the hole transport layer and applied to the substrates via spin-coating at 3500 rpm for 45 seconds. The films were then annealed at 150 °C for 15 minutes in ambient air. All subsequent processing steps took place in a nitrogen-filled glove box. Perovskite films incorporating different amounts of cyclic molecular additives were deposited on top of the PEDOT:PSS via spin-coating at 5000 rpm for 1 minute, followed by thermal annealing at 70 °C for 10 minutes. The device architecture was completed by thermally evaporating successive layers of TPBi (30 nm), LiF (1 nm), and aluminum (100 nm) under high vacuum conditions, maintained below  $10^{-6}$  torr.

**Characterization.** Quasi-2D perovskite films for characterizations were prepared by spin-coating the precursor solutions at 5000 rpm for 1 min. UV-vis absorption was measured using a Jasco V-730 spectrometer. Temperature-dependent PL and time-resolved PL (TRPL) were recorded using a Horiba Fluorolog-3 and a Hamamatsu Universal Streak Camera C10910 at NSRRC (TPS 23A). SEM (Hitachi S4800), XRD (PANalytical X'Pert3), XPS (PerkinElmer PHI 5400), and UPS (specs UVS 10/35) were used for structural and electronic characterization. Electrical performance, including J-V-L characteristics, external quantum efficiency (EQE), and electroluminescence (EL), was evaluated using an Enlitech LQ-100 system with a 100 mm<sup>2</sup> integrating sphere.

### 3.2.3 Results and Discussion

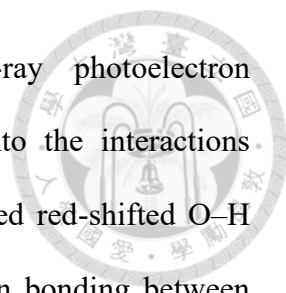


**Phase regulation effect caused by cyclodextrin additives.** We systematically studied the effects of  $\alpha$ -cyclodextrin ( $\alpha$ -CD) and  $\beta$ -cyclodextrin ( $\beta$ -CD) on the phase distribution of quasi-2D perovskite films with the composition  $\text{PEA}_2\text{Cs}_2\text{Pb}_3\text{Br}_{10}$  ( $n = 3$ ). These cyclic molecules possess different cavity sizes and hydroxyl-rich chemical functionalities, which enable varying degrees of interaction with perovskite precursors. UV-vis absorption spectroscopy (**Fig. 3.12a,b**) revealed the influence of these additives on quantum-well phase formation. UV-vis absorption spectra revealed that the pristine quasi-2D perovskite film displayed multiple absorption peaks centered at  $\sim 402$ ,  $433$ , and  $462$  nm, which correspond to the formation of low- $n$  phases ( $n = 1, 2$ , and  $3$ ). Upon incorporating  $\alpha$ -CD into the precursor solution, the intensities of the peaks at  $402$  nm and  $433$  nm were significantly suppressed with increasing additive concentration, and disappeared completely at a doping ratio of  $0.07$ . This observation confirms that  $\alpha$ -CD effectively inhibits the formation of low- $n$  phases. In contrast,  $\beta$ -CD exhibited a more gradual suppression effect, with notable reductions in the  $462$  nm peak at higher doping concentrations, suggesting better regulation of medium- $n$  ( $n = 3$ ) phases than low- $n$  phases. Photoluminescence (PL) spectra further supported this trend. The pristine film showed three emission peaks at  $433$ ,  $467$ , and  $502$  nm, indicative of insufficient exciton funneling. In  $\alpha$ -CD-doped films, a single, narrow emission peak at  $\sim 505$  nm was observed across all doping levels, indicating enhanced energy funneling to high- $n$  phases and suppressed nonradiative recombination.  $\beta$ -CD-doped films exhibited residual emission from low- $n$  phases at lower doping ratios, but converged to a single peak at  $\sim 508$  nm when the doping ratio reached  $0.1$ . To further evaluate the photophysical performance, time-resolved photoluminescence (TRPL) measurements were conducted. TRPL decay curves fitted with a bi-exponential model revealed that  $\alpha$ -CD extended both fast and slow



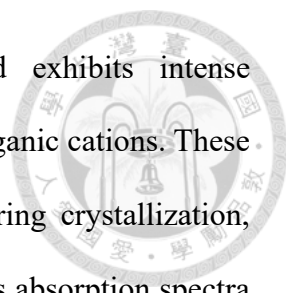
carrier lifetimes ( $\tau_{\text{fast}} = 0.65$  ns,  $\tau_{\text{slow}} = 3.88$  ns), resulting in an average lifetime ( $\tau_{\text{avg}}$ ) of 3.45 ns, significantly longer than the pristine film ( $\tau_{\text{avg}} = 1.49$  ns).  $\beta$ -CD also improved carrier lifetime ( $\tau_{\text{avg}} = 1.62$  ns), though less significantly. These results underscore the additive-induced suppression of nonradiative recombination. XRD analysis further supported these observations. For  $\alpha$ -CD-doped films, diffraction peaks associated with low- $n$  phases (notably at  $\sim 4^\circ$  and  $5.3^\circ$ ) were significantly suppressed, while higher- $n$  phase peaks ( $\sim 15.3^\circ$  and  $30.5^\circ$ ) became more pronounced and better defined. In addition, temperature-dependent PL measurements provided further insight into exciton dynamics and localization. The pristine film exhibited enhanced low- $n$  phase emissions (435 and 465 nm) at lower temperatures due to exciton localization. In contrast,  $\alpha$ -CD and  $\beta$ -CD-doped films showed greatly reduced temperature dependency, with  $\alpha$ -CD being more effective in maintaining a single dominant emission peak across the temperature range. These findings demonstrate that both TRPL and temperature-dependent PL consistently support the improved energy funneling and defect passivation achieved through cyclic additive incorporation, particularly for  $\alpha$ -CD.

X-ray diffraction (XRD) measurements revealed that the pristine film featured characteristic peaks at  $4^\circ$  and  $5.3^\circ$  corresponding to  $n = 1$  and  $2$  phases, along with higher-angle peaks at  $15.5^\circ$  and  $30.7^\circ$  indicative of high- $n$  phases. For  $\alpha$ -CD-doped films, the low-angle peaks vanished entirely, while the high-angle peaks became sharper and more intense, signifying improved crystallinity and phase purity.  $\beta$ -CD-doped films retained some low-angle features but showed weakened intensity, confirming partial suppression of low- $n$  phases. Scanning electron microscopy (SEM) imaging showed that both additives improved film morphology by reducing surface roughness and pinhole density. Among them,  $\alpha$ -CD-treated films displayed the smoothest and most uniform morphology, correlating with the best phase purity and carrier dynamics.



Fourier-transform infrared spectroscopy (FTIR) and X-ray photoelectron spectroscopy (XPS) analyses provided molecular-level insight into the interactions responsible for phase regulation. FTIR spectra in **Fig. 3.15** revealed red-shifted O–H stretching vibrations in both CD-doped films, suggesting hydrogen bonding between hydroxyl groups of CDs and perovskite constituents. XPS analysis revealed a downshift in the Pb 4f binding energies in the doped perovskite films, indicating electron donation from the additives to undercoordinated Pb<sup>2+</sup> sites (**Fig. 3.16a**). Additionally, the O 1s signal intensity was higher for the  $\alpha$ -CD/PVSK film than for the  $\beta$ -CD/PVSK film (**Fig. 3.15b**), which correlates with the higher doping ratio used (0.1 for  $\alpha$ -CD vs. 0.07 for  $\beta$ -CD). These observations suggest that the interactions between cyclodextrins (CDs) and the perovskite lattice are primarily mediated by electron donation from the hydroxyl oxygen atoms to Pb<sup>2+</sup> ions. Furthermore, more pronounced shifts in the Cs 3d and N 1s XPS signals were observed in  $\alpha$ -CD-doped films compared to  $\beta$ -CD-doped ones (**Fig. 3.16c&d**), implying stronger interactions with Cs<sup>+</sup> and PEA<sup>+</sup> cations. This enhanced binding is attributed to the smaller cavity size and higher hydroxyl group density of  $\alpha$ -CD, which confer a greater phase-regulating capability. Consequently,  $\alpha$ -CD facilitates greater incorporation of Cs<sup>+</sup> into the perovskite lattice during crystallization, favoring the formation of high-*n* quasi-2D phases.<sup>[78]</sup> Moreover, the higher hydroxyl content in  $\alpha$ -CD enhances interactions with the PEA<sup>+</sup> cation more effectively than  $\beta$ -CD, thereby better suppressing the formation of low-*n* phases, as corroborated by structural and phase distribution analyses.

**Phase regulation effect caused by cryptand additives.** The incorporation of a three-dimensional cyclic additive, cryptand, into quasi-2D perovskite films with the nominal composition PEA<sub>2</sub>Cs<sub>2</sub>Pb<sub>3</sub>Br<sub>10</sub> (*n* = 3) has also been investigated. Owing to its



unique cage-like geometry and donor-rich structure, cryptand exhibits intense coordination with  $\text{Pb}^{2+}$  ions and favorable hydrogen bonding with organic cations. These interactions enable cryptand to regulate the phase distribution during crystallization, suppress defect formation, and enhance device performance. UV-vis absorption spectra of quasi-2D perovskite films with varying cryptand doping ratios (0–0.075 relative to  $\text{PbBr}_2$ ) show clear phase regulation behavior in **Fig. 3.17a**. The pristine film exhibits absorption peaks at ~403, 432, and 459 nm, corresponding to  $n = 1, 2,$  and  $3$  phases, with the dominant  $n = 1$  peak reflecting random and unbalanced phase distribution. Upon cryptand addition, the 403 nm peak is significantly suppressed, while the  $n = 2$  and  $3$  peaks are enhanced, indicating a more concentrated distribution of higher- $n$  phases. Compared to 18-crown-6 in **Fig. 3.17b**, cryptand shows superior suppression of the  $n = 1$  phase, attributed to its stronger cation coordination capabilities. PL spectra further reveal photophysical improvements with cryptand. The pristine film shows multiple emissions including low- $n$  peaks, while cryptand-containing films exhibit a single dominant emission peak that blue-shifts from 514 to 505 nm with increasing doping (**Fig. 3.17c**). This shift results from both surface passivation and quantum well structure refinement. TRPL measurements reinforce these observations. The film doped with 0.05 cryptand shows the longest average carrier lifetime ( $\tau_{\text{avg}} = 19.5$  ns), compared to 5.2 ns for the pristine film (**Fig. 3.17d**). This result, in conjunction with a PLQY increase from 0.4% to 24.74%, confirms efficient energy funneling and reduced nonradiative recombination under optimal doping (**Fig. 3.18**).

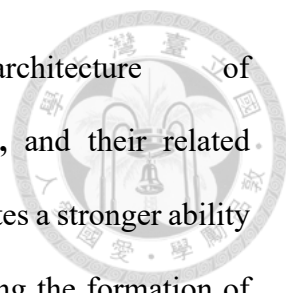
Temperature-dependent PL measurements provide further insight into the phase distribution and exciton dynamics at cryogenic conditions (**Fig. 3.19**). In pristine films, multiple emission peaks, especially at 406, 436, 470, and 485 nm, are significantly enhanced as temperature decreases, indicating pronounced exciton localization within

low-n domains. In contrast, cryptand-doped films with optimized ratios (0.05–0.075) show strong suppression or complete elimination of low-n emissions at low temperatures, maintaining a single sharp peak around 505 nm. This behavior signifies efficient energy transfer from low-n to high-n phases and a more uniform quantum-well structure.

X-ray diffraction (XRD) data show a clear structural transformation induced by cryptand (**Fig. 3.20a-d**). The characteristic peak of the 2D perovskite at  $5.3^\circ$  diminishes with increased doping, and at  $\geq 0.05$  doping, it vanishes completely, replaced by new features at  $4^\circ$  and sharpened peaks at  $15.3^\circ$  and  $30.5^\circ$  corresponding to high-n and 3D-like phases. These changes confirm suppression of the  $n = 1$  phase and improved crystallinity. SEM imaging supports this, showing significantly smoother films with fewer pinholes and blurred grain boundaries as cryptand is added. Optimal morphology is observed at 0.05 doping, while higher ratios introduce defects such as black spots, indicating over-doping (**Fig. 3.20e-h**).

To uncover the mechanism of cryptand-induced phase regulation,  $^1\text{H}$  NMR and XPS analyses were performed. NMR reveals the strongest chemical shift when cryptand is mixed with  $\text{PbBr}_2$  (2.58 to 2.87 ppm), indicating strong coordination. Additionally, a shift and broadening of the PEABr  $\text{NH}_3^+$  peak confirm hydrogen bonding with the organic cation (**Fig. 3.21**). XPS spectra further validate these interactions, with a notable O 1s shift upon  $\text{PbBr}_2$  addition, showing electron donation from cryptand to  $\text{Pb}^{2+}$  (**Fig. 3.22**). These results support a dual interaction mechanism: cryptand's cage captures  $\text{Pb}^{2+}$  to delay low-n phase crystallization, while O/N atoms passivate defects, collectively contributing to improved film quality and energy transfer.

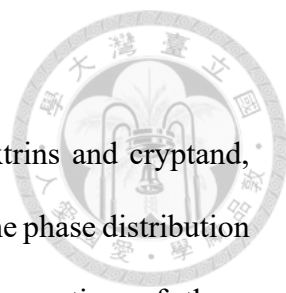
**Fabrication and performance of PeLEDs.** To evaluate the practical implications of the additives, we fabricated PeLED devices based on pristine and additive-doped quasi-



2D perovskite films with a device architecture of ITO/PEDOT:PSS/perovskite/TPBi/LiF/Al as shown in **Fig. 3.23a**, and their related energy level is shown in **Fig. 3.23b&c**. The  $\alpha$ -CD additive demonstrates a stronger ability to suppress the formation of low- $n$  phases ( $n \leq 2$ ), thereby promoting the formation of higher- $n$  phases and facilitating more efficient exciton funneling. As a result, the  $\alpha$ -CD-based PeLED achieves a maximum luminance ( $L_{\max}$ ) of 37,825 cd/m<sup>2</sup> and an external quantum efficiency (EQE) of 3.81% (**Fig. 3.24a&d**). In contrast,  $\beta$ -CD shows a better modulation of medium- $n$  phases ( $n = 3$ ), resulting in slightly lower performance with a  $L_{\max}$  of 24,793 cd/m<sup>2</sup> and EQE of 3.09% (**Fig. 3.24b&e**). On the other hand, the use of a three-dimensional cyclic molecule, cryptand, yields a more pronounced phase regulation effect due to its strong interaction with Pb<sup>2+</sup> ions, which effectively suppresses the formation of the  $n = 1$  phase and leads to a more concentrated phase distribution. The cryptand-based PeLED achieves an EQE of 4.02% and a  $L_{\max}$  of 15,532 cd/m<sup>2</sup>, reflecting a  $\sim 10$ -fold and  $\sim 5$ -fold enhancement, respectively, compared to the pristine device (**Fig. 3.24c&f**). Energy level analyses via photoelectron spectroscopy and absorption edge estimation further reveal that all three additives induce a slight reduction in the perovskite bandgap, improving energy level alignment and charge injection balance (**Fig. 3.23b&c**). Notably, the cryptand's multidentate coordination enables superior passivation of defect sites and more effective modulation of the quantum well structure, thereby facilitating radiative recombination and reducing nonradiative losses. These results underscore the importance of additive molecular structure in tailoring phase purity, optimizing energy alignment, and boosting device performance in quasi-2D PeLEDs.



### 3.2.4 Summary



In this work, two classes of cyclic organic additives, cyclodextrins and cryptand, were systematically investigated as molecular regulators to improve the phase distribution and optoelectronic performance of quasi-2D PeLEDs. The incorporation of these additives effectively modulates the crystallization dynamics of the  $\text{PEA}_2\text{Cs}_2\text{Pb}_3\text{Br}_{10}$  ( $n = 3$ ) quasi-2D perovskite, suppressing the formation of undesired low- $n$  phases and promoting a more concentrated distribution of mid- to high- $n$  phases. This optimized phase composition facilitates more efficient charge and energy transfer across the multi-quantum well structure, thereby reducing non-radiative recombination and enhancing radiative emission. Cyclodextrins ( $\alpha$ - and  $\beta$ -CD) serve as sterically hindered supramolecular hosts that interact with the perovskite precursor components, leading to improved film uniformity, reduced trap densities, and enhanced photophysical properties. Devices incorporating cyclodextrin-modified perovskite films exhibited notable improvements in external quantum efficiency and luminance compared to control devices. In addition, cryptand, a three-dimensional molecule, exhibits a stronger coordination affinity toward  $\text{Pb}^{2+}$  ions due to its cage-like structure containing multiple electron-donating O and N atoms. This enables more effective suppression of the  $n = 1$  phase, enhanced passivation of uncoordinated metal sites, and superior control over crystallization. As a result, PeLEDs with an optimized cryptand doping ratio achieved a peak luminance of  $15,532 \text{ cd m}^{-2}$  and an external quantum efficiency (EQE) of 4.02%.

In conclusion, these results highlight the critical role of molecular-phase regulation via cyclic additives in tailoring the structural and electronic landscape of quasi-2D perovskite films. The findings provide a robust framework for future molecular design strategies aimed at simultaneously optimizing phase purity, defect passivation, and carrier

dynamics in layered perovskite systems, thereby advancing the development of high-performance, stable PeLEDs for practical optoelectronic applications.



### 3.2.5 Tables and Figures

**Table 3.4** The fitting parameters for the TRPL results of pristine, hybrid  $\alpha$ -CD/quasi-2D perovskite and  $\beta$ -CD/quasi-2D.

	$A_1$	$\tau_1$ (ns)	$A_2$	$\tau_2$ (ns)	$\tau_{avg}$ (ns)
<b>Control</b>	0.45	1.75	0.40	0.40	1.49
<b><math>\alpha</math>-CD</b>	0.47	3.88	0.65	0.65	3.45
<b><math>\beta</math>-CD</b>	0.66	1.71	0.20	0.20	1.62

**Table 3.5** The fitting parameters for the TRPL results of quasi-2D perovskite films with different added doping ratios of the cryptand.

	$A_1$	$\tau_1$ (ns)	$A_2$	$\tau_2$ (ns)	$\tau_{avg}$ (ns)
<b>Control</b>	0.89	2.25	0.12	9.92	5.2
<b>Cry_0.025</b>	0.82	3.39	0.2	21.2	14.3
<b>Cry_0.05</b>	0.75	3.57	0.26	25.77	19.5
<b>Cry_0.075</b>	0.87	3.93	0.18	25.77	16.8

**Table 3.6** PLQY of quasi-2D perovskite films with different added doping ratios of the cryptand.

	PLQY (%)
<b>Control</b>	0.4
<b>Cry_0.025</b>	13.27
<b>Cry_0.05</b>	24.74
<b>Cry_0.075</b>	19.23

Table 3.7 Performance of fabricated PeLEDs

	EL peak (nm)	Max. Lum. (cd m <sup>-2</sup> )	Max. EQE (%)
Control	514	5177	0.65
$\alpha$ -CD_0.04	511	5485	2.16
$\alpha$ -CD_0.07	521	37825	3.81
$\alpha$ -CD_0.1	519	16697	1.27
$\beta$ -CD_0.04	518	24793	3.09
$\beta$ -CD_0.07	517	14518	0.96
$\beta$ -CD_0.1	515	13476	0.35
Cry_0.025	511	7458	3.68
Cry_0.05	511	15532	4.02
Cry_0.075	506	4563	2.98

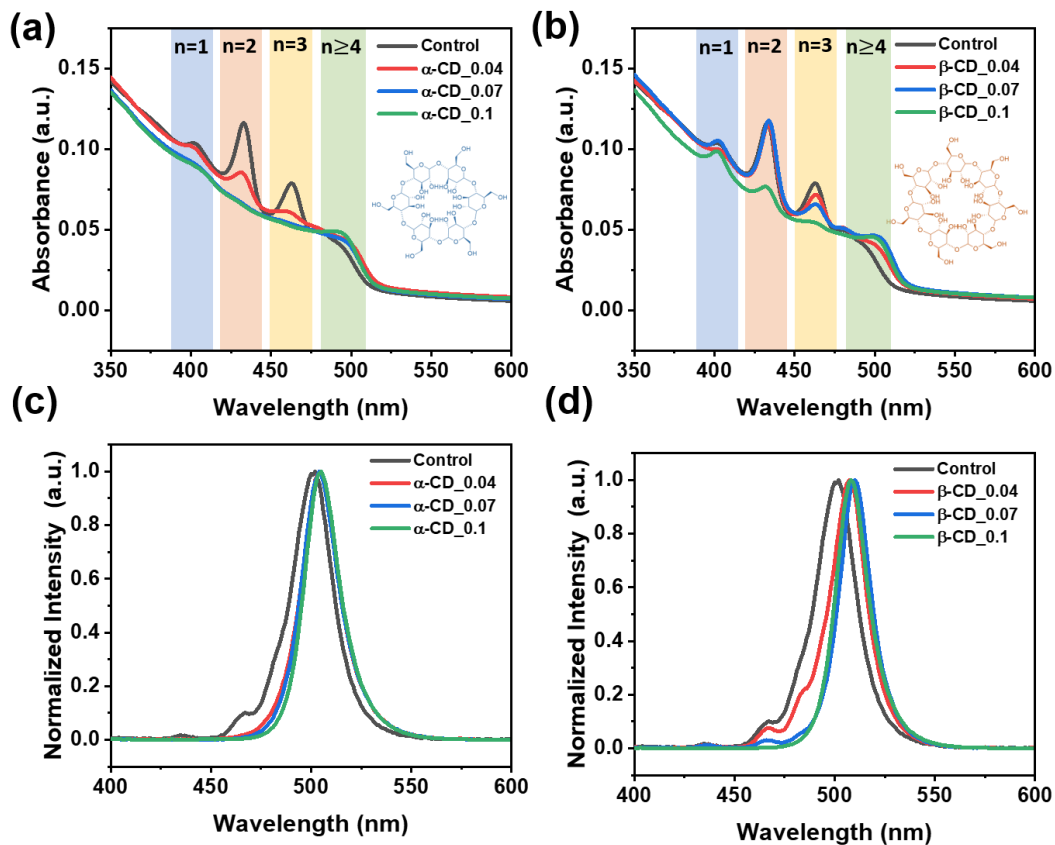
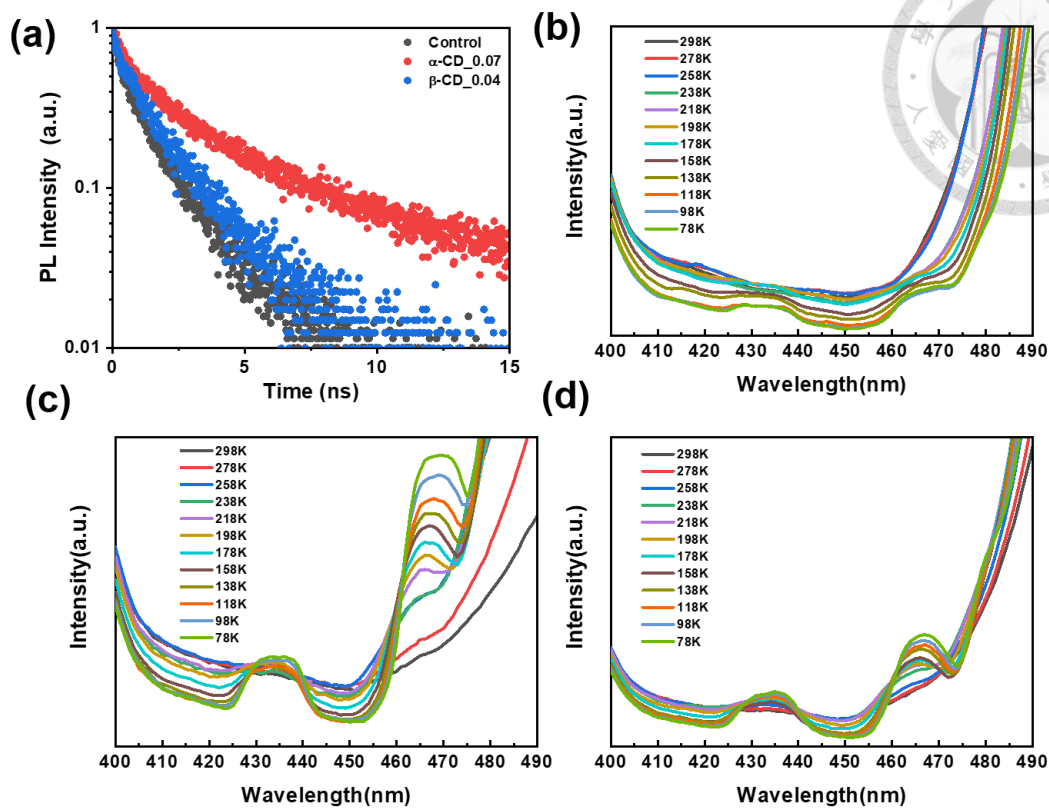
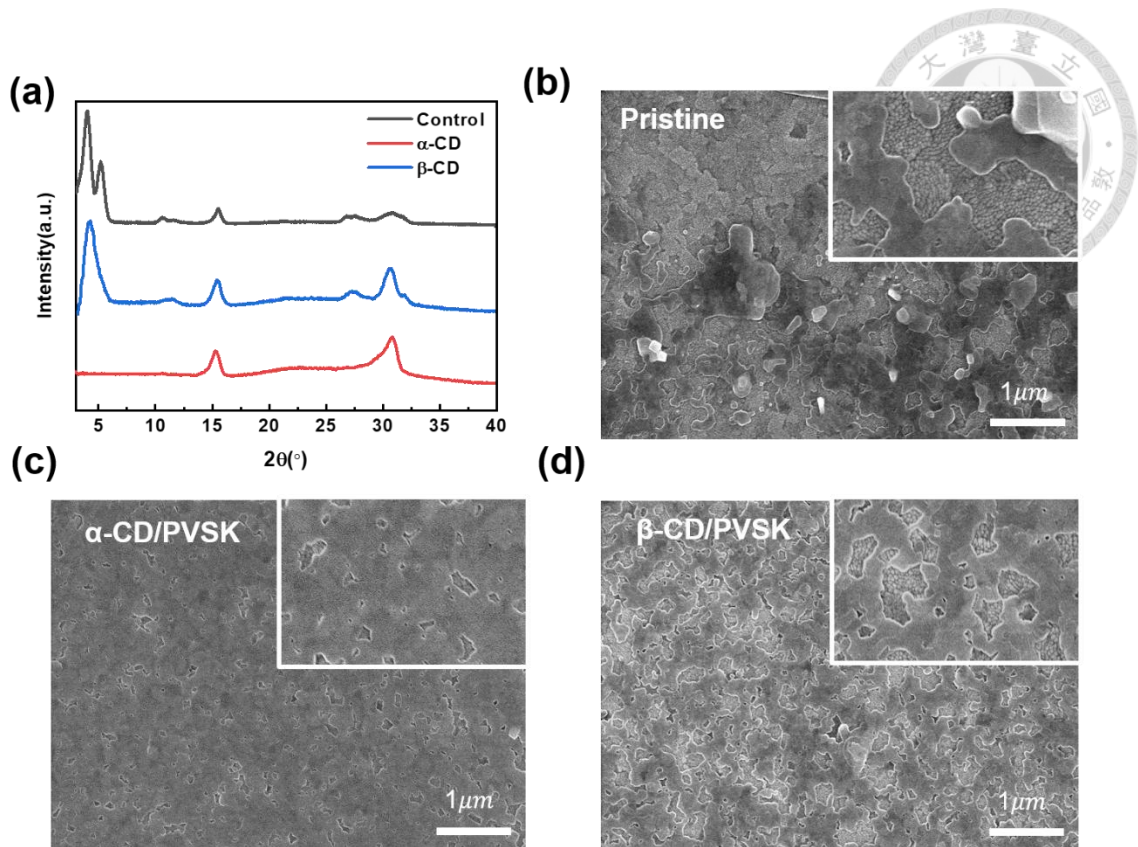


Fig. 3.12 (a,b) UV-vis absorption and (c,d) PL emission spectra of the hybrid quasi-2D perovskite films with different doping ratios of (a,c)  $\alpha$ -CD and (b,d)  $\beta$ -CD.



**Fig. 3.13** (a) TRPL curves of the hybrid  $\alpha$ -CD/quasi-2D perovskite and  $\beta$ -CD/quasi-2D perovskite films. Temperature-dependent PL measurement of the (b) pristine perovskite, (c)  $\alpha$ -CD/PVSK, and (d)  $\beta$ -CD/PVSK films.



**Fig. 3.14** (a) XRD characteristics of the hybrid  $\alpha$ -CD/quasi-2D perovskite (with a ratio of 0.1:1) and  $\beta$ -CD/quasi-2D perovskite (with a ratio of 0.07:1) films. SEM images of the (b) pristine perovskite, (c)  $\alpha$ -CD/PVSK, and (d)  $\beta$ -CD/PVSK films.

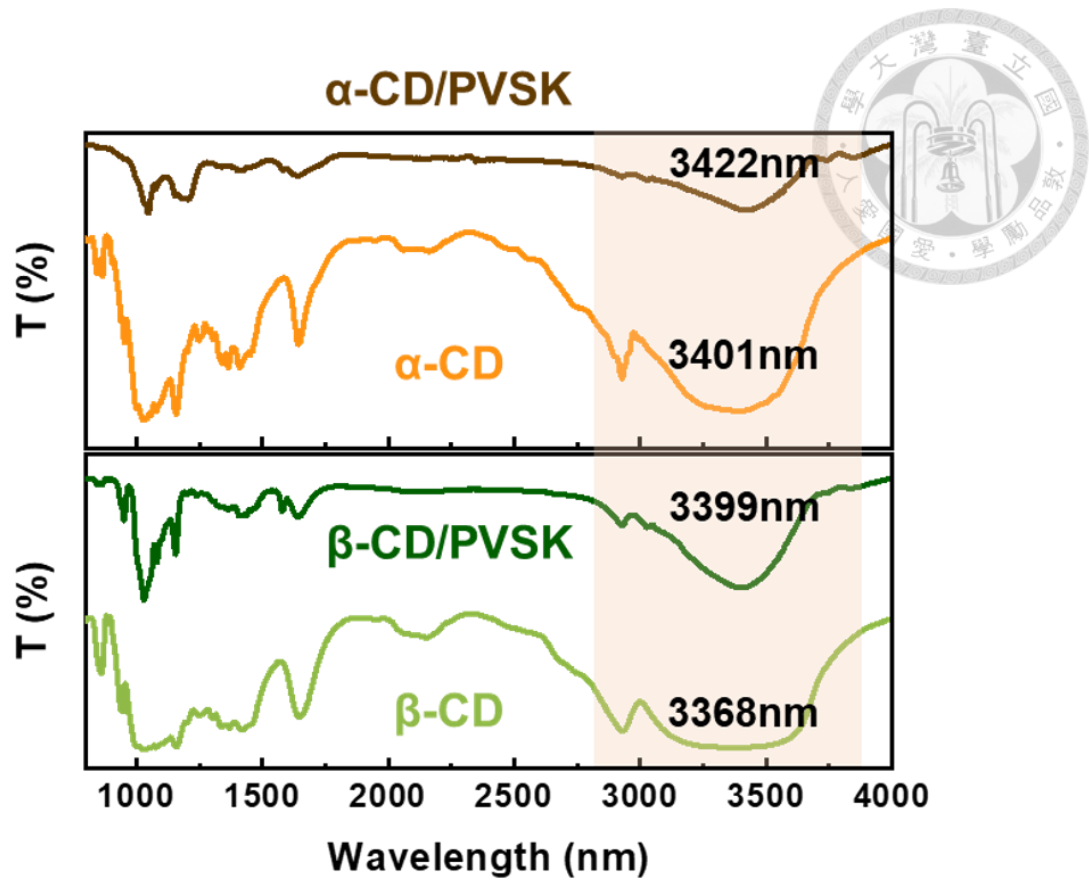
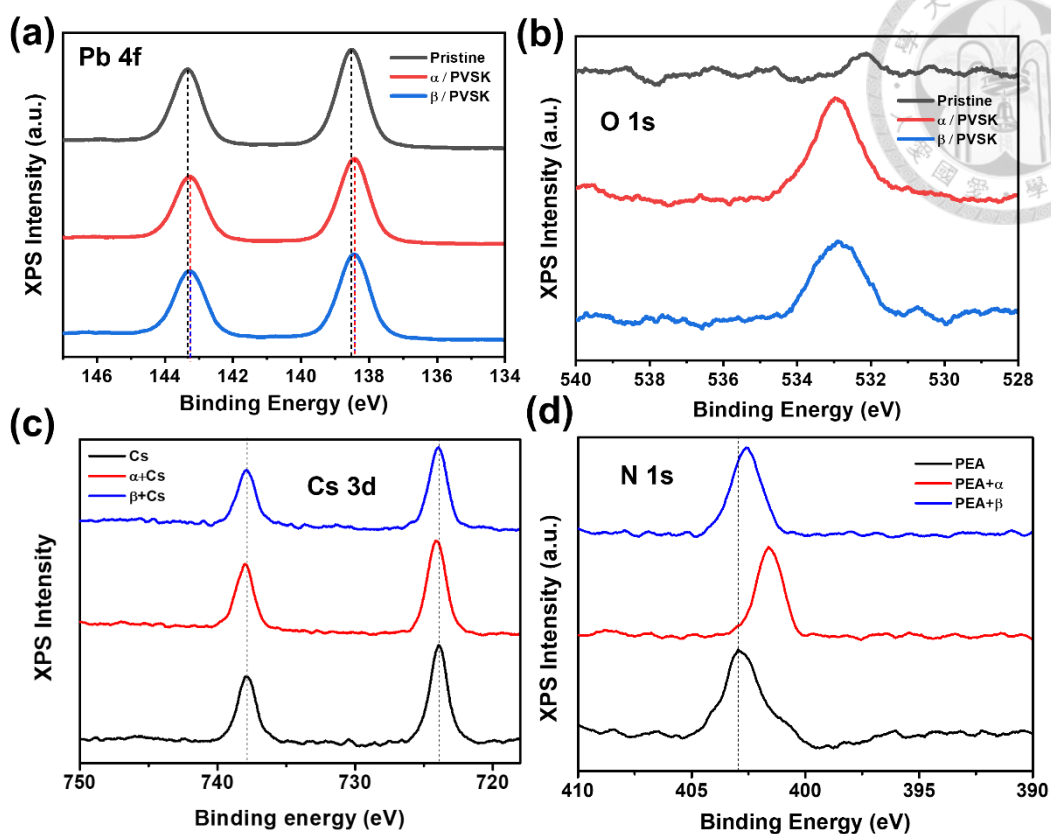
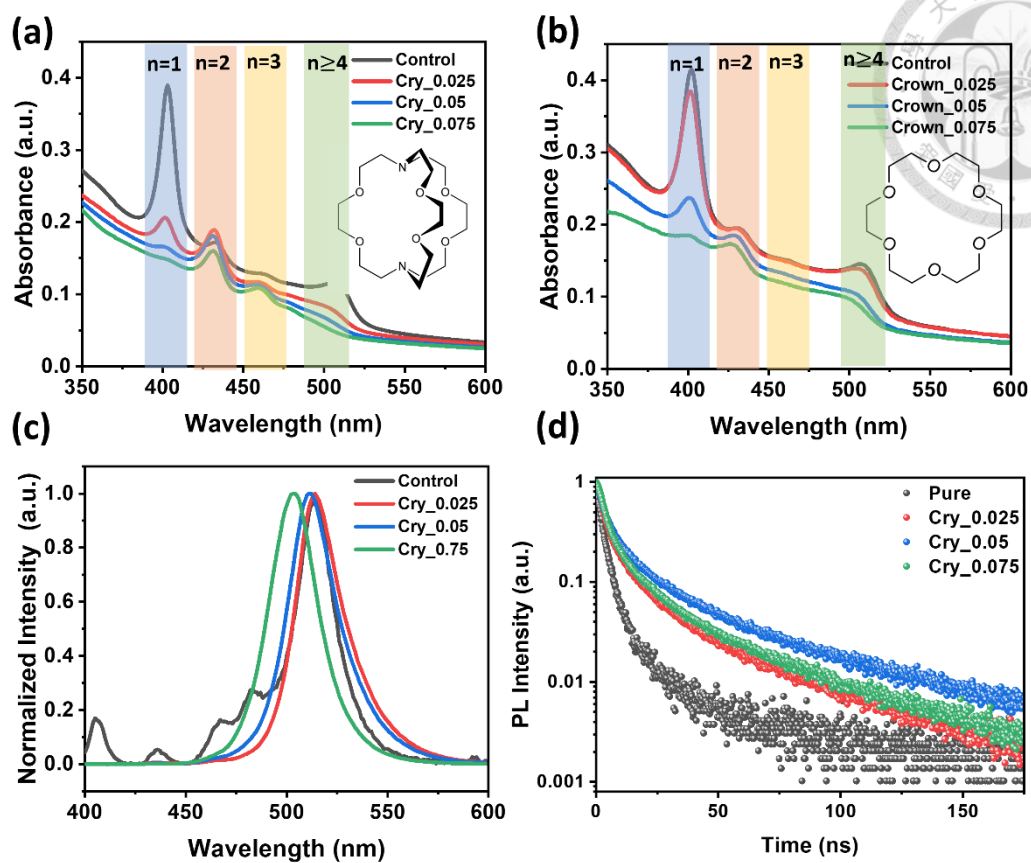


Fig. 3.15 FTIR spectroscopy of  $\alpha$ -CD/PVSK,  $\beta$ -CD/PVSK,  $\alpha$ -CD, and  $\beta$ -CD.



**Fig. 3.16** XPS spectra of (a) Pb 4f signal, (b) O 1s signal for the pristine quasi-2D,  $\alpha$ -CD/PVSK, and  $\beta$ -CD/PVSK films. XPS spectra of (c) Cs 3d signal for the pure CsBr,  $\alpha$ -CD/CsBr, and  $\beta$ -CD/CsBr films and (d) N 1s signal for the pure PEABr,  $\alpha$ -CD/PEABr, and  $\beta$ -CD/PEABr films.



**Fig. 3.17** UV-vis absorption measurement of quasi-2D perovskite films with (a) different doping ratios of Cryptand and (b) with different doping ratios of 18-Crown-6 added. (c) PL emission spectra, (d)TRPL curves of quasi-2D perovskite films with different doping ratios of Cryptand.



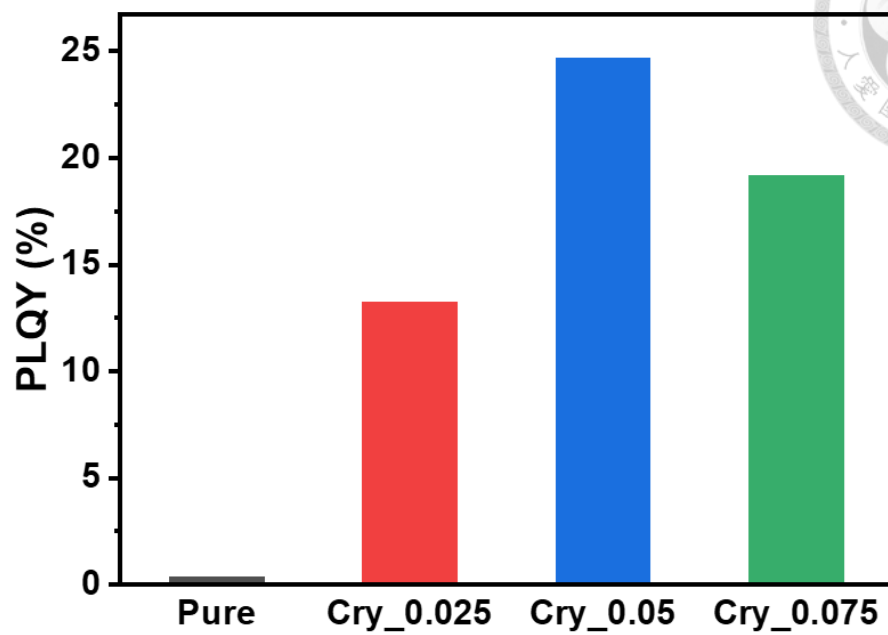


**Fig. 3.18** PLQY of quasi-2D perovskite films with different doping ratios of Cryptand.

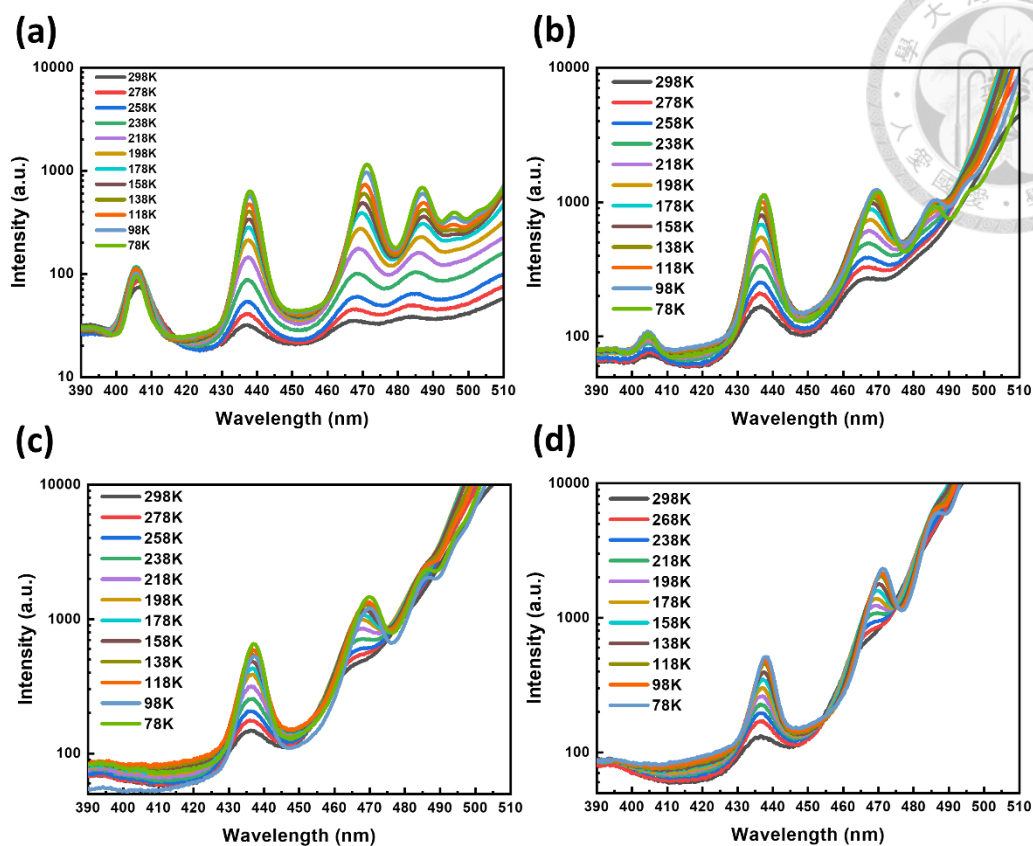


**Fig. 3.19** Temperature-dependent PL of (a) the pristine quasi-2D perovskite film, and the film with (b) 0.025 doping ratio (c) 0.05 doping ratio (d) 0.075 doping ratio of the cryptand.

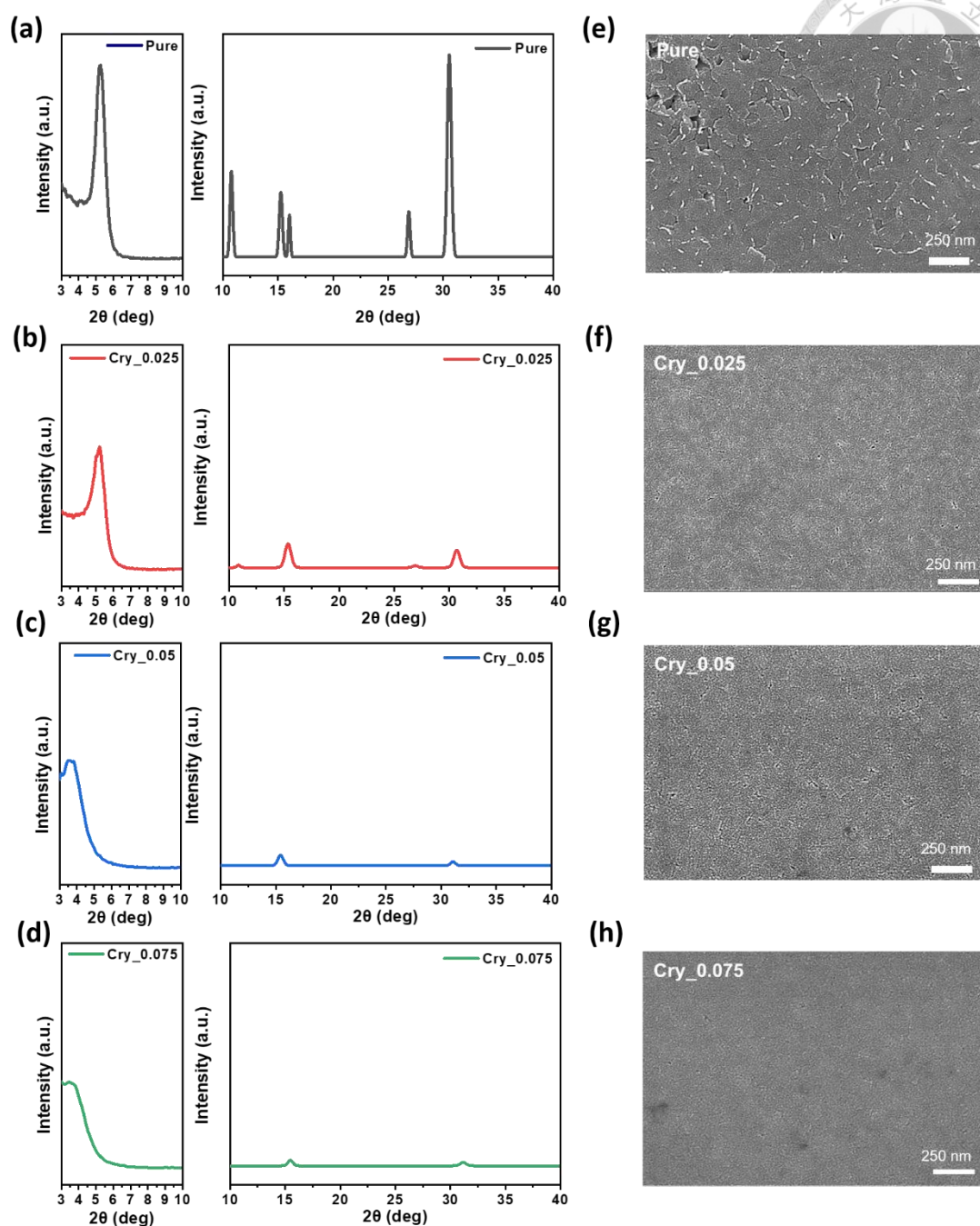


**Fig. 3.20** (a-d) The XRD measurement and (e-h) SEM images of the quasi-2D perovskite films with different added doping ratios of the crytand.

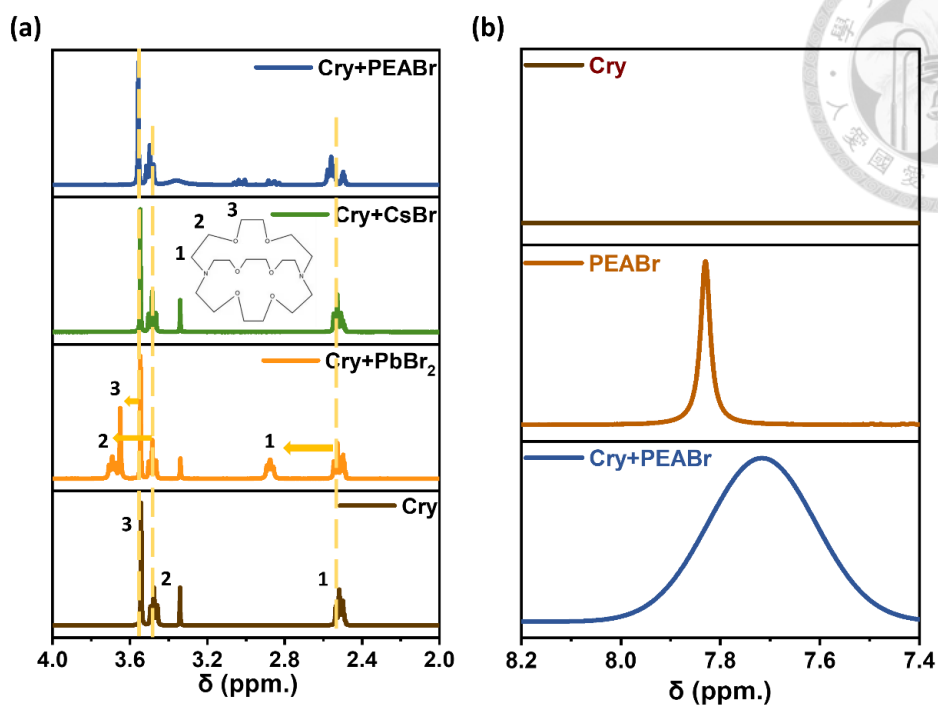


**Fig. 3.21** (a) The NMR spectra of the cryptand without and with different perovskite precursors as noted and (b) NMR spectra of the cryptand, PEABr, and their mixture in the range of 7.4 to 8.2 ppm.

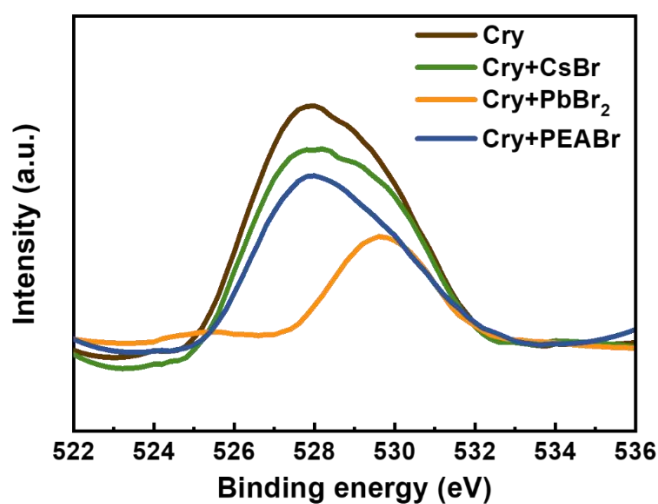


**Fig. 3.22** XPS measurement of O 1s spectra of the cryptand without and with different perovskite precursors as noted.

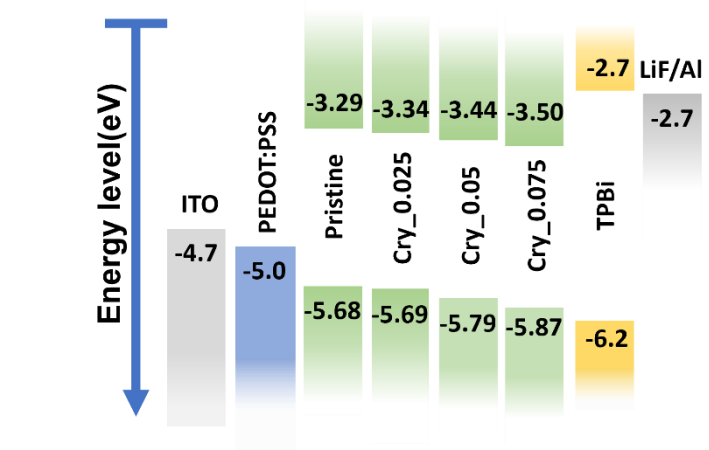
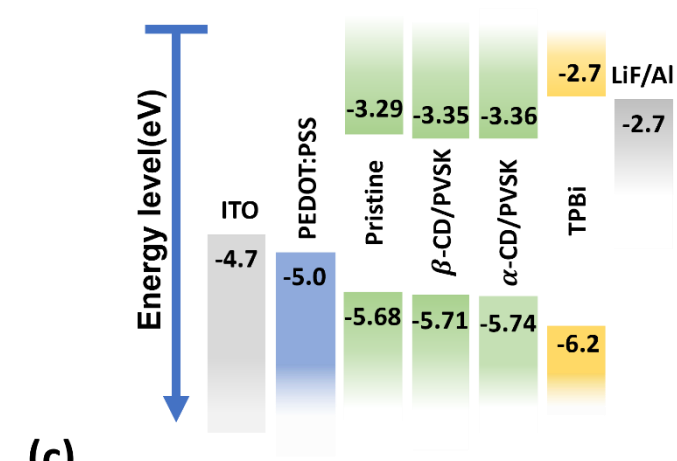
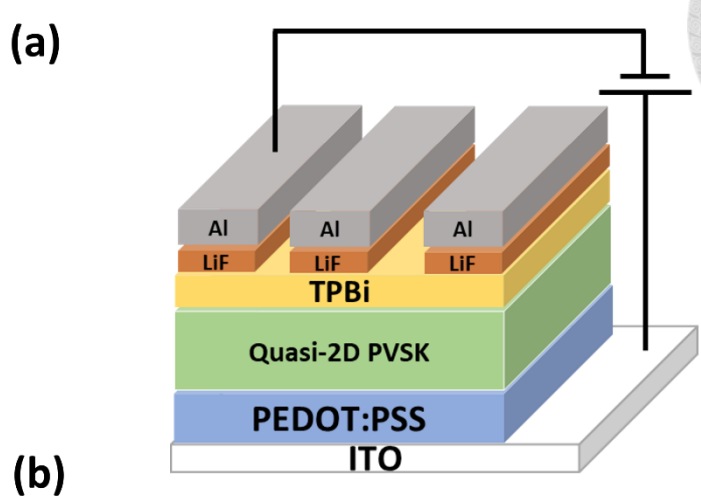


Fig. 3.23 (a) Structure and (b,c) the energy-level diagram of the fabricated PeLEDs.

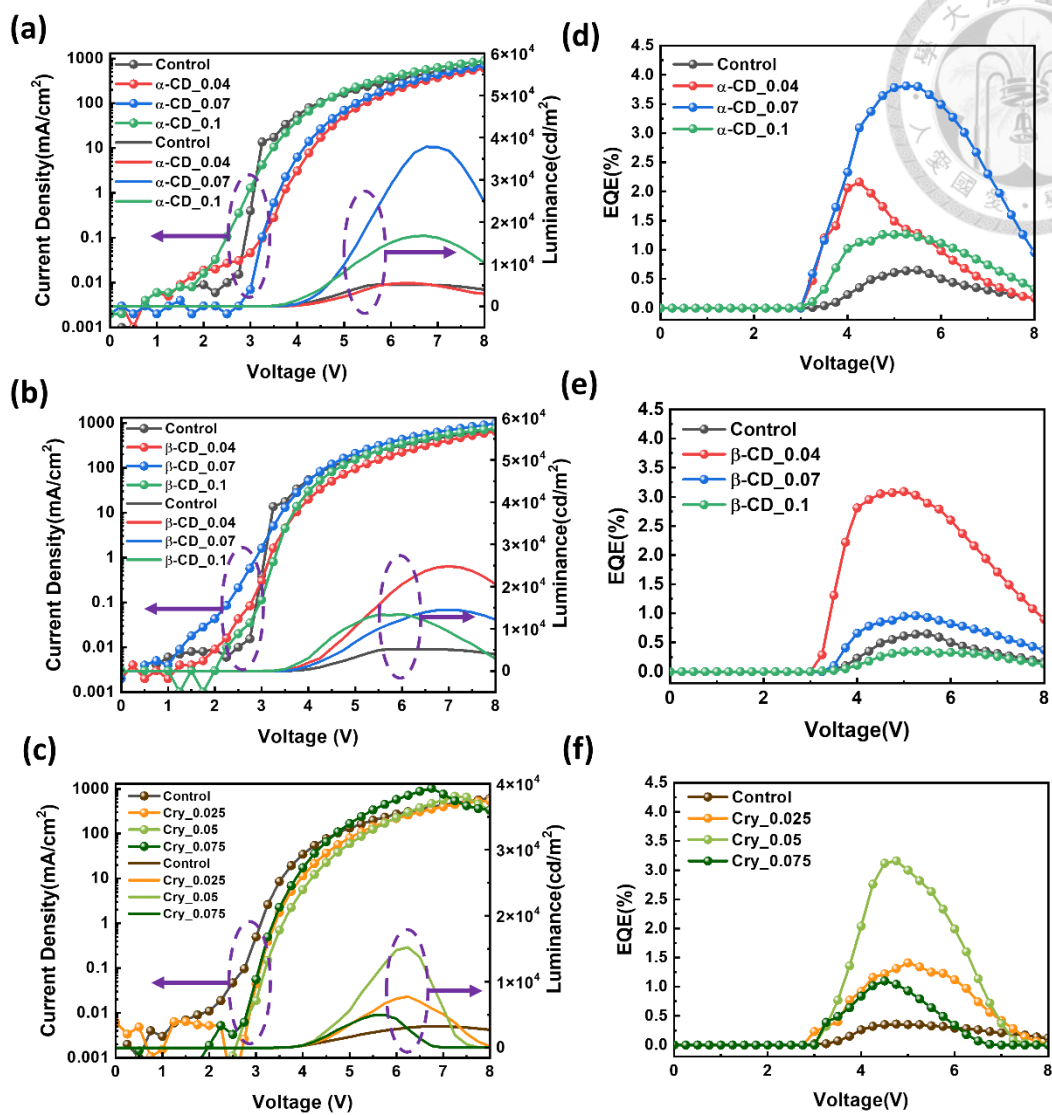


Fig. 3.24 (a-c) J-V-L, and (d-f) EQE-voltage curves of the fabricated devices.

### 3.3 Realizing High Brightness Quasi-2D Perovskite Light-Emitting Diodes with Reduced Efficiency Roll-Off via Multifunctional Interface Engineering

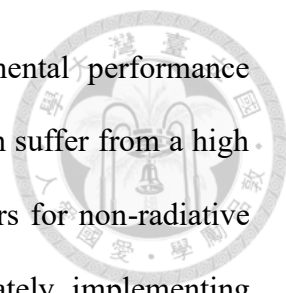


The text and figures in this section are reproduced with permission from:

Y. K. Lin, **C. H. Chen**, Y. Y. Wang, M. H. Yu, J. W. Yang, I. C. Ni, B. H. Lin, I. S. Zhidkov, E. Z. Kurmaev, Y. J. Lu\*, C. C. Chueh\*, “Realizing High Brightness Quasi-2D Perovskite Light-Emitting Diodes with Reduced Efficiency Roll-Off via Multifunctional Interface Engineering”, *Adv. Sci.*, 10, 2302232 (2023).

#### 3.3.1 Background

In recent years, metal halide perovskites have garnered significant global attention as next-generation optoelectronic materials, owing to their tunable electronic characteristics and solution-processable nature.<sup>[154-157]</sup> Within this class, quasi-two-dimensional (quasi-2D) structures exemplified by compositions like  $\text{PEA}_2\text{Cs}_n\text{-1Pb}_n\text{Br}_{3n+1}$  stand out for their strong emission properties, which arise from enhanced material stability and distinct quantum confinement effects.<sup>[15, 45, 83, 158-162]</sup> Furthermore, the presence of energy funnels across various quasi-2D phases effectively promotes exciton migration and radiative recombination, thus boosting the overall photoluminescence efficiency.<sup>[77, 78, 163]</sup> Notably, green-emitting PeLEDs based on quasi-2D perovskites have already reached an impressive external quantum efficiency (EQE) of 28%,<sup>[27]</sup> showcasing their competitive performance in emissive technologies. Importantly, by tailoring the phase distribution or adjusting the chemical composition of these quasi-2D materials, researchers can precisely tune emission wavelengths, enabling the development of multicolor PeLEDs with high efficiency.<sup>[164, 165]</sup>



Despite their potential, quasi-2D PeLEDs still face fundamental performance bottlenecks. Perovskite films fabricated via solution processing often suffer from a high concentration of surface defects and trap states, which act as centers for non-radiative recombination and significantly reduce emission efficiency. Fortunately, implementing surface passivation strategies has proven effective in alleviating these issues by reducing surface defects and minimizing non-radiative losses, leading to notable improvements in device efficiency.<sup>[166-169]</sup>

Phosphine oxides have become some of the most frequently adopted surface passivation agents in PeLED fabrication, primarily due to the strong electron-donating nature of their P=O functional groups.<sup>[81, 170-173]</sup> Nevertheless, many of the phosphine oxide compounds used in perovskite passivation are inherently electrically insulating, which hampers charge carrier flow across the perovskite and adjacent transport layers.<sup>[81, 170, 174]</sup> Additionally, quasi-2D perovskites inherently suffer from poorer charge injection and reduced conductivity compared to 3D perovskites, largely because of the insulating organic spacer cations within their structure. These drawbacks result in limited luminance output and significant efficiency roll-off under high current and voltage stress,<sup>[175]</sup> posing major barriers to the practical integration and commercialization of quasi-2D PeLEDs.<sup>[176, 177]</sup> Consequently, achieving high-performance quasi-2D PeLEDs with improved brightness and reduced efficiency degradation remains a central goal in ongoing research.

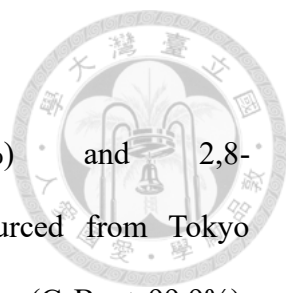
Recent studies have demonstrated that carefully tuning the composition ratio of multiple quantum wells in quasi-2D perovskites promotes efficient energy transfer and lowers local carrier concentrations, thereby diminishing non-radiative losses and mitigating efficiency roll-off under elevated driving voltages.<sup>[178]</sup> Moreover, implementing charge injection layers without energy barriers has proven beneficial in resolving charge imbalance within the emissive region, further stabilizing device



performance at high operating conditions.<sup>[179]</sup> Building upon these insights, we introduce a conductive phosphine oxide interlayer into quasi-2D PeLEDs to assess its potential in addressing efficiency roll-off. This material presents a dual advantage besides effectively passivating surface defects, its inherent conductivity and favorable energy-level alignment support improved electron injection and charge transport modulation.<sup>[180-183]</sup>

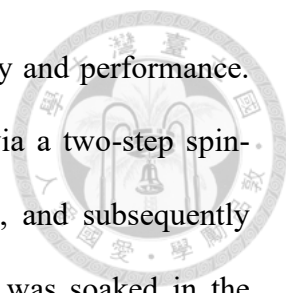
In this work, we employ two conductive phosphine oxide compounds—2,8-bis(diphenyl-phosphoryl)-dibenzo[b,d]thiophene (PPT) and 2,8-bis(diphenyl-phosphoryl)-dibenzo[b,d]furan (PPF) as interfacial modifiers between the perovskite emissive layer and the electron transport layer (ETL). Thanks to their phosphine oxide moieties, both PPT and PPF contribute to defect passivation at the perovskite surface and effectively suppress non-radiative recombination pathways. Their energy levels are also favorably aligned with those of the adjacent layers, allowing them to act as electron transport interlayers that promote efficient electron injection while simultaneously blocking unwanted hole transport.<sup>[180-183]</sup> Improving the charge dynamics at this key interface is critical, and transient absorption (TA) measurements confirm that the incorporation of PPT or PPF preserves the energy cascade among the quasi-2D perovskite phases. Benefiting from these interfacial enhancements, the resulting devices demonstrate notable performance improvements, including a peak brightness of 73,897 cd m<sup>-2</sup>, an external quantum efficiency (EQE) surpassing 10%, and significantly mitigated efficiency roll-off at elevated operating voltages outperforming devices based on the same perovskite composition. These results highlight a practical and highly effective route to addressing one of the most persistent limitations in quasi-2D PeLED development.

### 3.3.2 Experimental Section



**Materials.** Lead(II) bromide ( $\text{PbBr}_2$ , >99.9%) and 2,8-bis(diphenylphosphoryl)dibenzo[b,d]furan (PPF,  $\geq 96\%$ ) were sourced from Tokyo Chemical Industry Co., Ltd. Materials including cesium bromide ( $\text{CsBr}$ , >99.9%), phenethylammonium bromide (PEABr,  $\geq 98\%$ ), 2,8-bis(diphenylphosphoryl)dibenzo[b,d]thiophene (PPT, >96.5%), poly[N,N''-bis(4-butylphenyl)-N,N''-bis(phenyl)-benzidine] (Poly-TPD), poly(9-vinylcarbazole) (PVK), lithium fluoride ( $\text{LiF}$ , >99.99%), along with solvents such as chlorobenzene (CB, 99.8%) and dimethyl sulfoxide (DMSO,  $\geq 99.9\%$ ) were purchased from Sigma-Aldrich and used without any further purification. The electron transport compound 2,2',2''-(1,3,5-benzenetriyl)-tris(1-phenyl-1H-benzimidazole) (TPBi) was obtained from Ultra Fine Chemical Technology Corp., while 1,4,7,10,13,16-hexaoxacyclooctadecane (18-crown-6, 99%) was supplied by Alfa Aesar.

**Device fabrication.** The precursor solution for the quasi-2D perovskite was prepared by dissolving 16.2 mg of PEABr, 42.6 mg of CsBr, and 73.4 mg of  $\text{PbBr}_2$  in 1 mL of DMSO, along with 3.5 mg of 18-crown-6. The solution was stirred overnight at room temperature to ensure complete dissolution. Separately, PPT and PPF solutions were prepared by dissolving 2 mg of each additive in 1 mL of chlorobenzene (CB). ITO-coated glass substrates were sequentially cleaned with detergent, followed by ultrasonic treatment in deionized water, acetone, and isopropyl alcohol for 15 minutes each. The substrates were then dried in an oven at 60 °C to remove residual solvents. Prior to film deposition, the cleaned substrates were treated with oxygen plasma and transferred into a nitrogen-filled glovebox for device fabrication. A hole transport bilayer was formed by sequentially spin-coating Poly-TPD at 2000 rpm for 60 s and PVK at 2000 rpm for 30 s,



followed by thermal annealing at 150 °C to improve film uniformity and performance. The quasi-2D perovskite layer was then deposited onto the HTL via a two-step spin-coating process: 1000 rpm for 5 s, followed by 3000 rpm for 55 s, and subsequently annealed at 100 °C for 60 s. After perovskite deposition, the film was soaked in the precursor solution for 30 s, followed by spin-coating of a thin PPT or PPF interlayer at 5000 rpm for 60 s. Finally, the device was completed by sequential thermal evaporation of TPBi (25 nm), LiF (1 nm), and aluminum (100 nm) under high vacuum conditions ( $<10^{-6}$  Torr).

**Characterization.** Quasi-2D perovskite thin films were prepared for characterization using a method consistent with previously reported protocols. UV–visible absorption spectra were obtained with a Jasco V-730 spectrophotometer, and photoluminescence (PL) measurements were performed using a Horiba Fluorolog-3 instrument. Time-resolved PL (TRPL) experiments were conducted with a Hamamatsu Universal Streak Camera C10910 at beamline TPS 23A at the National Synchrotron Radiation Research Center (NSRRC). X-ray diffraction (XRD) analysis was performed using a Rigaku SmartLab SE to probe the crystal structures. Surface features were examined by scanning electron microscopy (SEM) with a Hitachi S4800. Proton nuclear magnetic resonance ( $^1\text{H}$  NMR) spectra were acquired on a Bruker AVIII 500 MHz FT-NMR system. The molecular geometries of PPT and PPF in their ground states were optimized using density functional theory (DFT) calculations with the B3LYP functional and 6-311G(d,p) basis set in Gaussian 09W. Photoluminescence quantum yield (PLQY) and electrical device characterizations—including current density–voltage–luminance (J–V–L) curves, external quantum efficiency (EQE), space-charge-limited current (SCLC), and electroluminescence (EL) spectra—were measured using an LQ-100 system

(Enlitech Co. Ltd.) equipped with a 4 mm<sup>2</sup> integrating sphere. All tests were conducted in an inert nitrogen environment, and devices were evaluated in an unencapsulated state.

Transient absorption spectroscopy (TA) was used to study carrier dynamics. A Femto Frame II setup (IB Photonics) was employed, driven by a 400 nm femtosecond laser (pulse width: 100 fs, 1 kHz repetition rate) generated by a TOPAS-C optical parametric amplifier pumped with a Spectra-Physics Tsunami Ti:sapphire laser. The excitation and probing spots were ~300 μm and ~100 μm in diameter, respectively. A supercontinuum white-light probe (450–800 nm, 30 fs) was produced via a sapphire crystal. Pump fluence ranged between 1.4 and 28 μJ cm<sup>-2</sup>. TA measurements were carried out in ambient atmosphere with relative humidity controlled under 50%.

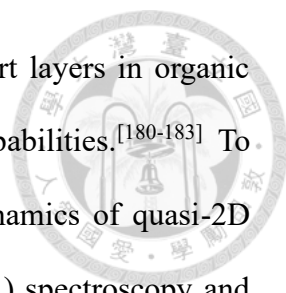
X-ray photoelectron spectroscopy (XPS) and ultraviolet photoelectron spectroscopy (UPS) were performed using a PerkinElmer PHI 5400 (monochromatic Al Kα X-ray source) and a Specs UVS 10/35 UV lamp, respectively. The optical bandgap (E<sub>g</sub>) and HOMO energy levels were derived via Tauc plot analysis under the assumption of a direct bandgap. Electrochemical impedance spectroscopy (EIS) and capacitance–voltage (C–V) profiling were carried out on encapsulated devices in air using a Bio-Logic SP-200 impedance analyzer with AC modulation.

### 3.3.3 Results and Discussion

**Modification of quasi-2D perovskites by PPT/PPF post-treatment.** As discussed earlier, our objective is to introduce conductive phosphine oxides to passivate quasi-2D perovskites and evaluate their effectiveness in mitigating efficiency roll-off. Considering their favorable conductivity and well-aligned energy levels, we have selected two phosphine oxides, PPT and PPF, for incorporation at the perovskite/ETL interface.<sup>[184, 185]</sup> This additional interfacial layer is expected to enhance charge injection through cascade

charge transfer, as illustrated in **Fig. 3.25a**. Furthermore, the P=O bond in phosphine oxides has been demonstrated to effectively passivate surface defects in the perovskite emitting layer, thereby suppressing non-radiative recombination and enabling high-performance light-emitting devices. To achieve this, we spin-coat an additional layer of PPT or PPF onto the perovskite film before depositing the ETL, rather than employing the conventional post-treatment method of dissolving phosphine oxides in a washing solvent for drip-casting, as reported in previous studies. To further enhance the passivation effect of PPT/PPF, the as-prepared perovskite layer is soaked in precursor solutions of PPT/PPF for a specific duration before spin coating.<sup>[81]</sup> Detailed experimental procedures are provided in the Experimental Section.

The incorporation of phosphine oxide into perovskite precursors has been reported to affect the crystallinity and phase distribution of quasi-2D perovskite films.<sup>[186, 187]</sup> To assess these effects, we systematically examined the crystallinity, optoelectronic properties, and film morphology of PPT/PPF-modified perovskite films. **Fig. 3.26a** presents the X-ray diffraction (XRD) patterns of pristine, PPT-modified, and PPF-modified perovskite films. Notably, no significant changes in peak intensity or position are observed among these samples, indicating that the introduction of PPT and PPF does not alter the crystallinity or phase distribution of quasi-2D perovskites. The ultraviolet-visible (UV-Vis) absorption spectra, shown in **Fig. 3.26b**, further support this observation. All films exhibit similar absorption profiles, with no distinct absorption peaks associated with small-*n* phases ( $n < 5$ ), suggesting the suppression of these lower-*n* phases. Collectively, the XRD and UV-Vis results confirm that PPT/PPF modification preserves the structural integrity and phase distribution of quasi-2D perovskite films without adversely affecting their optoelectronic properties.



PPT and PPF have been widely employed as electron transport layers in organic light-emitting diodes due to their excellent electron transport capabilities.<sup>[180-183]</sup> To investigate the impact of PPT/PPF modification on the charge dynamics of quasi-2D perovskite films, we conducted steady-state photoluminescence (PL) spectroscopy and time-resolved photoluminescence (TRPL) measurements. As shown in **Fig. 3.25b**, the steady-state PL spectra of PPT- and PPF-modified films exhibit clear PL quenching. This observation indicates efficient charge transfer between the perovskite layer and the PPT/PPF layer, which can be attributed to the favorable electron transport properties of these molecules and their well-matched energy levels, as discussed later in the text.<sup>[73, 184]</sup> A similar trend is observed in the photoluminescence quantum yield (PLQY) measurements, presented in **Fig. 3.25c**, further supporting the occurrence of charge transfer. To gain deeper insights into the charge recombination dynamics, we performed TRPL measurements (**Fig. 3.25d**), and the biexponential fitting results are summarized in **Table 3.8**. Both modified films exhibit longer average carrier lifetimes compared to the pristine perovskite film. This suggests that, despite inducing PL quenching, PPT and PPF effectively passivate the perovskite films by mitigating surface defects. Consequently, the suppression of non-radiative recombination leads to extended carrier lifetimes.<sup>[188]</sup> A more detailed discussion of the interactions between perovskite and PPT/PPF is provided in the following section.

We further investigated the morphological characteristics of the perovskite films using scanning electron microscopy (SEM). As shown in **Fig. 3.27a**, the pristine perovskite film exhibits a smooth and homogeneous surface. To rule out potential recrystallization effects induced by the solvent used in the PPT/PPF precursor solution, we also examined the morphology of a film treated with pure chlorobenzene (CB). As depicted in **Fig. 3.27b**, the CB-treated film maintains a morphology comparable to that

of the pristine film, confirming that the solvent itself does not alter the perovskite surface in the absence of PPT or PPF. **Fig. 3.27c&d** presents the SEM images of the PPT- and PPF-modified perovskite films. Notably, the modified films exhibit the presence of nanoplatelets on the surface, which are likely formed due to the aggregation of PPT or PPF. Despite the appearance of these nanoplatelets, the overall morphology of both films remains largely consistent with that of the pristine perovskite film, indicating that the introduction of PPT/PPF does not induce significant structural alterations.

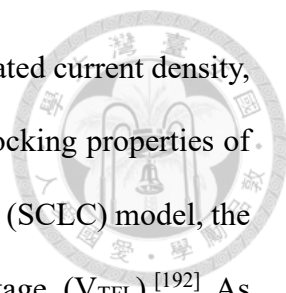
**Interaction between PPT/PPF and perovskite.** To elucidate the interactions between PPT/PPF and the perovskite layer, we employed nuclear magnetic resonance (NMR), electrostatic potential (ESP) mapping, and X-ray photoelectron spectroscopy (XPS). The  $^{31}\text{P}$  NMR spectra (**Fig. 3.28a,b**) reveal a chemical shift in the phosphorus peaks upon mixing PPT or PPF with perovskite precursors. The original phosphorus peak of PPT at 25.9 ppm shifts slightly to  $\sim 26.1$  ppm after the introduction of  $\text{PbBr}_2$ , CsBr, or PEABr. Similarly, the PPF peak shifts from 25.6 ppm to  $\sim 25.7$  ppm upon interaction with the perovskite precursors. These chemical shifts suggest a change in the chemical environment of phosphorus due to coordination interactions between the P=O group and cationic species within the perovskite.<sup>[173]</sup> To further investigate these interactions, density functional theory (DFT)-based ESP mapping was conducted. As depicted in **Fig. 3.28c** and **Fig. 3.29**, the electron density in PPT and PPF is concentrated around the P=O group, highlighting their strong Lewis basicity. This enables effective coordination with uncoordinated  $\text{Pb}^{2+}$  ions, supporting the notion that PPT/PPF contribute to defect passivation.<sup>[189]</sup> XPS analysis further confirms these findings. The characteristic P 2p peak (**Fig. 3.30**) verifies the presence of phosphorus on the perovskite surface, indicating the successful formation of a PPT/PPF layer. Additionally, the Pb 4f peak in PPT/PPF-

modified films shifts toward a higher binding energy (**Fig. 3.30d**), suggesting an interaction between P=O and the  $\text{PbBr}_6^{4-}$  octahedral unit. This interaction stabilizes the perovskite surface and mitigates non-radiative recombination by passivating defects and vacancies.<sup>[190]</sup> In summary, based on  $^{31}\text{P}$  NMR, XPS, and ESP mapping results, we confirm that the P=O groups in PPT/PPF effectively coordinate with  $\text{Pb}^{2+}$  ions, leading to efficient passivation of perovskite surface defects (illustrated in **Fig. 3.30e**). This coordination mechanism aligns well with previous literature, reinforcing the crucial role of phosphine oxides in stabilizing and enhancing perovskite optoelectronic properties.

**Influence of PPT/PPF modification on device performance.** Based on the above understanding of the PPT/PPF interaction with perovskite films, we proceeded to fabricate perovskite light-emitting diodes (PeLEDs) incorporating these modified films. Their performance was then compared with PeLEDs based on pristine perovskite films. The device architecture used in this study follows the structure: ITO/poly-TPD/PVK/quasi-2D perovskite/TPBi/LiF/Al, as illustrated in **Fig. 3.31a**. A key distinction in our approach is that, unlike simple surface decoration, the PPT/PPF layer is strategically introduced at the perovskite/TPBi interface. This modification is expected to facilitate improved charge injection and transport, as well as enhanced surface passivation, ultimately leading to better PeLED performance.

**Fig. 3.31b** presents the energy level diagram of the fabricated devices, highlighting the role of PPT and PPF in mitigating hole leakage. The deeper HOMO levels of PPT and PPF compared to TPBi effectively suppress hole transport from the perovskite layer into the electron transport layer (ETL).<sup>[191]</sup> To validate this effect, hole-only devices with the configuration ITO/poly-TPD/PVK/quasi-2D perovskite/ $\text{MoO}_3$ /Ag were fabricated using pristine, PPT-modified, and PPF-modified perovskite films. As depicted in **Fig. 3.32a**, the





PPT/PPF-modified devices exhibit significantly reduced hole-dominated current density, indicating enhanced transport resistance due to the effective hole-blocking properties of PPT and PPF. Furthermore, based on the space charge limited current (SCLC) model, the trap density is primarily determined by the trap-filled limit voltage ( $V_{TFL}$ ).<sup>[192]</sup> As observed, both PPT- and PPF-modified devices exhibit a lower  $V_{TFL}$  compared to the control device, indicating a reduction in trap density.<sup>[76]</sup> This finding aligns with the previously discussed passivation effect of phosphine oxides. Additionally, while the lowest unoccupied molecular orbital (LUMO) level of PPF is comparable to that of TPBi, the LUMO level of PPT lies below that of TPBi but remains above the conduction band minimum (CBM) of the perovskite layer. This favorable energy level alignment facilitates efficient electron injection from TPBi into the perovskite layer. This effect is further corroborated by the performance of electron-only devices, as illustrated in **Fig. 3.32b**, where a notable increase in electron-dominated current density is observed in PPT/PPF-modified devices, confirming enhanced electron transport.

**Fig. 3.31c** illustrates the current density–voltage–luminance (J–V–L) characteristics of the fabricated devices incorporating pristine, PPT-modified, and PPF-modified perovskite films (designated as the control, PPT, and PPF devices, respectively). The key performance parameters of each device are summarized in **Table 3.9**. Notably, the PPT- and PPF-modified devices exhibit more than a twofold increase in luminance compared to the control device, achieving maximum brightness values of 73,896.6  $\text{cd m}^{-2}$  and 61,025.3  $\text{cd m}^{-2}$ , respectively. Moreover, both devices achieve a maximum external quantum efficiency (EQE) exceeding 10%, positioning their performance particularly in terms of luminance among the highest reported for pure Cs-based quasi-2D PeLEDs. This enhancement is primarily attributed to the improved electron transport characteristics and enhanced hole-blocking capability provided by PPT and PPF, as previously discussed.

Additionally, the facilitated electron injection in these devices leads to a notably lower turn-on voltage compared to the control device. Furthermore, as shown in **Fig. 3.33**, the electroluminescence (EL) spectra of the PPT- and PPF-modified devices closely resemble that of the control device, which is consistent with the PL results, indicating that the modifications do not induce significant spectral shifts.

Quasi-2D perovskites generally exhibit lower electrical conductivity and slower carrier injection rates compared to their 3D perovskite counterparts, resulting in reduced luminance in quasi-2D perovskite-based PeLEDs.<sup>[175]</sup> Moreover, Joule heating and carrier leakage at elevated voltages contribute to a rapid decline in external quantum efficiency (EQE), which is a primary factor limiting device performance and leading to severe efficiency roll-off.<sup>[176, 193, 194]</sup> However, as illustrated in **Fig. 3.31d–f**, the PPT- and PPF-modified devices exhibit significantly suppressed efficiency roll-off at high voltages. This enhancement can be attributed to the stronger hole-blocking effect introduced by PPT and PPF, which mitigates charge imbalance and suppresses undesired non-radiative recombination. A more detailed analysis of the brightness improvement and efficiency roll-off mitigation will be presented in the following sections.

**Investigation of the recombination dynamics by TA measurement.** To gain deeper insight into the mechanism behind the enhanced brightness and reduced efficiency roll-off, transient absorption (TA) spectroscopy was conducted to investigate the relaxation dynamics of photoexcited carriers in the perovskite layer. As illustrated in **Fig. 3.34a–c**, all perovskite films exhibit a single ground state bleaching (GSB) signal at 505 nm, suggesting that other quasi-2D phases are significantly suppressed.<sup>[78]</sup> It is noteworthy that the spectral band beyond 505 nm is associated with trap-assisted nonradiative recombination, whereas photocarriers are generated at 505 nm within an

ultrafast timescale ( $<1$  ps), as shown in **Fig. 3.34a–c**.<sup>[195]</sup> These findings confirm the presence of a single, dominantly emissive domain in the solution-processed perovskite films, in agreement with the steady-state absorption spectra presented in **Fig. 3.26b**.<sup>[196]</sup>

Subsequently, the photocarriers associated with the GSB gradually decay without the emergence of additional spectral peaks (**Fig. 3.34d–f**), indicating effective carrier confinement within the quantum well structure and successful radiative recombination. Notably, the modified films exhibit a larger change in transmittance compared to the control film, suggesting that a greater number of carriers are localized at the perovskite band edge and excited by the laser following PPT/PPF modification. However, the absorption dynamics before and after the modification remain largely unchanged, implying that the relaxation process of photoexcited carriers in the perovskite layer is not significantly influenced by the PPT/PPF treatment. Therefore, the observed enhancement in device brightness and reduction in efficiency roll-off are unlikely to result from differences in energy transfer between multiple quasi-2D phases within the perovskite film.

### **Investigation of the carrier dynamics between interfaces in PeLED devices.**

Given the well-established link between efficiency roll-off and carrier dynamics in perovskite light-emitting layers,<sup>[197, 198]</sup> we sought to investigate this relationship further. Generally, the recombination pathways of free carriers can be categorized into three types, according to the number of carriers involved: monomolecular trap-assisted recombination, bimolecular radiative recombination, and trimolecular Auger recombination.<sup>[158]</sup> In metal halide perovskite materials, both trap-assisted and Auger recombination are considered non-radiative processes, meaning they release energy without generating photons. Among these, Auger recombination involves a higher number of carriers and tends to dominate

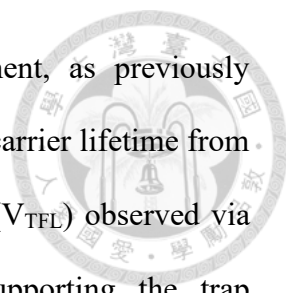
under high injection conditions, such as at elevated voltages. Consequently, the interplay between radiative recombination and non-radiative Auger recombination significantly influences the maximum external quantum efficiency (EQE), luminance, and efficiency roll-off in perovskite light-emitting diodes (PeLEDs). This recombination behavior can be quantitatively described by the following rate equation:<sup>[158]</sup>

$$-\frac{dn}{dt} = k_1 n + k_2 n^2 + k_3 n^3 \quad (1)$$

In this equation,  $n$  represents the free charge carrier density, while  $k_1$ ,  $k_2$ , and  $k_3$  correspond to the rate coefficients for monomolecular trap-assisted recombination, bimolecular radiative recombination, and trimolecular Auger recombination, respectively. To further elucidate the relationship between recombination dynamics and the enhanced performance of the device, fluence-dependent transient absorption (TA) measurements were conducted to extract the values of these recombination coefficients.

Since recombination dynamics are highly dependent on carrier concentration, as described by Equation (1), accurately determining the initial carrier concentration is critical for fluence-dependent TA analysis. To obtain a comprehensive recombination profile, measurements must be conducted at various initial carrier concentrations, which are achieved by using excitation beams with different pump powers. However, extracting the monomolecular recombination constant ( $k_1$ ) solely from TA measurements is insufficient, as the time window of TA spectroscopy is limited to only a few nanoseconds. Therefore,  $k_1$  was instead determined by fitting time-resolved photoluminescence (TRPL) data using a single-exponential decay model.<sup>[197]</sup> The resulting carrier dynamics and fitting results are presented in **Fig. 3.35** and summarized in **Table 3.10**. Additional details regarding the fluence-dependent TA methodology can be found in the literature.<sup>[197, 198]</sup>

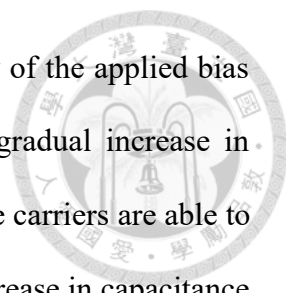
In summary, the global fitting results reveal an increase in the bimolecular recombination coefficient ( $k_2$ ) following post-modification, likely due to a higher



population of photoexcited carriers induced by PPT/PPF treatment, as previously discussed. This trend aligns with the observed extension in average carrier lifetime from TRPL measurements and the reduction in trap-filled limit voltage ( $V_{TFL}$ ) observed via space-charge limited current (SCLC) measurements, further supporting the trap passivation effect of PPT/PPF. Surprisingly, however, the Auger recombination coefficient ( $k_3$ ) remained largely unchanged after modification. This finding suggests that PPT/PPF treatment does not significantly suppress Auger recombination in the perovskite films. Consequently, the observed reduction in efficiency roll-off cannot be attributed to diminished Auger recombination, and the underlying mechanism responsible for this improvement remains unresolved.

Since the recombination dynamics alone could not fully account for the enhanced performance and reduced efficiency roll-off, we shifted our focus to examining the carrier behavior across the entire device. To investigate the electrical characteristics of the fabricated PeLEDs, electrochemical impedance spectroscopy (EIS) measurements were performed at an applied bias of 4 V, as shown in **Fig. 3.37a**. The modified PeLEDs exhibit a significantly smaller arc radius in the Nyquist plot, indicating improved electron injection and enhanced carrier transport as a result of the PPT/PPF interfacial modification.<sup>[199-201]</sup> To gain further insight into the carrier dynamics, capacitance–voltage (C–V) measurements were also carried out, with the results presented in **Fig. 3.37b**. Given the dielectric nature of perovskite materials, the PeLED structure can be regarded as a capacitor.<sup>[202, 203]</sup> Accordingly, the carrier behavior within the device can be inferred from the capacitance response under varying applied voltages.

Initially, the number of carriers within the device is very small and negligible, so the capacitance can be approximated by the geometric capacitance, which remains constant. As the applied voltage increases, carriers begin to be injected into the device. However,



the number of carriers that can be injected is limited by the inability of the applied bias to overcome the energy barrier between the layers, leading to a gradual increase in capacitance. Once the applied voltage reaches a sufficient level, more carriers are able to overcome the energy barrier and enter the device, causing a rapid increase in capacitance with rising voltage. However, as the applied voltage exceeds the turn-on voltage, a significant number of carriers begin to recombine within the perovskite layer, resulting in a reduction in the overall carrier population and, consequently, a decrease in capacitance. Thus, the balance between carrier injection, driven by the increasing applied voltage, and carrier recombination ultimately determines the capacitance after the turn-on voltage. If the recombination rate is sufficiently fast, the capacitance will continue to decrease. In other words, the more efficiently the carriers recombine in the perovskite layer, the lower the capacitance value will be.<sup>[23]</sup>

Returning to the experimental results shown in **Fig. 3.37b**, the capacitance of the control device begins to increase only at 3 V, while the capacitance of the modified devices increases more gradually at first. This indicates that carriers are more easily injected into the modified devices, where the overall energy barrier is reduced. This behavior can be attributed to the improved energy level alignment resulting from the incorporation of the PPT/PPF layer. Additionally, the capacitance of the PPT/PPF-modified devices starts to decrease at 3.0 and 3.5 V, respectively, whereas the capacitance of the control device decreases at a higher voltage of approximately 3.8 V. This reduction in turn-on voltage observed in the modified devices further supports the notion of an enhanced energy barrier in these devices. More importantly, after the turn-on voltage, the capacitance of the modified devices decreases rapidly, while that of the control device declines more gradually. This suggests that the recombination behavior improves with the introduction of the PPT/PPF layer.<sup>[23, 202]</sup> This improvement is likely due to the hole-

blocking capabilities of PPT and PPF. Generally, holes tend to escape from the perovskite layer when the energy gained by each carrier exceeds the highest occupied molecular orbital (HOMO) energy difference between perovskite and the electron transport layer (ETL). This results in poor recombination behavior in the control device at higher voltages. In contrast, in the modified devices, the potential barrier between the perovskite and ETL is significantly larger, allowing for more efficient electron-hole recombination within the perovskite layer, regardless of the applied bias voltage.

To further understand the impact of the PPT/PPF modification, the energy levels of perovskite films with and without the modification were calculated. **Fig. 3.37c** displays the energy levels of the perovskite films, including the conduction band minimum (CBM), valence band minimum (VBM), and Fermi levels, which were determined through ultraviolet photoelectron spectroscopy (UPS) and UV-Vis absorption measurements.<sup>[204]</sup> The UPS results are provided in **Fig. 3.38**. As the PPT and PPF layers are too thin to be measured directly by UPS, the energy levels were obtained only for the perovskite surfaces modified by PPT and PPF. Moreover, as discussed earlier, the bulk properties of the perovskite layer are largely unaffected by the surface modification. Therefore, we assume that the energy levels of the modified perovskite layers are the same as those of the control film, except at the interface with TPBi. Since the Fermi level must align across layers in equilibrium, band bending occurs to achieve a continuous vacuum level.<sup>[205]</sup> Initially, the energy levels of TPBi exhibited unfavorable upward band bending, while the perovskite layer showed downward band bending at the interface with TPBi. This resulted in a significant energy barrier to electron injection and poor hole blocking, as shown in the schematic on the left of **Fig. 3.37d**. However, after the introduction of the PPT/PPF layer, the energy level alignment improves, as depicted on the right of **Fig. 3.37d**. The energy levels of the PPT- and PPF-modified perovskite films show not only downward

bending of the TPBi band but also upward bending of the perovskite band edge at the surface. This modification facilitates electron injection from TPBi into the perovskite layer while preventing the escape of holes from the emitting layer.<sup>[206]</sup>

This result aligns with the analyses discussed earlier. Following the PPT/PPF modification, the energy barrier for electron injection is reduced, facilitating easier carrier injection into the perovskite layer. This leads to an increase in current density and a reduction in the turn-on voltage. Additionally, the improved hole-blocking capability in the modified devices enhances the recombination of electrons and holes at higher applied bias voltages, resulting in increased brightness and external quantum efficiency (EQE) at elevated voltages. More importantly, the introduction of the PPT/PPF layer significantly suppresses efficiency roll-off, providing a straightforward and effective solution to one of the most persistent challenges in quasi-2D PeLEDs. However, despite the successful defect passivation at the perovskite surface, as confirmed by XPS and SCLC measurements, the maximum EQEs of the modified devices did not surpass those of the control device. This suggests that further detailed analysis is necessary to fully understand the underlying reasons for this limitation.

### 3.3.4 Summary

In conclusion, this study introduces a straightforward yet impactful interfacial engineering approach to suppress efficiency roll-off in perovskite light-emitting diodes (PeLEDs). By inserting a thin conductive phosphine oxide layer (either PPT or PPF) at the junction between the perovskite and the electron transport layer (ETL), we simultaneously achieve defect passivation on the perovskite surface and enhanced charge carrier management at the interface. This modification leads to more efficient electron injection and improved hole-blocking capabilities, resulting in significantly increased



luminance and reduced efficiency degradation under high driving voltages when compared to unmodified devices. Notably, these performance gains were achieved without altering the perovskite composition, underscoring the effectiveness of the interlayer. Detailed analysis confirms that the primary enhancement stems from improved interfacial charge dynamics rather than from changes in energy transfer among quasi-2D phases. These findings highlight the pivotal role of interfacial properties in dictating PeLED performance and present a promising direction for the development of robust, high-efficiency devices.

### 3.3.5 Tables and Figures

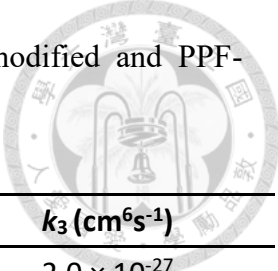
**Table 3.8** Bi-exponential fitting parameters for the TRPL results.

	$A_1$	$\tau_1$ (ns)	$A_2$	$\tau_2$ (ns)	$\tau_{avg}$ (ns)
<b>Control</b>	$4.44 \times 10^4$	6.26	$4.88 \times 10^3$	45.5	10.1
<b>PPT</b>	$3.67 \times 10^4$	6.83	$4.33 \times 10^3$	57.4	12.2
<b>PPF</b>	$1.90 \times 10^4$	8.21	$3.82 \times 10^3$	67.6	18.2

**Table 3.9** Performance of the fabricated PeLEDs.

	$V_{on}$ (V)	EL peak (nm)	Max. Lum. ( $cd\ m^{-2}$ )	Max. EQE (%)
<b>Control</b>	3.0	512	26471.2	14.5
<b>PPT</b>	2.8	513	73896.6	10.7
<b>PPF</b>	2.8	512	61025.3	12.6

**Table 3.10** Recombination decay constants of the control, PPT-modified and PPF-modified perovskite films.



	$k_1 (s^{-1})$	$k_2 (cm^3s^{-1})$	$k_3 (cm^6s^{-1})$
<b>Control</b>	$1.5 \times 10^8$	$8.0 \times 10^{-10}$	$2.0 \times 10^{-27}$
<b>PPT</b>	$1.4 \times 10^8$	$1.8 \times 10^{-9}$	$1.3 \times 10^{-27}$
<b>PPF</b>	$1.2 \times 10^8$	$1.3 \times 10^{-9}$	$2.2 \times 10^{-27}$

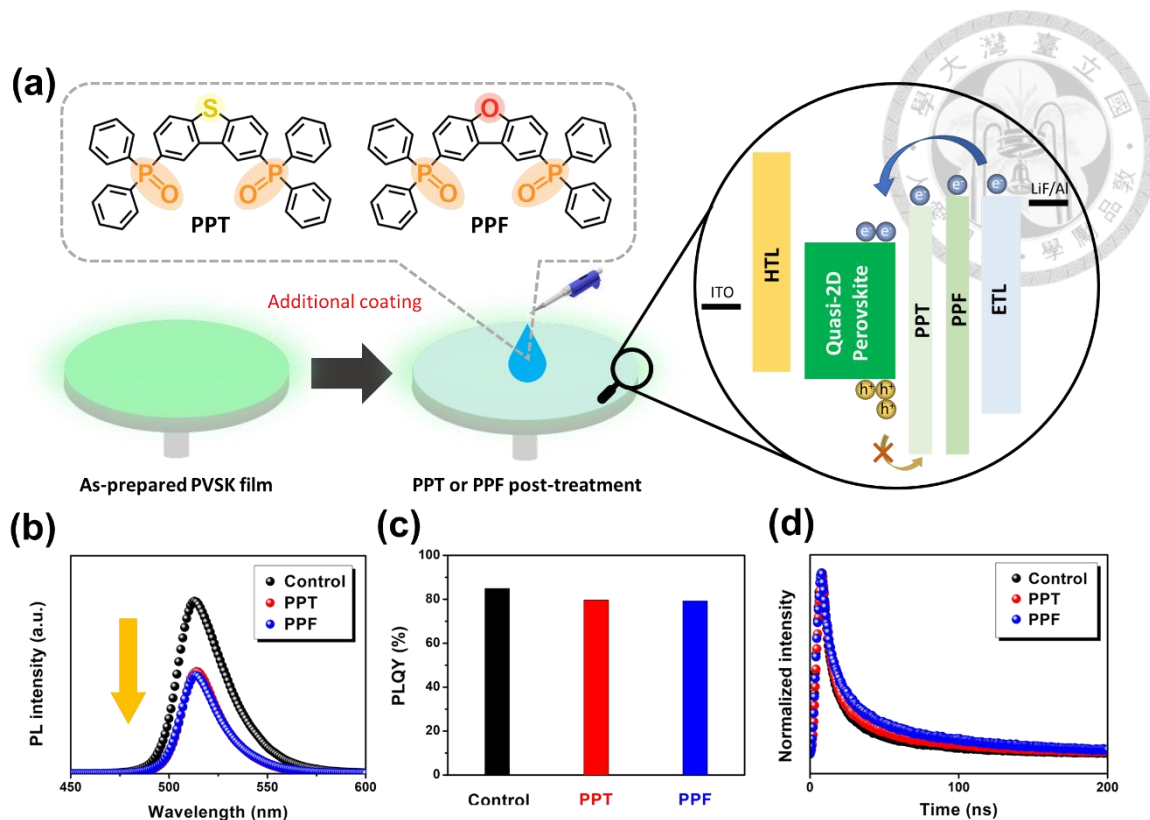


**Fig. 3.25** (a) Chemical structures of PPT and PPF and schematic representation of the post-treatment process and illustration of the interfacial engineering. (b) PL emission spectra, (c) PLQYs, and (d) TRPL curves of pristine, PPT-treated and PPF-treated perovskite films, where the PLQYs were measured by a 368 nm laser.

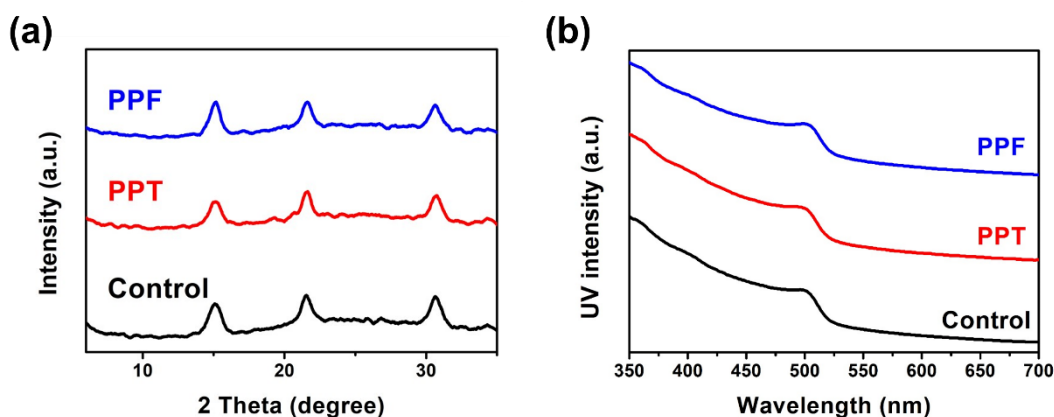


**Fig. 3.26** (a) XRD characteristics and (b) UV-vis absorption spectra of the pristine, PPT-modified and PPF-modified perovskite films.

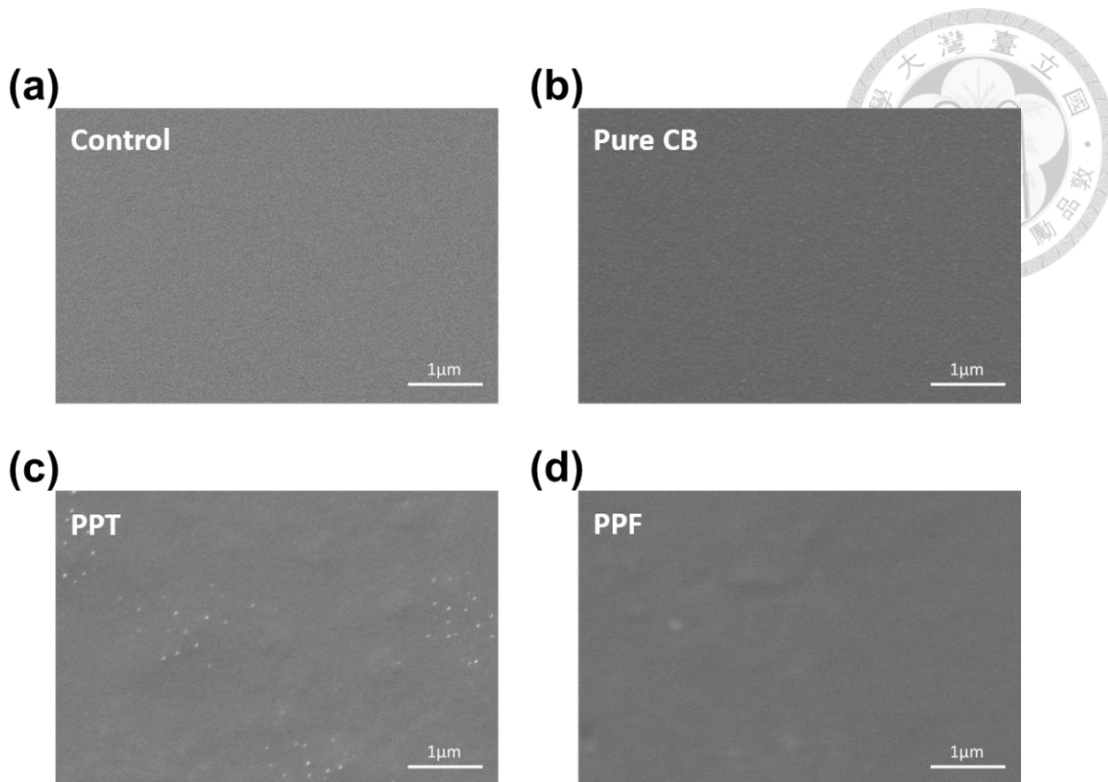


**Fig. 3.27** SEM images of the (a) pristine, (b) CB-treated, (c) PPT-modified and (d) PPF-modified perovskite films

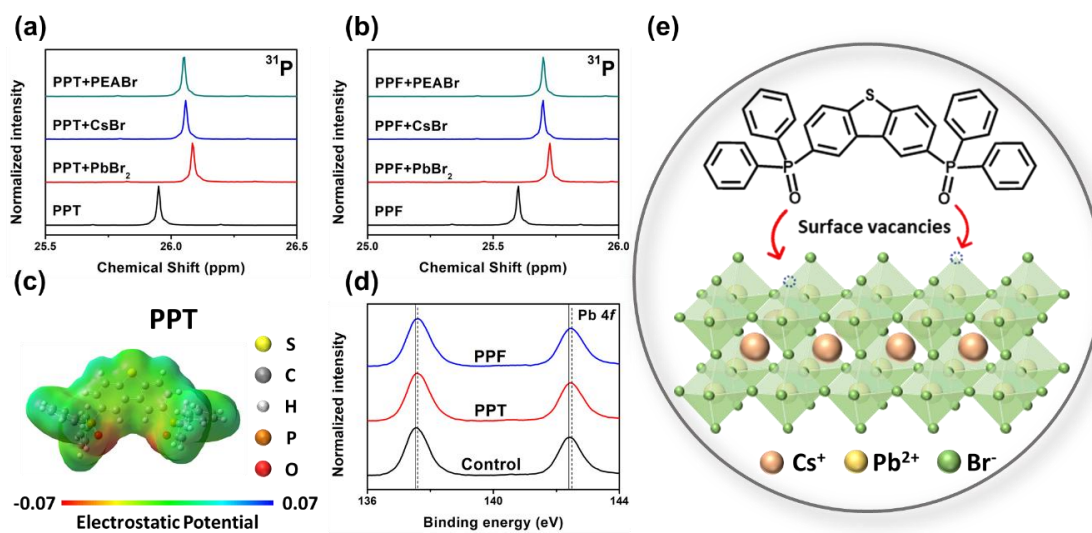


**Fig. 3.28**  $^{31}\text{P}$  NMR spectra of (a) PPT and (b) PPF and their mixtures with different perovskite precursor components. (c) ESP map of PPT molecule. (d) XPS spectra of Pb

4f signal for the pristine, PPT-modified and PPF-modified perovskite films. (e) Schematic illustration of the passivation function of PPT on a perovskite surface.

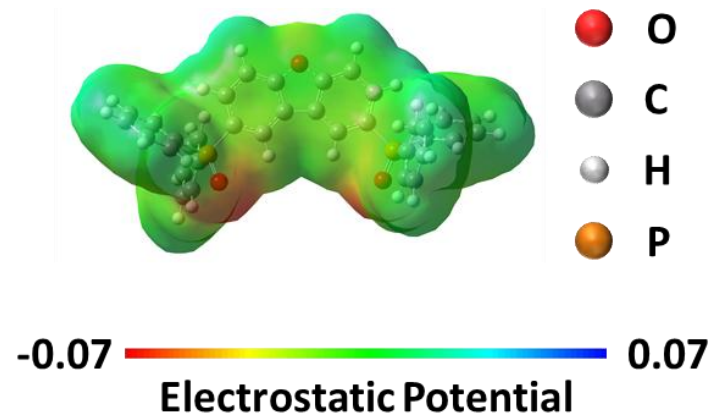


Fig. 3.29 ESP map of PPF molecule

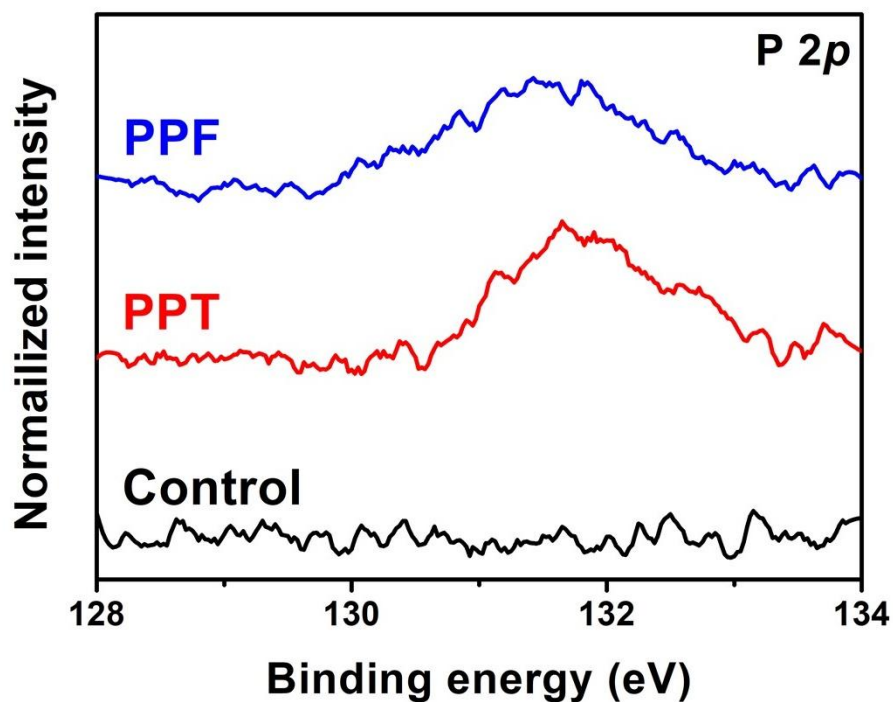
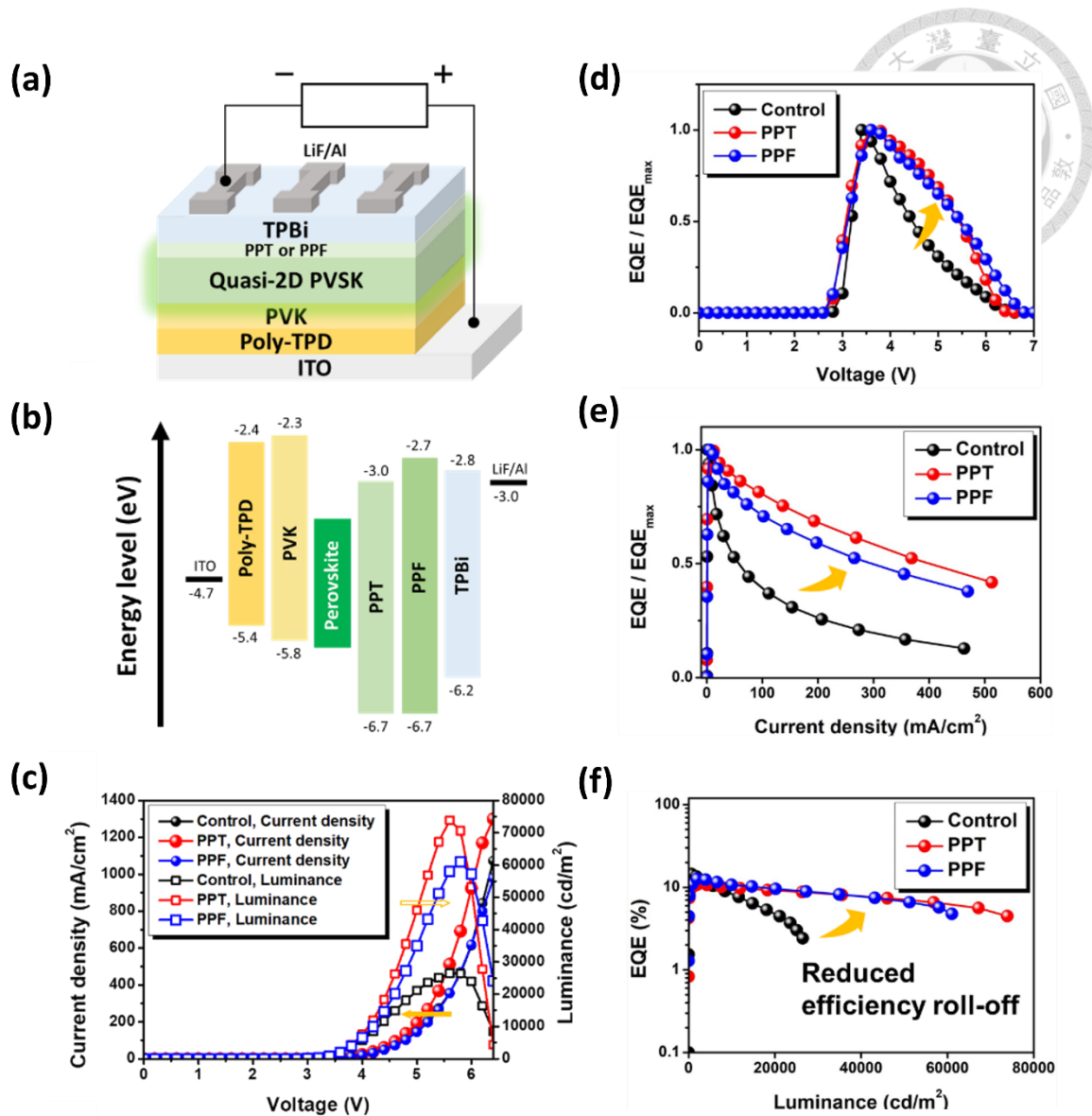


Fig. 3.30 XPS spectra of P 2p signal for the pristine, PPT-modified and PPF-modified perovskite films.



**Fig. 3.31** (a) Structure and (b) the energy-level diagram of the fabricated PeLEDs. (c) J-V-L characteristics, (d) normalized EQE-voltage curves, (e) normalized EQE-current density curves and (f) EQE-luminance curves of the fabricated devices.

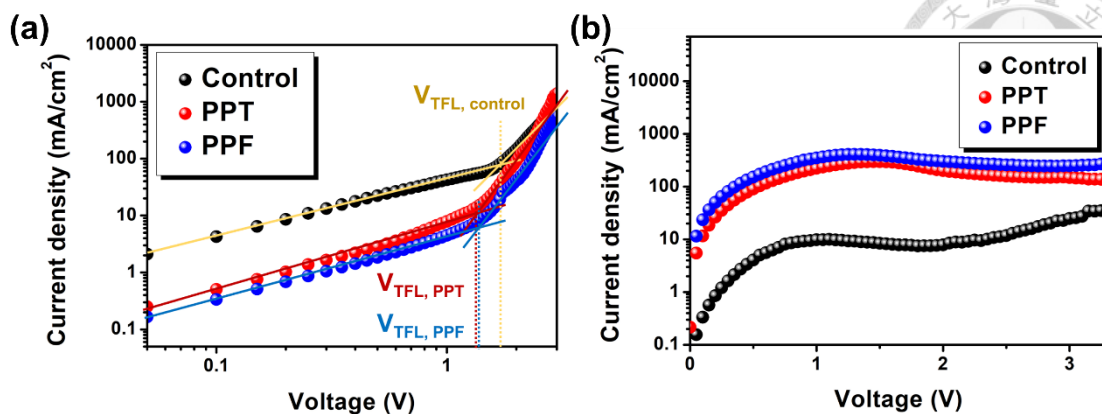


Fig. 3.32 J-V characteristics of the studied (a) hole-only devices (b) electron-only devices.

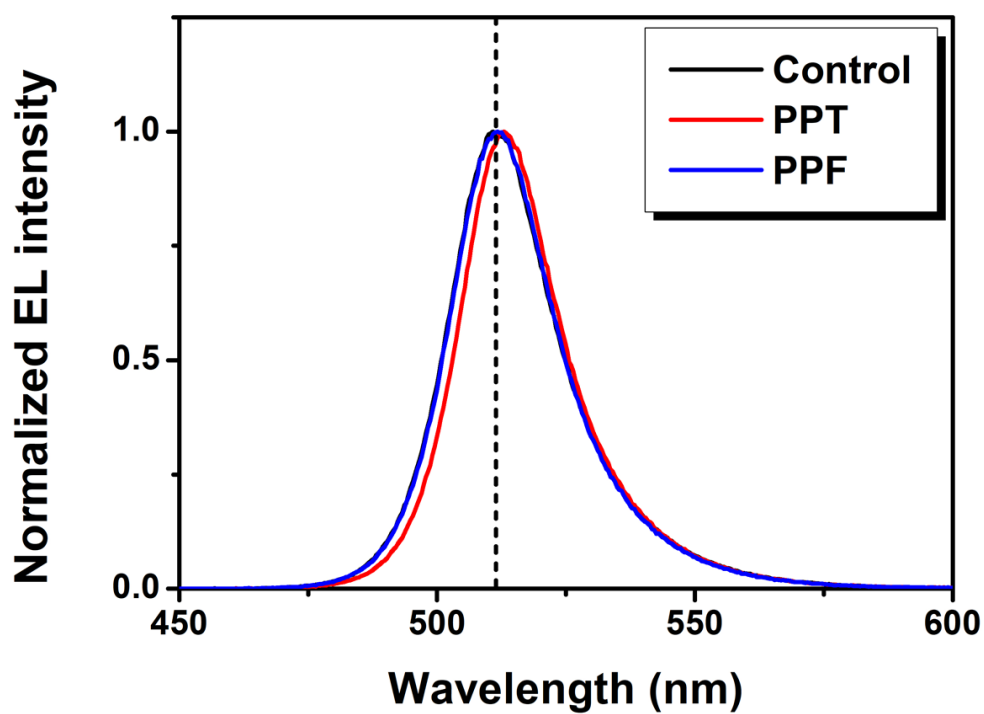
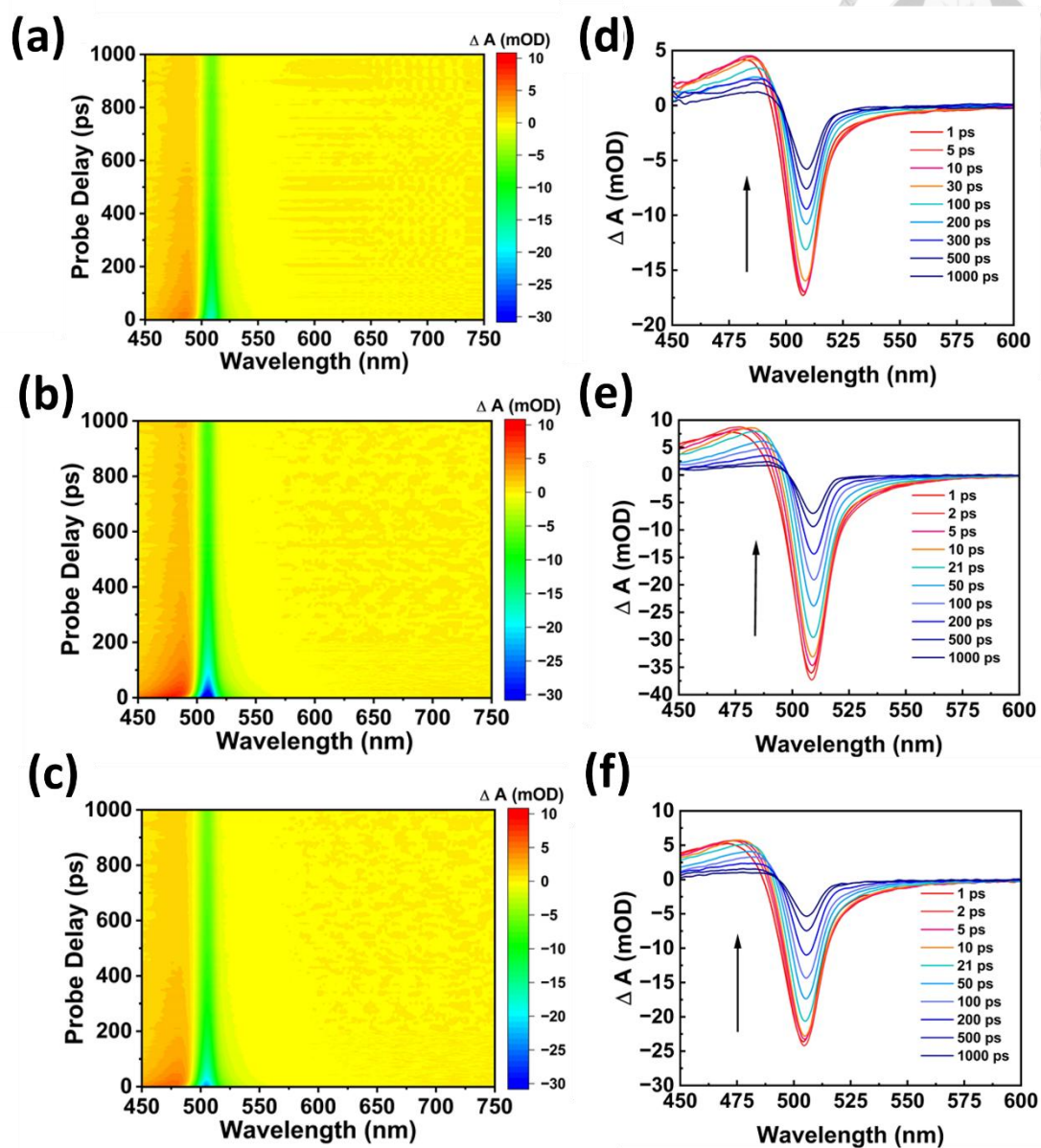
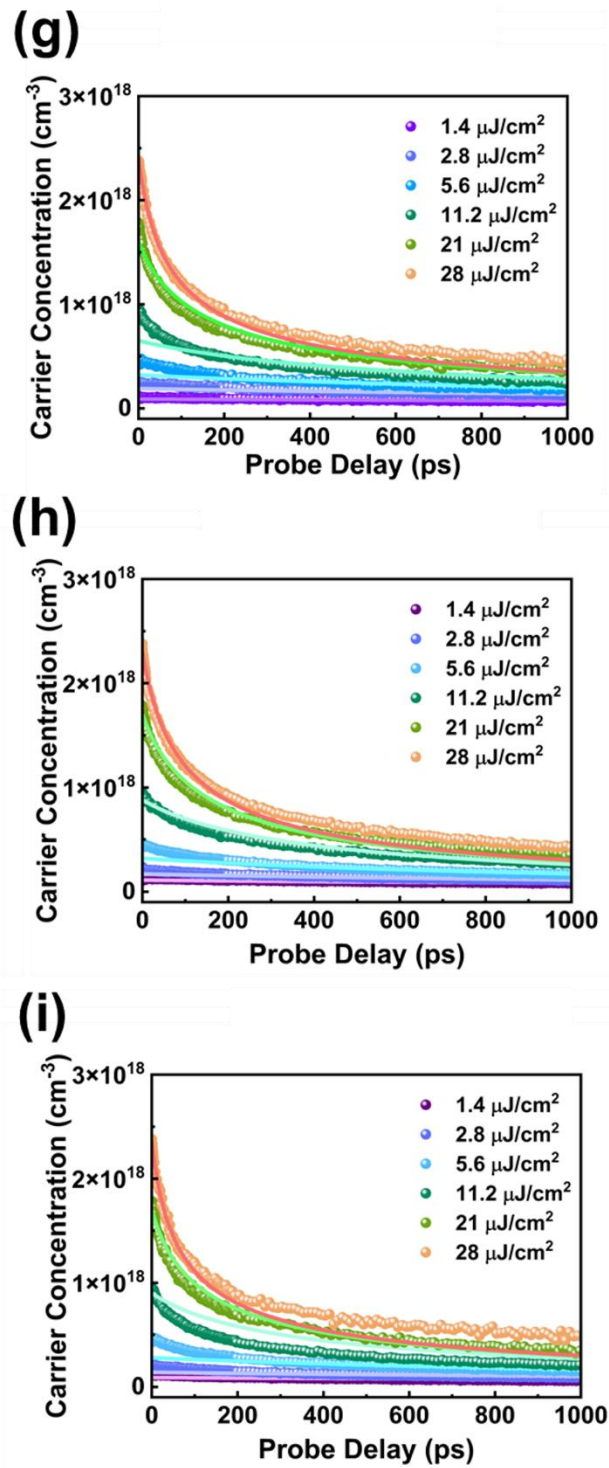


Fig. 3.33 EL curves of the fabricated PeLEDs measured at 4V.



**Fig. 3.34** Color plot for transient absorption (TA) in the visible regions for (a) pristine, (b) PPT-modified, and (c) PPF-modified perovskite films. Ultrafast time-resolved TA spectra of (d) pristine, (e) PPT-modified, and (f) PPF-modified perovskite films.





**Fig. 3.35** Power-dependent carrier dynamics at the probe wavelength of 505 nm for (g) pristine, (h) PPT-modified, and (i) PPF-modified perovskite films.

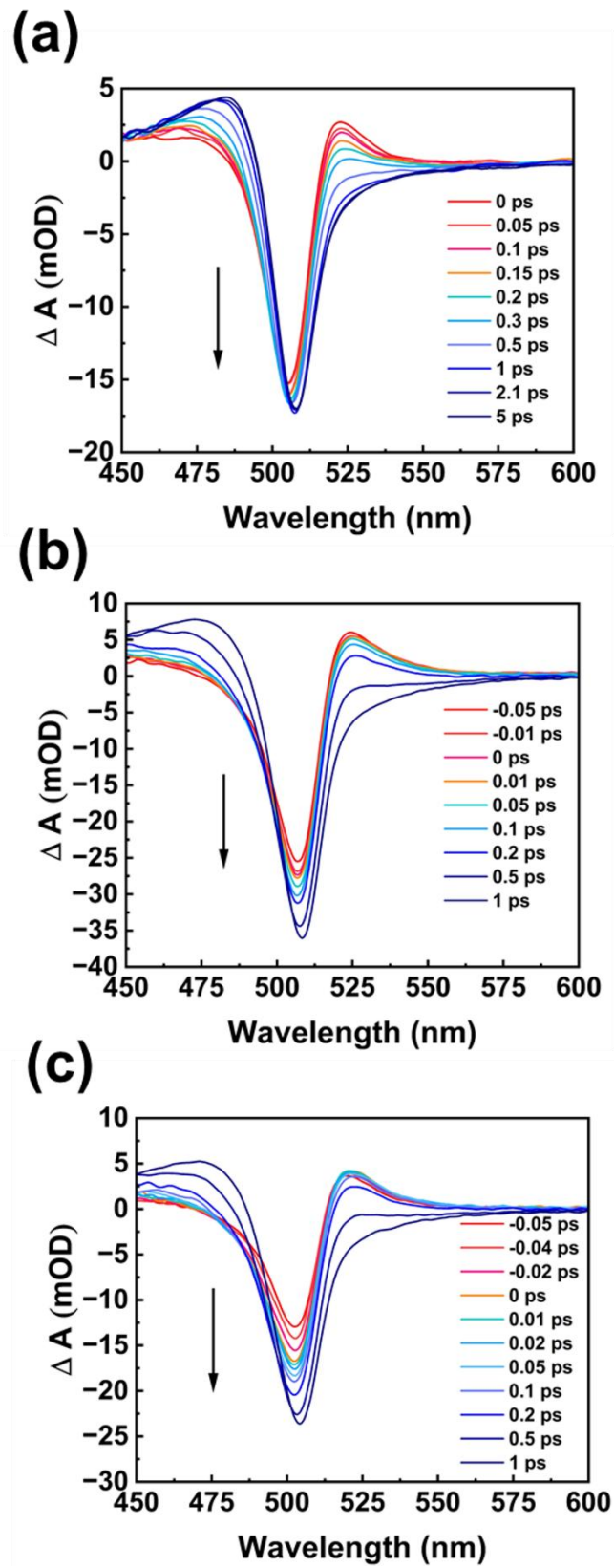


**Fig. 3.36** Femtosecond time-resolved TA spectra of (a) pristine, (b) PPT-modified and (c) PPF-modified perovskite films.

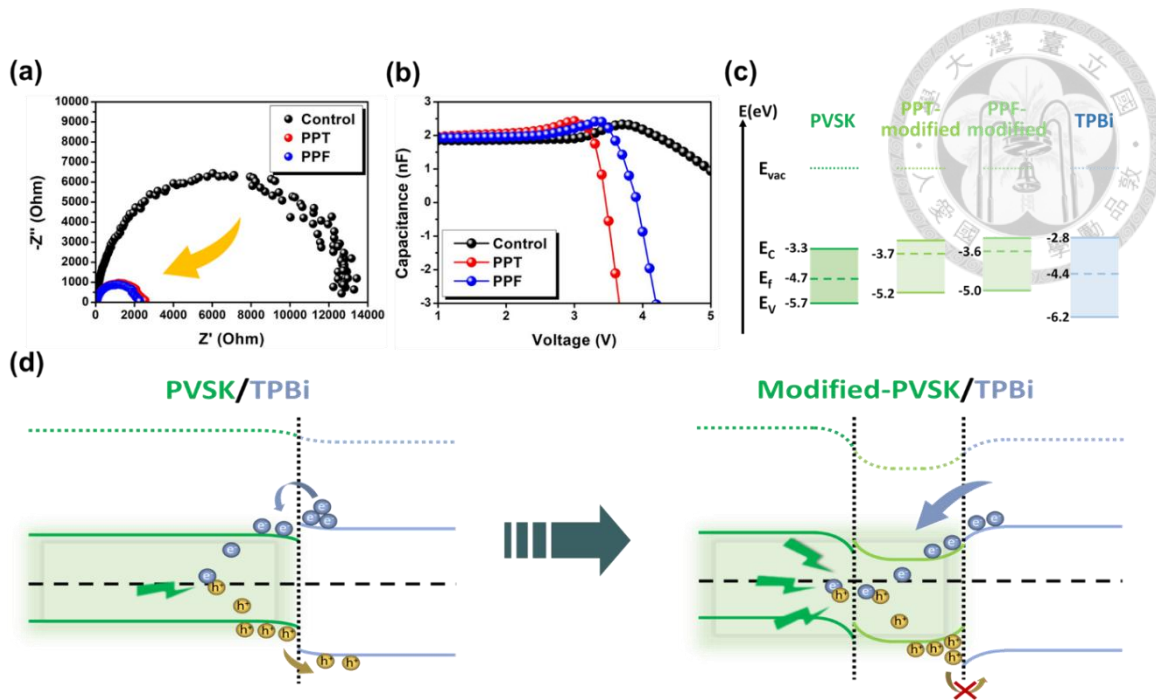


**Fig. 3.37** (a) EIS analyses and (b) capacitance-voltage curves of control, PPT-modified and PPF-modified devices. (c) Energy levels of the pristine, PPT-modified, PPF-modified perovskite films and TPBi. (d) Schematic representation of the better carrier dynamics in the modified device.

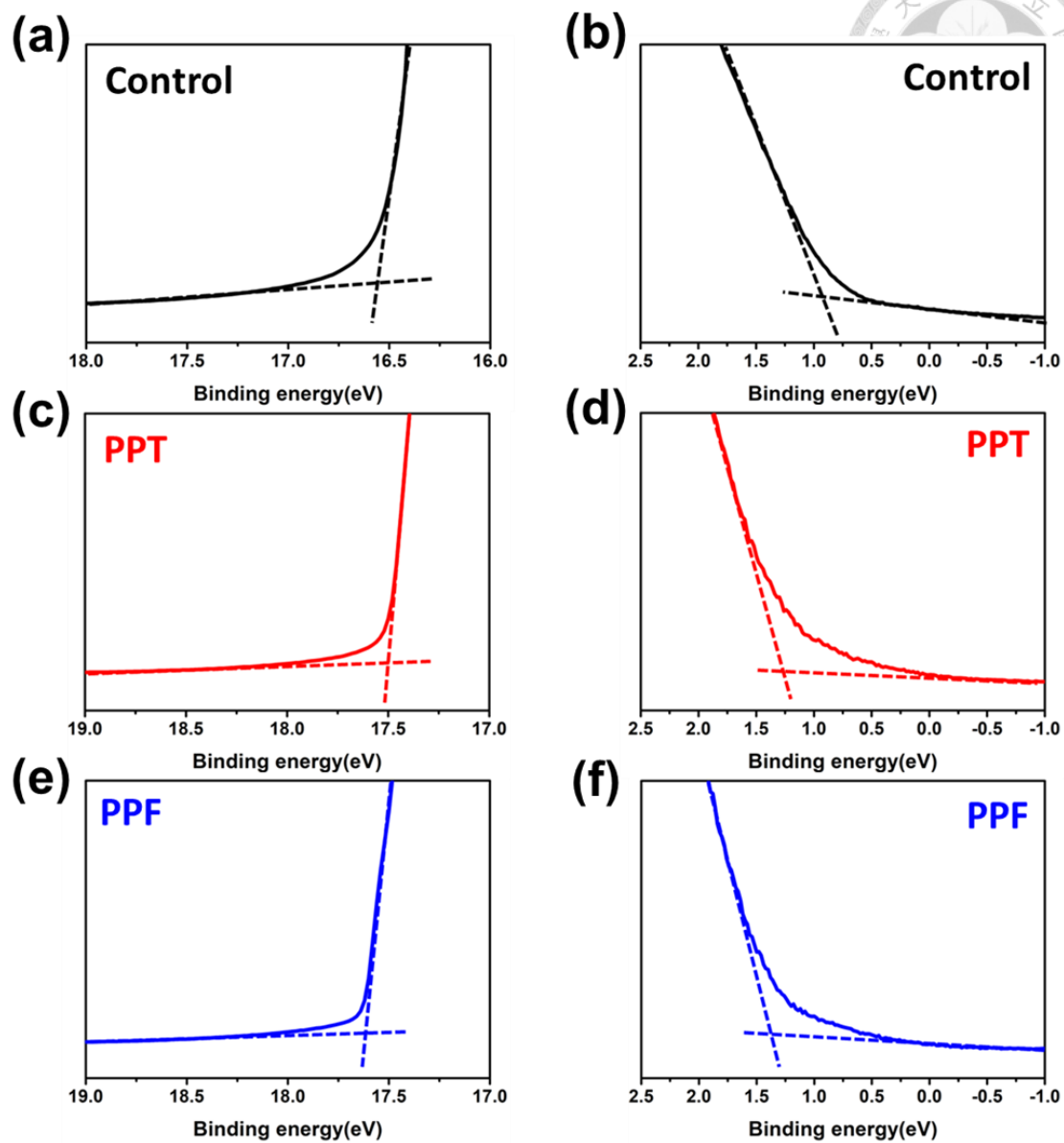


**Fig. 3.38** UPS results of the (a,b) pristine, (c,d) PPT-modified and (e,f) PPF-modified perovskite films.

# Chapter 4 2D Lead-Free Perovskite Light-Emitting Diodes



## 4.1 Improving Performance of Lead-Free Two-Dimensional Pure Red Perovskite Light Emitting Diodes via Natural Antioxidants Additive

The text and figures in this section are reproduced with permission from:

**C. H. Chen**, M. H. Yu, Y. Y. Wang, Y. C. Tseng, I. H. Chao, I. C. Ni, B. H. Lin, Y. J. Lu, C. C. Chueh\*, “Enhancing the Performance of Two-Dimensional Tin-Based Pure Red Perovskite Light-Emitting Diodes through the Synergistic Effect of Natural Antioxidants and Cyclic Molecular Additives”, *Small*, 2307774 (2024).

### 4.1.1 Background

Metal halide perovskites have garnered widespread attention as promising materials for light-emitting diodes (LEDs) due to their solution-processability, tunable optical bandgap, excellent color purity, and high photoluminescence quantum yield (PLQY).<sup>[168, 207-209]</sup> Over the past decade, tremendous progress has been achieved in developing high-efficiency perovskite light-emitting diodes (PeLEDs) across the visible spectrum, reflecting the sustained effort and innovation within the field.<sup>[24, 209-217]</sup> Nevertheless, a major concern remains: the majority of high-performing PeLEDs are based on lead-containing perovskites, raising serious environmental and health issues that pose challenges for widespread commercialization. In response, several strategies have emerged to promote sustainable development, including the design of Pb-free perovskite

alternatives, adoption of greener solvents, and the integration of bio-derived additives.<sup>[77, 218-220]</sup>

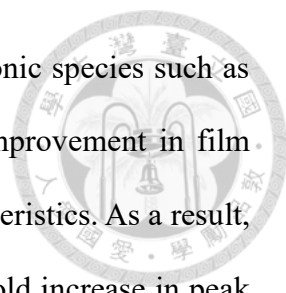
Driven by the need to reduce lead toxicity, researchers have actively pursued lead-free perovskite systems for electroluminescence applications. Various metallic substitutes such as tin (Sn),<sup>[221-224]</sup> copper (Cu),<sup>[225, 226]</sup> germanium (Ge),<sup>[227]</sup> bismuth (Bi),<sup>[228, 229]</sup> and europium (Eu),<sup>[230, 231]</sup> have been explored for their potential to replace Pb. Among them, Sn-based perovskites have gained particular interest due to their similar electronic structure to Pb, offering a promising platform not only for LEDs but also for solar and electronic devices.<sup>[82, 232-238]</sup> However, fabrication of high-quality Sn-based perovskite films is impeded by several intrinsic issues. Sn<sup>2+</sup> ions are easily oxidized to Sn<sup>4+</sup>, and their strong Lewis acidity accelerates crystallization, leading to poor film formation and a high density of defects such as Sn vacancies and uncoordinated Sn<sup>2+</sup>. These defects degrade the film's optoelectronic quality and hamper device performance.<sup>[239, 240]</sup> To address these challenges, researchers have proposed various strategies. To mitigate oxidation issues, reducing agents such as SnF<sub>2</sub>, Sn powder, and hypophosphorous acid have been introduced as additives in Sn-based precursor solutions, showcasing remarkable effects in preventing Sn<sup>2+</sup> oxidation.<sup>[221, 232, 241-243]</sup> Meanwhile, additives with strong coordination affinity for Sn<sup>2+</sup>, such as valeric acid (VA) and DSAS, help slow crystallization kinetics and improve film uniformity.<sup>[239, 244]</sup> Additionally, halide-rich environments and Lewis base additives have been used to passivate uncoordinated Sn centers and reduce trap-state density.<sup>[245, 246]</sup>

Beyond additive engineering, tailoring the dimensionality of Sn-based perovskites also offers a viable route to improved film and device stability. Transitioning from traditional 3D structures to 2D or quasi-2D configuration by incorporating bulky organic cation can shield the perovskite lattice from moisture and oxygen while slowing crystal

growth.<sup>[247-250]</sup> These layered structures typically exhibit a blue shift in emission compared to 3D systems, shifting from near-infrared to red light. Despite the altered semiconducting nature due to insulating spacer cations, the enhanced quantum confinement in 2D Sn perovskites makes them appealing for red-light emission.<sup>[251, 252]</sup>

Significant milestones have been achieved in the realm of 2D Sn-based PeLEDs, particularly for red emitters. The earliest demonstration in 2017 exhibited a luminance of just 0.15 cd/m<sup>2</sup>, alongside an initial study of halide composition effects on emission behavior.<sup>[253]</sup> Later advancements centered on enhancing film quality, especially in the archetypal PEA<sub>2</sub>SnI<sub>4</sub> system. For instance, Liang et al. employed hypophosphorous acid (HPA) to inhibit SnI<sub>4</sub> formation and improve film smoothness, while Gao et al. demonstrated that DSAS could effectively delay crystallization, enhancing film morphology and device efficiency.<sup>[239, 254]</sup> In a notable example, Wang et al. replaced the traditional PEA<sup>+</sup> cation with BTm<sup>+</sup> to construct (BTm)<sub>2</sub>SnI<sub>4</sub>, a 2D perovskite that facilitated better energy transfer and achieved a peak luminance of 3466 cd/m<sup>2</sup> with an EQE of 3.33%.<sup>[223]</sup> Similarly, Yuan et al. reported that VA's strong coordination with Sn<sup>2+</sup> both prevented oxidation and refined crystal growth, yielding a record-high EQE of ~5% and luminance of 170 cd/m<sup>2</sup>.<sup>[244]</sup> Despite these achievements, progress in 2D Sn-based PeLEDs has plateaued, underscoring the need for renewed innovation.

In this work, we introduce a new synergistic strategy to advance 2D Sn-based red PeLEDs by combining natural antioxidants with cyclic molecular additives. To promote greener synthesis, we first evaluated naturally derived antioxidants, including ascorbic acid (VitC), caffeic acid, ferulic acid, and p-coumaric acid, as additives in the Sn precursor solution. Among them, VitC demonstrated the most promising performance, effectively suppressing Sn<sup>2+</sup> oxidation and slowing crystallization via coordination interactions, which significantly improved film morphology. Building upon this, we incorporated 18-



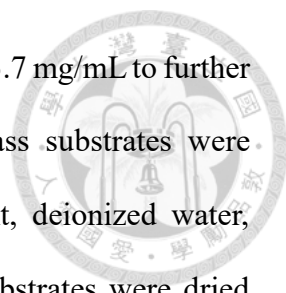
Crown-6, a well-known cyclic ether, which helped chelate excess ionic species such as  $\text{Sn}^{2+}$  and/or  $\text{PEA}^+$ . This dual-additive approach led to a marked improvement in film quality, reducing defect density and enhancing overall device characteristics. As a result, PeLEDs treated with VitC and 18-Crown-6 exhibited a nearly fourfold increase in peak luminance (from 25.3 to 98.7  $\text{cd/m}^2$ ) and a sevenfold improvement in external quantum efficiency (from 0.21% to 1.87%) relative to untreated controls. These results clearly demonstrate the powerful synergistic effect of combining natural antioxidants and crown ethers, offering a viable route to enhancing performance and sustainability in 2D Sn-based PeLED technologies.

#### 4.1.2 Experimental Section

**Materials.** Tin iodide ( $\text{SnI}_2$ , > 99.9%), phenethylammonium iodide (PEAI,  $\geq 98\%$ ), ascorbic acid, lithium fluoride ( $\text{LiF}$ , > 99.99%), and solvents including dimethylformamide (DMF, 99.8%) and dimethyl sulfoxide (DMSO,  $\geq 99.9\%$ ) were acquired from Sigma-Aldrich and employed without additional purification. 18-Crown-6 2,2',2''-(1,3,5-benzinetriyl)-tris(1-phenyl-1-H-benzimidazole) (TPBi) was purchased from Ultra Fine Chemical Technology Corp. PEDOT:PSS (Clevios™ P AI 4083) was purchased from Uniregion bio-tech and used without further purification.

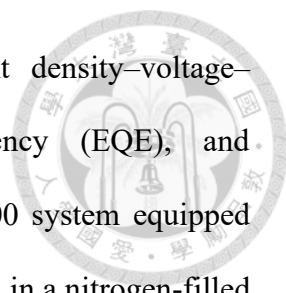
**Device fabrication.** The precursor solution for the 2D perovskite  $\text{PEA}_2\text{SnI}_4$  was prepared by dissolving phenethylammonium iodide (PEAI) and tin(II) iodide ( $\text{SnI}_2$ ) in 1 mL of a mixed solvent system (DMF/DMSO = 1:1 by volume) at a molar ratio of 2:1. The solution was stirred at room temperature for two hours. To inhibit the oxidation of  $\text{Sn}^{2+}$  to  $\text{Sn}^{4+}$ , ascorbic acid was introduced at varying molar concentrations (15%, 25%,





and 35%). Additionally, 18-Crown-6 was added at a concentration of 3.7 mg/mL to further improve film quality. Prior to device fabrication, ITO-coated glass substrates were thoroughly cleaned using a sequential ultrasonic bath in detergent, deionized water, acetone, and isopropanol (15 minutes each). After cleaning, the substrates were dried under a nitrogen stream and baked at 60 °C to remove residual solvents, followed by surface activation via plasma treatment. A hole-transporting layer (HTL) of PEDOT:PSS was then spin-coated onto the treated substrates at 6000 rpm for 60 seconds and subsequently annealed at 150 °C for 15 minutes in ambient air. The PEDOT:PSS-coated substrates were then transferred into a nitrogen-filled glove box for the deposition of the perovskite layer. The  $\text{PEA}_2\text{SnI}_4$  films, containing various ascorbic acid doping levels, were deposited onto the HTL via a two-step spin-coating process: 1000 rpm for 10 seconds followed by 5000 rpm for 60 seconds. The films were then annealed at 100 °C for 10 minutes to complete crystallization. Device fabrication was completed through sequential thermal evaporation of TPBi (30 nm), LiF (1 nm), and aluminum (100 nm) under high vacuum conditions ( $<10^{-6}$  torr).

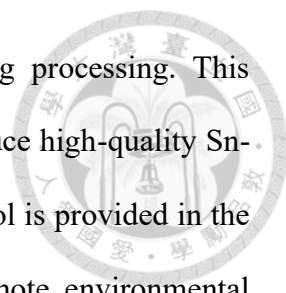
**Characterization.** The 2D perovskite films used for characterization were prepared by spin-coating the precursor solutions under the same conditions as those employed in device fabrication. UV-visible absorption spectra were recorded using a Hitachi U-4100 spectrophotometer, while photoluminescence (PL) measurements were obtained with a Horiba Fluorolog-3 system. Time-resolved PL (TRPL) analysis was performed using a Hamamatsu Universal Streak Camera C10910 at the TPS 23A beamline of the National Synchrotron Radiation Research Center (NSRRC). Surface morphology was examined via scanning electron microscopy (SEM) using a Nova<sup>TM</sup> NanoSEM 230. The crystal structure of the perovskite films was analyzed with a Rigaku SmartLab SE X-ray



diffractometer. Electrical performance metrics, including current density–voltage–luminance (J–V–L) characteristics, external quantum efficiency (EQE), and electroluminescence (EL) were measured using an Enlitech LQ-100 system equipped with a 100 mm integrating sphere. All measurements were conducted in a nitrogen-filled glovebox without device encapsulation. Carrier dynamics were probed through transient absorption spectroscopy (TAS) using a Femto Frame II system (IB Photonics). The excitation source consisted of 400 nm pulses (100 fs duration, 1 kHz repetition rate), generated by an optical parametric amplifier (OPA, TOPAS-C, Light Conversion) pumped by a mode-locked Ti:Sapphire laser (Spectra-Physics, Tsunami). Pump and probe beams were focused separately onto the sample, with respective spot sizes of approximately 300  $\mu\text{m}$  and 100  $\mu\text{m}$ . The white-light probe (450–800 nm) was produced via supercontinuum generation from a sapphire plate, with a pulse width of 30 fs. X-ray photoelectron spectroscopy (XPS) and ultraviolet photoelectron spectroscopy (UPS) were carried out using a PerkinElmer PHI 5400 system (equipped with a monochromatic Al K $\alpha$  X-ray source) and a Specs UVS 10/35 UV lamp, respectively. The highest occupied molecular orbital (HOMO) levels and optical bandgaps ( $E_g$ ) were estimated from Tauc plots, assuming a direct bandgap transition. Electrochemical impedance spectroscopy (EIS) was conducted on encapsulated devices in ambient air using a BioLogic SP-200 frequency response analyzer. Capacitance–voltage (C–V) and transient electroluminescence (TEL) measurements were performed with a Fluxim Paios system under room conditions.

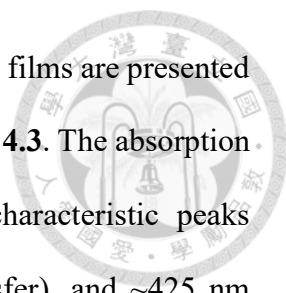
### 4.1.3 Results and Discussion

**Effects of natural antioxidants and 18-Crown-6 additives on film properties.** In this study, 2D lead-free perovskite films based on  $\text{PEA}_2\text{SnI}_4$  were fabricated using a spin-



coating method, with toluene employed as the antisolvent during processing. This approach, well-established in the literature, has been shown to produce high-quality Sn-based perovskite films.<sup>[236, 244, 254-256]</sup> The detailed fabrication protocol is provided in the Experimental Section. To address the oxidation of Sn<sup>2+</sup> and promote environmental sustainability, we explored the use of naturally derived antioxidants ascorbic acid (VitC), caffeic acid, ferulic acid, and p-coumaric acid as additives to the PEA<sub>2</sub>SnI<sub>4</sub> precursor solution. Given that high concentrations of organic additives may negatively impact film quality due to their insulating nature, we first evaluated the photoluminescence quantum yield (PLQY) of PEA<sub>2</sub>SnI<sub>4</sub> films with varying antioxidant loadings. As summarized in **Table 4.1**, all antioxidant-treated films exhibited higher PLQY values than the pristine film (0.67%), confirming their beneficial role in improving luminescence. Among them, VitC showed the most pronounced effect, yielding a peak PLQY of 3.32% at a 25% molar ratio. Notably, the corresponding film emitted the brightest red light under UV illumination (**Fig. 4.1**), highlighting VitC's strong interaction with Sn<sup>2+</sup> and its ability to suppress oxidation and regulate crystallization.

Building on these findings, we incorporated 18-Crown-6, a cyclic ether known to coordinate with metal ions, into the precursor solution to further enhance film quality. Although 18-Crown-6 has previously been used to improve 3D and quasi-2D perovskite systems,<sup>[27, 78, 257, 258]</sup> its effects on 2D Pb-free perovskites had not been reported. PLQY results, detailed in **Table 4.2** and **Fig. 4.2a**, demonstrate that the addition of 18-Crown-6 significantly boosted the PLQY of both pristine and VitC-treated films. The pristine film's PLQY rose to 2.47%, while the 25% VitC + 18-Crown-6 sample reached a maximum PLQY of 5.78%, indicating a strong synergistic interaction between the two additives. Consequently, the following analysis focuses on three representative film types: pristine PEA<sub>2</sub>SnI<sub>4</sub> (Pure), 25% VitC-treated (25C), and dual-additive-treated (25CC). UV-vis



absorption and photoluminescence (PL) spectra of the 25C and 25CC films are presented in **Fig. 4.2b,c**, while results for other compositions are shown in **Fig. 4.3**. The absorption spectra remained unchanged after additive incorporation, with characteristic peaks observed at ~610 nm (exciton absorption), ~520 nm (charge transfer), and ~425 nm (higher energy transitions),<sup>[259]</sup> indicating that neither additive significantly alters the optical band structure.

PL emission profiles for all samples featured a main emission peak around 625 nm. A slight blue shift was observed upon additive treatment, attributed to reduced shallow defect densities and fewer grain boundaries, consistent with prior findings.<sup>[260]</sup> Furthermore, PL intensity trends mirrored PLQY measurements, with the 25CC film exhibiting the strongest emission (**Fig. 4.2c**), confirming the additive-induced enhancement in film quality.

To gain further insights into the enhanced PL intensity, time-resolved photoluminescence (TRPL) measurements were performed and fitted using a biexponential decay curve, as shown in **Fig. 4.2d**. The fitting results, listed in **Table 4.3**, reveal that the average lifetime increases from 0.23 ns to 1.32 ns with the addition of 25% VitC, further increasing to 1.95 ns with the additional inclusion of 18-Crown-6. To analyze the prolongation of the average lifetime, we combined the TRPL results with the PLQY data. According to the definition of PLQY, it represents the ratio of the radiative recombination rate ( $k_{\text{rad}}$ ) to the total recombination rate ( $k_{\text{rad}} + k_{\text{nonrad}}$ ), where  $k_{\text{nonrad}}$  denotes the nonradiative recombination rate. Furthermore, the average lifetime can be defined as  $1/(k_{\text{rad}} + k_{\text{nonrad}})$ .<sup>[244,261]</sup> On this basis, we calculated the values of  $k_{\text{rad}}$  and  $k_{\text{nonrad}}$  and summarized the results in **Table 4.3**. The results indicate that the addition of VitC and 18-Crown-6 does not significantly change  $k_{\text{rad}}$  but leads to a remarkable decrease in  $k_{\text{nonrad}}$ . Therefore, the addition of VitC and 18-Crown-6 effectively reduces the nonradiative

recombination pathways in the  $\text{PEA}_2\text{SnI}_4$  film, correlating with the blue-shifting of the PL peak.

Structural characterization via X-ray diffraction (XRD) and grazing-incidence wide-angle X-ray scattering (GIWAXS) is shown in **Fig. 4.2e&f** and **Fig. 4.4**. All samples displayed similar peak positions and scattering patterns, indicating that the additives do not disrupt the perovskite's crystalline phase. However, morphological differences were evident from SEM and AFM images (**Fig. 4.3g-i** & **Fig. 4.5**). SEM analysis revealed larger grain sizes and fewer grain boundaries in additive-treated films. AFM measurements showed a progressive decrease in surface roughness: from  $R_q = 17.8$  nm (Pure) to 9.37 nm (25C) and 6.10 nm (25CC), indicating enhanced film uniformity, consistent with previous studies.<sup>[78]</sup> These morphological improvements directly correlate with the observed enhancements in optoelectronic properties.

In order to have a comprehensive understanding of the optical properties of the Pure, 25C, and 25CC films, we analyzed their temperature-dependent photoluminescence (PL) emission spectra. As shown in **Fig. 4.6a-c**, we examined their emission properties over the temperature range of 50 K to 300 K. The corresponding pseudo-color 2D plots are plotted in **Fig. 4.6d-e** to highlight the variation in peak position more effectively. The temperature-dependent PL results of the Pure film showed two peaks at low temperatures, centered at 649 nm (S2) and 632 nm (S1), suggesting the existence of two distinct states in  $\text{PEA}_2\text{SnI}_4$ .<sup>[262]</sup> Previous reports have indicated that the peak at 649 nm corresponds to the emission of shallow defects, while the peak at 632 nm originates from free excitons.<sup>[262]</sup> It is noteworthy that above 130 K, only one emission peak at 632 nm is observed, indicating thermal repopulation from S2 to S1. Based on the very different PL properties of these two states, a rough comparison of the number of defect states in the Pure, 25C, and 25CC films can be made by analyzing the temperature-dependent PL at

low temperatures. The results presented in **Fig. 4.6** indicate that the transition from S2 to S1 occurs at  $\sim 70$  K in both 25C and 25CC films, which is significantly lower than in the Pure film. In addition, the emission peak of S2 is less pronounced at a low temperature of 50 K for the 25 CC film as compared to the 25C film. These observations further confirm the favorable effect of the addition of VitC and 18-Crown-6 to the pristine  $\text{PEA}_2\text{SnI}_4$  film on reducing the number of defective states, which is consistent with the results in **Table 4.3**.

**Influence of dual additives on carrier dynamics of the film.** To further investigate the differences in carrier dynamics among the Pure, 25C, and 25CC films, transient absorption spectroscopy (TAS) measurements were conducted using an excitation wavelength of 400 nm and a white-light probe beam spanning the range of 450–800 nm. **Fig. 4.7a-c** depicts 2D pseudo-color plots of the intensity differences among these three films in the time-delay range from 0 to 1000 ps. Additionally, **Fig. 4.7d-f** displays the TAS spectra for different time delays (ranging from 200 fs to 500 ps) in each case. These spectra reveal two distinct ground-state bleach (GSB) peaks at approximately 610 nm and 530 nm, consistent with the results from the steady-state absorption spectra shown in **Fig. 4.7b**.

The decay kinetics of the 610 nm peak in each case were recorded and plotted as a function of time in **Fig. 4.7g-i**, and **Fig. 4.8**. A tri-exponential decay curve was fitted to the data by using formula (2), and **Table 4.4** presents the fitting data. In the fitting, the average lifetime of the pristine, 25C, and 25CC samples is 30.8 ps, 368.7 ps, and 579.7 ps, respectively. The 25CC sample exhibits the longest average lifetime. These results align well with the higher photoluminescence quantum yield (PLQY) values observed for the 25C and 25CC films in **Fig. 4.2a**.

$$y = y_0 + A_1 e^{-(t-t_0)/\tau_1} + A_2 e^{-(t-t_0)/\tau_2} + A_3 e^{-(t-t_0)/\tau_3} \quad (2)$$

To further explore the carrier dynamics, Leung, T.L., et al. investigated the carrier dynamics in the 2D tin-based perovskite series.<sup>[263]</sup> They identified three relaxation processes of excitons. The first one (sub-picosecond) represents the defect trapping exciton and the bandgap renormalization. The second one (hundred picoseconds) represents the interband radiation recombination process, and the last one (nanoseconds) represents the defect-assisted exciton recombination process. All samples exhibit similar  $\tau_1$ , indicating that additives do not alter the exciton trapping process. The  $\tau_2$  contribution in the fitting is minimal, suggesting that trap-assisted exciton recombination dominates the radiative recombination channel rather than free exciton recombination in our sample. The  $\tau_3$  values for the pristine, 25C, and 25CC samples are 161 ps, 1168 ps, and 1404 ps, respectively. These results suggest that the trap-assist process in the presence of 25C and 25CC is approximately ten and twenty times longer, respectively, compared to the Pure film. The TAS results demonstrate the synergistic effect of natural antioxidants and cyclic molecular additives in reducing exciton scattering, thereby improving device efficiency.

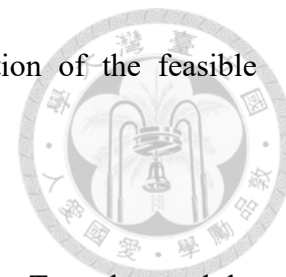
In the investigation of the passivation effect of the additives VitC and 18-Crown-6 on the  $\text{PEA}_2\text{SnI}_4$  film, X-ray photoelectron spectroscopy (XPS) analyses were conducted on Pure, 25C, and 25CC  $\text{PEA}_2\text{SnI}_4$  films to compare their  $\text{Sn}^{4+}$  to  $\text{Sn}^{2+}$  ratios. **Fig. 4.9a-c** depict the Sn 3d spectra of these films, showing two peaks at 484.3 eV and 492.6 eV, corresponding to the spin-orbit splitting of the  $\text{Sn}_{5/2}$  and  $\text{Sn}_{3/2}$  states of  $\text{Sn}^{2+}$ . Deconvolution of these peaks reveals the  $\text{Sn}^{4+}$  states at 485 eV and 493.4 eV, allowing for the calculation of the  $\text{Sn}^{4+}/\text{Sn}^{2+}$  ratio. The Pure film exhibits the highest  $\text{Sn}^{4+}/\text{Sn}^{2+}$  ratio of 0.42, indicating significant oxidation of  $\text{Sn}^{2+}$ . With the addition of VitC, the  $\text{Sn}^{4+}/\text{Sn}^{2+}$  ratio in the 25C film is markedly decreased to 0.16, providing evidence of VitC's reducing ability to retard the oxidation of  $\text{Sn}^{2+}$ . Moreover, the  $\text{Sn}^{4+}/\text{Sn}^{2+}$  ratio in the 25CC film is

further reduced to 0.1, indicating that 18-Crown-6 contributes to the passivation of PEA<sub>2</sub>SnI<sub>4</sub>. This aligns with the results in **Table 4.3**, emphasizing that the synergistic effect of VitC and 18-Crown-6 significantly mitigates  $k_{\text{nonrad}}$  and Sn vacancy formation in EA<sub>2</sub>SnI<sub>4</sub>. Overall, the XPS analyses provide insights into the reduction of Sn<sup>2+</sup> oxidation and passivation of PEA<sub>2</sub>SnI<sub>4</sub> facilitated by VitC and 18-Crown-6, reinforcing their roles in enhancing the film quality.

The effect of VitC on the crystallization process of PEA<sub>2</sub>SnI<sub>4</sub> was investigated through <sup>1</sup>H NMR measurements on perovskite precursors (PEAI and SnI<sub>2</sub>) mixed with VitC. **Fig. 4.9d** shows a noticeable chemical shift of VitC when mixed with SnI<sub>2</sub>, indicating a strong interaction between VitC and SnI<sub>2</sub>. In contrast, no shift was observed when mixing VitC with PEA<sub>2</sub>SnI<sub>4</sub>, confirming the interaction between VitC and SnI<sub>2</sub>. Further insights were gained through <sup>13</sup>C NMR measurements (**Fig. 4.9e**). Mixing VitC with SnI<sub>2</sub> induced a significant shift in the peak of the C=O group, suggesting a strong bonding interaction between VitC and Sn<sup>2+</sup> (-C=O...Sn<sup>2+</sup>). Additionally, FTIR spectra in **Fig. 4.9f** revealed a shift in the carboxylate stretching vibrational signal in both 25C and 25CC films, confirming the interaction between VitC and Sn<sup>2+</sup> (-C=O...Sn<sup>2+</sup>). The electrostatic potential (ESP) calculation for the VitC molecule (**Fig. 4.10**) showed a high density of electron cloud on the C=O functional group, indicating its ability to form bonds with Sn<sup>2+</sup>. These results collectively confirm that the interaction between the C=O group of VitC and Sn<sup>2+</sup> retards the crystallization process of PEA<sub>2</sub>SnI<sub>4</sub>, leading to an improvement in film quality.<sup>[236, 244]</sup> On the other hand, the effect of 18-Crown-6 was explored through <sup>1</sup>H NMR measurements (**Fig. 4.9g**), showing interactions with both SnI<sub>2</sub> and PEA<sub>2</sub>SnI<sub>4</sub>. This supports the conclusion that 18-Crown-6 contributes to reducing the crystallization process of PEA<sub>2</sub>SnI<sub>4</sub> by capturing excess ions, such as Sn<sup>2+</sup> or PEA<sup>+</sup>, acting as an

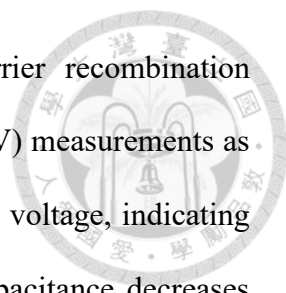


additional passivator. **Fig. 4.9h** presents a schematic representation of the feasible interactions between VitC, 18-Crown-6, and PEA<sub>2</sub>SnI<sub>4</sub>.



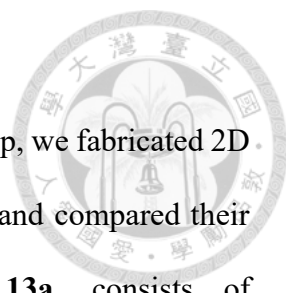
**Electrical characterization of the Pure, 25C and 25CC Films.** To understand the reduction in trap density after the additions of VitC and 18-Crown-6, space-charge-limited current (SCLC) measurements were performed, and the results are illustrated in **Fig. 4.11a-c**. The hole-only device structure used for these measurements was ITO/PEDOT:PSS/2D perovskites (Pure, 25C, 25CC)/MoO<sub>3</sub>/Ag. In SCLC measurements, the trap density can be estimated from the onset voltage, known as the trap-filled limit voltage ( $V_{TFL}$ ). For the device based on the Pure film, the highest  $V_{TFL}$  value was 0.47 V, while the  $V_{TFL}$  values decreased for the devices based on 25C and 25CC films, measuring 0.40 V and 0.36 V, respectively. The trap density difference was quantified using the equation  $N_t = 2\epsilon_0\epsilon_r V_{TFL} / eL^2$ , which allowed the calculation of the exact trap density ( $N_t$ ). The results showed that the addition of VitC led to a significant decrease in trap density from  $1.05 \times 10^{17} \text{ cm}^{-3}$  to  $6.56 \times 10^{16} \text{ cm}^{-3}$ . Furthermore, the additional addition of 18-Crown-6 further reduced the trap density to  $5.90 \times 10^{16} \text{ cm}^{-3}$ . These findings suggest that the synergistic effect of VitC and 18-Crown-6 contributes to a substantial reduction in trap density, which is indicative of improved charge carrier transport properties in the perovskite films. interactions between VitC, 18-Crown-6, and PEA<sub>2</sub>SnI<sub>4</sub>.

**Fig. 4.11d** illustrates the electrochemical impedance spectroscopy (EIS) of devices based on these three films. The device structure is identical to that of the PeLED device and the information is provided in the next section. The smaller arc radius in the Nyquist plot clearly confirms the better carrier transport performance of the devices based on 25C and 25CC films. This is due to the fact that the VitC and 18-Crown-6 additives effectively decreases the trap density in the film, which reduces the leakage current during device



operation and improves carrier transport.<sup>[264]</sup> To investigate carrier recombination capacity and charge transfer, we performed capacitance-voltage (C-V) measurements as shown in **Fig. 4.11e**. The capacitance increases with increasing bias voltage, indicating that charge is injected into the PeLED. At higher voltages, the capacitance decreases sharply, indicative of a decrease in carriers due to recombination of electrons and holes in the light-emitting layer. Of all the conditions, 25CC has the fastest capacitance drop at high voltage, demonstrating a more efficient charge transfer during the recombination of electrons and holes. Due to the higher charge transfer efficiency of 25CC, it is expected that 25CC produces the brightest PeLED compared to the other conditions.<sup>[23, 265]</sup>

Transient electroluminescence (EL) decay measurements were conducted to further investigate the exciton recombination behaviors in the perovskite films. The onset time ( $t_d$ ), rising time ( $t_r$ ), and decay rate of electroluminescence (EL) are depicted in **Fig. 4.11f**, where  $t_d$  is defined as the time when holes and electrons start to be captured together. A PeLED with a faster  $t_d$  indicates a quick response and higher carrier mobility. On the other hand,  $t_r$  is defined as the time during which carriers penetrate each other and the traps are filled, leading to an increase in the density of excited states in the recombination region. A faster  $t_r$  indicates a lower trap density and quicker carrier transfer.<sup>[266-268]</sup> **Fig. 4.11f** compares the transient EL results of the studied PeLEDs. Under the same voltage bias, 25CC exhibited the fastest  $t_d$  of 0.428  $\mu\text{s}$  and the fastest  $t_r$  of 2.412  $\mu\text{s}$ , suggesting that 25CC possesses the highest carrier mobility and the lowest trap density among the studied devices. Moreover, the decay time varied for each PeLED device (**Fig. 4.12**), with 25CC exhibiting the fastest decay time, indicating the lowest trap density among the devices studied.<sup>[268]</sup> These results from transient EL measurements align with the findings discussed in the previous sections, providing further evidence of the enhanced performance of the PeLEDs with the addition of VitC and 18-Crown-6.



**Device performance of the fabricated PeLEDs.** In the final step, we fabricated 2D Sn-based PeLEDs based on the three films (Pure, 25C, and 25CC) and compared their performances. The device structure, as shown in **Fig. 4.13a**, consists of ITO/PEDOT:PSS/2D perovskites (Pure, 25C, 25CC)/TPBi/LiF/Al, with fabrication details described in the Experimental Section. To assess the energy levels of these perovskite films, Ultraviolet photoelectron spectroscopy (UPS) was employed (**Fig. 4.14**), and the results are summarized in the energy-level diagram in **Fig. 4.13b**. The results demonstrate an upward shift of the valence band maximum (VBM) from -5.49 eV (Pure) to -5.37 eV (25C) and -5.02 eV (25CC). This shift in the VBM favors the injection of holes into the light-emitting layer from the hole transport layer, thereby suppressing the unwanted injection of holes into the electron transport layer.<sup>[221]</sup> Additionally, the upshift of the Fermi level in the cases of 25C and 25CC indicates that the p-type behavior of the perovskite film is attenuated due to the presence of fewer Sn<sup>4+</sup> ions.<sup>[234, 269]</sup> This modification contributes to the improved performance of the PeLEDs based on 25C and 25CC films.

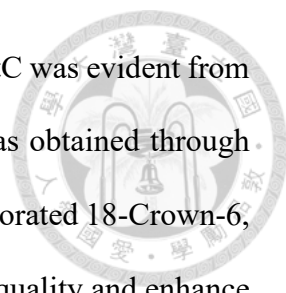
The performance of the PeLED devices based on the Pure, 25C, and 25CC PEA<sub>2</sub>SnI<sub>4</sub> films is evaluated through current density-voltage-luminance (J-V-L) curves (**Fig. 4.13c**), EQE-current density curves (**Fig. 4.13d**), and summarized in **Table 4.5**. The results reveal that the 25C and 25CC devices exhibit lower current densities before the turn-on voltage compared to the Pure device, aligning with the V<sub>TFL</sub> results in the SCLC analysis (**Fig. 4.11a-c**). Additionally, the 25C and 25CC devices operate at higher voltages than the Pure device. The CIE coordinates of these PeLED devices at different bias voltages are depicted in **Fig. 4.13e** and **Fig. 4.15**. Notably, the 25CC device demonstrates superior color stability across bias voltages, maintaining a consistent CIE coordinate of (0.7, 0.3)

from 2.4 V to 5 V. This color stability aligns with the Rec. 2100 specification for red emitters. In contrast, the CIE coordinate of the Pure device undergoes notable changes, moving from (0.56, 0.44) to (0.69, 0.31) at 2.4 V to 3.6 V and further to (0.66, 0.34) at 4 V. The instability in the Pure device is attributed to the high density of defects in the pristine  $\text{PEA}_2\text{SnI}_4$  film. Despite the improved color stability of the 25C device at different bias voltages, it remains less stable than the 25CC device, underscoring the significance of the synergistic effect of VitC and 18-Crown-6.

The electroluminescence (EL) spectra of the devices at different bias voltages are captured in **Fig. 4.16a-c**, and the corresponding 2D color contour plots are presented in Figure 6f-h. Notably, the Pure device reaches a maximum voltage of 4 V, while the 25CC device operates at a higher voltage of up to 5.6 V. The contour plots exhibit a narrowing trend with the addition of VitC or dual additives (VitC + 18-Crown-6), indicating a more concentrated emission of pure red color. Furthermore, the full-width half maximum (FWHM) of each device at the same operating voltage of 3.6 V is depicted in **Fig. 4.16d-f**. The addition of dual additives results in a slight decrease in the FWHM value from 32 nm to 29.7 nm, indicating an enhancement in color purity. In summary, the collaborative action of VitC and 18-Crown-6 serves as effective passivators for the  $\text{PEA}_2\text{SnI}_4$  film. They not only mitigate the oxidation from  $\text{Sn}^{2+}$  to  $\text{Sn}^{4+}$  but also significantly improve the film quality, thereby enhancing the performance of the derived PeLED device.

#### 4.1.4 Summary

In summary, we adopted a dual-additives approach to address the performance challenges of lead-free perovskite light-emitting diodes (PeLEDs). Firstly, we utilized the natural oxidant, VitC, as an additive to hinder the oxidation of  $\text{Sn}^{2+}$  to  $\text{Sn}^{4+}$ . X-ray photoelectron spectroscopy (XPS) results illustrated a significant reduction in the



presence of Sn<sup>4+</sup> in the film. Furthermore, the passivation effect of VitC was evident from photoluminescence (PL) measurements, and supportive evidence was obtained through nuclear magnetic resonance (NMR) interactions. Secondly, we incorporated 18-Crown-6, a cyclic molecule, as an additional additive to further refine the film quality and enhance the overall performance of lead-free 2D PeLEDs. The dual-additives strategy resulted in an improved performance in the fabricated lead-free PeLEDs. Despite achieving an enhanced external quantum efficiency (EQE) of nearly 2%, luminance reaching approximately 100 cd/m<sup>2</sup>, and a purer red color with a FWHM value of only 29.7nm, there remains room for further enhancements. Moving forward, our future endeavors will involve continued exploration of passivation methods and the investigation of alternative additives to create even more efficient lead-free perovskite light-emitting diodes.

#### 4.1.5 Tables and Figures



**Table 4.1** PLQY of PEA<sub>2</sub>SnI<sub>4</sub> film containing different ratios of the studied natural antioxidants.

Natural antioxidant additive	15 mol%	25 mol%	35 mol%
VitC	1.88 %	3.32 %	3.19 %
Caffeic acid	0.97 %	0.90 %	1.28 %
Ferulic acid	1.04 %	1.02 %	1.23 %
p-Coumaric acid	1.07 %	0.87 %	1.12 %

**Table 4.2** PLQY of PEA<sub>2</sub>SnI<sub>4</sub> films with or w/o 18-Crown-6 containing different molar ratios of VitC.

	0 mol% VitC	15 mol% VitC	25 mol% VitC	35 mol% VitC
w/o Crown	0.67 %	1.88 %	3.32 %	3.19 %
w/ Crown	2.47 %	4.70 %	5.78 %	5.64 %

**Table 4.3** TRPL fitting parameters and the radiative and nonradiative recombination rates of pristine, 25C and 25CC PEA<sub>2</sub>SnI<sub>4</sub> films.

	A <sub>1</sub>	τ <sub>1</sub> (ns)	A <sub>2</sub>	τ <sub>2</sub> (ns)	τ <sub>avg</sub> (ns)	k <sub>rad</sub> (10 <sup>6</sup> /s)	k <sub>nonrad</sub> (10 <sup>6</sup> /s)
Pure	0.015	1.52	0.985	0.21	0.23	29.1	4318.7
25C	0.364	2.27	0.636	0.77	1.32	25.2	732.4
25CC	0.423	3.88	0.576	0.53	1.95	29.6	483.2

**Table 4.4** The carrier lifetime calculated from transient absorption measurement of different 2D Sn-based perovskite.

	A <sub>1</sub>	τ <sub>1</sub> (ns)	A <sub>2</sub>	τ <sub>2</sub> (ns)	A <sub>3</sub>	τ <sub>3</sub> (ns)	τ <sub>avg</sub> (ns)
Pure	0.88	0.2	0.14	9.2	0.23	161	30.8
25C	0.85	0.21	0.04	6.2	0.41	1168	368.7
25CC	0.7	0.2	0.04	5.3	0.52	1404	579.7

Table 4.5 Device performance of the fabricated PeLEDs.

	$V_{on}$ (V)	EL peak (nm)	Max. Lum. ( $cd\ m^{-2}$ )	Max. EQE (%)
Pure	2.4	634	25.3	0.21
25C	2.4	633	78.3	0.57
25CC	2.4	633	98.7	1.87

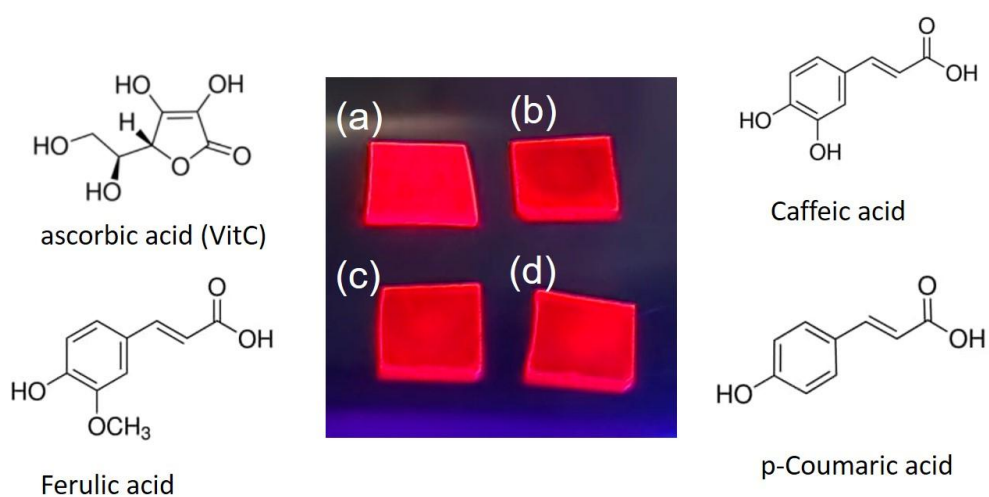
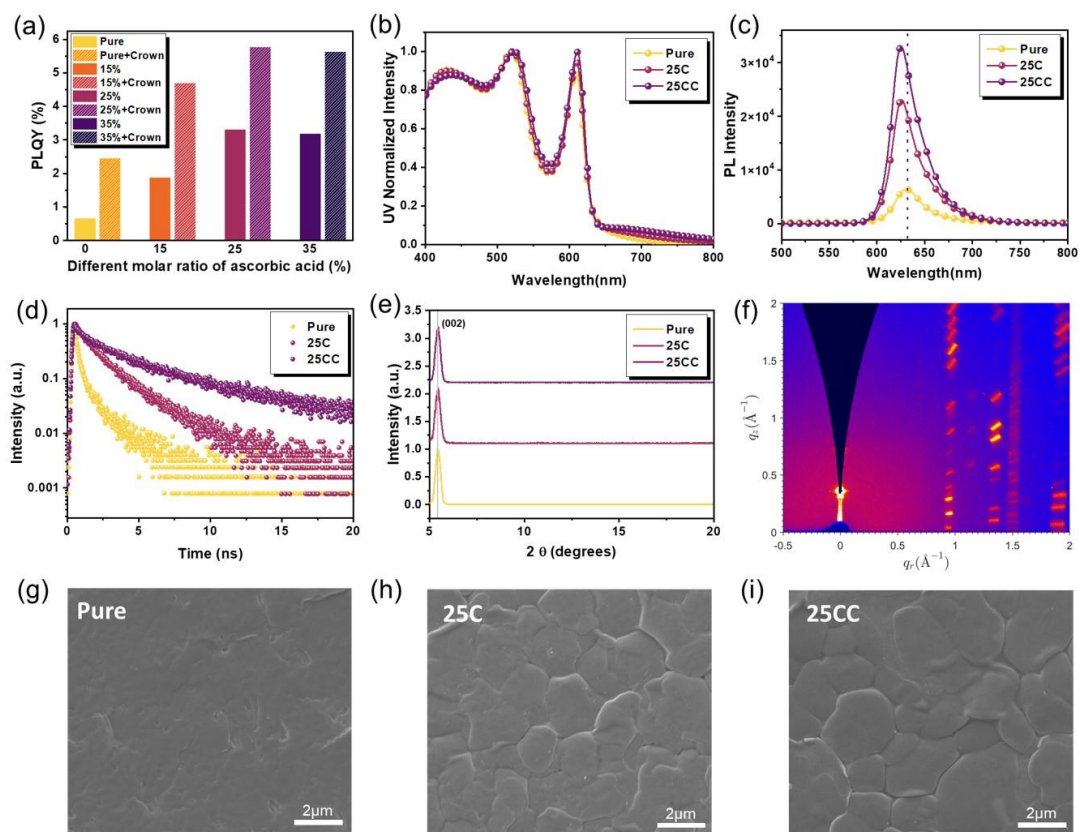
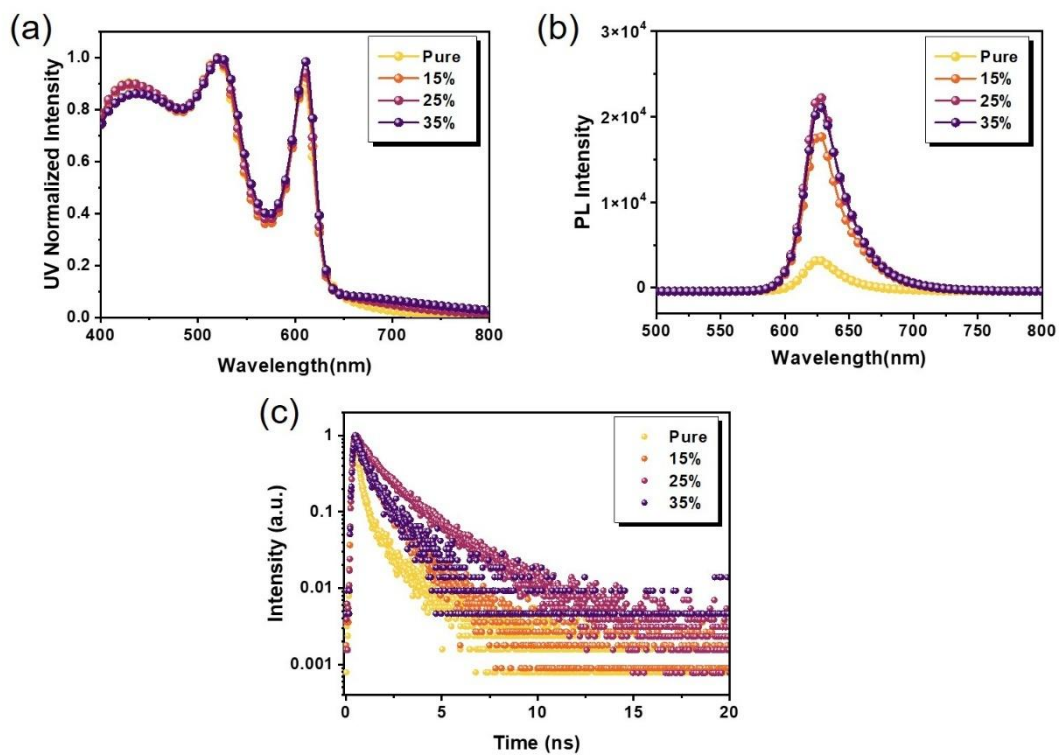


Fig. 4.1 UV irradiated  $PEA_2SnI_4$  films containing 25% molar ratio of (a) Vit C, (b) Caffeic acid, (c) Ferulic acid, and (d) p-Coumaric acid.



**Fig. 4.2** (a) Photoluminescence quantum yield (PLQY) of PEA<sub>2</sub>SnI<sub>4</sub> films with varying molar ratios of ascorbic acid (VitC), with and without the addition of 18-Crown-6. (b) UV–vis absorption spectra, (c) photoluminescence (PL) emission spectra, (d) time-resolved PL (TRPL) decay curves, and (e) X-ray diffraction (XRD) patterns of pristine, 25C (25% VitC), and 25CC (25% VitC + 18-Crown-6) PEA<sub>2</sub>SnI<sub>4</sub> films. (f) Grazing-incidence wide-angle X-ray scattering (GIWAXS) pattern of the 25CC PEA<sub>2</sub>SnI<sub>4</sub> film. (g–i) Scanning electron microscopy (SEM) images of (g) pristine, (h) 25C, and (i) 25CC PEA<sub>2</sub>SnI<sub>4</sub> films.





**Fig. 4.3** (a) UV-vis absorption and (b) PL emission spectra as well as (c) TRPL measurements of Pure, 25C, and 25CC PEA<sub>2</sub>SnI<sub>4</sub> films.

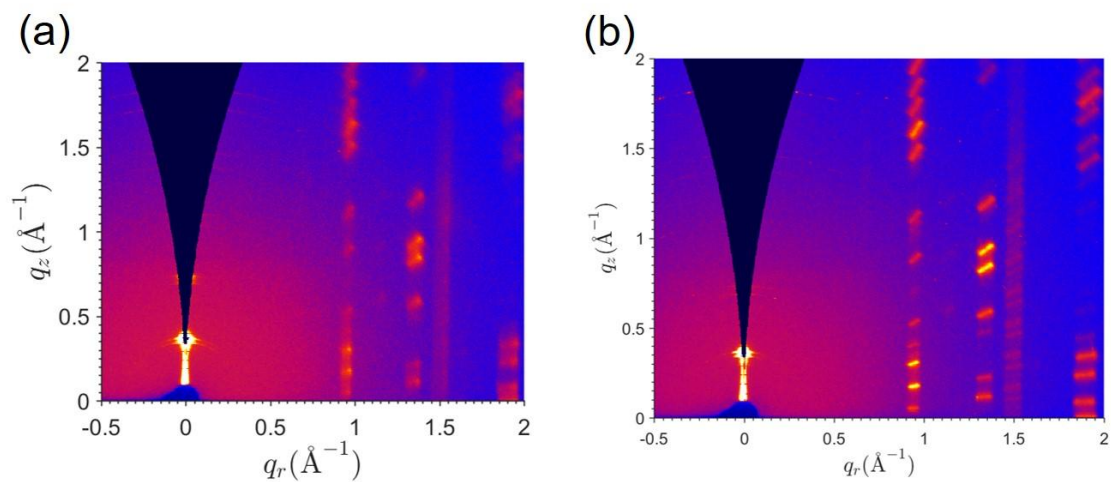


**Fig. 4.4** GIWAX patterns of (a) pristine and (b) 25CC PEA<sub>2</sub>SnI<sub>4</sub> films.

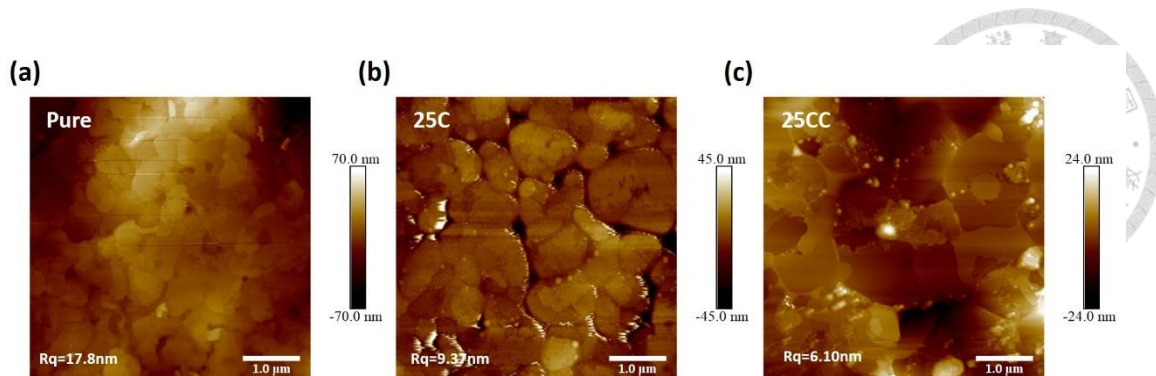


**Fig. 4.5** The AFM images of Pure, 25C, and 25CC PEA<sub>2</sub>SnI<sub>4</sub> films.

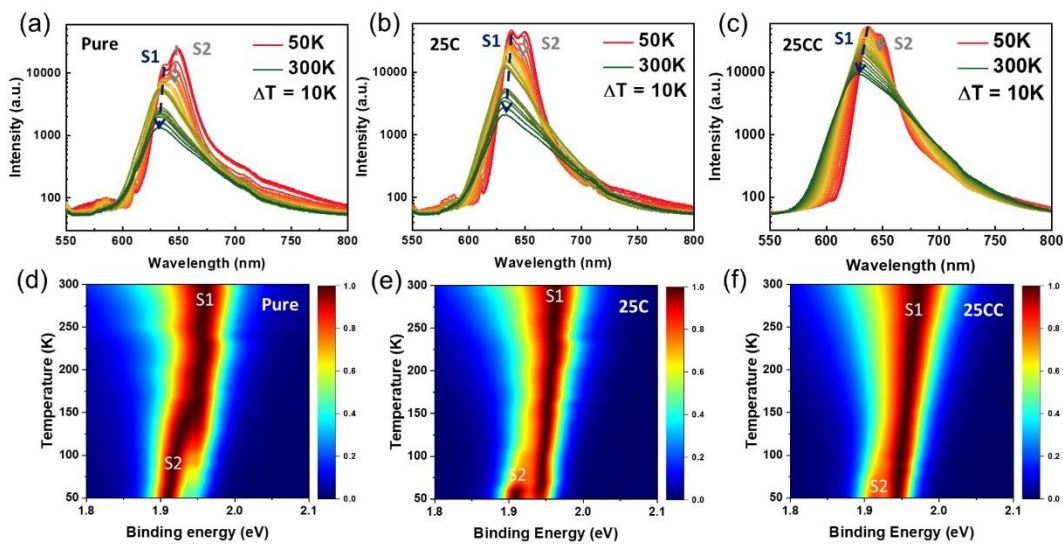


**Fig. 4.6** Temperature-dependent PL measurements from 50 K to 300 K and the corresponding 2D contour plots of (a, d) pristine, (b, e) 25C, and (c, f) 25CC PEA<sub>2</sub>SnI<sub>4</sub> films.

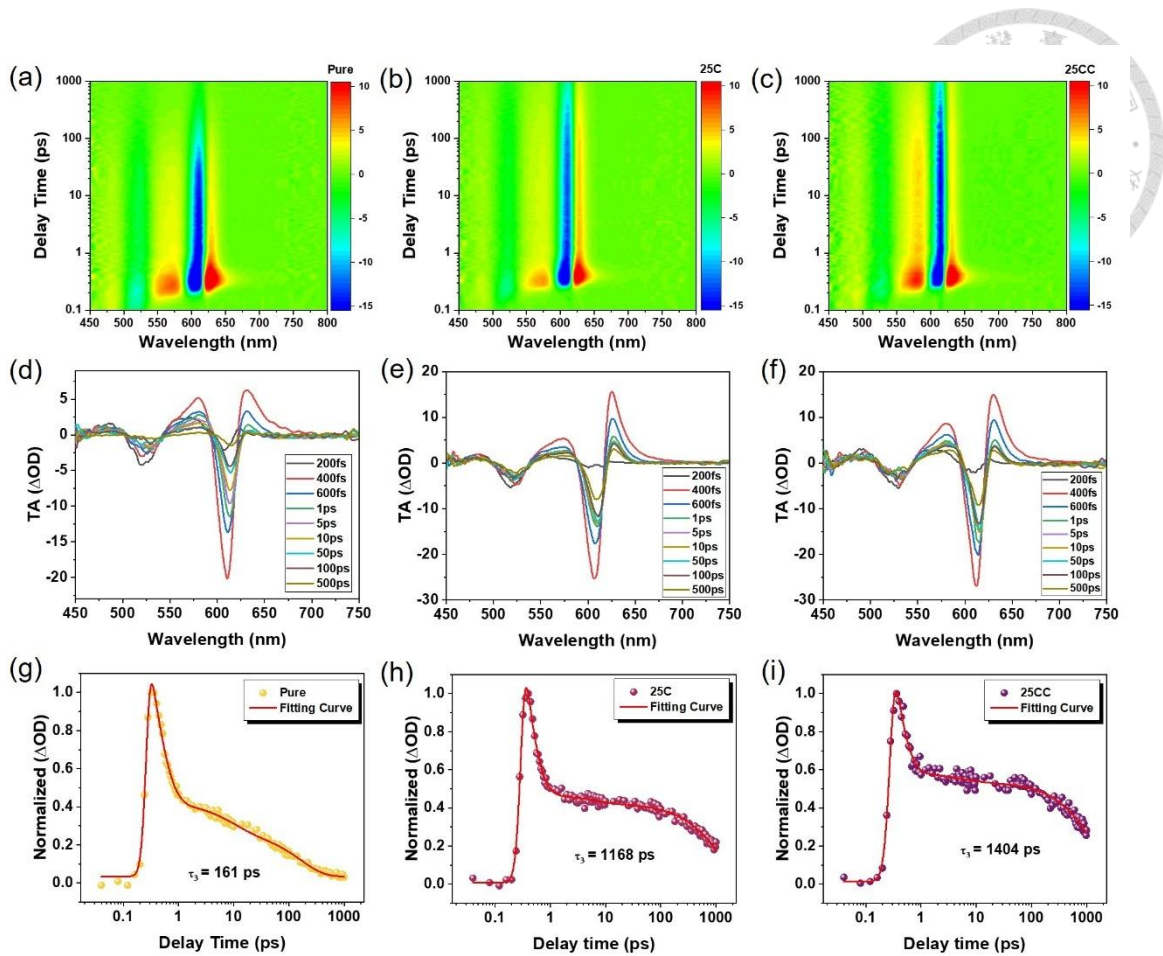


**Fig. 4.7** Pseudocolor plots of transient absorption spectra (TAS) of (a, d) pristine, (b, e) 25C and (c, f) 25CC PEA<sub>2</sub>SnI<sub>4</sub> films excited at 400 nm with different scanning delay times. Kinetic traces of (g) pristine, (h) 25C and (i) 25CC PEA<sub>2</sub>SnI<sub>4</sub> films at the probe wavelength of 610 nm.

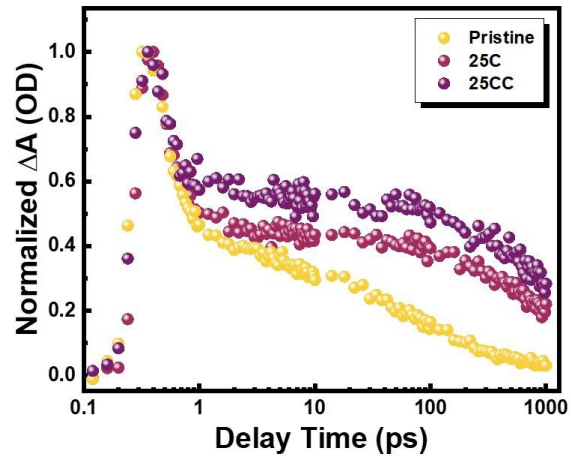


**Fig. 4.8** Kinetic traces of pristine, 25C and 25CC PEA<sub>2</sub>SnI<sub>4</sub> films at 610 nm probe wavelength.

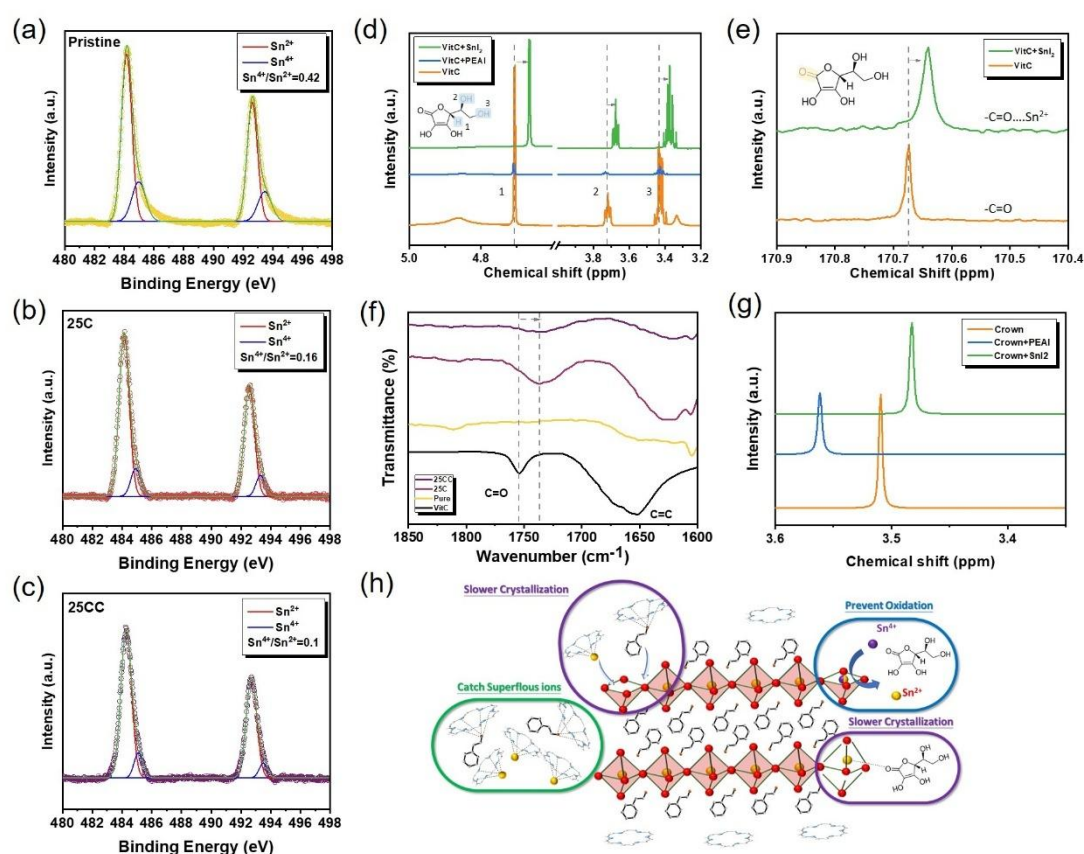


**Fig. 4.9** (a–c) X-ray photoelectron spectroscopy (XPS) spectra of the Sn 3d core levels for (a) pristine, (b) 25C (25% VitC), and (c) 25CC (25% VitC + 18-Crown-6) PEA<sub>2</sub>SnI<sub>4</sub> films. (d) <sup>1</sup>H NMR spectra of VitC, VitC + PEAI, and VitC + SnI<sub>2</sub>, and (e) <sup>13</sup>C NMR spectra of VitC and VitC + SnI<sub>2</sub> in DMSO- d<sub>6</sub> solution. (f) Fourier-transform infrared (FTIR) spectra of pristine, 25C, and 25CC PEA<sub>2</sub>SnI<sub>4</sub> films. (g) <sup>1</sup>H NMR spectra of 18-Crown-6, 18-Crown-6 + PEAI, and 18-Crown-6 + SnI<sub>2</sub> in DMSO-d<sub>6</sub>. (h) Schematic illustration of the proposed interactions between VitC, 18-Crown-6, and the PEA<sub>2</sub>SnI<sub>4</sub> perovskite structure.

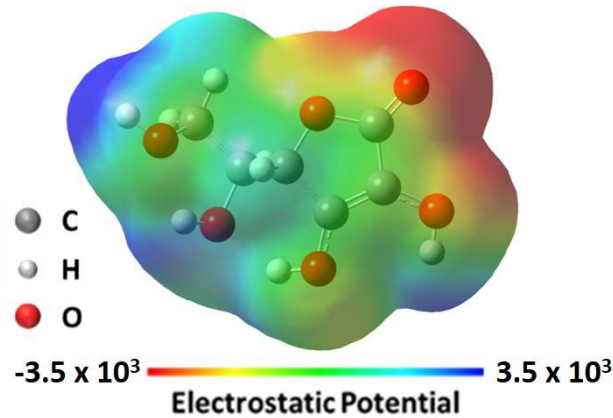


Fig. 4.10 ESP map of VitC molecule.

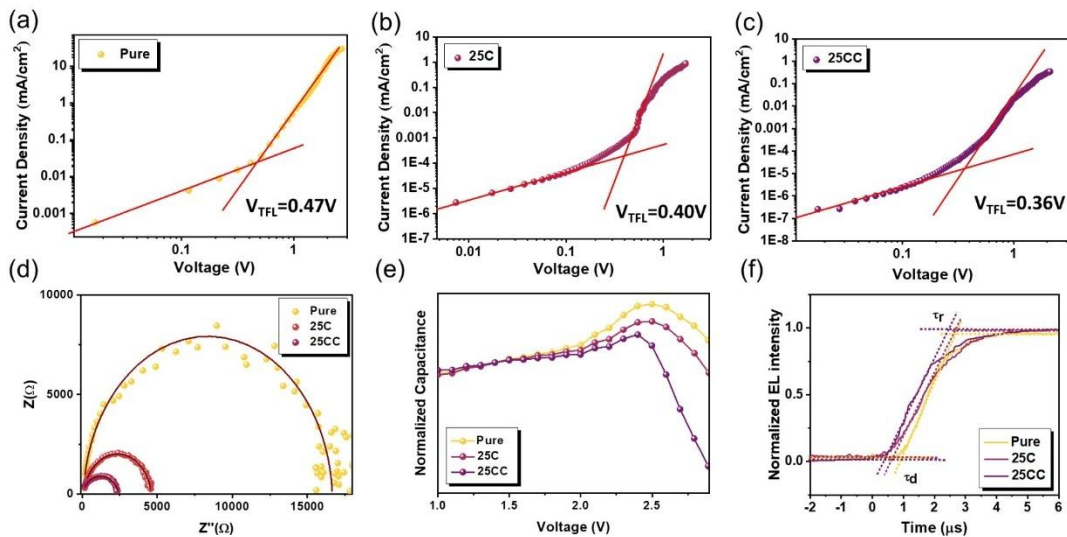
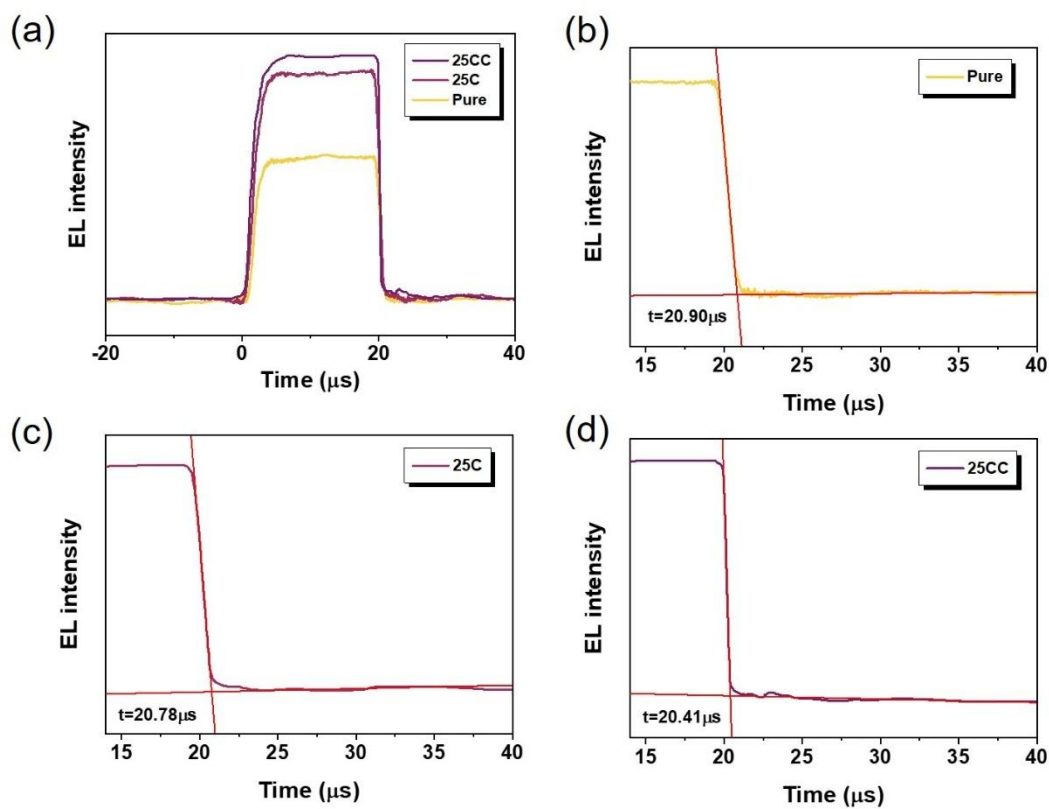
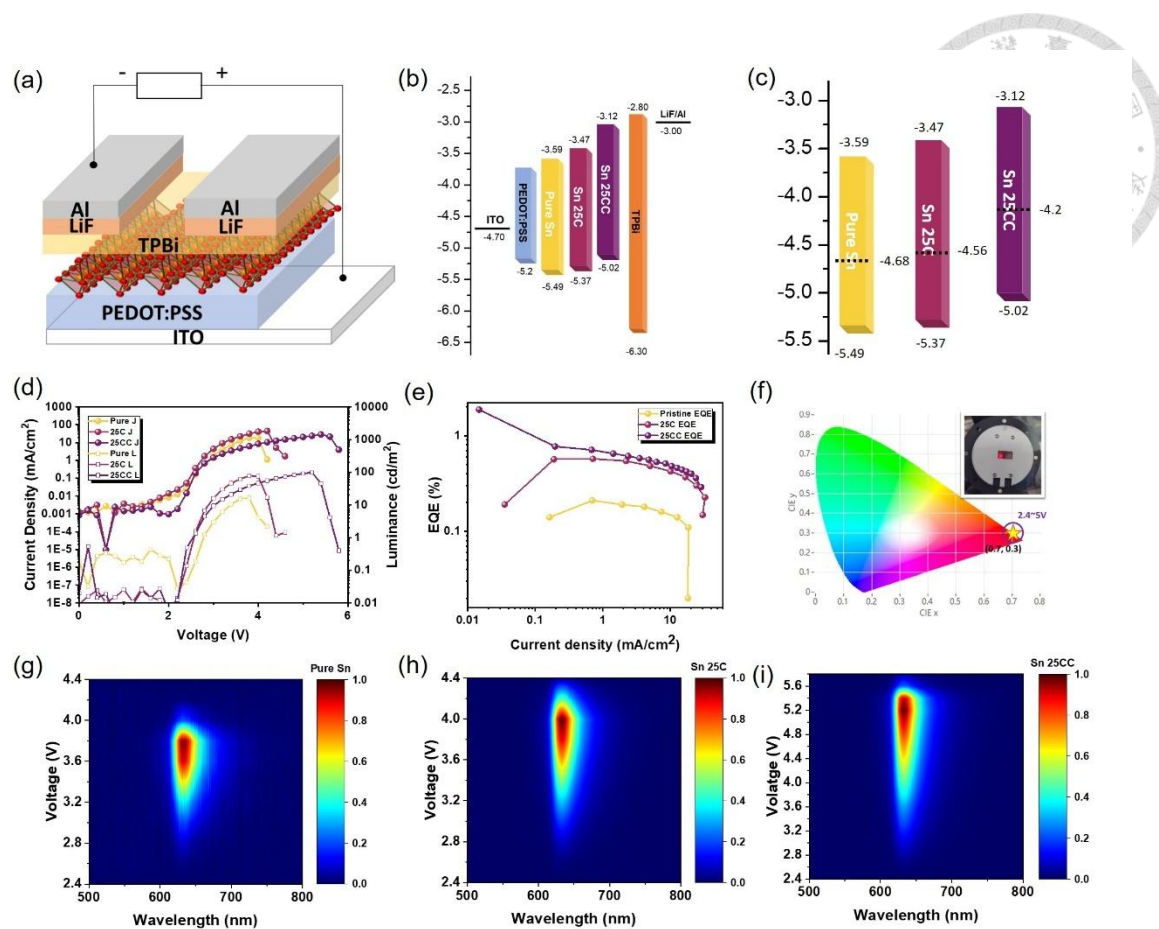


Fig. 4.11 SCLC measurements of devices based on (a) pristine, (b) 25C and (c) 25CC PEA<sub>2</sub>SnI<sub>4</sub> films. (d) EIS measurements, (e) C-V measurements, and (f) transient EL measurements of the devices based on pristine, 25C and 25CC PEA<sub>2</sub>SnI<sub>4</sub> films.



**Fig. 4.12** Transient EL results of the devices based on pristine, 25C and 25CC PEA<sub>2</sub>SnI<sub>4</sub> films.



**Fig. 4.13** (a) Schematic illustration of the device architecture and (b) corresponding energy-level diagrams for pristine, 25C (25% VitC), and 25CC (25% VitC + 18-Crown-6)  $\text{PEA}_2\text{SnI}_4$  films and their respective PeLEDs. (c) Current density–voltage–luminance (J–V–L) characteristics and (d) external quantum efficiency (EQE) versus current density curves of devices based on the three film types. (e) CIE 1931 chromaticity coordinates of the 25CC device under various applied voltages; inset: photograph of the 25CC device in operation. Electroluminescence (EL) intensity contour plots for devices incorporating (f) pristine, (g) 25C, and (h) 25CC  $\text{PEA}_2\text{SnI}_4$  emissive layers.



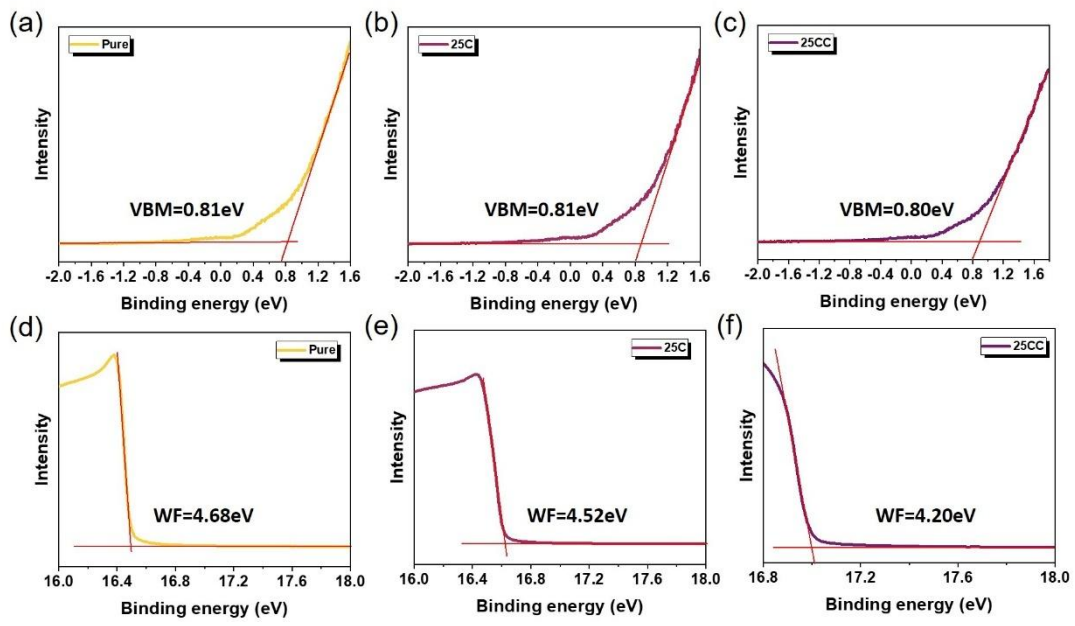


**Fig. 4.14** UPS results of (a, d) Pure, (b, e) 25C and (c, f) 25CC PEA<sub>2</sub>SnI<sub>4</sub> films.

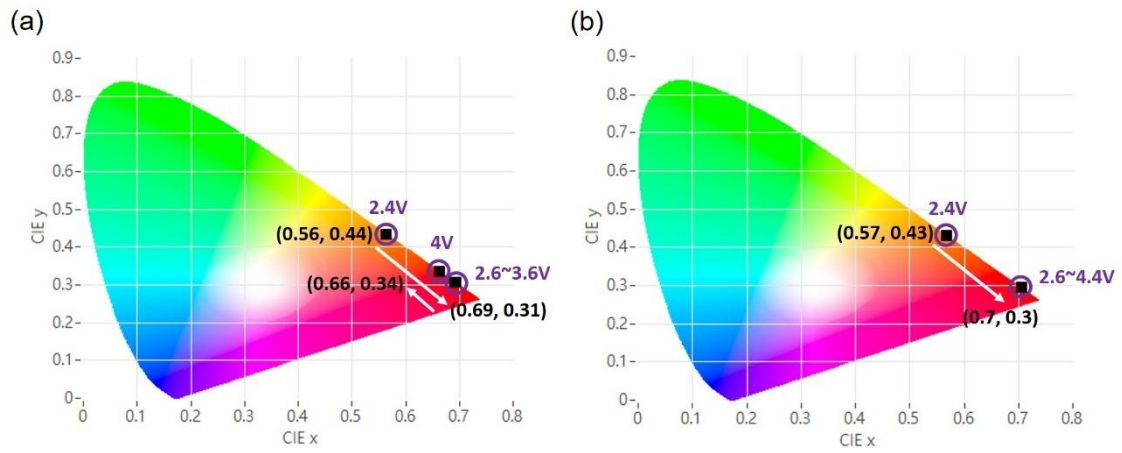


**Fig. 4.15** CIE coordinates for (a) Pure and (b) 25C devices when operating at the biases from 2.4 V to 3.6 V.

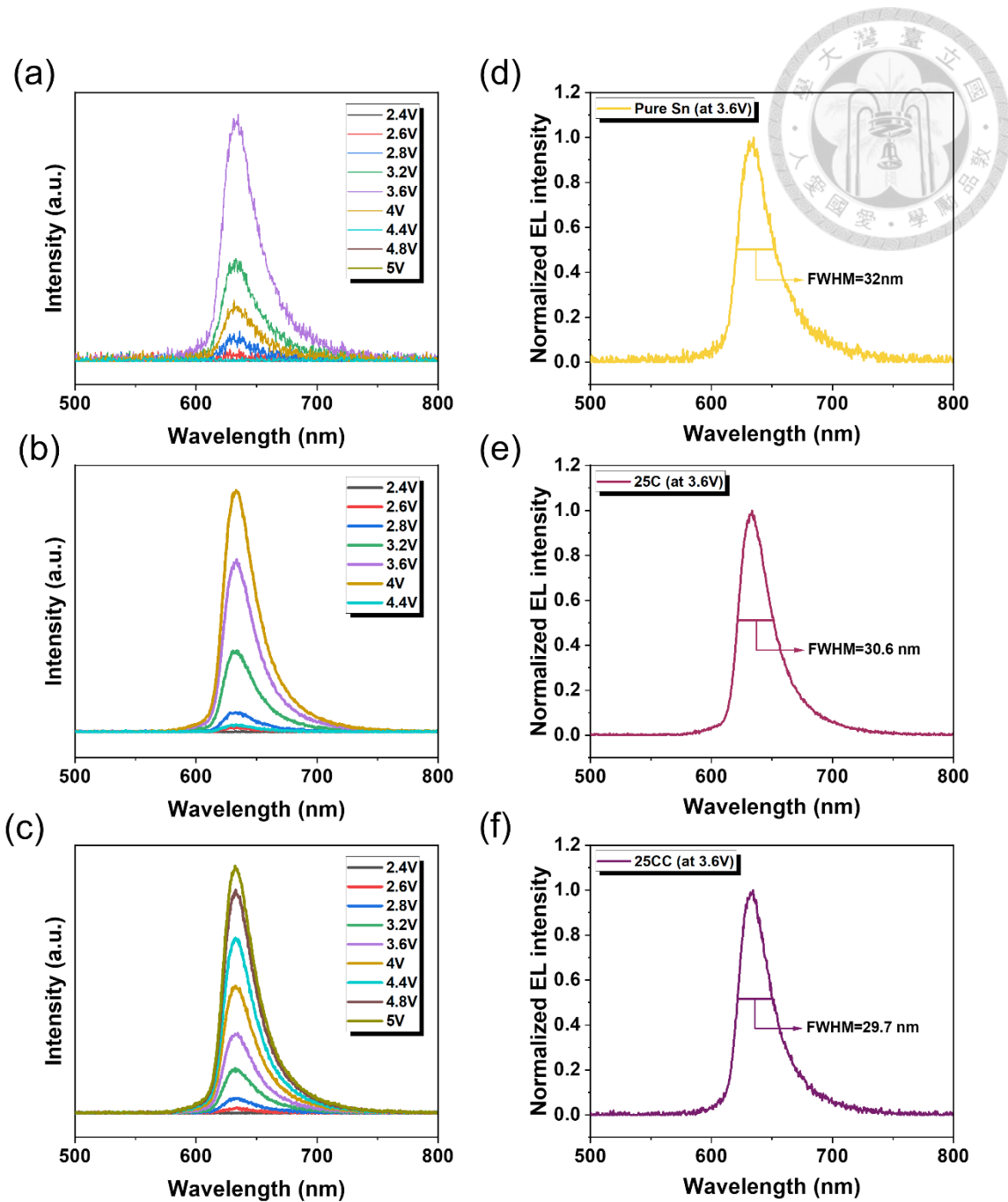


**Fig. 4.16** EL results of devices based on (a) Pure, (b) 25C and (c) 25CC PEA<sub>2</sub>SnI<sub>4</sub> films when operating at different bias voltages. EL results and the calculated FWHM values of devices based on (d) Pure, (e) 25C and (f) 25CC PEA<sub>2</sub>SnI<sub>4</sub> films when operating at 3.6 V.

## Chapter 5 Conclusion and Future Works



### 5.1 Conclusion

In these works, we systematically investigated the design, engineering, and performance optimization of perovskite light-emitting diodes (PeLEDs) based on perovskite materials with varying dimensionalities including 3D, quasi-2D, and 2D lead-free perovskites. A dimension-specific strategy was employed to address the intrinsic challenges associated with each system, thereby improving film quality, exciton dynamics, energy alignment, and overall device efficiency.

For 3D all-inorganic perovskite PeLEDs, we demonstrated that the incorporation of conjugated polymer interlayers significantly enhanced interfacial contact and hole injection, leading to improved crystallinity and suppressed leakage current. Specifically, polar-bridged pyrene-based polymers enabled superior energy-level alignment at the PEDOT:PSS/CsPbBr<sub>3</sub> interface, yielding a sixfold increase in luminance and 3.6-fold improvement in EQE compared to unmodified devices.

In the quasi-2D regime, we explored both additive and interface engineering to mitigate phase heterogeneity and efficiency roll-off. Through the incorporation of cyclic molecular additives such as  $\alpha$ - and  $\beta$ -cyclodextrins, we successfully tuned the phase distribution to suppress undesirable low-*n* domains and enhance energy funneling to high-*n* phases. Furthermore, cryptand—a 3D cage-like molecule—demonstrated strong coordination with Pb<sup>2+</sup> ions and efficient passivation, yielding a narrowed phase distribution and significantly enhanced PLQY and TRPL lifetimes. The optimized cryptand-based PeLEDs reached an EQE of 4.02%. Beyond phase regulation, we employed multifunctional phosphine oxide interfacial layers (PPT and PPF) to improve

electron injection and defect passivation. This approach elevated device brightness beyond 73,000 cd/m<sup>2</sup> and pushed EQEs above 10%, while simultaneously suppressing efficiency roll-off—representing a major step forward in quasi-2D PeLED performance.

Finally, to address lead toxicity, we investigated 2D Sn-based PeLEDs. By combining vitamin C as a reducing agent and 18-crown-6 as a cation chelator, we developed a dual-additive strategy that significantly inhibited Sn<sup>2+</sup> oxidation, reduced defect density, and enhanced film uniformity. This synergistic approach led to a near ninefold increase in EQE (from 0.21% to 1.87%) and improved device operational stability, paving the way for high-performance lead-free red PeLEDs.

Collectively, the results from this study underscore the importance of dimensionality-tailored strategies in the advancement of PeLEDs. From interface modification and additive engineering to phase regulation and trap-state passivation, our findings offer a comprehensive blueprint for the rational design of next-generation light-emitting perovskite devices.

## 5.2 Future Works

Although significant progress has been made in these works, several key directions also deserve to be further explored to drive the PeLEDs closer to their theoretical performance limits and enhance their competitiveness with OLEDs and QLEDs in next-generation display and lighting applications (**Fig. 5.1**).

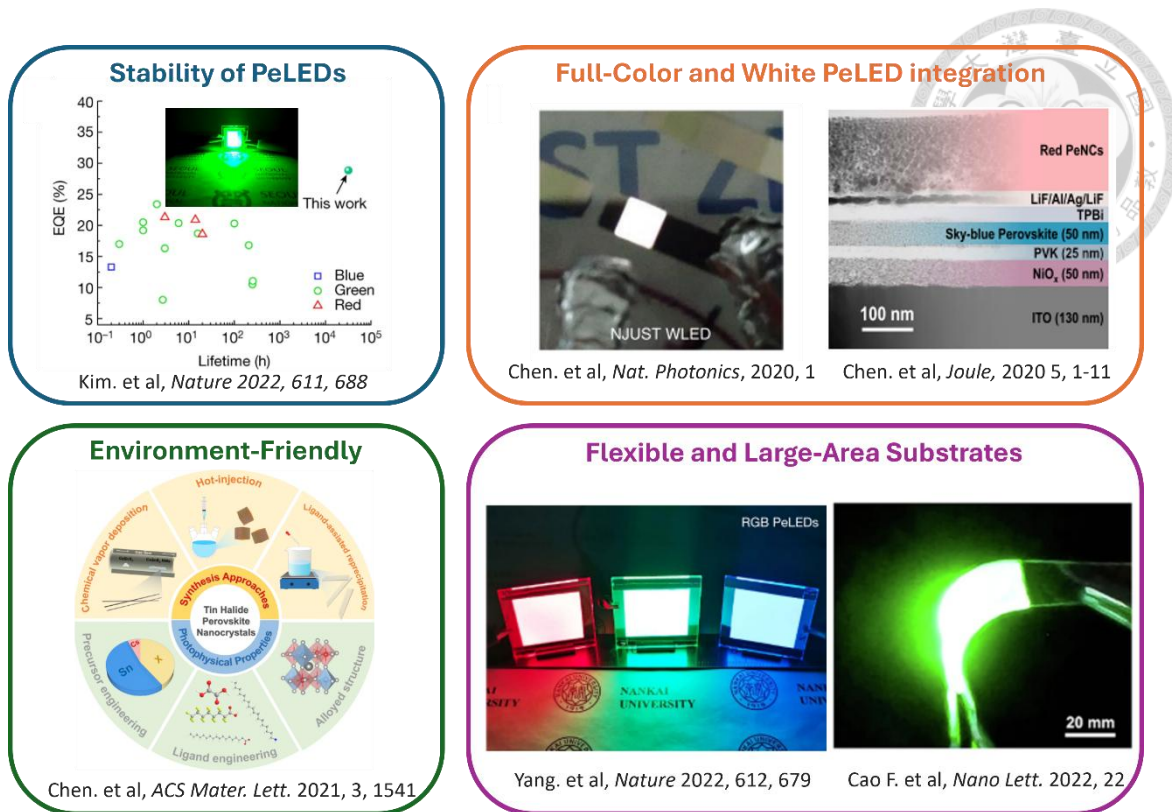
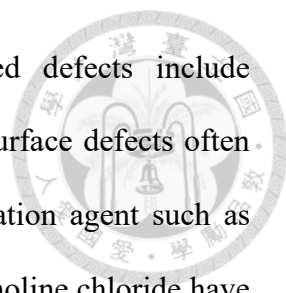


**Fig. 5.1** Future research directions for commercialized PeLEDs.

### 5.2.1 Stability of PeLEDs

Although recent advancements have significantly improved the efficiency of PeLEDs, achieving long-term operational stability remains one of the most critical challenges impeding their commercial viability. Unlike photovoltaic devices that operate under continuous illumination, PeLEDs are driven by constant electrical injection, which induces various degradation mechanisms, such as ion migration, interfacial delamination, phase segregation, and defect formation under high current densities.<sup>[63]</sup>

Future studies should thus explore several key areas such as tuning of the A-site (e.g., incorporation of sterically hindered or rigid cations), B-site (partial alloying with divalent or trivalent metals), and X-site (mixed halide systems with more robust bonding) can enhance the tolerance factor and lattice rigidity, thereby improving intrinsic structural stability.<sup>[270-274]</sup> Defect passivation is a key strategy to suppress ion migration in PeLEDs



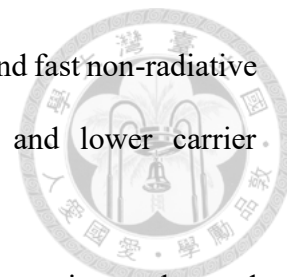
by blocking ion transport pathways. Common migration-related defects include uncoordinated ions and vacancies of halides and organic cations. Surface defects often stem from under-coordinated  $\text{Pb}^{2+}$  and halide ions. Various passivation agent such as Lewis base molecules, alkali metal ions, and charged organics like choline chloride have been shown to effectively neutralize these defects.<sup>[90, 170, 275-277]</sup> Lewis bases coordinate with  $\text{Pb}^{2+}$ , while alkali halides fill halide vacancies. These agents saturate dangling bonds and eliminate electronic trap states, reducing non-radiative recombination. Stability can also be enhanced by using more chemically and thermally stable charge transport layers. For example, replacing PEDOT:PSS with inert inorganic HTLs (e.g., NiOx) or introducing ultrathin buffer layers (e.g., MoOx, polyTPD) can mitigate interfacial reactions and reduce charge accumulation at the interface.<sup>[278-280]</sup>

Ultimately, achieving PeLED devices with an operational lifetime exceeding 1,000~10,000 hours at practical brightness levels (e.g.,  $>1,000 \text{ cd/m}^2$ ) under ambient conditions remains a key milestone. Combining materials innovation with device encapsulation, interfacial stability, and mechanistic understanding will be vital for transitioning perovskite-based LEDs from the lab to real-world applications.

### 5.2.2 Full-Color and White PeLED Integration

Realizing full-color (RGB) and white-emitting perovskite LEDs is essential for the development of next-generation display and solid-state lighting technologies. While green and red PeLEDs have achieved impressive external quantum efficiencies (EQEs), the development of stable and efficient blue PeLEDs remains a significant challenge due to several intrinsic and extrinsic factors. One of the main limitations in blue-emitting perovskites is their poor phase stability and high defect density, particularly in wide-bandgap quasi-2D systems like  $\text{PEA}_2\text{PbBr}_4$  or mixed-halide  $\text{CsPb}(\text{Cl}/\text{Br})_3$ . These

materials tend to suffer from halide segregation, exciton quenching, and fast non-radiative recombination under electrical bias. Additionally, lattice strain and lower carrier confinement reduce the radiative efficiency of blue emitters.



To overcome the challenge in blue-emitting perovskites, some strategies can be used such as compositional engineering of wide-bandgap perovskites by incorporating mixed cations (e.g., formamidinium, cesium) or passivating organic ligands can help stabilize wide-bandgap phases and reduce nonradiative losses. A fine control over quantum well thickness (n-phase distribution) in quasi-2D perovskites is also crucial to achieve high color purity and efficient exciton funneling in blue-emitting systems.<sup>[281-283]</sup> Additive engineering and robust lattice anchoring can be employed to suppress halide segregation in mixed-halide systems, which is especially critical for stable blue and white emission.

For white PeLEDs, achieving high-quality broadband emission with balanced spectral components requires precise stacking or blending of RGB emissive layers or the use of single-component perovskites with broadband emission characteristics. Several strategies can be used to fabricate perovskite white light-emitting diodes including using multilayer emissive architectures by sequentially depositing different colors of perovskite layers with optimized energy level alignment can enable white emission, although interlayer energy transfer and exciton quenching must be carefully controlled.<sup>[25, 284-286]</sup> Also, using a single-component white emitters is also a feasible way to fabricate white PeLEDs. Using 2D or quasi-2D perovskites with strong self-trapped exciton (STE) emission or dual-phase coexistence can achieve broadband white emission with simpler device architectures.<sup>[226]</sup> Last but not least, a strategy of using a hybrid emitters and down-conversion layers is also feasible by combining perovskite LEDs with down-conversion phosphor or commercial LED chips can also enable white emission.<sup>[287, 288]</sup>

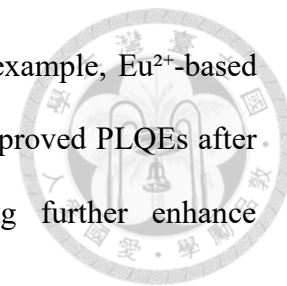
### 5.2.3 Exploration of Environment-Friendly Materials for PeLEDs

The environmental and health concerns associated with lead-based perovskites have spurred extensive research into alternative, eco-friendly materials for PeLEDs. Exploring such materials is crucial for sustainable and safe optoelectronic applications. While Sn-based perovskites offer a lead-free pathway, challenges related to oxidation and low PLQY persist. Further work is needed to investigate other B-site elements (e.g., Bi<sup>3+</sup>, Sb<sup>3+</sup>, Ge<sup>2+</sup>) and mixed-valence strategies to develop high-performance, eco-friendly perovskite emitters.

As for tin-based perovskites are promising lead-free alternatives due to their similar electronic configurations. Tin-based perovskites have direct and tunable bandgaps, emitting from visible to near-infrared (NIR-II). These materials offer good conductivity but suffer from Sn<sup>2+</sup> oxidation, self-doping, and defect formation. Strategies like using 2D structures and organic spacer cations can improve crystallinity and stability. 2D Sn-based perovskites, like PEA<sub>2</sub>SnI<sub>4</sub>, show strong red emission and improved PLQEs up to 60%. Tin-based materials enable efficient red PeLEDs without halide mixing, avoiding phase separation. As for germanium-based perovskites, they are non-toxic and exhibit strong NLO (nonlinear optical) properties.<sup>[289]</sup> Bandgaps are highly tunable with A-site cation selection (e.g., FA<sup>+</sup> vs. Cs<sup>+</sup>).<sup>[290]</sup> Ge<sup>2+</sup> suffers from oxidation but can form a passivating oxide layer, improving film stability. Ge inclusion in Sn-based systems can also reduce Sn oxidation and improves device lifetimes.<sup>[291]</sup> Lead-free double perovskites (e.g., Cs<sub>2</sub>AgBiBr<sub>6</sub>, Cs<sub>2</sub>Ag<sub>0.6</sub>Na<sub>0.4</sub>InCl<sub>6</sub>) are structurally stable and allow for diverse cation combinations.<sup>[292, 293]</sup> Their broad emissions come from self-trapped excitons (STEs), but most have low PLQEs. Doping (e.g., with Bi<sup>3+</sup> or Sb<sup>3+</sup>) significantly improves emission and thermal stability.<sup>[293]</sup> Some doped systems achieved PLQEs over 85% and ultrabroadband white emission. Other rare-earth-based perovskites (e.g., CsEuCl<sub>3</sub>,



CsYbI<sub>3</sub>) also show sharp emissions and high stability.<sup>[231, 294]</sup> For example, Eu<sup>2+</sup>-based materials emit blue or red light depending on composition, with improved PLQEs after doping. Techniques like thermal evaporation and Ni<sup>2+</sup> doping further enhance luminescence and structural stability.<sup>[295]</sup>



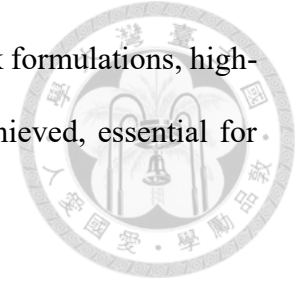
#### 5.2.4 Integration with Flexible and Large-Area Substrates

The integration of perovskite light-emitting diodes (PeLEDs) with flexible and large-area substrates is pivotal for the advancement of next-generation optoelectronic devices, including wearable electronics, foldable displays, and large-scale lighting panels. Recent research has focused on developing materials and fabrication techniques to achieve high-performance, mechanically robust, and scalable PeLEDs.<sup>[296, 297]</sup>

As for flexible substrate integration, material selection of flexible substrates is important such as polyethylene terephthalate (PET), polyimide (PI), and ultrathin glass are potential candidates due to their mechanical flexibility and thermal stability.<sup>[298, 299]</sup> In addition, the surface modification of perovskite to enhance perovskite film formation on flexible substrates is also important. Surface treatments like the application of branched polyethylenimine (PEI) have been utilized. PEI modifies the substrate surface energy, promoting uniform perovskite crystallization and reducing defect densities, leading to improved device performance.

As for the fabrication of large-area PeLED, inkjet printing has emerged as a promising technique for fabricating large-area PeLEDs.<sup>[300]</sup> This method allows for precise deposition of perovskite inks, enabling uniform film formation over extensive areas. Liu et al. demonstrated large-area (28 cm<sup>2</sup>) red PeLEDs on flexible substrates using inkjet printing, achieving an external quantum efficiency (EQE) of 14.3%.<sup>[300]</sup> Blade coating are also techniques being employed to produce uniform perovskite layers over

large substrates.<sup>[301, 302]</sup> By optimizing the coating parameters and ink formulations, high-quality films with controlled thickness and morphology can be achieved, essential for consistent device performance across large areas.



## Chapter 6 (Appendix) Perovskite Tandem Solar Cells

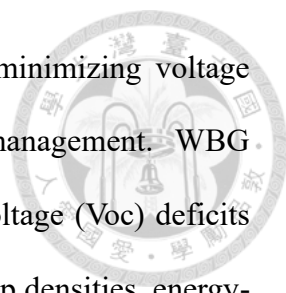


### 6.1 Optimization of ALD SnO<sub>2</sub> in All-Perovskite Tandem Solar Cells

This appendix records the experimental work conducted during my research exchange in Professor Edward Sargent's group at Northwestern University from May 2024 to June 2025. During this period, my research focused on the fabrication of all-perovskite tandem solar cells and perovskite/organic tandem solar cells (PO-TSCs). I would like to express my sincere gratitude to the National Science and Technology Council (NSTC) for providing the scholarship that supported this exchange program. Special thanks to Professor Edward Sargent (Ted) and Dr. Bin for their invaluable guidance and unwavering support throughout the year.

#### 6.1.1 Introduction

All-perovskite tandem solar cells (TSCs) have emerged as an attractive photovoltaic technology, promising to exceed the theoretical efficiency limits imposed by single-junction solar cells by effectively utilizing a broader portion of the solar spectrum. Recently, perovskite materials have gained attention due to their tunable bandgaps, high absorption coefficients, and cost-effective solution-based processing methods, enabling power conversion efficiencies (PCE) above 25% in single-junction configurations. Despite these advancements, substantial challenges related to efficiency and stability remain, particularly regarding the wide-bandgap (WBG, approximately 1.75–1.8 eV) and narrow-bandgap (NBG, approximately 1.2–1.3 eV) perovskite materials.

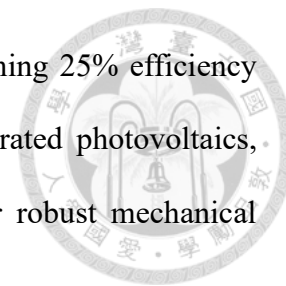


The efficiency of all-perovskite TSCs critically depends on minimizing voltage losses, enhancing interfacial quality, and optimizing carrier management. WBG perovskite subcells commonly encounter significant open-circuit voltage ( $V_{oc}$ ) deficits and reduced fill factors (FF), issues that primarily stem from high trap densities, energy-level mismatches at charge-selective interfaces, and interfacial recombination losses. Recent strategies to mitigate these challenges involve the introduction of self-assembled monolayers (SAMs) as hole-selective contacts, particularly those derived from carbazole-based molecules with phosphonic acid anchoring groups, which effectively reduce interfacial non-radiative recombination and improve hole extraction. Such molecular engineering techniques have successfully enhanced  $V_{oc}$  and FF, enabling certified efficiencies beyond 26% for large-area ( $>1 \text{ cm}^2$ ) tandem cells.

Conversely, the performance of NBG perovskite subcells, typically composed of Sn–Pb mixed perovskites, is hindered by rapid oxidation of  $\text{Sn}^{2+}$  ions to  $\text{Sn}^{4+}$ , high intrinsic carrier densities, and defects in film morphology, leading to limited carrier lifetimes and compromised stability. To address these challenges, strategies including the incorporation of two-dimensional (2D) perovskite additives and diammonium molecular passivation have been developed. Notably, quasi-2D perovskite structures containing phenethylammonium (PEA) and guanidinium (GA) cations have effectively reduced defect densities and significantly increased carrier lifetimes. Additionally, molecular dynamics-informed passivation approaches utilizing fluorinated aromatic ammonium cations have shown enhanced binding affinity to perovskite surfaces, improving carrier diffusion lengths and enabling thicker absorber layers.

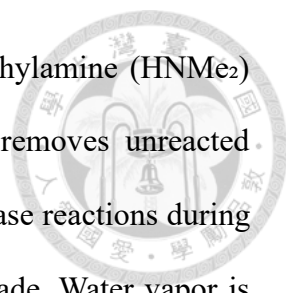
Recent achievements include the demonstration of certified PCEs up to 28.1% in small-area all-perovskite TSCs and over 26% in larger-area devices, accompanied by substantially improved operational stability under continuous illumination and ambient

conditions. Moreover, flexible all-perovskite tandem cells approaching 25% efficiency have shown significant promise for applications in building-integrated photovoltaics, wearable electronics, and portable power systems, owing to their robust mechanical durability.



However, besides the importance of building up a high performance of all-perovskite TSC by improving the performance of WBG and NBG perovskite subcells, the quality of the interconnecting layer also plays a key role in the device structure of all-perovskite TSCs. Therefore, the deposition conditions of SnO<sub>2</sub> play a critical role in the fabrication of tandem perovskite solar cells, particularly because the SnO<sub>2</sub> layer often functions as both the electron transport layer (ETL) and a protective barrier during the sequential processing of top and bottom cells. Atomic Layer Deposition (ALD) is a widely adopted method for fabricating high-quality SnO<sub>2</sub> thin films due to its precision in thickness control, excellent conformality, and low-temperature processability.

Beyond optimizing WBG and NBG perovskite subcells, the interconnecting layer quality is also crucial for all-perovskite TSC performance. SnO<sub>2</sub> is widely used in TSCs as both an electron transport layer (ETL) and a protective barrier. Atomic Layer Deposition (ALD), noted for its exceptional thickness precision, conformality, and low-temperature compatibility, is a preferred method for fabricating SnO<sub>2</sub> films. According to the detailed ALD mechanism for SnO<sub>2</sub> formation which is illustrated in **Fig. 6.1**, several steps are included to form layer by layer of SnO<sub>2</sub>. First of all, the hydroxylated surface preparation, the ALD process begins with a substrate surface terminated by hydroxyl groups (–OH), typically achieved through pre-treatment or exposure to humid air. These –OH groups serve as reactive sites for precursor chemisorption. Second, there is the tin precursor pulse. Upon pulsing the organotin precursor, tetrakis(dimethylamino)tin [Sn(NMe<sub>2</sub>)<sub>4</sub>], allows it to chemisorb onto the –OH-terminated surface. A ligand-exchange

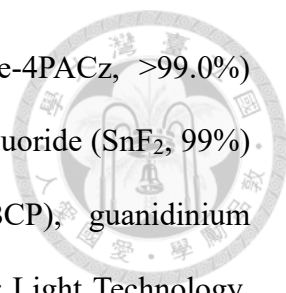


reaction occurs, anchoring Sn atoms while releasing volatile dimethylamine ( $\text{HNMe}_2$ ) byproducts. Third, is the purging step, a subsequent purge step removes unreacted  $\text{Sn}(\text{NMe}_2)_4$  and the byproducts from the chamber, preventing gas-phase reactions during the next precursor pulse. Then, the oxidant ( $\text{H}_2\text{O}$ ) pulse is being made. Water vapor is introduced, reacting with the surface-bound tin complexes to form Sn–O bonds while regenerating –OH surface terminations, enabling the continuation of the layer-by-layer growth process. Last but not least, final purge and cycle Completion, a second purge clears excess  $\text{H}_2\text{O}$  and reaction byproducts, concluding one ALD cycle and preparing the surface for the next  $\text{Sn}(\text{NMe}_2)_4$  pulse. Repetition of this cycle builds up a uniform  $\text{SnO}_2$  film with precise thickness control. This self-limiting, sequential process ensures conformal and uniform  $\text{SnO}_2$  deposition with atomic-scale thickness precision, crucial for applications in perovskite tandem solar cells where interface quality and film uniformity directly influence device performance.

In this work, optimizing critical ALD parameters such as the Sn/O ratio, purge durations, and chamber temperature has been done to significantly elevate the baseline performance of all-perovskite TSCs to approximately 28%, establishing a solid foundation for further advancements in this promising research field for the group.

### 6.1.2 Experimental Section

**Materials.** Formamidinium bromide (FABr, >99.99%), Formamidinium iodide (FAI, >99.99%), methylammonium iodide (MAI, >99.99%), methylammonium chloride (MACl, >99.99%) and 4-fluoro-phenethylammonium bromide (4F-PEABr) were purchased from Greatcell Solar Materials. Lead halide precursors, including lead(II) iodide ( $\text{PbI}_2$ , 99.999%), lead(II) bromide ( $\text{PbBr}_2$ , 99.999%), and lead(II) chloride ( $\text{PbCl}_2$ , 99.999%), as well as cesium bromide ( $\text{CsBr}$ , 99.999%) and cesium iodide ( $\text{CsI}$ , 99.999%)

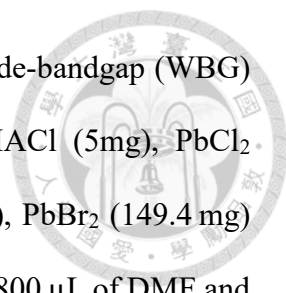


and [4-(3,6-Dimethyl-9H-carbazol-9-yl)butyl]phosphonic acid (Me-4PACz, >99.0%) were obtained from TCI Chemicals. Tin iodide ( $\text{SnI}_2$ , 99.99%), tin fluoride ( $\text{SnF}_2$ , 99%) were purchased from Sigma-Aldrich. C60, bathocuproine (BCP), guanidinium thiocyanate (GuaSCN,  $\geq 99\%$ ) were purchased from Xi'an Polymer Light Technology. The 1,3-propane diammonium diiodide ( $\text{PDAI}_2$ , >99.5%) was purchased from Luminescence Technology Corp.

1,2-Diaminopropane (DAP, 99%), dimethyl sulfoxide (DMSO,  $\geq 99.9\%$ ), anisole (99.7%), chlorobenzene (CB,  $\geq 99.5\%$ ), isopropanol (IPA,  $\geq 99.5\%$ ), toluene (99.8%), and dimethylformamide (DMF,  $\geq 99.5\%$ ) were obtained from Sigma-Aldrich. The nickel oxide (NiOx) nanoparticle dispersion was sourced from Avantama. Poly(3,4-ethylenedioxythiophene):polystyrene sulfonate (PEDOT:PSS, A1-4083) was acquired from Ossila. Tetrakis(dimethylamino)tin(IV) (50-1815 Tin, 99.99% Sn) was supplied by Strem Chemicals. Indium tin oxide (ITO) coated glass substrates with a sheet resistance of  $15 \Omega/\text{sq}$  and dimensions of  $25 \text{ mm} \times 25 \text{ mm}$  were purchased from Suzhou ShangYang Solar Technology Co. Metallic copper, silver, and gold were obtained from Kurt J. Lesker.

### Preparation of perovskite solutions

**Narrow-bandgap (NBG) perovskite solution.** To prepare the narrow-bandgap (NBG) perovskite precursor solution (1.8 M,  $\text{Cs}_{0.05}\text{FA}_{0.7}\text{MA}_{0.25}\text{Sn}_{0.5}\text{Pb}_{0.5}\text{I}_3$ ), CsI (23.4 mg), FAI (216.7 mg), MAI (71.55 mg),  $\text{SnI}_2$  (335.3 mg), and  $\text{PbI}_2$  (414.9 mg) were dissolved in a solvent mixture comprising  $750 \mu\text{L}$  of DMF and  $250 \mu\text{L}$  of DMSO. The resulting solution was further supplemented with additives such as guanidinium thiocyanate (GuaSCN, 4 mg), tin(II) fluoride ( $\text{SnF}_2$ , 14.1 mg), and 4-fluorophenylethylammonium bromide (4F-PEABr, 1.5 mg).



**Wide-bandgap (WBG) perovskite solution** To prepare the wide-bandgap (WBG) perovskite precursor solution (1.1 M,  $\text{FA}_{0.8}\text{Cs}_{0.2}\text{Pb}(\text{I}_{0.62}\text{Br}_{0.38})_3$ ),  $\text{MACl}$  (5mg),  $\text{PbCl}_2$  (15mg),  $\text{CsBr}$  (18.7 mg),  $\text{CsI}$  (34.3 mg),  $\text{FABr}$  (44 mg),  $\text{FAI}$  (91 mg),  $\text{PbBr}_2$  (149.4 mg) and  $\text{PbI}_2$  (319.5 mg) were dissolved in a solvent mixture comprising 800  $\mu\text{L}$  of DMF and 200  $\mu\text{L}$  of DMSO.

**Post-treatment and hole transport material solutions** DAP was prepared at a concentration of 0.25  $\mu\text{L}/\text{mL}$  in chlorobenzene (CB).  $\text{PDAI}_2$  was dissolved at 1 mg/mL in a mixed solvent system of isopropanol (IPA) and CB with a volume ratio of 2:1. The  $\text{NiOx}$  nanoparticle dispersion was diluted to 0.025 wt% using ethanol. Me-4PACz was also dissolved in ethanol at a concentration of 0.3 mg/mL. All perovskite precursor solutions were stirred magnetically at ambient temperature without any heating treatment. Prior to use, the solutions were passed through a 0.22  $\mu\text{m}$  polytetrafluoroethylene (PTFE) membrane filter to ensure purity and remove particulates.

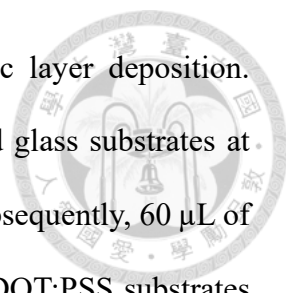
### **Device Fabrication.**

Pre-patterned ITO-coated glass substrates were sequentially cleaned by ultrasonication with detergent, deionized water, acetone, and isopropanol for 15min, respectively. Before fabricating thin films, these ITO-coated glass substrates were cleaned by using UV-ozone cleaner for 15 minutes.

### **Narrow-bandgap (NBG) perovskite single junction solar cells**

The narrow-bandgap (NBG) perovskite solar cells were fabricated using the device structure glass/ITO/PEDOT:PSS/ $\text{Cs}_{0.05}\text{FA}_{0.7}\text{MA}_{0.25}\text{Sn}_{0.5}\text{Pb}_{0.5}\text{I}_3/\text{C}_{60}/\text{ALD-SnO}_2/\text{Ag}$ . In this configuration, ITO refers to indium tin oxide, PEDOT:PSS to poly(3,4-

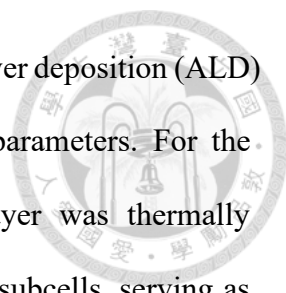




ethylenedioxythiophene):polystyrene sulfonate, and ALD to atomic layer deposition. Initially, PEDOT:PSS was spin-coated onto pre-cleaned ITO-coated glass substrates at 4,000 rpm for 25 s, followed by drying at 150 °C for 20 minutes. Subsequently, 60  $\mu\text{L}$  of the perovskite precursor solution was spin-coated onto the ITO/PEDOT:PSS substrates inside a nitrogen-filled glovebox at 1,000 rpm for 10 s and then 3,800 rpm for 40 s. At 30 s into the spin-coating process, 250  $\mu\text{L}$  of chlorobenzene was dispensed dropwise onto the spinning substrate to induce crystallization. The resulting perovskite films were annealed at 96 °C for 10 minutes. Following this, 150  $\mu\text{L}$  of a diamine solution was deposited via spin-coating at 4,000 rpm for 25 s, and then thermally treated at 100 °C for 5 minutes. A  $\sim 27$  nm  $\text{C}_{60}$  layer was deposited by thermal evaporation at a rate of 0.2  $\text{\AA}/\text{s}$  as the electron transport layer. This was followed by the deposition of a  $\sim 20$  nm  $\text{SnO}_2$  layer via atomic layer deposition (ALD) under varied processing conditions. Finally, silver electrodes were deposited through a shadow mask by thermal evaporation under high vacuum to define the device's active area.

### **Wide-bandgap perovskite solar cells and all-perovskite tandem solar cells**

A NiOx hole transport layer was deposited by spin coating at 4000 rpm for 25 seconds and used directly without additional thermal treatment. Once transferred into a nitrogen-filled glovebox, a self-assembled monolayer (SAM) of Me-4PACz was applied onto the NiOx layer via spin coating at 4000 rpm for 25 seconds, followed by annealing at 100 °C for 10 minutes. Perovskite precursor solutions (60  $\mu\text{L}$ ) were then spin-coated at 4000 rpm for 30 seconds. During the spin-coating process, 150  $\mu\text{L}$  of anisole was added dropwise onto the substrate at the 25-second mark to aid crystallization. The resulting perovskite films were subsequently annealed at 100 °C for 15 minutes. The deposition of the  $\text{C}_{60}$  electron transport layer and metal electrodes was carried out using the same

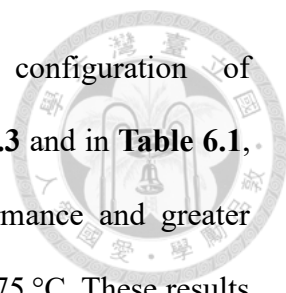


method as for the NBG perovskite solar cells. However, the atomic layer deposition (ALD) conditions for the SnO<sub>2</sub> layer were adjusted by varying process parameters. For the fabrication of all-perovskite tandem solar cells, a 1 nm gold layer was thermally evaporated onto the appropriately thick SnO<sub>2</sub>-coated wide-bandgap subcells, serving as the recombination layer. The NBG subcell was then constructed on top using the same procedure described above. Finally, 140 nm of silver was deposited by thermal evaporation to form the top electrode for performance evaluation.

### 6.1.3 Results and Discussion

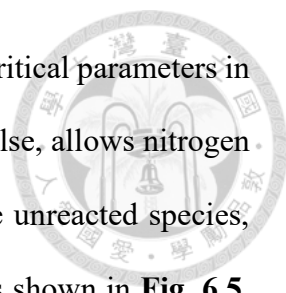
As introduced in the previous section, the ALD SnO<sub>2</sub> process involves a sequence of self-limiting surface reactions designed to produce high-quality SnO<sub>2</sub> thin films. The quality of the resulting films is highly sensitive to several key deposition parameters, all of which can be precisely adjusted through the operation interface, as illustrated in **Fig. 6.2**. As shown in **Fig. 6.2**, parameters such as chamber temperature, precursor pulse durations, purge times, and cycle number must be systematically optimized to ensure conformal film growth, minimal defect density, and favorable interfacial properties for integration in tandem perovskite solar cells.

First of all, the chamber temperature (heater, outer ring and inner ring) are being considered. The temperature must be optimized to ensure good film crystallinity and reduce defect density. While higher temperatures generally yield better SnO<sub>2</sub> quality, they risk damaging thermally sensitive perovskite layers. Therefore, a trade-off must be considered between the quality of the SnO<sub>2</sub> and the quality of perovskites. For instance, the standard ALD deposition temperature is typically set at 90 °C. However, this temperature is excessively high for PbSn perovskite, a narrow-bandgap material known for its high sensitivity to thermal stress. Therefore, we fabricate a batch of NBG



perovskite single junction solar cells with the device configuration ITO/PEDOT:PSS/PbSn perovskite/C<sub>60</sub>/SnO<sub>2</sub>/Ag. As shown in **Fig. 6.3** and in **Table 6.1**, devices utilizing ALD-grown SnO<sub>2</sub> at 90 °C exhibit lower performance and greater variability compared to those fabricated at a reduced temperature of 75 °C. These results highlight the critical importance of carefully optimizing the ALD chamber temperature, particularly when working with thermally sensitive perovskite compositions.

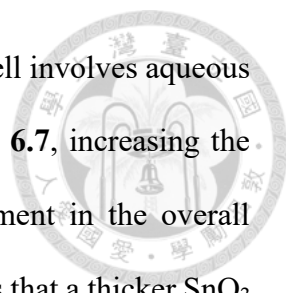
Second, the precursor pulse times (Sn source and H<sub>2</sub>O) are being considered. Adjusting the pulse durations directly affects the Sn-to-O ratio in the final film. A longer Sn precursor pulse relative to H<sub>2</sub>O can produce oxygen-deficient SnO<sub>2</sub>, increasing oxygen vacancy concentration. These vacancies act as shallow donor states, improving electron conductivity. However, excessive oxygen deficiency can lead to charge imbalance and increased trap states, negatively impacting device performance. Due to the inherent differences in conductivity and optoelectronic properties among perovskites with varying bandgaps, the optimal ALD SnO<sub>2</sub> deposition conditions must be tailored accordingly. As such, further experimental optimization is necessary for each bandgap category. To address this, a series of experiments were conducted, and the results are presented in **Fig. 6.4**. The data clearly indicate that each perovskite bandgap requires distinct ALD SnO<sub>2</sub> parameters to achieve optimal device performance. For example, in the case of the 1.78 eV perovskite, which is commonly employed as the top cell in all-perovskite tandem solar cells, the optimal ALD conditions were found to be a water pulse time of 0.015 s and a Sn precursor pulse time of 0.1 s. In contrast, for a wider-bandgap perovskite with a bandgap of 1.88 eV, typically used in perovskite/organic tandem solar cells, the optimal conditions shifted to a water pulse time of 0.015 s and a Sn pulse time of 0.5 s. These findings underscore the critical importance of bandgap-specific optimization of the ALD SnO<sub>2</sub> process to ensure proper interface formation and maximize device efficiency.



Third, the purge time and vacuum pumping efficiency are also critical parameters in the ALD process. The purging step, which follows each precursor pulse, allows nitrogen gas to distribute the precursors throughout the chamber and remove unreacted species, while the vacuum pump helps re-establish a stable base pressure. As shown in **Fig. 6.5**, the use of a more powerful pump significantly reduces the chamber's base pressure from 0.25 torr to 0.18 torr, demonstrating improved evacuation efficiency. This enhancement allows for shorter purge durations, thereby enabling faster ALD cycling and promoting better film uniformity.

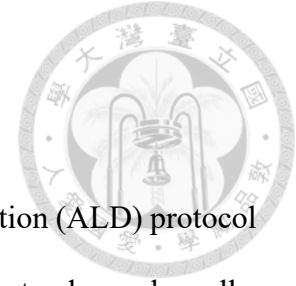
However, excessively long purge times can be detrimental; prolonged exposure may lead to partial desorption of the already-formed SnO<sub>2</sub> layer and extended thermal stress on the perovskite films, which are sensitive to high-temperature environments. To investigate the optimal purge time, we used an all-perovskite tandem solar cell architecture as the test platform, as illustrated in **Fig. 6.6a**. The corresponding device performance results in **Fig. 6.6b** show that purge time significantly affects the efficiency of the tandem cells. Specifically, reducing the purge time led to notable improvements in device performance, highlighting the importance of carefully optimizing this parameter to balance complete precursor removal with minimal thermal degradation of the perovskite layers.

Last but not least, the number of ALD cycles plays a key role in determining the thickness of the SnO<sub>2</sub> film. In single-junction perovskite solar cells, an excessively thick SnO<sub>2</sub> layer can lead to increased series resistance due to the inherently lower conductivity of SnO<sub>2</sub> compared to other transport layers, ultimately compromising device performance. In contrast, tandem solar cell, particularly all-perovskite architectures, require a thicker SnO<sub>2</sub> layer not only for efficient electron transport but also as a protective interlayer during the bottom-cell fabrication process. This protective function is essential, as the



deposition of the hole transport layer (PEDOT:PSS) for the bottom cell involves aqueous solvents that can damage the underlying top cell. As shown in **Fig. 6.7**, increasing the ALD cycle number from 140 to 600 leads to a marked improvement in the overall performance of all-perovskite tandem solar cells. This result indicates that a thicker SnO<sub>2</sub> interconnect layer offers more robust protection to the top cell, effectively preventing solvent-induced damage during the subsequent processing steps. Therefore, while there is a trade-off between minimizing resistive losses and ensuring structural protection, these findings highlight the critical role of SnO<sub>2</sub> thickness optimization in achieving high-performance tandem devices.

In summary, precise control over ALD parameters, including chamber temperature, precursor pulse and purge durations, and cycle number, is crucial for engineering SnO<sub>2</sub> films with optimal stoichiometry, thickness, and functional properties. These parameters collectively influence charge transport, interfacial quality, and the overall structural integrity of tandem perovskite solar cells. By further optimizing the SnO<sub>2</sub> layer in terms of thickness, deposition temperature, and Sn/O ratio, a 1.78 eV wide-bandgap (WBG) perovskite single-junction solar cell with the architecture ITO/NiO<sub>x</sub>/Me-4PACz/1.78 eV WBG perovskite/C<sub>60</sub>/SnO<sub>2</sub>/Ag achieves excellent performance, delivering a power conversion efficiency (PCE) of 20.35%, an open-circuit voltage (Voc) of 1.339 V, a short-circuit current density (Jsc) of 17.86 mA cm<sup>-2</sup>, and an outstanding fill factor (FF) of 85.81%, with high device reproducibility (**Fig. 6.8 & Table 6.2**). Meanwhile, all-perovskite tandem solar cells employing the configuration ITO/NiO<sub>x</sub>/Me-4PACz/1.78 eV WBG perovskite/C<sub>60</sub>/SnO<sub>2</sub>/Au/PEDOT:PSS/1.25 eV NBG perovskite/C<sub>60</sub>/BCP/Ag fabricated under optimized SnO<sub>2</sub> processing conditions achieve a champion PCE of 27.91%, with a high Voc of 2.112 V, a Jsc of 16.23 mA cm<sup>-2</sup>, and an impressive FF of 83.03%. (**Table 6.3**)



#### 6.1.4 Summary and Future works

This study successfully established a robust atomic layer deposition (ALD) protocol for SnO<sub>2</sub> tailored to the fabrication of high-performance all-perovskite tandem solar cells. Key process parameters, including chamber temperature, precursor pulse duration, and purge times, were systematically optimized to yield high-quality SnO<sub>2</sub> films. These efforts enabled the realization of tandem devices with efficiencies comparable to internationally leading benchmarks. Notably, due to significant differences between the ALD systems used at Northwestern University and those previously employed at the University of Toronto, it was necessary to re-establish a new baseline through extensive parameter tuning. Through this optimization, I successfully implemented a reproducible high-efficiency tandem device architecture within the Sargent group at Northwestern. As shown in **Fig. 6.9**, the resulting device performance closely parallels that of previously optimized counterparts and is competitive with state-of-the-art results in the literature. This newly established baseline provides both valuable experience and a strategic foundation for the future development of triple-junction all-perovskite tandem solar cells in the Sargent group.

To further enhance device stability, attention must also be directed toward the interconnecting layer (ICL). While gold (Au) is widely used as an ICL for efficient charge recombination, it suffers from metal diffusion issues that compromise long-term stability. Replacing Au with conductive metal oxides such as indium tin oxide (ITO) or indium zinc oxide (IZO) presents a promising alternative to mitigate this diffusion problem and also improve the optical loss problem. Furthermore, a transition from Au to metal oxides opens opportunities to replace conventional organic hole-transport layers like

PEDOT:PSS with self-assembled monolayers (SAMs) in the PbSn NBG subcell, further enhancing device stability.

Based on this rationale, I explored the incorporation of ITO nanoparticles as a replacement for ICL.<sup>[303]</sup> Initial optimization was conducted using the structure of ITO glass/ITO nanoparticle/co-SAMs (MeO+Me4)/1.25 eV NBG perovskite/C<sub>60</sub>/BCP/Ag. Various surface treatments were investigated, including UV-ozone, IPA rinse, and DMF solvent treatment to improve the ITO nanoparticle film quality obtained via spin coating. As shown in **Fig. 6.10a-d**, the DMF-treated ITO surface yielded the best device performance and reproducibility. Compared to PEDOT:PSS-based devices, this approach demonstrated competitive performance and improved light absorption in the 450–700 nm range, as seen in EQE spectra in **Fig. 6.11**, suggesting reduced parasitic absorption due to the absence of PEDOT:PSS. Following this validation, I integrated the ITO nanoparticle layer into all-perovskite tandem devices. Results indicate that increasing the concentration of ITO nanoparticles enhances device performance, with EQE curves showing reduced leakage current in the top cell (**Fig. 6.12 & Fig. 6.13**). Although the overall performance remains slightly lower than those achieved with PEDOT:PSS, the ITO nanoparticle-based architecture offers significant promise for future development, especially in the context of device stability and scalable fabrication.

### 6.1.5 Tables and Figures



**Table 6.1** Performance of NBG perovskite solar cells with different chamber temperatures but in same batch.

	<b>Voc (V)</b> <b>(AVG)</b>	<b>Jsc (mA/cm<sup>2</sup>)</b> <b>(AVG)</b>	<b>FF (%)</b> <b>(AVG)</b>	<b>PCE (%)</b> <b>(AVG)</b>
<b>90°C</b>	0.854 (0.823)	30.53 (26.75)	69.67 (58.46)	17.98 (13.07)
<b>75°C</b>	0.839 (0.833)	31.83 (30.22)	68.24 (64.58)	17.95 (16.27)

**Table 6.2** Performance of 1.78eV WBG perovskite solar cells with optimized ALD conditions.

	<b>Voc (V)</b> <b>(AVG)</b>	<b>Jsc (mA/cm<sup>2</sup>)</b> <b>(AVG)</b>	<b>FF (%)</b> <b>(AVG)</b>	<b>PCE (%)</b> <b>(AVG)</b>
<b>1.78eV</b>	1.339 (1.326)	17.86 (17.73)	85.81 (84.84)	20.35 (19.95)

**Table 6.3** Performance of all-perovskite tandem solar cells with optimized ALD conditions.

	<b>Voc (V)</b> <b>(AVG)</b>	<b>Jsc (mA/cm<sup>2</sup>)</b> <b>(AVG)</b>	<b>FF (%)</b> <b>(AVG)</b>	<b>PCE (%)</b> <b>(AVG)</b>
<b>PP Tandem</b>	2.112 (2.083)	16.23 (15.79)	83.03 (80.88)	27.91 (26.61)



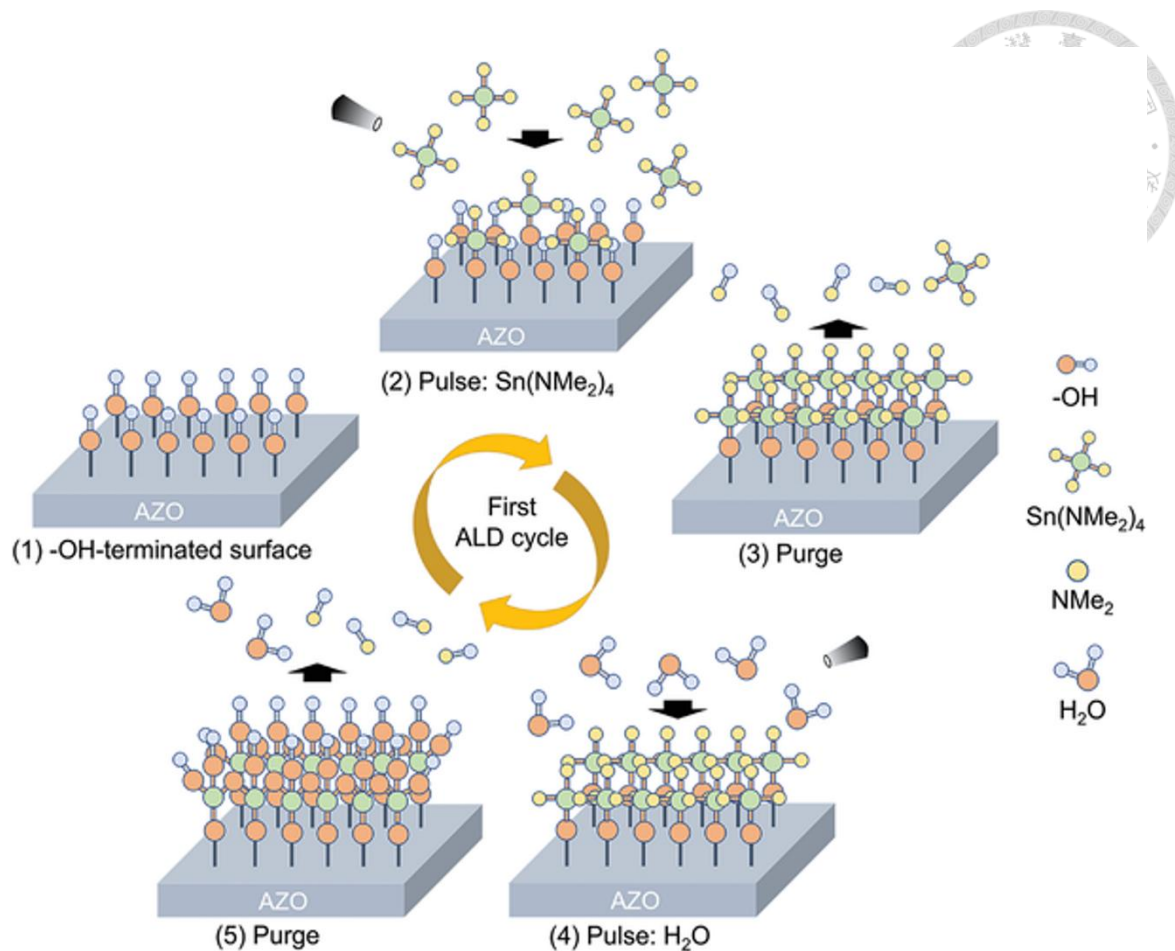


Fig. 6.1 The detailed ALD mechanism for  $\text{SnO}_2$  formation.<sup>[304]</sup>

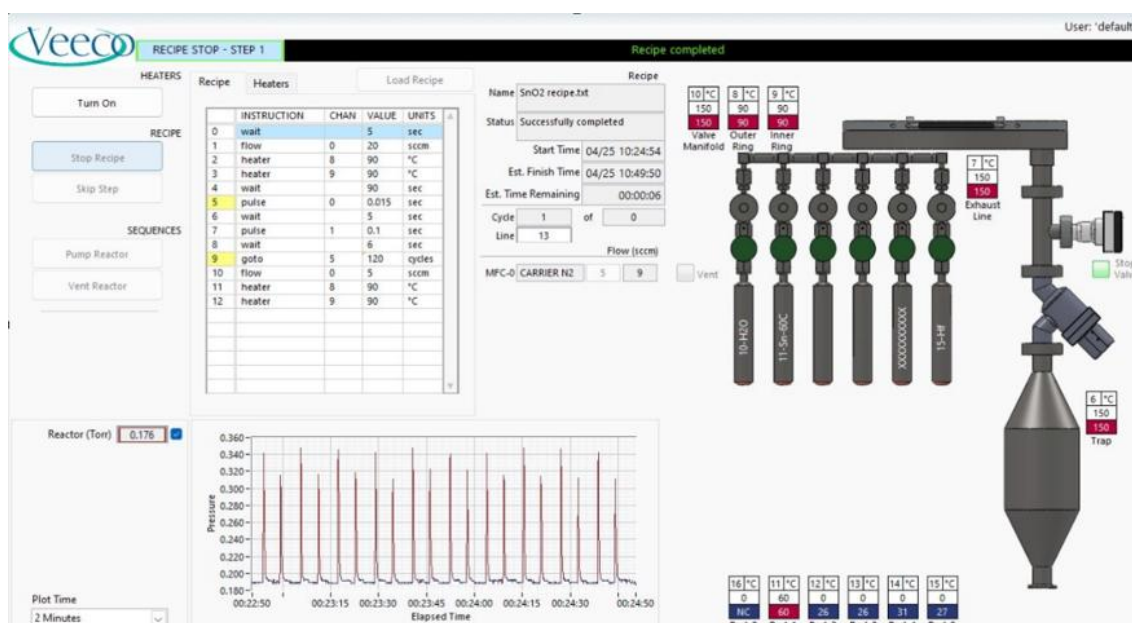
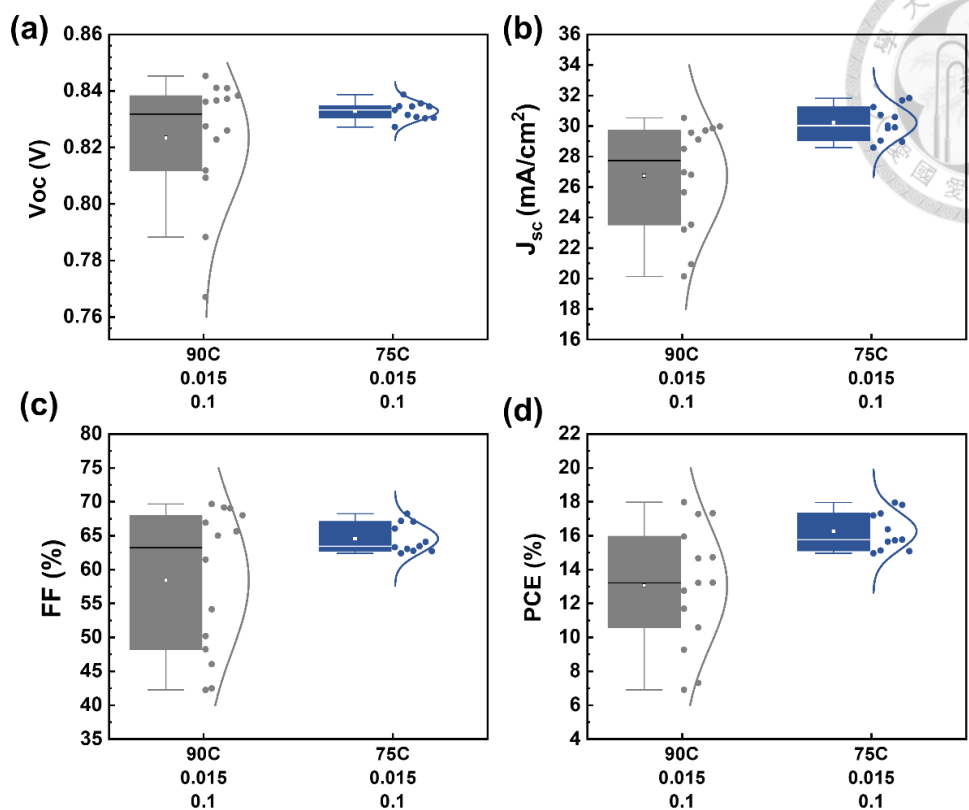
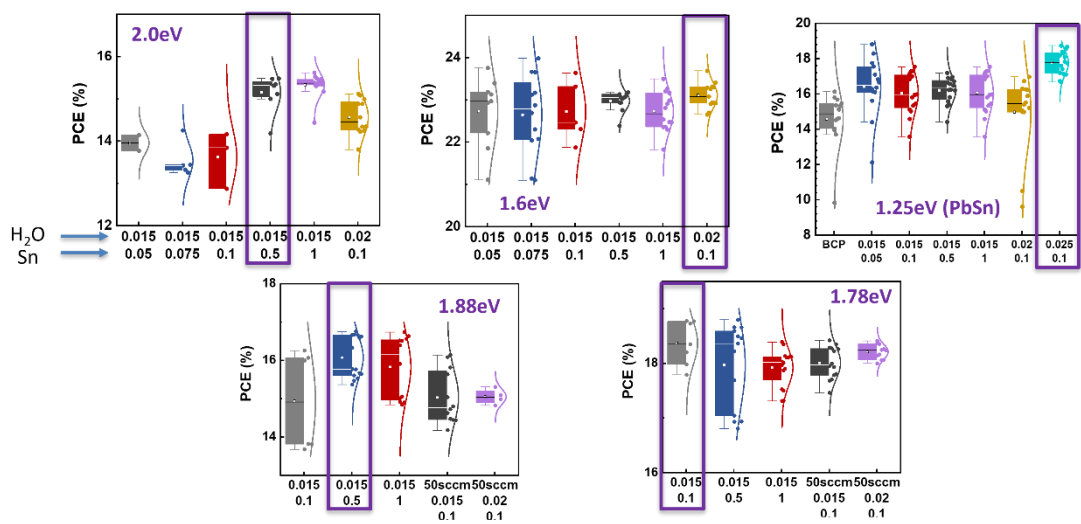


Fig. 6.2 The operating panel of ALD machine for  $\text{SnO}_2$  formation.



**Fig. 6.3** Performance variation of single-junction PbSn perovskite solar cells with the device structure ITO/PEDOT:PSS/PbSn perovskite/C<sub>60</sub>/SnO<sub>2</sub>/Ag under different ALD SnO<sub>2</sub> deposition temperatures.



**Fig. 6.4** ALD optimization process based on different bandgaps of perovskites.

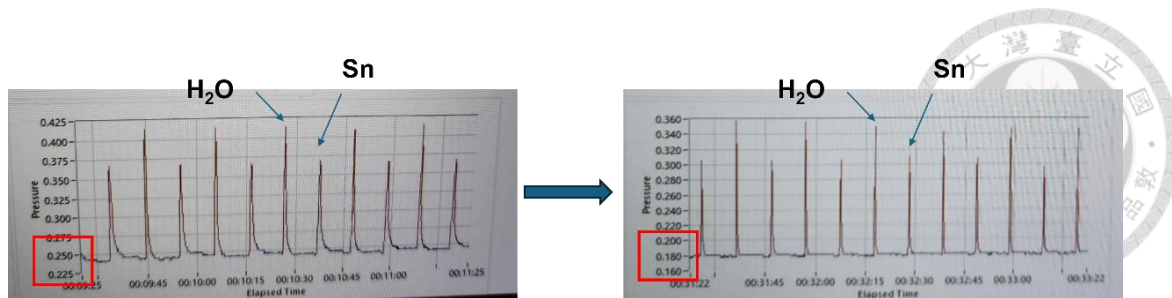


**Fig. 6.5** The base pressure changes after using a powerful pump.

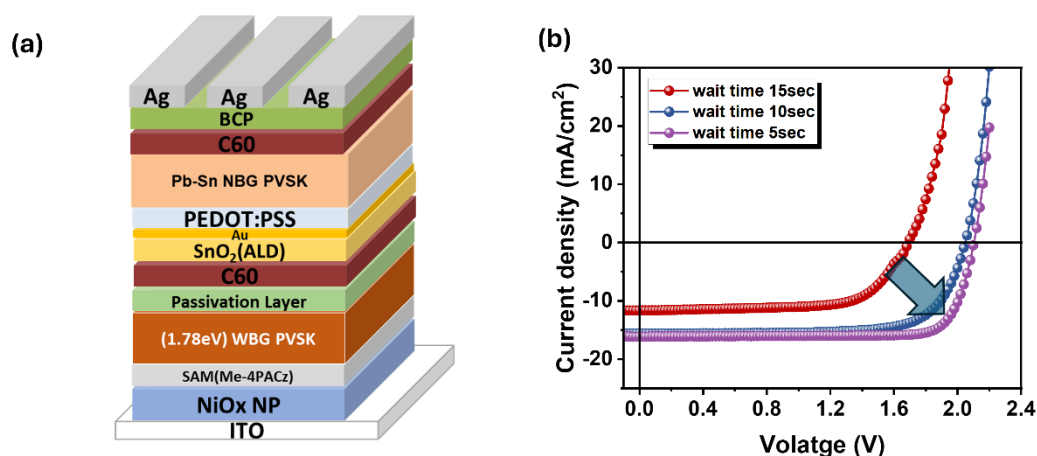


**Fig. 6.6** (a) The device structure of all-perovskite tandem solar cells. (b) J-V curves of all-perovskite tandem solar cells under different purging time.

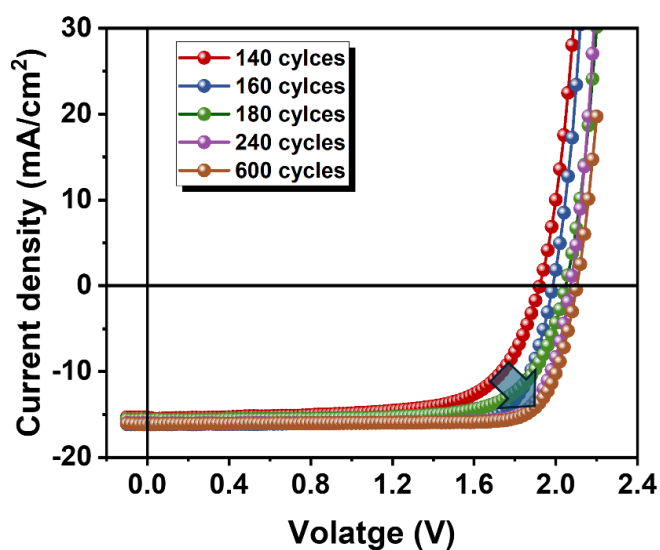


**Fig. 6.7** J-V curves of all-perovskite tandem solar cells under different cycles of ALD  $\text{SnO}_2$ .

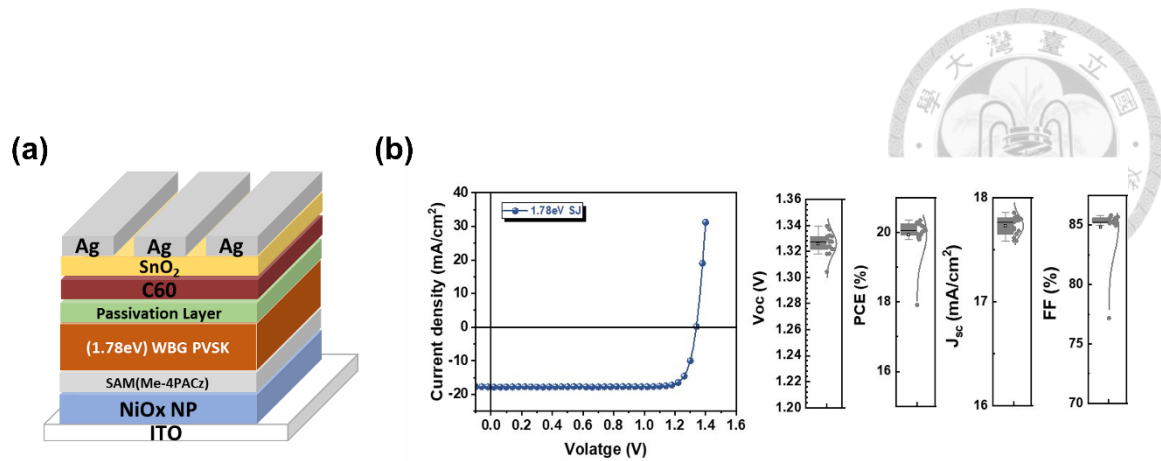


**Fig. 6.8** (a) The device structure of 1.78eV WBG perovskite solar cells. (b) J-V curves of the champion device and the box chart of the performance of 1.78eV WBG perovskite solar cells.

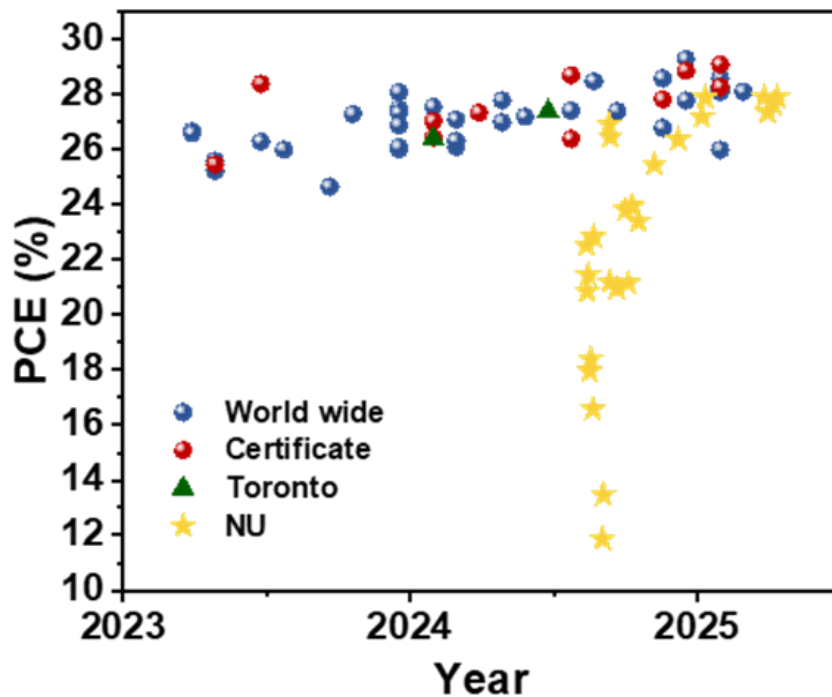


**Fig. 6.9** The baseline of all-perovskite tandem solar cells developed in the Sargent group (indicated by the yellow star) is shown in comparison with previously published results worldwide, as well as with devices fabricated by our group at the University of Toronto.

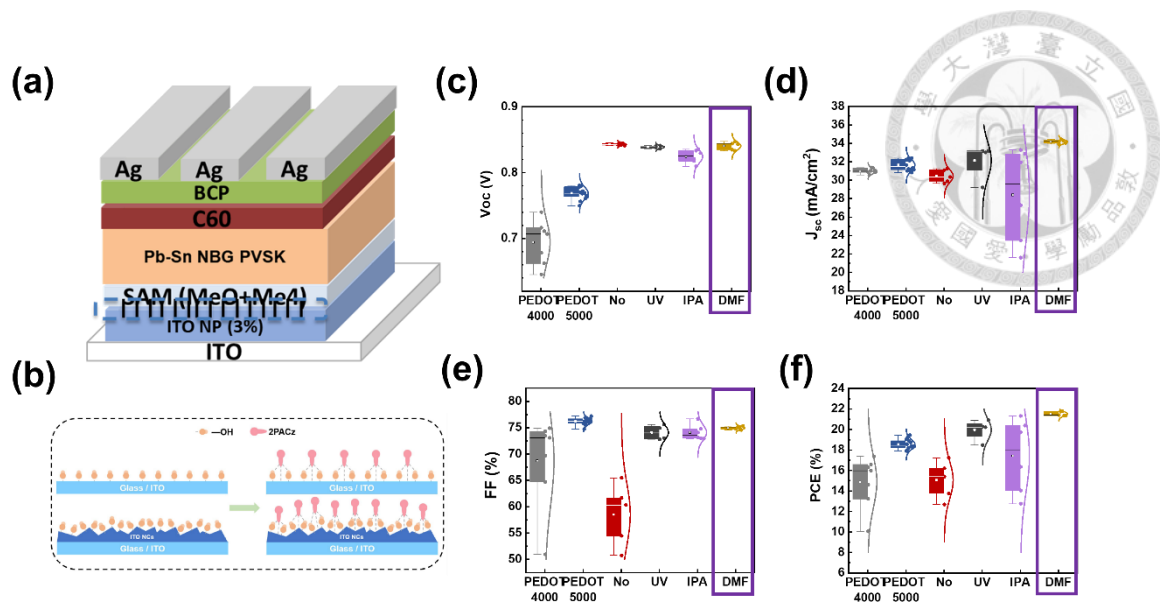


**Fig. 6.10** (a) Device architecture of PbSn NBG solar cells integrated with ITO nanoparticles. (b) Schematic diagram of bonding between 2PACz and ITO or ITO NCs.<sup>[303]</sup> (c-f) Box charts of the PV parameter of PbSn NBG perovskite solar cells by using different conditions of hole transporting layer.

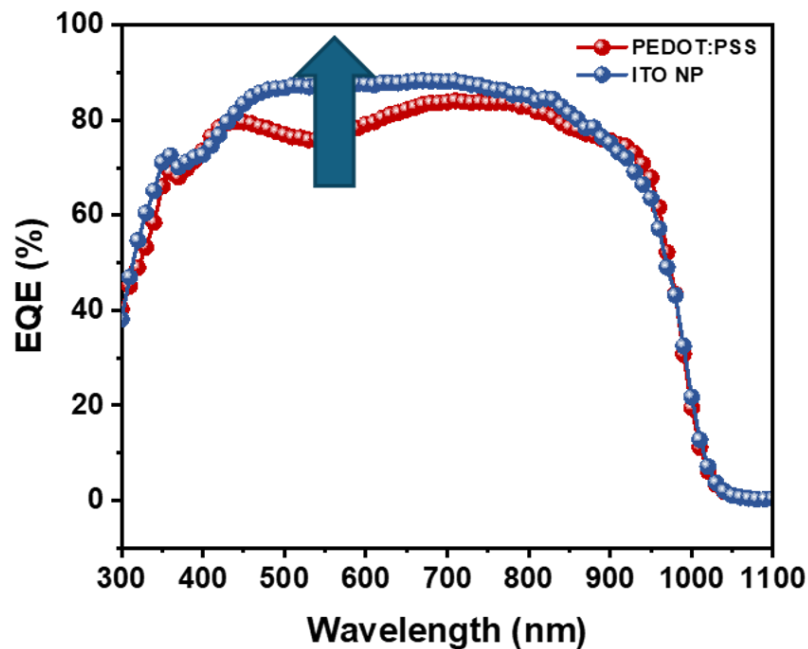


**Fig. 6.11** Comparison of EQE curves with different device configuration by using different HTL.

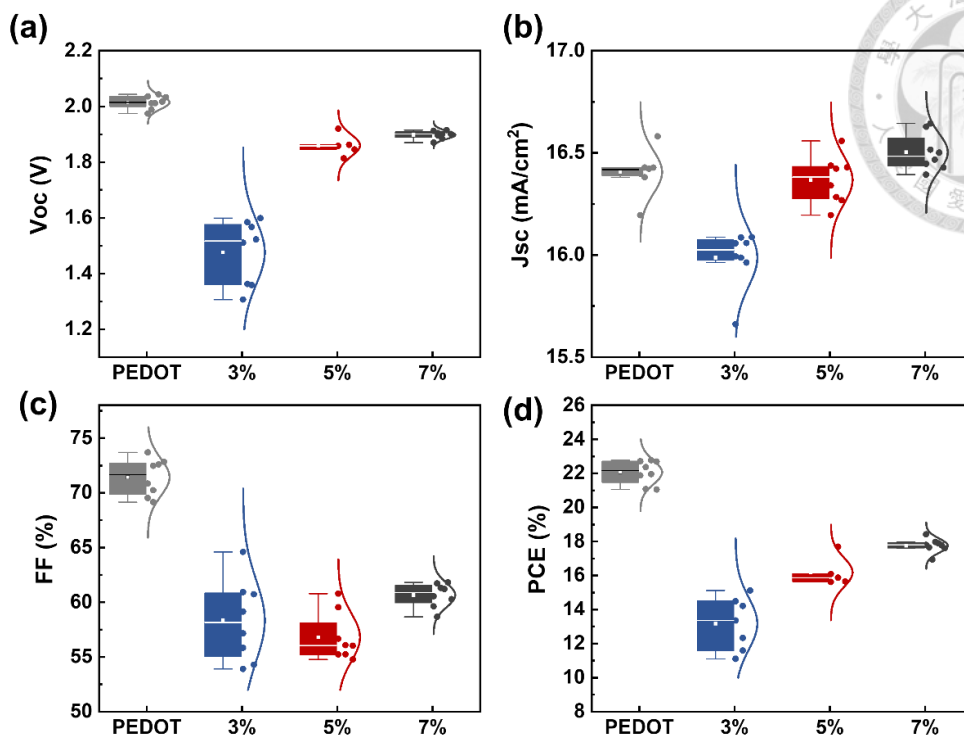


**Fig. 6.12** Box charts of the PV parameter of PbSn NBG perovskite solar cells by using different concentration of ITO nanoparticles.

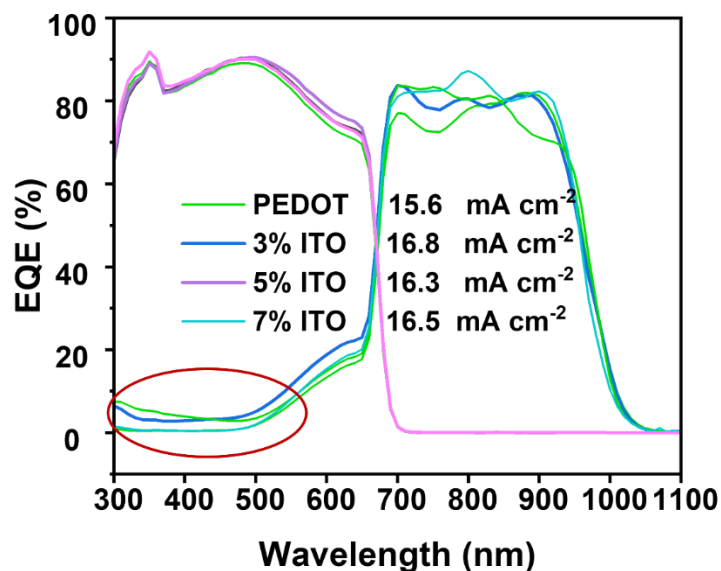


**Fig. 6.13** EQE curves with different device configuration by using different concentration of ITO nanoparticles.

## 6.2 Improving the Performance of Perovskite/Organic Tandem Solar Cells

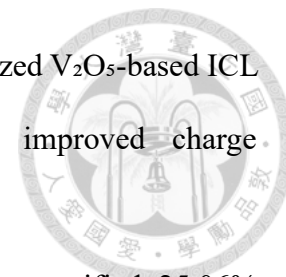


### 6.2.1 Introduction

To overcome the Shockley–Queisser (S–Q) efficiency limit inherent to single-junction solar cells, tandem architectures have emerged as a promising solution by enabling spectral splitting and more efficient utilization of the solar spectrum. Among various tandem configurations, perovskite–organic tandem solar cells (PO-TSCs) have garnered growing interest due to their excellent solution-processability, tunable bandgaps, and compatibility with lightweight and flexible substrates. These devices typically consist of a wide-bandgap (WBG) perovskite front subcell and a narrow-bandgap (NBG) organic subcell, working synergistically to harvest high-energy and near-infrared (NIR) photons, respectively.

Meanwhile, recent years have seen remarkable breakthroughs in PO-TSC performance, driven by synergistic advances in wide-bandgap perovskite engineering, interfacial passivation, organic acceptor design, and interconnecting layer (ICL) optimization. For instance, Jiang et al. reported a certified efficiency of 25.7% by introducing *cis*-CyDAI<sub>2</sub> as a surface passivating agent for the WBG perovskite subcell, effectively suppressing non-radiative recombination at the perovskite/C<sub>60</sub> interface and enhancing the open-circuit voltage (V<sub>oc</sub>). The tandem architecture utilized a 1.88 eV perovskite front cell and a 1.24 eV ternary organic rear cell (PM6:BTPSe-Ph4F:MO-ITIC-2F), achieving excellent spectral coverage and current matching.<sup>[305]</sup> Similarly, He et al. demonstrated a 25.1% efficient PO-TSC by minimizing energy losses in both subcells and the ICL. Their strategy involved pyridinium bromide perbromide (PBP) to

stabilize the WBG perovskite against halide migration and an optimized  $V_2O_5$ -based ICL that exhibited low optical and electrical losses, facilitating improved charge recombination and NIR transparency.<sup>[306]</sup>

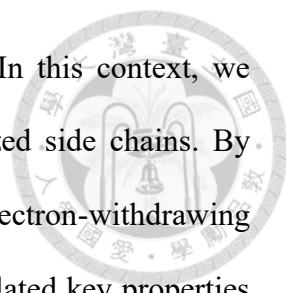


Another milestone was set by Zhang et al., who achieved a certified 25.06% efficiency by doping WBG perovskites with thiocyanate ( $SCN^-$ ) ions. These pseudo-halogen ions effectively suppressed halide segregation and enhanced crystallinity by occupying halogen vacancies, leading to increased stability over 1000 hours under continuous illumination.<sup>[307]</sup> Wu et al. further tackled phase instability in WBG perovskites by incorporating redox mediators derived from anthraquinone. These additives selectively reduced oxidized iodide and metallic  $Pb^0$ , stabilizing the perovskite composition and maintaining over 95% efficiency after 500 hours of operational testing. Their monolithic PO-TSC achieved a certified efficiency of 24.27%, demonstrating both high performance and improved long-term stability.<sup>[308]</sup>

Collectively, these studies reflect the rapid progress in addressing key limitations in PO-TSCs, including voltage losses in WBG perovskites, halide phase instability, interconnect layer inefficiencies, and non-radiative recombination. Despite these achievements, significant challenges remain, particularly in the development of narrow-bandgap (NBG) organic subcells that offer high current output, minimized  $V_{oc}$  losses, and long-term stability. Future research is expected to focus on further reducing voltage losses in both subcells, optimizing ICL design, and implementing scalable, low-temperature processing methods compatible with flexible substrates and roll-to-roll manufacturing.

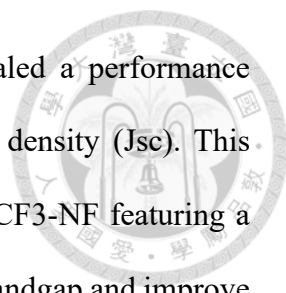
To address the intrinsic challenges associated with the rear organic subcell in PO-TSCs, particularly limited photocurrent generation and  $V_{oc}$  losses, we focused on the rational design of nonfullerene acceptors (NFAs) with extended  $\pi$ -conjugation to reduce





the optical bandgap and enhance near-infrared (NIR) absorption. In this context, we developed a novel NFA design strategy based on CF<sub>3</sub>-functionalized side chains. By precisely tuning the length of the  $-(\text{CH}_2)_n-$  linker that connects the electron-withdrawing CF<sub>3</sub> group to the fused aromatic backbone, we systematically modulated key properties including molecular packing, electrostatic interactions, and miscibility with donor polymers. This side-chain engineering approach facilitated the formation of distinctive two-dimensional mesh-like crystal structures, stabilized by CF<sub>3</sub>···F intermolecular interactions, which in turn promoted enhanced film crystallinity, improved charge transport, and favorable blend morphology. Among the designed NFA series, the  $-(\text{CH}_2)_2-$  substituted variant, Y2CF<sub>3</sub> (also referred to as YCF3-BF), exhibited the most balanced optoelectronic properties. Devices based on YCF3-BF achieved a power conversion efficiency (PCE) of 19.08%, a high fill factor of 80.09%, and an extended absorption onset at 928 nm, corresponding to a bandgap of 1.34 eV. This narrowed bandgap is particularly advantageous for tandem integration, as it enhances spectral complementarity with the wide-bandgap (WBG) perovskite front subcell and facilitates current matching, both of which are essential for boosting tandem device efficiency.

Beyond efficiency, the side-chain engineering also contributed significantly to device stability. The improved donor–acceptor miscibility and controlled domain morphology provided by the CF<sub>3</sub>-functionalized NFAs imparted strong morphological robustness under prolonged illumination and elevated temperature conditions, improving both operational and thermal stability. These findings underscore the importance of integrating material design and interfacial engineering to advance PO-TSC technologies. The incorporation of CF<sub>3</sub>-functionalized NBG acceptors offers a promising pathway to reduce optical and electrical losses while simultaneously achieving high efficiency and long-term durability.



However, further analysis of YCF3-BF-based PO-TSCs revealed a performance limitation stemming from a relatively modest short-circuit current density ( $J_{sc}$ ). This bottleneck motivated the development of a next-generation NFA-YCF3-NF featuring a more extended  $\pi$ -conjugated backbone to further reduce the optical bandgap and improve NIR absorption. The enhanced absorption profile of YCF3-NF is expected to boost photocurrent generation in the organic rear subcell, addressing the  $J_{sc}$  limitation observed in YCF3-BF-based devices. Although fully optimized PO-TSCs based on YCF3-NF are still under development, the promising results obtained with YCF3-BF provide a solid foundation. Building on this, we anticipate that the integration of YCF3-NF will lead to further improvements in overall tandem performance, offering new insights into molecular design principles and scalable strategies for next-generation, high-efficiency tandem solar cells.

## 6.2.2 Experimental Section

**Materials.** Formamidinium bromide (FABr, >99.99%), Formamidinium iodide (FAI, >99.99%) and methylammonium chloride (MACl, >99.99%) were purchased from Greatcell Solar Materials. Lead halide precursors, including lead(II) iodide ( $PbI_2$ , 99.999%), lead(II) bromide ( $PbBr_2$ , 99.999%), and lead(II) chloride ( $PbCl_2$ , 99.999%), as well as cesium bromide (CsBr, 99.999%) and cesium iodide (CsI, 99.999%) and [4-(3,6-Dimethyl-9H-carbazol-9-yl)butyl]phosphonic acid (Me-4PACz, >99.0%) were obtained from TCI Chemicals.  $CF_3$ -functionalized nonfullerene acceptors (YCF3-BF and YCF3-NF) were synthesized according to previously reported procedures.<sup>[309]</sup> The donor polymer PM6, standard acceptor Y6, compatibilizer L8BO, and electron transporting material PNDIT-F3N were procured from Solarmer or 1-Material Inc. C60 and bathocuproine (BCP) were purchased from Xi'an Polymer Light Technology. The 1,3-

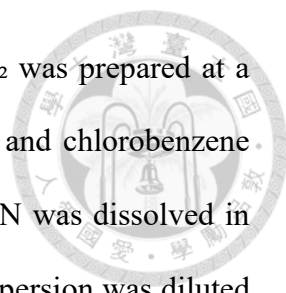
propane diammonium diiodide (PDAI<sub>2</sub>, >99.5%) was purchased from Luminescence Technology Corp.

Dimethyl sulfoxide (DMSO, ≥99.9%), anisole (99.7%), chlorobenzene (CB, ≥99.5%), isopropanol (IPA, ≥99.5%), and dimethylformamide (DMF, ≥99.5%) were sourced from Sigma-Aldrich. A nickel oxide (NiOx) nanoparticle dispersion was obtained from Avantama. The PEDOT:PSS solution (Al-4083 grade) was acquired from Ossila. Tetrakis(dimethylamino)tin(IV) (50-1815 Tin, 99.99% Sn) was supplied by Strem Chemicals. Indium tin oxide (ITO) coated glass substrates, with a sheet resistance of 15 Ω/sq and dimensions of 25 mm × 25 mm, were purchased from Suzhou ShangYang Solar Technology Co. High-purity copper, silver, and gold used for electrode deposition were obtained from Kurt J. Lesker.

### Preparation of perovskite and organic solutions

**Wide-bandgap (WBG) perovskite solution** WBG perovskite precursor solution (0.8 M, FA<sub>0.8</sub>Cs<sub>0.2</sub>Pb(I<sub>0.5</sub>Br<sub>0.5</sub>)<sub>3</sub>) was prepared by dissolving MAI (3.6 mg), PbCl<sub>2</sub> (10.9 mg), CsBr (13.6 mg), CsI (25 mg), FABI (32 mg), FAI (66.2 mg), PbBr<sub>2</sub> (161.5 mg) and PbI<sub>2</sub> (166 mg) in mixed solvent of DMF (800 μl) and DMSO (200 μl).

**Organic photovoltaic (OPV) solution** OPV solution was prepared by using different donor–acceptor combinations depending on the target system. For binary blends, the donor polymer PM6 was blended with either YCF3-BF or YCF3-NF at a weight ratio of 1:1.2 in mixed solvent of CF:CN = 99.5:0.5 with 0.5% (v/v) 1,8-diiodooctane (DIO) as a processing additive. For ternary blends, PM6, YCF3-BF, and the compatibilizer L8BO were blended at a weight ratio of 1:1.2:0.6 under the same solvent and additive conditions. In both cases, the total solid concentration was 7 mg mL<sup>-1</sup>.



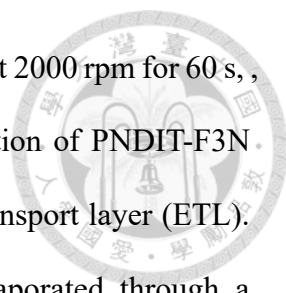
**Post-treatment and hole transport material solutions** PDAI<sub>2</sub> was prepared at a concentration of 1 mg/mL in a mixed solvent of isopropanol (IPA) and chlorobenzene (CB) with a volume ratio of 2:1. A 1 mg/mL solution of PNDIT-F3N was dissolved in methanol containing 0.3 wt% acetic acid. The NiO<sub>x</sub> nanoparticle dispersion was diluted to a final concentration of 0.025 wt% in ethanol. Me-4PACz was dissolved in IPA at a concentration of 0.3 mg/mL.

Perovskite precursor solutions were stirred at room temperature using a magnetic stir bar without applying heat, while organic solutions were stirred overnight at 50 °C to ensure complete dissolution and uniformity. Prior to application, both perovskite and organic solutions were passed through a 0.22 μm PTFE (polytetrafluoroethylene) membrane filter to remove particulates.

### **Device Fabrication.**

Pre-patterned ITO-coated glass substrates were sequentially cleaned by ultrasonication with detergent, deionized water, acetone, and isopropanol for 15min, respectively. Before fabricating thin films, these ITO-coated glass substrates were cleaned by using UV-ozone cleaner for 15 minutes.

**Organic Subcell (NBG Cell).** Organic solar cells (OSCs) were fabricated using a conventional device structure of ITO/PEDOT:PSS/BHJ/PNDIT-F3N/Ag. Indium tin oxide (ITO)-coated glass substrates were cleaned by sequential sonication in detergent, deionized water, acetone, and isopropanol for 15 minutes each. This was followed by UV-ozone treatment for 15 minutes to improve surface wettability. A thin layer of PEDOT:PSS (Clevios P VP AI 4083) was deposited by spin-coating at 4000 rpm for 40 s, followed by annealing at 150 °C for 10 minutes to serve as the hole transport layer (HTL).

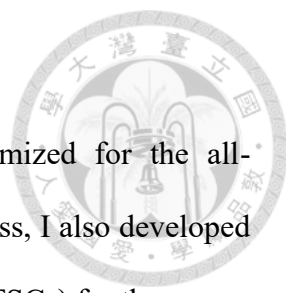


The BHJ solution was then spin-coated in a nitrogen-filled glovebox at 2000 rpm for 60 s, followed by annealing at 110 °C for 10 minutes. A methanolic solution of PNDIT-F3N (1 mg mL<sup>-1</sup>) was spin-coated at 3000 rpm for 60 s as the electron transport layer (ETL). Finally, a ~100 nm-thick silver (Ag) electrode was thermally evaporated through a shadow mask under high vacuum conditions ( $<5 \times 10^{-6}$  Torr) to complete the device.

### **Wide-bandgap perovskite solar cells and perovskite/organic tandem solar cells**

A NiOx hole transport layer was deposited by spin coating at 4000 rpm for 25 seconds and used without additional thermal treatment. The substrates were then transferred into a nitrogen-filled glovebox, where a self-assembled monolayer (SAM) of Me-4PACz was applied on top of the NiOx via spin coating at 4000 rpm for 25 seconds, followed by annealing at 100 °C for 10 minutes. Subsequently, 60 μL of the perovskite precursor solution was spin-coated onto the prepared substrates at 4000 rpm for 30 seconds. During the spin process, 150 μL of anisole was dropped onto the substrate at the 25-second mark to assist in film formation. The resulting perovskite films were then annealed at 100 °C for 15 minutes to promote crystallization. The deposition of the C<sub>60</sub> electron transport layer and top electrodes followed the same protocol as that used for the NBG perovskite solar cells. However, the SnO<sub>2</sub> interlayer was deposited using atomic layer deposition (ALD) under modified conditions, varying specific parameters to optimize performance. For constructing perovskite/organic tandem solar cells, a 1 nm layer of gold was deposited onto the appropriately thick SnO<sub>2</sub> layer of the wide-bandgap subcell to serve as the recombination contact. The organic top subcells were then fabricated using the same methods described above. Finally, a 140 nm silver layer was thermally evaporated to complete the device structure for efficiency characterization.

### 6.2.3 Results and Discussion



Building upon the ALD SnO<sub>2</sub> conditions I previously optimized for the all-perovskite tandem solar cell baseline, during the optimization progress, I also developed a new research direction, perovskite/organic tandem solar cells (PO-TSCs) for the group. PO-TSCs share a similar working mechanism with all-perovskite TSCs, except that the narrow-bandgap (NBG) PbSn perovskite bottom subcell is replaced by an organic photovoltaic (OPV) subcell as showed in **Fig. 6.14**. To enhance the overall efficiency of PO-TSCs, this work focused on improving the performance of the OPV subcell particularly by increasing its open-circuit voltage (V<sub>oc</sub>), which is a critical factor in determining tandem device efficiency. This research was conducted in collaboration with the Tobin Marks group.

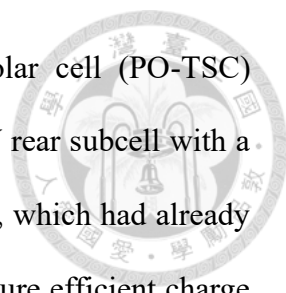
In order to increase the open-circuit voltage (V<sub>oc</sub>) in OPV subcell, a series of CF<sub>3</sub>-functionalized nonfullerene acceptors (NFAs), designated as Y<sub>n</sub>CF<sub>3</sub> (n = 1, 2, 3), were rationally designed and synthesized, based on our previous research.<sup>[309]</sup> The molecular design strategy involved systematically varying the length of the alkyl linker (–(CH<sub>2</sub>)<sub>n</sub>–) that connects the electron-withdrawing CF<sub>3</sub> moiety to the electron-rich azole core (**Fig. 6.15a**). This approach enabled fine-tuning of the electrostatic interactions and molecular packing properties, ultimately influencing the energy level alignment, morphological behavior, and electronic performance of the resulting OPV subcells. This molecular engineering strategy allows for precise modulation of intermolecular electrostatic interactions and molecular packing behavior. UV–vis absorption spectroscopy revealed that extending the alkyl chain length leads to red-shifted absorption maxima and increased absorption coefficients in both solution and solid-state films, indicating enhanced light-harvesting capability and stronger molecular aggregation (**Fig. 6.15b**). Simultaneously, electrochemical measurements showed an upshift in HOMO levels with increasing linker

length, while the LUMO remained relatively stable, suggesting that the CF<sub>3</sub> group predominantly influences the HOMO via a  $\sigma$ -electron-withdrawing effect (**Fig. 6.15c**).

Single-crystal X-ray diffraction revealed a transition from the three-dimensional  $\pi$ - $\pi$  stacked mesh-like structure observed in Y6 to a unique two-dimensional hollow topology in the Y<sub>n</sub>CF<sub>3</sub> series (**Fig. 6.16a**). These structures emerged from electrostatic interactions between the CF<sub>3</sub> termini and fluorinated aryl groups in adjacent molecules. As the linker length increased, the vertical mesh size decreased while the horizontal mesh dimension expanded, modulating the electrostatic interaction site distribution and molecular packing anisotropy. Grazing incidence wide-angle X-ray scattering (GIWAXS) analyses of neat films demonstrated that the Y<sub>n</sub>CF<sub>3</sub> materials maintain a  $\pi$ -face-on orientation with shorter  $\pi$ - $\pi$  stacking distances and longer crystal coherence lengths than Y6, reflecting improved order and charge transport (**Fig. 6.16b-c**).

In donor-acceptor blend films with D18, the electrostatic potential (ESP) difference between the components increased with linker length, enhancing miscibility and leading to finer phase separation and reduced domain sizes, particularly in D18:Y3CF<sub>3</sub> blends (**Fig. 6.17a**). However, this high miscibility resulted in excessive recombination and reduced fill factor (FF). In contrast, D18:Y2CF<sub>3</sub> demonstrated an optimal balance between miscibility and domain purity, yielding a well-organized nanoscale morphology with favorable crystallinity and efficient exciton dissociation. This was reflected in the superior photovoltaic performance of Y2CF<sub>3</sub>-based devices, which achieved a power conversion efficiency (PCE) of 19.08%, a high short-circuit current density (J<sub>sc</sub>) of 27.64 mA cm<sup>-2</sup>, and an outstanding FF of 80.09%, surpassing the Y6-based control device (**Fig. 6.17b-d**).

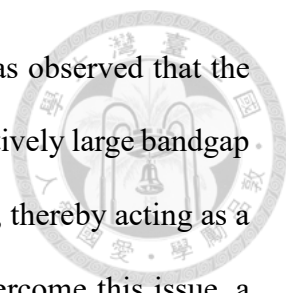
Building upon the promising performance of Y2CF<sub>3</sub> (hereafter referred to as YCF<sub>3</sub>-BF) in single-junction organic photovoltaic (OPV) devices, we further integrated this



high-efficiency OPV subcell into a perovskite/organic tandem solar cell (PO-TSC) architecture. The tandem device combines the YCF3-BF-based OPV rear subcell with a front subcell employing a wide-bandgap (WBG) 1.88 eV perovskite, which had already been optimized using an ALD-grown SnO<sub>2</sub> interconnect layer to ensure efficient charge extraction and thermal stability (**Fig. 6.18**).

To ensure proper spectral splitting and complementary absorption between the two subcells, the bulk heterojunction (BHJ) composition of the OPV subcell was slightly modified. Specifically, the donor polymer D18 was replaced with PM6 to avoid spectral overlap with the WBG perovskite. Moreover, to boost the photocurrent and improve charge transport, a ternary blend strategy was adopted by incorporating the compatibilizer L8BO into the active layer. As summarized in the corresponding **Fig. 6.19 & Table 6.4**, this ternary OPV subcell configuration led to a noticeable increase in short-circuit current density ( $J_{sc}$ ), reflecting improved photon harvesting and charge collection. The integration of these two optimized subcells resulted in a high-performance PO-TSC with a power conversion efficiency (PCE) of 25.24%, an extremely high open-circuit voltage ( $V_{oc}$ ) of 2.197 V, a  $J_{sc}$  of 14.21 mA cm<sup>-2</sup>, and an exceptional fill factor (FF) of 83.00%. In addition, the champion device also showed negligible hysteresis with a stabilized power output of 24.53% (**Fig. 6.19d-e**). In comparison, the control tandem device incorporating Y6 in the OPV subcell achieved a lower PCE of 23.04%, a  $V_{oc}$  of 2.114 V, a  $J_{sc}$  of 13.37 mA cm<sup>-2</sup>, and an FF of 81.74%. The significant performance enhancement in the YCF3-BF-based tandem device is primarily attributed to the higher  $V_{oc}$  enabled by the improved electronic properties and reduced nonradiative recombination losses of YCF3-BF, confirming its strong potential for next-generation tandem solar cell application.



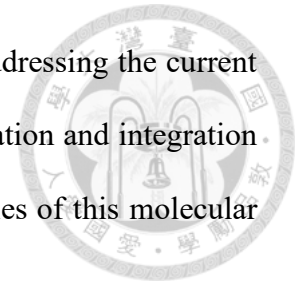


Following the development of YCF3-BF-based PO-TSCs, it was observed that the overall device performance faced limitations primarily due to the relatively large bandgap of the OPV subcell. This large bandgap constrained the photocurrent, thereby acting as a bottleneck for the total current density of the tandem device. To overcome this issue, a novel nonfullerene acceptor (NFA), YCF3-NF, was designed with the aim of reducing the bandgap and enhancing the current output. Guided by established molecular design principles for NFAs, the extension of the conjugation length in YCF3-NF was intended to red-shift the absorption profile, allowing the OPV subcell to harvest a broader range of the solar spectrum and thus achieve a higher photocurrent. As illustrated in **Fig. 6.20**, the molecular structures and optoelectronic characteristics of YCF3-BF and its extended-conjugation counterpart YCF3-NF are compared. **Fig. 6.20a** shows that while both molecules feature a trifluoromethyl-substitutedazole core, YCF3-NF incorporates a fused aromatic end group, resulting in a significantly extended  $\pi$ -conjugation framework.


This structural modification leads to notable optoelectronic differences. As presented in **Fig. 6.20b**, YCF3-NF exhibits a red-shifted absorption onset at 951 nm compared to 915 nm for YCF3-BF, along with stronger absorption in the near-infrared region. This enhancement is attributed to both the lower optical bandgap and the increased intermolecular interactions afforded by the extended conjugation. Furthermore, cyclic voltammetry (CV) measurements were conducted to estimate the HOMO and LUMO energy levels of both NFAs, with the results summarized in the corresponding **Fig. 6.20d** and **Table 6.5**. These electronic structure insights suggest favorable energy level alignment for efficient charge separation and collection in future OPV configurations.

Although the current work did not fully optimize the donor-to-acceptor ratio or the integration of YCF3-NF into tandem PO-TSC devices due to time constraints, the preliminary results are promising. The newly designed YCF3-NF molecule demonstrates

significant potential for advancing the efficiency of PO-TSCs by addressing the current density limitation seen in YCF3-BF-based devices. Further optimization and integration studies are still keep going to unlock the full performance capabilities of this molecular system in upcoming research.



## 6.2.4 Summary and Future works



Building upon this established baseline, our research extended into perovskite/organic tandem solar cell (PO-TSC) architectures by incorporating a newly developed CF<sub>3</sub>-functionalized non-fullerene acceptor, YCF3-BF, into the organic photovoltaic (OPV) subcell. Optimized PO-TSC devices demonstrated a notable power conversion efficiency (PCE) of 25.24%, outperforming conventional Y6-based configurations. To further address limitations related to current density, we synthesized a novel molecule, YCF3-NF, characterized by an extended  $\pi$ -conjugation structure, red-shifted absorption spectra, and advantageous energy alignment. While full integration of YCF3-NF into complete devices remains ongoing, preliminary results indicate significant promise. This study underscores the critical role of synergistic interface engineering, innovative molecular design, and meticulous process optimization in advancing tandem solar cell technology. Additionally, our findings provide foundational insights for future research endeavors into triple-junction and large-area solar devices.

Regarding future commercialization prospects for perovskite solar cells, PO-TSCs continue to represent a strategically valuable research direction. Structurally, the wide-bandgap (WBG) perovskite top subcell efficiently absorbs high-energy photons, converting them into electricity, while residual photons pass through an interconnecting layer to be absorbed by the OPV bottom subcell. This design not only optimizes photon utilization but also protects the OPV subcell from potential photodamage. Compared with all-perovskite tandem solar cells, PO-TSCs offer several advantages, notably improved device stability by substituting the Pb-Sn NBG perovskite component with an OPV subcell. Furthermore, integrating an OPV subcell enhances the feasibility of fabricating flexible devices, broadening future application opportunities in semiconductors.

Nevertheless, PO-TSC efficiency currently lags behind that of all-perovskite configurations, primarily due to lower OPV subcell performance and phase separation issues in the WBG perovskite top subcell. To tackle these challenges, I provided four strategically designed projects aimed at elevating PO-TSC performance. These projects target enhancing the open-circuit voltage (Voc) of the OPV subcell, designing infrared-responsive OPVs to boost current density, reducing Voc losses in the WBG perovskite subcell, and significantly improving the overall device stability by stabilizing the WBG perovskite subcell. Through these targeted strategies, we anticipate narrowing the performance and stability gaps between PO-TSCs and all-perovskite tandem solar cells, thus advancing the potential for their commercial application.

## 6.2.5 Tables and Figures

**Table 6.4** Device performance of perovskite and OPV single junction and PO-TSCs.

	<b>Voc (V)</b> <b>(AVG)</b>	<b>Jsc (mA/cm<sup>2</sup>)</b> <b>(AVG)</b>	<b>FF (%)</b> <b>(AVG)</b>	<b>PCE (%)</b> <b>(AVG)</b>
<b>Perovskite SJ</b>	1.362 (1.352)	15.36 (14.44)	85.11 (83.48)	17.56 (16.28)
<b>OPV SJ</b> <b>[PM6:YCF3-BF:L8BO]</b>	0.841 (0.838)	26.59 (25.10)	78.48 (75.10)	17.13 (16.43)
<b>PO-TSCs</b> <b>[PM6:Y6:L8BO]</b>	2.114 (2.106)	13.37 (13.32)	81.74 (81.42)	23.04 (22.83)
<b>PO-TSCs</b> <b>[PM6:YCF3-BF:L8BO]</b>	2.197 (2.171)	14.21 (13.44)	83.00 (81.05)	25.24 (23.65)

**Table 6.5** The summarized results of UV-vis absorption and CV measurement.

	$\Lambda_{\text{sol}}^{\text{max}}$ [nm]	$\Lambda_{\text{film}}^{\text{max}}$ [nm]	$\Lambda_{\text{onste}}$ [nm]	$E_{\text{g}}^{\text{opt}}$ [eV]	$E_{\text{HOMO}}^{\text{CV}}$ [eV]	$E_{\text{LUMO}}^{\text{CV}}$ [eV]	$E_{\text{g}}^{\text{CV}}$ [eV]
<b>YCF3-BF</b>	748	833	915	1.35	-5.64	-4.00	1.64
<b>YCF3-NF</b>	781	862	951	1.30	-5.48	-4.00	1.48

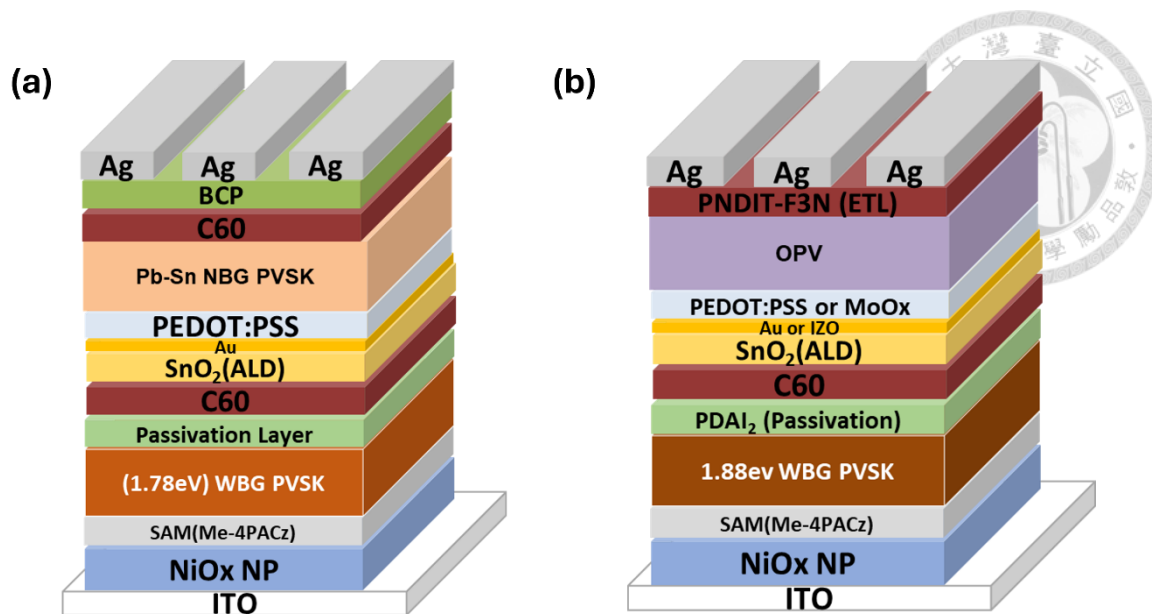


**Fig. 6.14** The device architecture of (a) all-perovskite tandem solar cells and (b) perovskite/organic tandem solar cells (PO-TSCs)

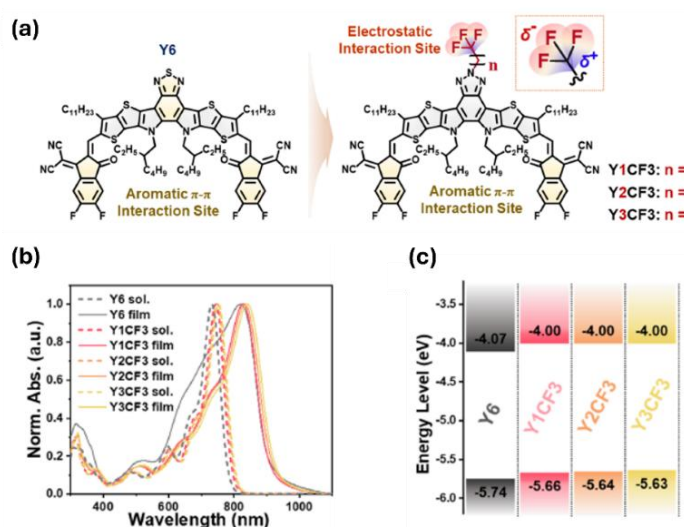


**Fig. 6.15** NFA chemical structures and their optoelectronic and thermal properties. (a) Chemical structures of the benchmark NFA Y6 and the CF<sub>3</sub>-functionalized series Y<sub>n</sub>CF<sub>3</sub> (n = 1, 2, 3). (b) Normalized UV-vis absorption spectra of Y6 and Y<sub>n</sub>CF<sub>3</sub>s measured in chloroform solution (dashed lines) and as thin films (solid lines). (c) Energy level diagram illustrating the HOMO and LUMO positions of Y6 and Y<sub>n</sub>CF<sub>3</sub>s as determined by cyclic voltammetry (CV).<sup>[309]</sup>

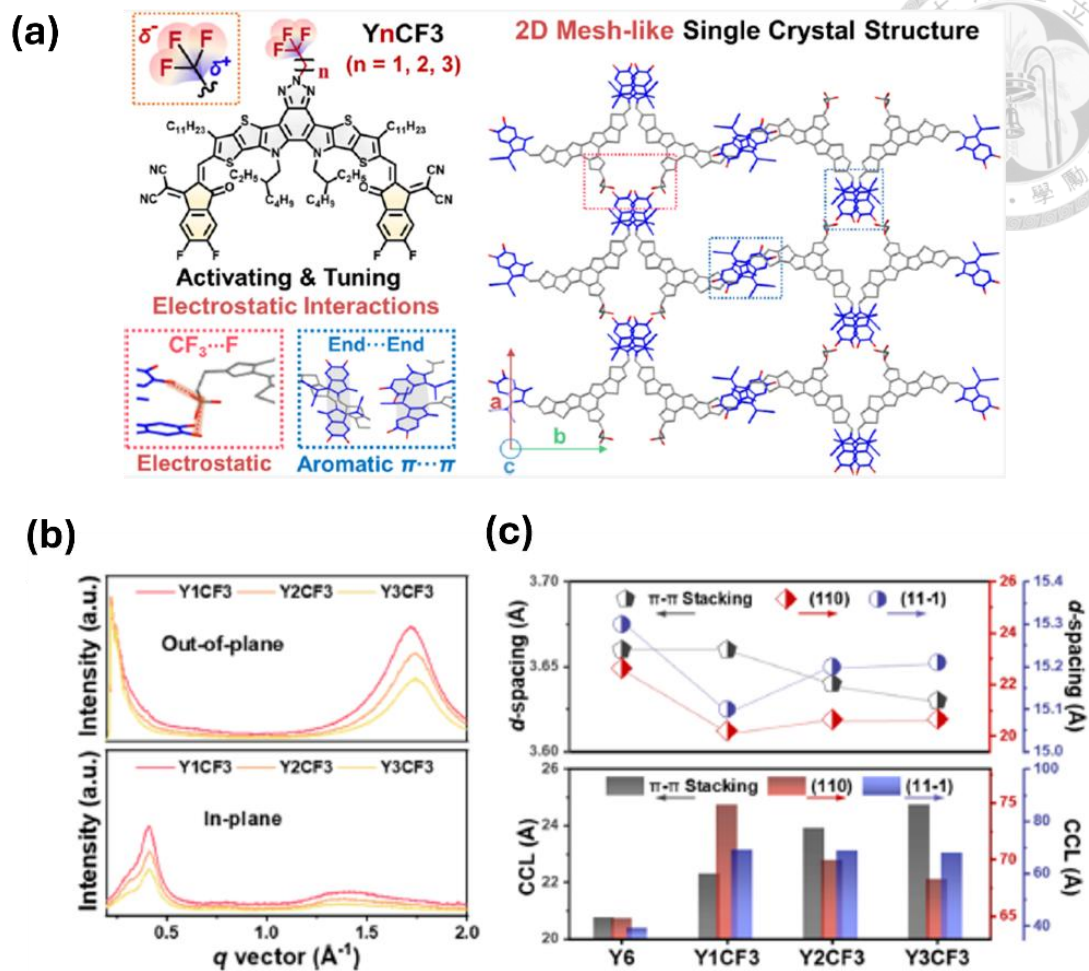


**Fig. 6.16** (a) YnCF3 series shows a 2D mesh-like structure from single crystal XRD. (b) GIWAXS line-cut profiles of YnCF3 neat films. (c) Comparison of the d-spacing and CCL values of Y6 and YnCF3 neat films from GIWAXS analyses.<sup>[309]</sup>

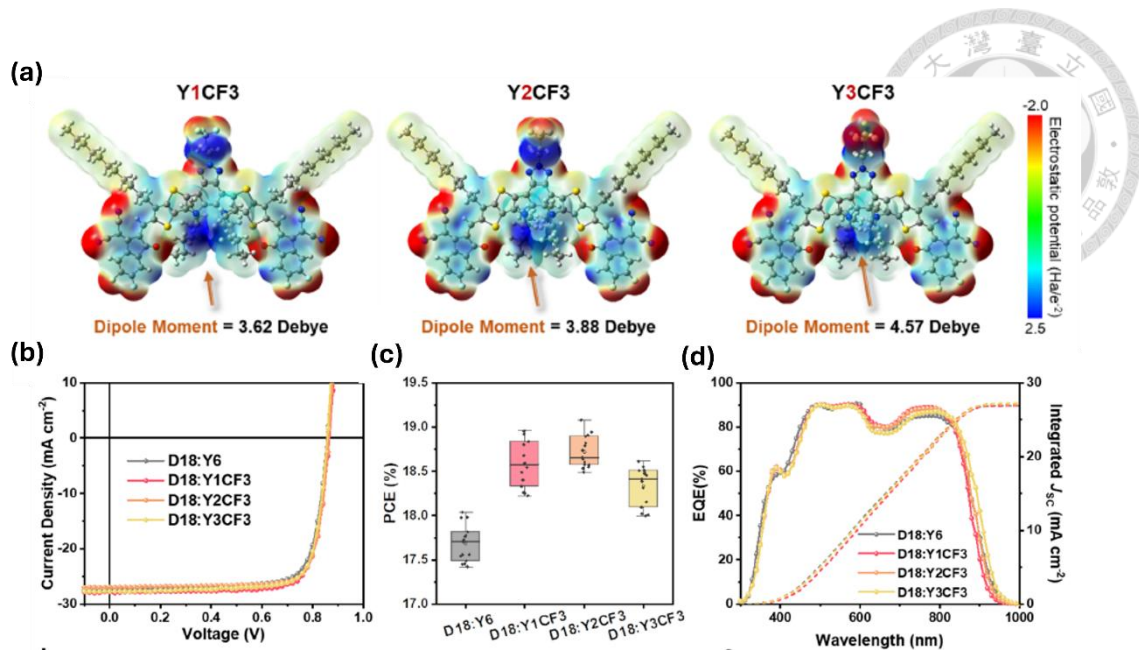


**Fig. 6.17** (a) DFT-calculated ESP distribution and dipole moment of Y<sub>n</sub>CF<sub>3</sub>. Photovoltaic performance of (a) J-V characteristics of D18:Y6 and D18:Y<sub>n</sub>CF<sub>3</sub> OSCs and (b) statistical distribution of PCEs with 15 individual devices. (c) Corresponding EQE spectra (scattered line) and integrated current densities (dashed line).<sup>[309]</sup>

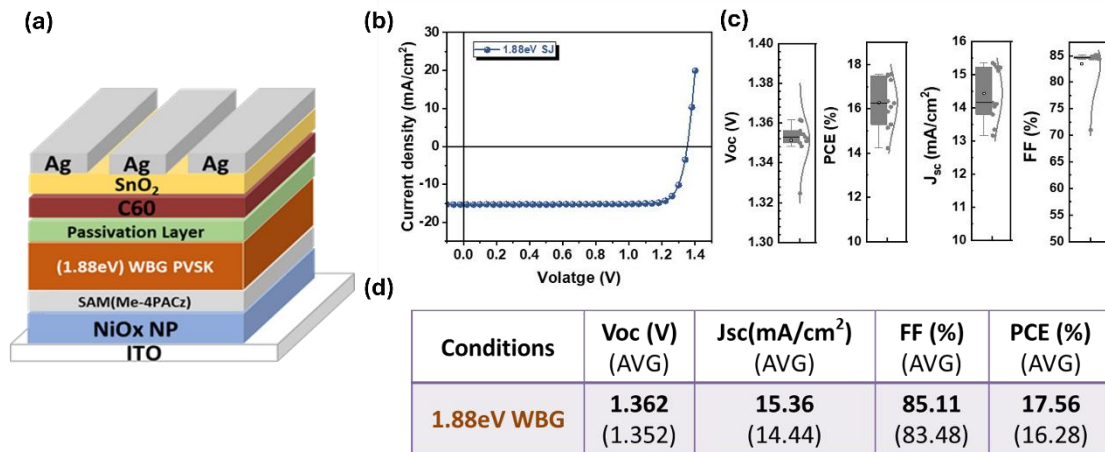


**Fig. 6.18** (a) Device architecture of 1.88eV WBG single junction perovskite solar cells. (b) J-V characteristics and (c) statistical distribution of Vocs, PCEs, Jscs and FFs with several individual devices. (d) The champion device and average performance of 1.88eV WBG single junction perovskite solar cells.

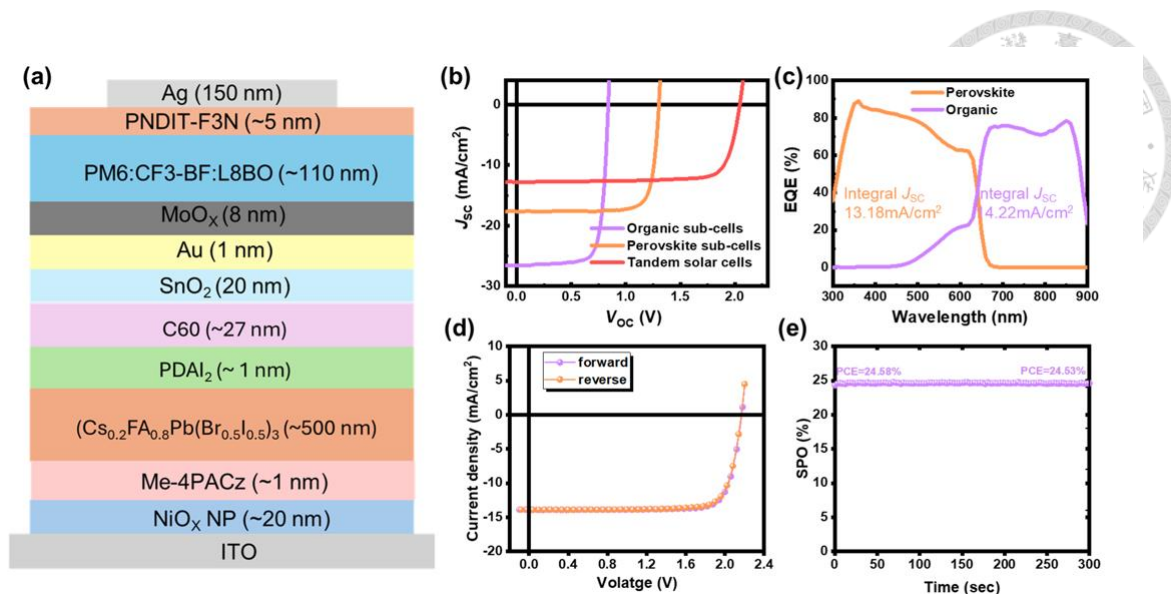


**Fig. 6.19** (a) Device architecture of PO-TSCs. (b) J-V characteristics of different subcells (c) EQE of PO-TSCs. (d) Reverse and forward J-V characteristics of champion device. (e) 5min of SPO measurement of PO-TSCs.

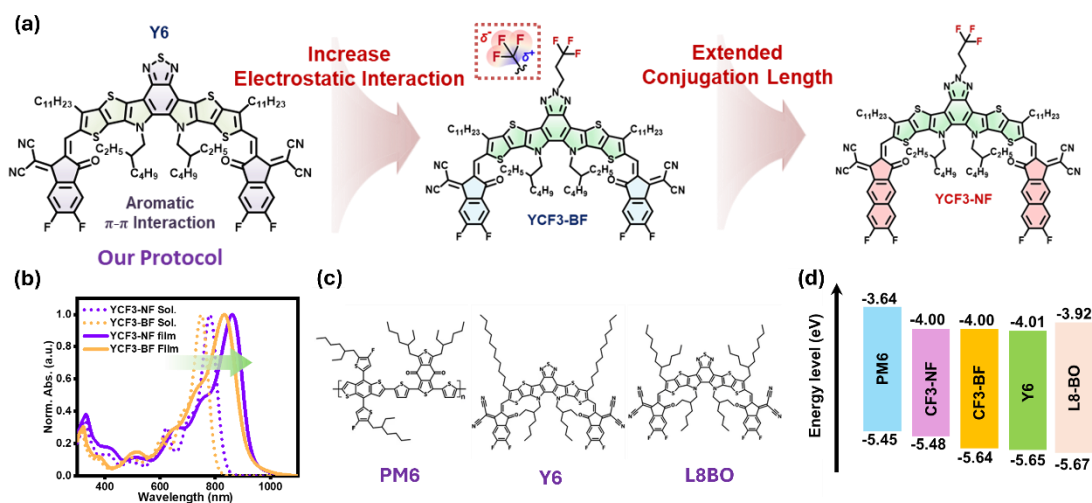


**Fig. 6.20** (a) Molecule structure and design strategy of YCF3-BF and YCF3-NF. (b) Normalized UV-vis absorption spectra of YCF3-BF and YCF3-NF measured in chloroform solution (dashed lines) and as thin films (solid lines). (c) Molecular structure of PM6, Y6 and L8BO. (d) Energy level of PM6, YCF3-NF, YCF3-BF, Y6 and L8BO.



➤ **Project 1 – High Voc POPV Tandem**

**Target : Improve POPV tandem by high Voc OPV subcell**

Strategy : We design novel Y-series acceptors to improve the Voc of OPV subcell

➤ **Project 2 – IR OPV Design**

**Target : Replace Pb-Sn perovskite subcell by OPV subcell**

- OPV subcell has similar band edge with Pb-Sn PVSK  
→By blending NIR small molecules  
→All-polymer solar cell

Strategy :

1. Design NIR small molecules
2. All-polymer solar cell baseline establishment

➤ **Project 3 – WBG PVSK Voc loss**

**Target : Improve POPV tandem by high Voc PVSK subcell**

- PVSK with higher bandgap  
→Voc loss is a main problem

Strategy :

Molecule screening for passivation or additive method

➤ **Project 4 – Stability of POPV Tandem**

**Target : Improve the stability of WBG PVSK**

- WBG PVSK has high Br content  
→Phase segregation problem is very serious

Strategy :

Additive method is being used to regulate the crystallization process of PVSK

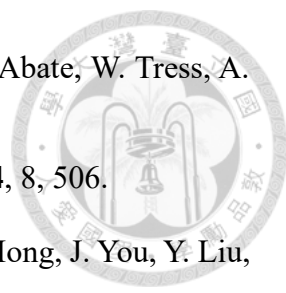


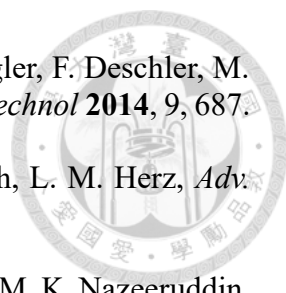
**Fig. 6.21** Four potential research directions for future development of PO-TSCs.

## REFERENCE

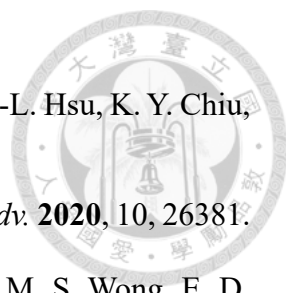


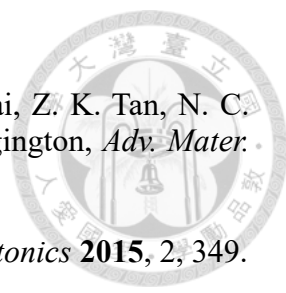
- [1] M. Saliba, T. Matsui, K. Domanski, J.-Y. Seo, A. Ummadisingu, S. M. Zakeeruddin, J.-P. Correa-Baena, W. R. Tress, A. Abate, A. Hagfeldt, *Science* **2016**, 354, 206.
- [2] M. Saliba, T. Matsui, J.-Y. Seo, K. Domanski, J.-P. Correa-Baena, M. K. Nazeeruddin, S. M. Zakeeruddin, W. Tress, A. Abate, A. Hagfeldt, *Energ. Environ. Sci.* **2016**, 9, 1989.
- [3] M. M. Lee, J. Teuscher, T. Miyasaka, T. N. Murakami, H. J. Snaith, *Science* **2012**, 338, 643.
- [4] N. K. Noel, S. D. Stranks, A. Abate, C. Wehrenfennig, S. Guarnera, A.-A. Haghighirad, A. Sadhanala, G. E. Eperon, S. K. Pathak, M. B. Johnston, *Energ. Environ. Sci.* **2014**, 7, 3061.
- [5] A. K. Jena, A. Kulkarni, T. Miyasaka, *Chem. Rev.* **2019**, 119, 3036.
- [6] D. P. McMeekin, G. Sadoughi, W. Rehman, G. E. Eperon, M. Saliba, M. T. Hörantner, A. Haghighirad, N. Sakai, L. Korte, B. Rech, *Science* **2016**, 351, 151.
- [7] V. M. Goldschmidt, *Naturwissenschaften* **1926**, 14, 477.
- [8] M. Johansson, P. Lemmens, *J. Phys.: Condens. Matter* **2008**, 20, 264001.
- [9] Z. Li, M. Yang, J.-S. Park, S.-H. Wei, J. J. Berry, K. Zhu, *Chem. Mater.* **2016**, 28, 284.
- [10] F. Ünlü, E. Jung, J. Haddad, A. Kulkarni, S. Öz, H. Choi, T. Fischer, S. Chakraborty, T. Kirchartz, S. Mathur, *APL Mater.* **2020**, 8.
- [11] G. Kieslich, S. Sun, A. K. Cheetham, *Chem. Sci.* **2015**, 6, 3430.
- [12] R. E. Brandt, V. Stevanović, D. S. Ginley, T. Buonassisi, *MRS Commun.* **2015**, 5, 265.
- [13] T. Umebayashi, K. Asai, T. Kondo, A. Nakao, *Phys. Rev. B* **2003**, 67, 155405.
- [14] A. Dey, J. Ye, A. De, E. Debroye, S. K. Ha, E. Bladt, A. S. Kshirsagar, Z. Wang, J. Yin, Y. Wang, *ACS Nano* **2021**, 15, 10775.
- [15] J.-W. Lee, S. Tan, S. I. Seok, Y. Yang, N.-G. Park, *Science* **2022**, 375, eabj1186.
- [16] S. Ahmad, S. Kazim, M. Grätzel, *Perovskite Solar Cells: Materials, Processes, and Devices*, John Wiley & Sons, Wiley-VCH GmbH **2022**.

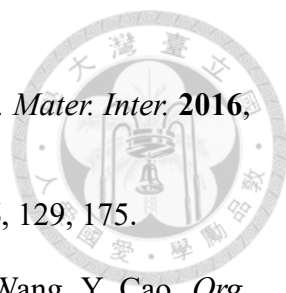
- 
- [17] J.-P. Correa-Baena, M. Saliba, T. Buonassisi, M. Grätzel, A. Abate, W. Tress, A. Hagfeldt, *Science* **2017**, 358, 739.
- [18] M. A. Green, A. Ho-Baillie, H. J. Snaith, *Nat. Photonics* **2014**, 8, 506.
- [19] H. Zhou, Q. Chen, G. Li, S. Luo, T.-b. Song, H.-S. Duan, Z. Hong, J. You, Y. Liu, Y. Yang, *Science* **2014**, 345, 542.
- [20] X. Wu, B. Li, Z. Zhu, C.-C. Chueh, A. K.-Y. Jen, *Chem. Soc. Rev.* **2021**.
- [21] H. Liu, M. H. Yu, C. C. Lee, X. Yu, Y. Li, Z. Zhu, C. C. Chueh, Z. a. Li, A. K. Y. Jen, *Adv. Mater. Technol.* **2021**, 6, 2000960.
- [22] Y. C. Kim, H. J. An, D. H. Kim, J. M. Myoung, Y. J. Heo, J. H. Cho, *Adv. Funct. Mater.* **2021**, 31, 2005553.
- [23] Z. Ren, J. Yu, Z. Qin, J. Wang, J. Sun, C. C. Chan, S. Ding, K. Wang, R. Chen, K. S. Wong, *Adv. Mater.* **2021**, 33, 2005570.
- [24] Y. Yang, S. Xu, Z. Ni, C. H. Van Brackle, L. Zhao, X. Xiao, X. Dai, J. Huang, *Adv. Mater.* **2021**, 33, 2100783.
- [25] Z. Chen, Z. Li, Z. Chen, R. Xia, G. Zou, L. Chu, S.-J. Su, J. Peng, H.-L. Yip, Y. Cao, *Joule* **2021**, 5, 456.
- [26] Z. Ren, K. Wang, X. W. Sun, W. C. Choy, *Adv. Funct. Mater.* **2021**, 31, 2100516.
- [27] Z. Liu, W. Qiu, X. Peng, G. Sun, X. Liu, D. Liu, Z. Li, F. He, C. Shen, Q. Gu, *Adv. Mater.* **2021**, 33, 2103268.
- [28] K.-L. Chu, C.-H. Chen, S.-W. Shen, C.-Y. Huang, Y.-X. Chou, M.-Y. Liao, M.-L. Tsai, C.-I. Wu, C.-C. Chueh, *Chemical Engineering Journal* **2021**, 130112.
- [29] C. H. Liao, C. H. Chen, J. Bing, C. Bailey, Y. T. Lin, T. M. Pandit, L. Granados, J. Zheng, S. Tang, B. H. Lin, *Adv. Mater.* **2021**, 2104782.
- [30] W. Tian, H. Zhou, L. Li, *Small* **2017**, 13, 1702107.
- [31] L. Dou, Y. M. Yang, J. You, Z. Hong, W.-H. Chang, G. Li, Y. Yang, *Nat. Commun.* **2014**, 5, 1.
- [32] S. González-Carrero, R. E. Galian, J. Pérez-Prieto, *Part. Part. Syst. Char* **2015**, 32, 709.
- [33] G. Grancini, M. K. Nazeeruddin, *Nat. Rev. Mater.* **2019**, 4, 4.
- [34] K. Han, J. Jin, B. Su, Z. Xia, *Trends in Chemistry* **2022**, 4, 1034.

- 
- [35] Z.-K. Tan, R. S. Moghaddam, M. L. Lai, P. Docampo, R. Higler, F. Deschler, M. Price, A. Sadhanala, L. M. Pazos, D. Credgington, *Nat. Nanotechnol* **2014**, 9, 687.
- [36] C. Wehrenfennig, G. E. Eperon, M. B. Johnston, H. J. Snaith, L. M. Herz, *Adv. Mater.* **2013**, 26, 1584.
- [37] J. Burschka, N. Pellet, S.-J. Moon, R. Humphry-Baker, P. Gao, M. K. Nazeeruddin, M. Grätzel, *Nature* **2013**, 499, 316.
- [38] A. Filippetti, A. Mattoni, *Phys. Rev. B* **2014**, 89, 125203.
- [39] G. Xing, N. Mathews, S. Sun, S. S. Lim, Y. M. Lam, M. Grätzel, S. Mhaisalkar, T. C. Sum, *Science* **2013**, 342, 344.
- [40] A. Sadhanala, S. Ahmad, B. Zhao, N. Giesbrecht, P. M. Pearce, F. Deschler, R. L. Hoye, K. C. Gödel, T. Bein, P. Docampo, *Nano Lett.* **2015**, 15, 6095.
- [41] M. M. Byranvand, C. Otero-Martínez, J. Ye, W. Zuo, L. Manna, M. Saliba, R. L. Hoye, L. Polavarapu, *Adv. Opt. Mater.* **2022**, 10, 2200423.
- [42] F. Zhang, R. Guo, H. Zeng, L. Wang, *Adv. Funct. Mater.* **2025**, 2500348.
- [43] M. D. Smith, B. A. Connor, H. I. Karunadasa, *Chem. Rev.* **2019**, 119, 3104.
- [44] M. D. Smith, H. I. Karunadasa, *Accounts Chem. Res.* **2018**, 51, 619.
- [45] C. Katan, N. Mercier, J. Even, *Chem. Rev.* **2019**, 119, 3140.
- [46] L. Mao, W. Ke, L. Pedesseau, Y. Wu, C. Katan, J. Even, M. R. Wasielewski, C. C. Stoumpos, M. G. Kanatzidis, *JACS* **2018**, 140, 3775.
- [47] J.-C. Blancon, H. Tsai, W. Nie, C. C. Stoumpos, L. Pedesseau, C. Katan, M. Kepenekian, C. M. M. Soe, K. Appavoo, M. Y. Sfeir, *Science* **2017**, 355, 1288.
- [48] H. Tsai, W. Nie, J.-C. Blancon, C. C. Stoumpos, R. Asadpour, B. Harutyunyan, A. J. Neukirch, R. Verduzco, J. J. Crochet, S. Tretiak, *Nature* **2016**, 536, 312.
- [49] J.-C. Blancon, A. V. Stier, H. Tsai, W. Nie, C. C. Stoumpos, B. Traore, L. Pedesseau, M. Kepenekian, F. Katsutani, G. Noe, *Nat. Commun.* **2018**, 9, 2254.
- [50] L. N. Quan, Y. Zhao, F. P. García de Arquer, R. Sabatini, G. Walters, O. Voznyy, R. Comin, Y. Li, J. Z. Fan, H. Tan, *Nano Lett.* **2017**, 17, 3701.
- [51] M. Yuan, L. N. Quan, R. Comin, G. Walters, R. Sabatini, O. Voznyy, S. Hoogland, Y. Zhao, E. M. Beauregard, P. Kanjanaboos, *Nat. Nanotechnol* **2016**, 11, 872.
- [52] Y. Cao, N. Wang, H. Tian, J. Guo, Y. Wei, H. Chen, Y. Miao, W. Zou, K. Pan, Y. He, *Nature* **2018**, 562, 249.

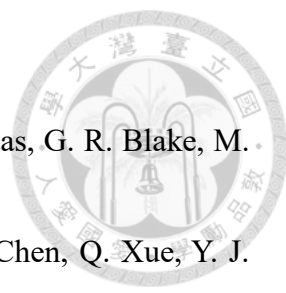
- 
- [53] J.-K. Chen, B.-B. Zhang, Q. Liu, N. Shirahata, O. F. Mohammed, O. M. Bakr, H.-T. Sun, *ACS Mater. Lett.* **2021**, 3, 1541.
- [54] M. Era, S. Morimoto, T. Tsutsui, S. Saito, *Appl. Phys. Lett.* **1994**, 65, 676.
- [55] S. Q. Sun, J. W. Tai, W. He, Y. J. Yu, Z. Q. Feng, Q. Sun, K. N. Tong, K. Shi, B. C. Liu, M. Zhu, *Adv. Mater.* **2024**, 36, 2400421.
- [56] S. C. Feng, Y. Shen, X. M. Hu, Z. H. Su, K. Zhang, B. F. Wang, L. X. Cao, F. M. Xie, H. Z. Li, X. Gao, *Adv. Mater.* **2024**, 36, 2410255.
- [57] Y. Gao, Q. Cai, Y. He, D. Zhang, Q. Cao, M. Zhu, Z. Ma, B. Zhao, H. He, D. Di, *Sci. Adv.* **2024**, 10, eado5645.
- [58] Z. Wei, J. Xing, *J. Phys. Chem. Lett.* **2019**, 10, 3035.
- [59] A. Fakharuddin, M. K. Gangishetty, M. Abdi-Jalebi, S.-H. Chin, A. R. bin Mohd Yusoff, D. N. Congreve, W. Tress, F. Deschler, M. Vasilopoulou, H. J. Bolink, *Nat. Electronics* **2022**, 5, 203.
- [60] Y. Xia, Y. H. Li, Z. K. Wang, L. S. Liao, *Adv. Funct. Mater.* **2023**, 2303423.
- [61] K. Yang, F. Li, H. Hu, T. Guo, T. W. Kim, *Nano Energy* **2019**, 65, 104029.
- [62] T.-H. Han, K. Y. Jang, Y. Dong, R. H. Friend, E. H. Sargent, T.-W. Lee, *Nat. Rev. Mater.* **2022**, 7, 757.
- [63] B. Zhao, B. Guo, S. Xing, Z. Liu, Y. Yuan, Z. Ren, W. Tang, Y. Lian, G. Zhang, C. Zou, *Matter* **2024**, 7, 772.
- [64] J. Li, S. G. R. Bade, X. Shan, Z. Yu, *Adv. Mater.* **2015**, 27, 5196.
- [65] M.-Y. Huang, L. Veeramuthu, C.-C. Kuo, Y.-C. Liao, D.-H. Jiang, F.-C. Liang, Z.-L. Yan, R. Borsali, C.-C. Chueh, *Org. Electron.* **2019**, 67, 294.
- [66] G. Li, Z.-K. Tan, D. Di, M. L. Lai, L. Jiang, J. H.-W. Lim, R. H. Friend, N. C. Greenham, *Nano Lett.* **2015**, 15, 2640.
- [67] P. Chen, Z. Xiong, X. Wu, M. Shao, Y. Meng, Z.-h. Xiong, C. Gao, *J. Phys. Chem. Lett.* **2017**, 8, 3961.
- [68] P. Chen, Z. Xiong, X. Wu, M. Shao, X. Ma, Z.-h. Xiong, C. Gao, *J. Phys. Chem. Lett.* **2017**, 8, 1810.
- [69] X. Sun, C. Han, K. Wang, H. Yu, J. Li, K. Lu, J. Qin, H. Yang, L. Deng, F. Zhao, *ACS Appl. Energy Mater.* **2018**, 1, 6992.
- [70] J. Wang, N. Wang, Y. Jin, J. Si, Z. K. Tan, H. Du, L. Cheng, X. Dai, S. Bai, H. He, *Adv. Mater.* **2015**, 27, 2311.

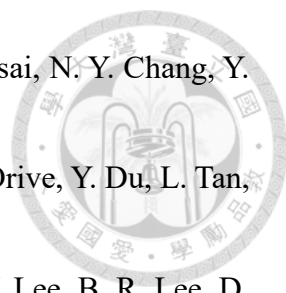
- 
- [71] C.-L. Tsai, Y.-C. Lu, S.-E. Chiang, C.-M. Yu, H.-M. Cheng, C.-L. Hsu, K. Y. Chiu, S. H. Chang, *Nanoscale* **2020**, 12, 4061.
- [72] Y. Zhou, S. Mei, J. Feng, D. Sun, F. Mei, J. Xu, X. Cao, *RSC Adv.* **2020**, 10, 26381.
- [73] B. R. Lee, J. C. Yu, J. H. Park, S. Lee, C.-K. Mai, B. Zhao, M. S. Wong, E. D. Jung, Y. S. Nam, S. Y. Park, *ACS Nano* **2018**, 12, 5826.
- [74] H. Cho, S.-H. Jeong, M.-H. Park, Y.-H. Kim, C. Wolf, C.-L. Lee, J. H. Heo, A. Sadhanala, N. Myoung, S. Yoo, *Science* **2015**, 350, 1222.
- [75] Y. H. Kim, H. Cho, J. H. Heo, T. S. Kim, N. Myoung, C. L. Lee, S. H. Im, T. W. Lee, *Adv. Mater.* **2015**, 27, 1248.
- [76] C.-H. Chen, C.-H. Hsu, I.-C. Ni, B.-H. Lin, C.-I. Wu, C.-C. Kuo, C.-C. Chueh, *Nanoscale* **2022**.
- [77] C.-H. Chen, Y.-H. Kuo, Y.-K. Lin, I.-C. Ni, B.-H. Lin, C.-I. Wu, H.-L. Yip, C.-C. Kuo, C.-C. Chueh, *ACS Appl. Mater. Inter.* **2022**, 14, 9587.
- [78] M. Ban, Y. Zou, J. P. Rivett, Y. Yang, T. H. Thomas, Y. Tan, T. Song, X. Gao, D. Credginton, F. Deschler, *Nat. Commun.* **2018**, 9, 1.
- [79] Y. H. Zhou, Y. H. Lou, X. Q. Wang, K. L. Wang, J. Chen, C. H. Chen, Z. K. Wang, *Adv. Opt. Mater.* **2022**, 10, 2101655.
- [80] Y. K. Lin, C. H. Chen, Y. Y. Wang, M. H. Yu, J. W. Yang, I. C. Ni, B. H. Lin, I. S. Zhidkov, E. Z. Kurmaev, Y. J. Lu, *Adv. Sci.* **2023**, 10, 2302232.
- [81] X. Yang, X. Zhang, J. Deng, Z. Chu, Q. Jiang, J. Meng, P. Wang, L. Zhang, Z. Yin, J. You, *Nat. Commun.* **2018**, 9, 1.
- [82] T. H. Chowdhury, Y. Reo, A. R. B. M. Yusoff, Y. Y. Noh, *Adv. Sci.* **2022**, 2203749.
- [83] L. Zhang, C. Sun, T. He, Y. Jiang, J. Wei, Y. Huang, M. Yuan, *Light-Sci. Appl.* **2021**, 10, 1.
- [84] S. A. Veldhuis, P. P. Boix, N. Yantara, M. Li, T. C. Sum, N. Mathews, S. G. Mhaisalkar, *Adv. Mater.* **2016**, 28, 6804.
- [85] C.-H. Chen, Y.-C. Lin, Y.-F. Yang, Y.-C. Chiang, Z. Li, H.-L. Yip, W.-C. Chen, C.-C. Chueh, *Mater. Chem. Front.* **2021**.
- [86] C. H. Chen, M. H. Yu, Y. Y. Wang, Y. C. Tseng, I. H. Chao, I. C. Ni, B. H. Lin, Y. J. Lu, C. C. Chueh, *Small* **2024**, 2307774.
- [87] J. C. Yu, D. B. Kim, G. Baek, B. R. Lee, E. D. Jung, S. Lee, J. H. Chu, D. K. Lee, K. J. Choi, S. Cho, *Adv. Mater.* **2015**, 27, 3492.

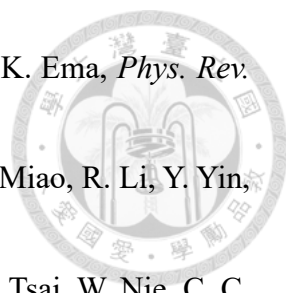
- 
- [88] R. L. Hoye, M. R. Chua, K. P. Musselman, G. Li, M. L. Lai, Z. K. Tan, N. C. Greenham, J. L. MacManus-Driscoll, R. H. Friend, D. Credgington, *Adv. Mater.* **2015**, 27, 1414.
- [89] N. K. Kumawat, A. Dey, K. Narasimhan, D. Kabra, *ACS Photonics* **2015**, 2, 349.
- [90] L. Xu, J. Li, B. Cai, J. Song, F. Zhang, T. Fang, H. Zeng, *Nat. Commun.* **2020**, 11, 1.
- [91] C. Zhang, S. Wang, X. Li, M. Yuan, L. Turyanska, X. Yang, *Adv. Funct. Mater.* **2020**, 30, 1910582.
- [92] J. H. Park, A.-y. Lee, J. C. Yu, Y. S. Nam, Y. Choi, J. Park, M. H. Song, *ACS Appl. Mater. Inter.* **2019**, 11, 8428.
- [93] X. Wan, Z. Yu, W. Tian, F. Huang, S. Jin, X. Yang, Y.-B. Cheng, A. Hagfeldt, L. Sun, *J. Energy Chem.* **2020**, 46, 8.
- [94] N. F. Jamaludin, N. Yantara, Y. F. Ng, A. Bruno, B. K. Chandran, X. Y. Chin, K. Thirumal, N. Mathews, C. Soci, S. Mhaisalkar, *J. Mater. Chem. C* **2018**, 6, 2295.
- [95] X. Liu, X. Guo, Y. Lv, Y. Hu, Y. Fan, J. Lin, X. Liu, X. Liu, *Adv. Opt. Mater.* **2018**, 6, 1801245.
- [96] H. Wang, X. Zhang, Q. Wu, F. Cao, D. Yang, Y. Shang, Z. Ning, W. Zhang, W. Zheng, Y. Yan, *Nat. Commun.* **2019**, 10, 1.
- [97] Y. S. Lau, Z. Lan, N. Li, F. Zhu, *ACS Appl. Electron. Mater.* **2020**, 2, 1113.
- [98] F. Jin, B. Zhao, B. Chu, H. Zhao, Z. Su, W. Li, F. Zhu, *J. Mater. Chem. C* **2018**, 6, 1573.
- [99] B. Liu, L. Wang, H. Gu, H. Sun, H. V. Demir, *Adv. Opt. Mater.* **2018**, 6, 1800220.
- [100] D.-H. Kang, S.-G. Kim, Y. C. Kim, I. T. Han, H. J. Jang, J. Y. Lee, N.-G. Park, *ACS Energy Lett.* **2020**, 5, 2191.
- [101] A. G. Ricciardulli, S. Yang, N. B. Kotadiya, G. J. A. Wetzelaer, X. Feng, P. W. Blom, *Adv. Electron. Mater.* **2019**, 5, 1800687.
- [102] J. Dong, D. Song, J. Meng, Y. Lu, Y. Li, B. Qiao, S. Zhao, Z. Xu, *J. Mater. Chem. C* **2020**, 8, 6743.
- [103] Y. Meng, M. Ahmadi, X. Wu, T. Xu, L. Xu, Z. Xiong, P. Chen, *Org. Electron.* **2019**, 64, 47.
- [104] X.-F. Peng, X.-Y. Wu, X.-X. Ji, J. Ren, Q. Wang, G.-Q. Li, X.-H. Yang, *J. Phys. Chem. Lett.* **2017**, 8, 4691.

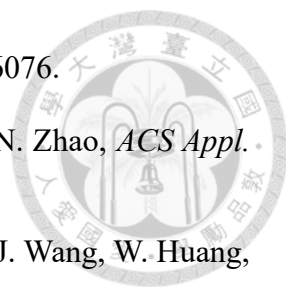
- 
- [105] Q. Wang, C.-C. Chueh, M. Eslamian, A. K.-Y. Jen, *ACS Appl. Mater. Inter.* **2016**, 8, 32068.
- [106] M. Wang, M. Zhou, L. Zhu, Q. Li, C. Jiang, *Sol. Energy* **2016**, 129, 175.
- [107] C. Song, Z. Zhong, Z. Hu, J. Wang, L. Wang, L. Ying, J. Wang, Y. Cao, *Org. Electron.* **2016**, 28, 252.
- [108] Z. Li, Z. Chen, Y. Yang, Q. Xue, H.-L. Yip, Y. J. N. c. Cao, **2019**, 10, 1.
- [109] C.-H. Gao, X.-J. Ma, Y. Zhang, F.-X. Yu, Z.-Y. Xiong, Z.-Q. Wang, R. Wang, Y.-L. Jia, D.-Y. Zhou, Z.-H. Xiong, *RSC Adv.* **2018**, 8, 15698.
- [110] C. Bi, Q. Wang, Y. Shao, Y. Yuan, Z. Xiao, J. Huang, *Nat. Commun.* **2015**, 6, 7747.
- [111] L.-C. Chen, Z.-L. Tseng, D.-W. Lin, Y.-S. Lin, S.-H. Chen, *Nanomaterials* **2018**, 8, 459.
- [112] Z. Wang, Z. Luo, C. Zhao, Q. Guo, Y. Wang, F. Wang, X. Bian, A. Alsaedi, T. Hayat, Z. a. J. T. J. o. P. C. C. Tan, **2017**, 121, 28132.
- [113] M. Zhao, Y. Shi, J. Dai, J. Lian, *J. Mater. Chem. C* **2018**, 6, 10450.
- [114] T. M. Brenner, D. A. Egger, L. Kronik, G. Hodes, D. Cahen, *Nat. Rev. Mater.* **2016**, 1, 1.
- [115] B. Saparov, D. B. Mitzi, *Chem. Rev.* **2016**, 116, 4558.
- [116] Y.-H. Kim, H. Cho, T.-W. Lee, *P. Natl. Acad. Sci* **2016**, 113, 11694.
- [117] Y. Zhao, K. J. C. S. R. Zhu, *Chem. Soc. Rev.* **2016**, 45, 655.
- [118] C. C. Stoumpos, M. G. Kanatzidis, *Accounts Chem. Res.* **2015**, 48, 2791.
- [119] W. Li, Z. Wang, F. Deschler, S. Gao, R. H. Friend, A. K. Cheetham, *Nat. Rev. Mater.* **2017**, 2, 1.
- [120] M. I. Saidaminov, O. F. Mohammed, O. M. J. A. E. L. Bakr, **2017**, 2, 889.
- [121] S. Chen, G. Shi, *Adv. Mater.* **2017**, 29, 1605448.
- [122] Y. Chen, Y. Sun, J. Peng, J. Tang, K. Zheng, Z. J. A. M. Liang, **2018**, 30, 1703487.
- [123] J.-P. Correa-Baena, A. Abate, M. Saliba, W. Tress, T. J. Jacobsson, M. Grätzel, A. Hagfeldt, *Energ. Environ. Sci.* **2017**, 10, 710.
- [124] T. M. Koh, K. Thirumal, H. S. Soo, N. Mathews, *Chem. Sus. Chem.* **2016**, 9, 2541.

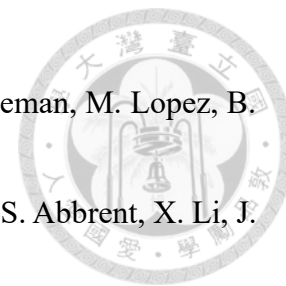


- 
- [125] Z. Cheng, J. Lin, *Cryst. Eng. Comm.* **2010**, 12, 2646.
- [126] M. E. Kamminga, H.-H. Fang, M. R. Filip, F. Giustino, J. Baas, G. R. Blake, M. A. Loi, T. T. Palstra, *Chem. Mater.* **2016**, 28, 4554.
- [127] Z. Chen, C. Zhang, X. F. Jiang, M. Liu, R. Xia, T. Shi, D. Chen, Q. Xue, Y. J. Zhao, S. J. A. M. Su, **2017**, 29, 1603157.
- [128] J. Byun, H. Cho, C. Wolf, M. Jang, A. Sadhanala, R. H. Friend, H. Yang, T. W. Lee, *Adv. Mater.* **2016**, 28, 7515.
- [129] C. C. Stoumpos, D. H. Cao, D. J. Clark, J. Young, J. M. Rondinelli, J. I. Jang, J. T. Hupp, M. G. Kanatzidis, *Chem. Mater.* **2016**, 28, 2852.
- [130] I. C. Smith, E. T. Hoke, D. Solis-Ibarra, M. D. McGehee, H. I. Karunadasa, *Angew. Chem.* **2014**, 53, 11232.
- [131] D. H. Cao, C. C. Stoumpos, O. K. Farha, J. T. Hupp, M. G. Kanatzidis, *JACS* **2015**, 137, 7843.
- [132] Y. Tian, C. Zhou, M. Worku, X. Wang, Y. Ling, H. Gao, Y. Zhou, Y. Miao, J. Guan, B. Ma, *Adv. Mater.* **2018**, 30, 1707093.
- [133] M. Dion, M. Ganne, M. Tournoux, *Mater. Res. Bull.* **1981**, 16, 1429.
- [134] M. Hojamberdiev, M. F. Bekheet, E. Zahedi, H. Wagata, Y. Kamei, K. Yubuta, A. Gurlo, N. Matsushita, K. Domen, K. Teshima, *Cryt. Growth Des.* **2016**, 16, 2302.
- [135] E. R. Dohner, A. Jaffe, L. R. Bradshaw, H. I. J. J. o. t. A. C. S. Karunadasa, **2014**, 136, 13154.
- [136] S. Ahmad, P. Fu, S. Yu, Q. Yang, X. Liu, X. Wang, X. Wang, X. Guo, C. J. J. Li, **2019**, 3, 794.
- [137] B. E. Cohen, M. Wierzbowska, L. J. A. F. M. Etgar, **2017**, 27, 1604733.
- [138] N. Wang, L. Cheng, R. Ge, S. Zhang, Y. Miao, W. Zou, C. Yi, Y. Sun, Y. Cao, R. Yang, *Nat. Photonics* **2016**, 10, 699.
- [139] J. Xing, F. Yan, Y. Zhao, S. Chen, H. Yu, Q. Zhang, R. Zeng, H. V. Demir, X. Sun, A. Huan, *ACS Nano* **2016**, 10, 6623.
- [140] H. Huang, F. Zhao, L. Liu, F. Zhang, X.-g. Wu, L. Shi, B. Zou, Q. Pei, H. Zhong, *ACS Appl. Mater. Inter.* **2015**, 7, 28128.
- [141] J. Wang, C. Song, Z. He, C. Mai, G. Xie, L. Mu, Y. Cun, J. Li, J. Wang, J. J. A. M. Peng, **2018**, 30, 1804137.

- 
- [142] W. L. Hong, Y. C. Huang, C. Y. Chang, Z. C. Zhang, H. R. Tsai, N. Y. Chang, Y. C. J. A. m. Chao, **2016**, 28, 8029.
- [143] Y. Ling, Y. Tian, X. Wang, J. C. Wang, J. M. Knox, F. Perez-Orive, Y. Du, L. Tan, K. Hanson, B. Ma, *Adv. Mater.* **2016**, 28, 8983.
- [144] J. C. Yu, D. W. Kim, D. B. Kim, E. D. Jung, J. H. Park, A.-Y. Lee, B. R. Lee, D. Di Nuzzo, R. H. Friend, M. H. Song, **2016**.
- [145] K. Albrecht, K. Matsuoka, D. Yokoyama, Y. Sakai, A. Nakayama, K. Fujita, K. Yamamoto, *Chem. Commun.* **2017**, 53, 2439.
- [146] X. Dai, Z. Zhang, Y. Jin, Y. Niu, H. Cao, X. Liang, L. Chen, J. Wang, X. Peng, *Nature* **2014**, 515, 96.
- [147] L. Duan, L. Hou, T.-W. Lee, J. Qiao, D. Zhang, G. Dong, L. Wang, Y. Qiu, *j. Mater. Chem.* **2010**, 20, 6392.
- [148] J. Song, J. Li, X. Li, L. Xu, Y. Dong, H. Zeng, *Adv. Mater.* **2015**, 27, 7162.
- [149] S. Y. Lee, T. Yasuda, Y. S. Yang, Q. Zhang, C. Adachi, *Angew. Chem. Int. Edit.* **2014**, 53, 6402.
- [150] K. Justin Thomas, J. T. Lin, M. Velusamy, Y. T. Tao, C. H. Chuen, *Adv. Funct. Mater.* **2004**, 14, 83.
- [151] S. Gong, Y. Chen, C. Yang, C. Zhong, J. Qin, D. Ma, *Adv. Mater.* **2010**, 22, 5370.
- [152] L. N. Quan, F. P. García de Arquer, R. P. Sabatini, E. H. Sargent, *Adv. Mater.* **2018**, 30, 1801996.
- [153] D. Yang, B. Zhao, T. Yang, R. Lai, D. Lan, R. H. Friend, D. Di, *Adv. Funct. Mater.* **2022**, 32, 2109495.
- [154] S. Adjokatse, H.-H. Fang, M. A. Loi, *Mater. Today* **2017**, 20, 413.
- [155] E. Unger, L. Kegelmann, K. Suchan, D. Sörell, L. Korte, S. Albrecht, *J. Mater. Chem. A* **2017**, 5, 11401.
- [156] M. R. Filip, G. E. Eperon, H. J. Snaith, F. Giustino, *Nat. Commun.* **2014**, 5, 5757.
- [157] S. D. Stranks, H. J. Snaith, *Nat. Nanotechnol.* **2015**, 10, 391.
- [158] A. Liu, C. Bi, R. Guo, M. Zhang, X. Qu, J. Tian, *Adv. Opt. Mater.* **2021**, 9, 2002167.
- [159] K. Wang, Z. Jin, L. Liang, H. Bian, D. Bai, H. Wang, J. Zhang, Q. Wang, S. Liu, *Nat. Commun.* **2018**, 9, 4544.

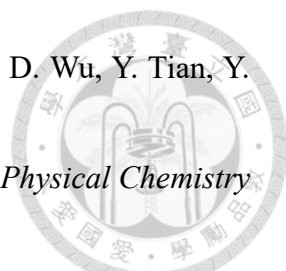
- 
- [160] K. Tanaka, T. Takahashi, T. Kondo, T. Umebayashi, K. Asai, K. Ema, *Phys. Rev. B* **2005**, 71, 045312.
- [161] S. Zhang, C. Yi, N. Wang, Y. Sun, W. Zou, Y. Wei, Y. Cao, Y. Miao, R. Li, Y. Yin, *Adv. Mater.* **2017**, 29, 1606600.
- [162] B. Traore, L. Pedesseau, L. Assam, X. Che, J.-C. Blancon, H. Tsai, W. Nie, C. C. Stoumpos, M. G. Kanatzidis, S. Tretiak, *ACS Nano* **2018**, 12, 3321.
- [163] J. Byun, H. Cho, C. Wolf, M. Jang, A. Sadhanala, R. H. Friend, H. Yang, T.-W. Lee, **2016**, 28, 7515.
- [164] Y. Jin, Z. K. Wang, S. Yuan, Q. Wang, C. Qin, K. L. Wang, C. Dong, M. Li, Y. Liu, L. S. J. A. F. M. Liao, **2020**, 30, 1908339.
- [165] F. Wang, Z. Wang, W. Sun, Z. Wang, Y. Bai, T. Hayat, A. Alsaedi, Z. a. Tan, *Small* **2020**, 16, 2002940.
- [166] Z. Chu, Q. Ye, Y. Zhao, F. Ma, Z. Yin, X. Zhang, J. You, *Adv. Mater.* **2021**, 33, 2007169.
- [167] B. Han, S. Yuan, T. Fang, F. Zhang, Z. Shi, J. Song, *ACS Appl. Mater. Interfaces.* **2020**, 12, 14224.
- [168] W. Xu, Q. Hu, S. Bai, C. Bao, Y. Miao, Z. Yuan, T. Borzda, A. J. Barker, E. Tyukalova, Z. Hu, *Nat. Photonics* **2019**, 13, 418.
- [169] J. Xing, Y. Zhao, M. Askerka, L. N. Quan, X. Gong, W. Zhao, J. Zhao, H. Tan, G. Long, L. J. N. c. Gao, **2018**, 9, 1.
- [170] L. Na Quan, D. Ma, Y. Zhao, O. Voznyy, H. Yuan, E. Bladt, J. Pan, F. P. García de Arquer, R. Sabatini, Z. Piontkowski, *Nat. Commun.* **2020**, 11, 170.
- [171] C. Zhao, W. Wu, H. Zhan, W. Yuan, H. Li, D. Zhang, D. Wang, Y. Cheng, S. Shao, C. Qin, *Angew. Chem., Int. Ed.* **2022**, 134, e202117374.
- [172] N. F. Jamaludin, N. Yantara, B. Febriansyah, Y. B. Tay, B. T. Muhammad, S. Laxmi, S. S. Lim, T. C. Sum, S. Mhaisalkar, N. Mathews, *ACS Energy Lett.* **2021**, 6, 4265.
- [173] M. Li, Y. Zhao, X. Qin, Q. Ma, J. Lu, K. Lin, P. Xu, Y. Li, W. Feng, W.-H. Zhang, *Nano Lett.* **2022**, 22, 2490.
- [174] C. Zhu, F. Yuan, X. Liu, J. Li, H. Dong, C. Zhao, L. Yan, Y. Xu, J. Dai, J. Si, *J. Phys. Chem. Lett.* **2021**, 12, 11723.
- [175] Y. Miao, X. Liu, Y. Chen, T. Zhang, T. Wang, Y. Zhao, *Adv. Mater.* **2021**, 33, 2105699.

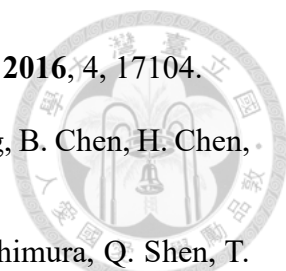
- 
- [176] C. Zou, Y. Liu, D. S. Ginger, L. Y. Lin, *ACS Nano* **2020**, 14, 6076.
- [177] Y. Jia, H. Yu, Y. Zhou, N. Li, Y. Guo, F. Xie, Z. Qin, X. Lu, N. Zhao, *ACS Appl. Mater. Interfaces* **2021**, 13, 28546.
- [178] M. Yang, N. Wang, S. Zhang, W. Zou, Y. He, Y. Wei, M. Xu, J. Wang, W. Huang, *J. Phys. Chem. Lett.* **2018**, 9, 2038.
- [179] M. U. Ali, J. Miao, J. Cai, D. F. Perepichka, H. Yang, H. Meng, *ACS Appl. Mater. Inter.* **2020**, 12, 18761.
- [180] R. Kabe, C. Adachi, *Nature* **2017**, 550, 384.
- [181] J. U. Kim, I. S. Park, C.-Y. Chan, M. Tanaka, Y. Tsuchiya, H. Nakanotani, C. Adachi, *Nat. Commun.* **2020**, 11, 1765.
- [182] T. Miwa, S. Kubo, K. Shizu, T. Komino, C. Adachi, H. Kaji, *Sci. Rep.* **2017**, 7, 284.
- [183] Y.-S. Tsai, L.-A. Hong, F.-S. Juang, C.-Y. Chen, *J. lumin.* **2014**, 153, 312.
- [184] Z. Yu, W. H. Jeong, K. Kang, H. Song, X. Shen, H. Ahn, S. W. Lee, X. Fan, J. W. Jang, S. R. Ha, *J. Mater. Chem. A* **2022**, 10, 13928.
- [185] J. Wang, M. Qin, H. Tao, W. Ke, Z. Chen, J. Wan, P. Qin, L. Xiong, H. Lei, H. Yu, *Appl. Phys. Lett.* **2015**, 106.
- [186] D. Ma, K. Lin, Y. Dong, H. Choubisa, A. H. Proppe, D. Wu, Y.-K. Wang, B. Chen, P. Li, J. Z. J. N. Fan, **2021**, 599, 594.
- [187] X. Chen, J. Huang, F. Gao, B. Xu, *Chem* **2023**, 9, 562.
- [188] G. Pan, X. Bai, X. Shen, L. Wang, Y. Mao, X. Chen, W. Xu, H. Shao, D. Zhou, B. Dong, *Nano Energy* **2021**, 81, 105615.
- [189] Y. Xia, Y. H. Lou, Y. H. Zhou, Y. R. Shi, K. L. Wang, L. Cai, C. H. Chen, F. Hu, Z. K. Wang, L. S. Liao, *Adv. Funct. Mater.* **2022**, 32, 2208538.
- [190] D. Jiang, T. Jiang, Y. Tian, K. Wen, C. Duan, N. Wang, Q. Li, J. Wang, H. Xu, *J. Mater. Chem. C* **2021**, 9, 6399.
- [191] R. Wang, Y. Zhang, F.-X. Yu, Y. Dong, Y.-L. Jia, X.-J. Ma, Q. Xu, Y. Deng, Z.-H. Xiong, C.-H. Gao, *J. Lumin.* **2020**, 219, 116915.
- [192] R. H. Bube, *J. Appl. Phys.* **1962**, 33, 1733.
- [193] A. Fakharuddin, W. Qiu, G. Croes, A. Devižis, R. Gegevičius, A. Vakhnin, C. Rolin, J. Genoe, R. Gehlhaar, A. Kadashchuk, *Adv. Funct. Mater.* **2019**, 29, 1904101.



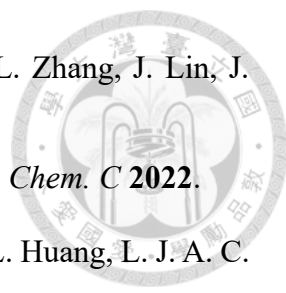
- [194] H. Kim, L. Zhao, J. S. Price, A. J. Grede, K. Roh, A. N. Brigeman, M. Lopez, B. P. Rand, N. C. Giebink, *Nat. Commun.* **2018**, 9, 4893.
- [195] Y. Zou, P. Teng, W. Xu, G. Zheng, W. Lin, J. Yin, L. Kobera, S. Abbrent, X. Li, J. A. Steele, *Nat. Commun.* **2021**, 12, 4831.
- [196] Y. Tian, X.-Y. Qian, C.-C. Qin, M.-H. Cui, Y.-Q. Li, Y.-C. Ye, J.-K. Wang, W.-J. Wang, J.-X. Tang, *Chem. Eng. J.* **2021**, 415, 129088.
- [197] D. Zhang, L. Chao, G. Jin, Z. Xing, W. Hong, Y. Chen, L. Wang, J. Chen, D. Ma, *Adv. Funct. Mater.* **2022**, 32, 2205707.
- [198] Z. Chen, Z. Li, C. Zhang, X. F. Jiang, D. Chen, Q. Xue, M. Liu, S. Su, H. L. Yip, Y. Cao, *Adv. Mater.* **2018**, 30, 1801370.
- [199] Y. Shen, K. C. Shen, Y. Q. Li, M. Guo, J. Wang, Y. Ye, F. M. Xie, H. Ren, X. Gao, F. Song, *Adv. Funct. Mater.* **2020**, 2006736.
- [200] M.-L. Guo, Y. Lu, X.-Y. Cai, Y. Shen, X.-Y. Qian, H. Ren, Y.-Q. Li, W.-J. Wang, J.-X. Tang, *J. Mater. Chem. C* **2022**, 10, 2998.
- [201] Y. Shen, J. K. Wang, Y. Q. Li, K. C. Shen, Z. H. Su, L. Chen, M. L. Guo, X. Y. Cai, F. M. Xie, X. Y. Qian, *Adv. Sci.* **2021**, 8, 2102213.
- [202] H. Zhang, H. Lin, C. Liang, H. Liu, J. Liang, Y. Zhao, W. Zhang, M. Sun, W. Xiao, H. Li, *Adv. Funct. Mater.* **2015**, 25, 7226.
- [203] X. Xiao, T. Ye, J. Sun, X. Qu, Z. Ren, D. Wu, S. Ding, X. W. Sun, W. C. Choy, K. Wang, *Appl. Phys. Lett.* **2022**, 120.
- [204] R. Trattnig, T. M. Figueira-Duarte, D. Lorbach, W. Wiedemair, S. Sax, S. Winkler, A. Vollmer, N. Koch, M. Manca, M. A. Loi, *Opt. Express* **2011**, 19, A1281.
- [205] S. Pisoni, F. Fu, R. Widmer, R. Carron, T. Moser, O. Groening, A. N. Tiwari, S. Buecheler, *Nano Energy* **2018**, 49, 300.
- [206] J. Byeon, J. Kim, J.-Y. Kim, G. Lee, K. Bang, N. Ahn, M. Choi, *ACS Energy Lett.* **2020**, 5, 2580.
- [207] L. Cheng, T. Jiang, Y. Cao, C. Yi, N. Wang, W. Huang, J. Wang, *Adv. Mater.* **2020**, 32, 1904163.
- [208] T. H. Han, S. Tan, J. Xue, L. Meng, J. W. Lee, Y. Yang, *Adv. Mater.* **2019**, 31, 1803515.
- [209] K. Lin, J. Xing, L. N. Quan, F. P. G. de Arquer, X. Gong, J. Lu, L. Xie, W. Zhao, D. Zhang, C. Yan, *Nature* **2018**, 562, 245.

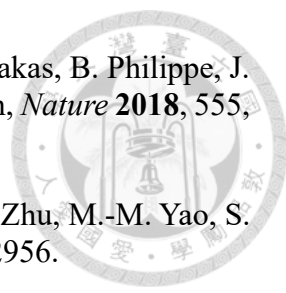
- 
- [210] W. Bai, T. Xuan, H. Zhao, H. Dong, X. Cheng, L. Wang, R. J. Xie, *Adv. Mater.* **2023**, 2302283.
- [211] J. S. Kim, J.-M. Heo, G.-S. Park, S.-J. Woo, C. Cho, H. J. Yun, D.-H. Kim, J. Park, S.-C. Lee, S.-H. Park, *Nature* **2022**, 611, 688.
- [212] J. Jiang, Z. Chu, Z. Yin, J. Li, Y. Yang, J. Chen, J. Wu, J. You, X. Zhang, *Adv. Mater.* **2022**, 34, 2204460.
- [213] L. Zhu, H. Cao, C. Xue, H. Zhang, M. Qin, J. Wang, K. Wen, Z. Fu, T. Jiang, L. Xu, *Nat. Commun.* **2021**, 12, 1.
- [214] Y. Sun, L. Ge, L. Dai, C. Cho, J. Ferrer Orri, K. Ji, S. J. Zelewski, Y. Liu, A. J. Mirabelli, Y. Zhang, *Nature* **2023**, 615, 830.
- [215] B. Guo, R. Lai, S. Jiang, L. Zhou, Z. Ren, Y. Lian, P. Li, X. Cao, S. Xing, Y. Wang, *Nat. Photonics* **2022**, 16, 637.
- [216] Z. Chu, W. Zhang, J. Jiang, Z. Qu, F. Ma, Y. Zhao, X. Chu, Y. Shen, Y. Li, Z. Yin, *Nat. Electronics* **2023**, 6, 360.
- [217] J. Dong, F. Lu, D. Han, J. Wang, Z. Zang, L. Kong, Y. Zhang, X. Ma, J. Zhou, H. Ji, *Angew. Chem.* **2022**, e202210322.
- [218] C. Wang, S. Cui, Y. Ju, Y. Chen, S. Chang, H. Zhong, *Adv. Funct. Mater.* **2023**, 2301304.
- [219] Z.-G. Ma, Y. Shen, K. Zhang, L.-X. Cao, H. Ren, W.-S. Chen, H. Wei, Y. Li, S. Kera, J. Tang, *J. Mater. Chem. C* **2023**, 11, 9916.
- [220] T. Li, H. Zhang, C. Yu, P. Wang, H. Wang, X. Zhang, Y. Sun, D. Liu, T. Wang, *J. Mater. Chem. C* **2021**, 9, 15488.
- [221] J.-M. Heo, H. Cho, S.-C. Lee, M.-H. Park, J. S. Kim, H. Kim, J. Park, Y.-H. Kim, H. J. Yun, E. Yoon, *ACS Energy Lett.* **2022**, 7, 2807.
- [222] Y.-H. Cheng, R. Moriyama, H. Ebe, K. Mizuguchi, R. Yamakado, S. Nishitsuji, T. Chiba, J. Kido, *ACS Appl. Mater. Inter.* **2022**, 14, 22941.
- [223] K. Wang, L. Jin, Y. Gao, A. Liang, B. P. Finkenauer, W. Zhao, Z. Wei, C. Zhu, T.-F. Guo, L. Huang, *ACS Nano* **2021**, 15, 6316.
- [224] J. Lu, X. Guan, Y. Li, K. Lin, W. Feng, Y. Zhao, C. Yan, M. Li, Y. Shen, X. Qin, *Adv. Mater.* **2021**, 33, 2104414.
- [225] Z. Ma, Z. Shi, C. Qin, M. Cui, D. Yang, X. Wang, L. Wang, X. Ji, X. Chen, J. Sun, *ACS Nano* **2020**, 14, 4475.

- 
- [226] Z. Ma, Z. Shi, D. Yang, Y. Li, F. Zhang, L. Wang, X. Chen, D. Wu, Y. Tian, Y. Zhang, *Adv. Mater.* **2021**, 33, 2001367.
- [227] P. Cheng, T. Wu, J. Liu, W.-Q. Deng, K. Han, *The Journal of Physical Chemistry Letters* **2018**, 9, 2518.
- [228] M. Leng, Y. Yang, K. Zeng, Z. Chen, Z. Tan, S. Li, J. Li, B. Xu, D. Li, M. P. Hautzinger, *Adv. Funct. Mater.* **2018**, 28, 1704446.
- [229] X. Li, B. Traore, M. Kepenekian, L. Li, C. C. Stoumpos, P. Guo, J. Even, C. Katan, M. G. Kanatzidis, *Chem. Mater.* **2021**, 33, 6206.
- [230] J. Luo, L. Yang, Z. Tan, W. Xie, Q. Sun, J. Li, P. Du, Q. Xiao, L. Wang, X. Zhao, *Adv. Mater.* **2021**, 33, 2101903.
- [231] J. Huang, T. Lei, M. Siron, Y. Zhang, S. Yu, F. Seeler, A. Dehestani, L. N. Quan, K. Schierle-Arndt, P. Yang, *Nano Lett.* **2020**, 20, 3734.
- [232] T. Nakamura, S. Yakumar, M. A. Truong, K. Kim, J. Liu, S. Hu, K. Otsuka, R. Hashimoto, R. Murdey, T. Sasamori, *Nat. Commun.* **2020**, 11, 1.
- [233] I. H. Chao, Y. T. Yang, M. H. Yu, C. H. Chen, C. H. Liao, B. H. Lin, I. C. Ni, W. C. Chen, A. W. Ho-Baillie, C. C. J. S. Chueh, **2023**, 2207734.
- [234] X. Guan, J. Lu, Q. Wei, Y. Li, Y. Meng, K. Lin, Y. Zhao, W. Feng, K. Liu, G. Xing, *ACS Energy Lett.* **2023**, 8, 1597.
- [235] F. Zhang, H. Min, Y. Zhang, Z. Kuang, J. Wang, Z. Feng, K. Wen, L. Xu, C. Yang, H. Shi, *Adv. Mater.* **2022**, 34, 2203180.
- [236] H. Jia, H. Shi, R. Yu, H. Ma, Z. Wang, C. Zou, Z. a. Tan, *Small* **2022**, 2200036.
- [237] T. Matsushima, S. Hwang, A. S. Sandanayaka, C. Qin, S. Terakawa, T. Fujihara, M. Yahiro, C. Adachi, *Adv. Mater.* **2016**, 28, 10275.
- [238] I. Zimmermann, S. Aghazada, M. K. J. A. C. Nazeeruddin, **2019**, 131, 1084.
- [239] C. Gao, Y. Jiang, C. Sun, J. Han, T. He, Y. Huang, K. Yao, M. Han, X. Wang, Y. Wang, *ACS Photonics* **2020**, 7, 1915.
- [240] Y. Su, J. Yang, G. Liu, W. Sheng, J. Zhang, Y. Zhong, L. Tan, Y. Chen, *Adv. Funct. Mater.* **2022**, 32, 2109631.
- [241] R. Lin, K. Xiao, Z. Qin, Q. Han, C. Zhang, M. Wei, M. I. Saidaminov, Y. Gao, J. Xu, M. Xiao, *Nat. Energy* **2019**, 4, 864.
- [242] T.-B. Song, T. Yokoyama, C. C. Stoumpos, J. Logsdon, D. H. Cao, M. R. Wasielewski, S. Aramaki, M. G. Kanatzidis, *JACS* **2017**, 139, 836.

- 
- [243] W. Li, J. Li, J. Li, J. Fan, Y. Mai, L. Wang, *J. Mater. Chem. A* **2016**, *4*, 17104.
- [244] F. Yuan, X. Zheng, A. Johnston, Y.-K. Wang, C. Zhou, Y. Dong, B. Chen, H. Chen, J. Z. Fan, G. Sharma, *Sci. Adv.* **2020**, *6*, eabb0253.
- [245] M. A. Kamarudin, D. Hirotsu, Z. Wang, K. Hamada, K. Nishimura, Q. Shen, T. Toyoda, S. Iikubo, T. Minemoto, K. Yoshino, *J. Phys. Chem. Lett.* **2019**, *10*, 5277.
- [246] B. Li, H. Di, B. Chang, R. Yin, L. Fu, Y. N. Zhang, L. Yin, *Adv. Funct. Mater.* **2021**, *31*, 2007447.
- [247] F. Wang, X. Jiang, H. Chen, Y. Shang, H. Liu, J. Wei, W. Zhou, H. He, W. Liu, Z. Ning, *Joule* **2018**, *2*, 2732.
- [248] C. Liang, H. Gu, Y. Xia, Z. Wang, X. Liu, J. Xia, S. Zuo, Y. Hu, X. Gao, W. Hui, *Nat. Energy* **2021**, *6*, 38.
- [249] T. Li, Y. Wang, W. Zhu, Q. Dang, Y. Zhang, Y. Li, X. Deng, *J. Mater. Chem. A* **2022**, *10*, 14441.
- [250] Z. Wang, Q. Wei, X. Liu, L. Liu, X. Tang, J. Guo, S. Ren, G. Xing, D. Zhao, Y. Zheng, *Adv. Funct. Mater.* **2021**, *31*, 2008404.
- [251] S. Narra, C.-Y. Lin, A. Seetharaman, E. Jokar, E. W.-G. Diao, *J. phys. Chem. Lett.* **2021**, *12*, 12292.
- [252] X. Jiang, F. Wang, Q. Wei, H. Li, Y. Shang, W. Zhou, C. Wang, P. Cheng, Q. Chen, L. Chen, *Nat. Commun.* **2020**, *11*, 1245.
- [253] L. Lanzetta, J. M. Marin-Beloqui, I. Sanchez-Molina, D. Ding, S. A. Haque, *ACS Energy Lett.* **2017**, *2*, 1662.
- [254] H. Y. Liang, F. L. Yuan, A. Johnston, C. C. Gao, H. Choubisa, Y. Gao, Y. K. Wang, L. K. Sagar, B. Sun, P. C. Li, G. Bappi, B. Chen, J. Li, Y. K. Wang, Y. T. Dong, D. X. Ma, Y. N. Gao, Y. C. Liu, M. J. Yuan, M. I. Saidaminov, S. Hoogland, Z. H. Lu, E. H. Sargent, *Adv Sci* **2020**, *7*.
- [255] X. Wang, L. Liu, Z. Qian, C. Gao, H. Liang, *J. Mater. Chem. C* **2021**, *9*, 12079.
- [256] Z. Wang, F. Wang, B. Zhao, S. Qu, T. Hayat, A. Alsaedi, L. Sui, K. Yuan, J. Zhang, Z. Wei, *J. Phys. Chem. Lett.* **2020**, *11*, 1120.
- [257] F. Zhang, B. Cai, J. Song, B. Han, B. Zhang, H. Zeng, *Adv. Funct. Mater.* **2020**, 2001732.
- [258] Y. Zhang, K. Sun, L. Song, H. Xu, X. Guo, S. Xu, Y. Xia, Y. Hu, F. Ma, *J. lumin.* **2022**, *252*, 119317.



- 
- [259] T. Zhang, C. Zhou, X. Feng, N. Dong, H. Chen, X. Chen, L. Zhang, J. Lin, J. Wang, *Nat. Commun.* **2022**, 13, 60.
- [260] H. Cheng, Y. Feng, Y. Fu, Y. Zheng, Y. Shao, Y. Bai, *J. Mater. Chem. C* **2022**.
- [261] A. Liang, K. Wang, Y. Gao, B. P. Finkenauer, C. Zhu, L. Jin, L. Huang, L. J. A. C. I. E. Dou, *Angew. Chem.* **2021**, 60, 8337.
- [262] S. Kahmann, H. Duim, H. H. Fang, M. Dyksik, S. Adjokatse, M. Rivera Medina, M. Pitaro, P. Plochocka, M. A. Loi, *Adv. Funct. Mater.* **2021**, 31, 2103778.
- [263] T. L. Leung, I. Ahmad, A. A. Syed, A. M. C. Ng, J. Popović, A. B. Djurišić, *Commun. Mater.* **2022**, 3, 63.
- [264] X. Huang, W. Liu, W. Wang, Y. Lu, J. Dong, Y. Li, D. Wei, B. Qiao, S. Zhao, Z. Xu, *RSC Adv.* **2022**, 12, 3081.
- [265] X. Qu, N. Zhang, R. Cai, B. Kang, S. Chen, B. Xu, K. Wang, X. W. Sun, *Appl. Phys. Lett.* **2019**, 114.
- [266] M. Xu, Q. Peng, W. Zou, L. Gu, L. Xu, L. Cheng, Y. He, M. Yang, N. Wang, W. Huang, *Appl. Phys. Lett.* **2019**, 115.
- [267] Y.-H. Kim, J. Park, S. Kim, J. S. Kim, H. Xu, S.-H. Jeong, B. Hu, T.-W. Lee, *Nat. Nanotechnol.* **2022**, 17, 590.
- [268] X. Qian, Y. Shen, L.-J. Zhang, M. Guo, X.-Y. Cai, Y. Lu, H. Liu, Y.-F. Zhang, Y. Tang, L. Chen, *ACS Nano* **2022**, 16, 17973.
- [269] T. Ye, X. Wang, K. Wang, S. Ma, D. Yang, Y. Hou, J. Yoon, K. Wang, S. Priya, *ACS Energy Lett.* **2021**, 6, 1480.
- [270] S. Tan, I. Yavuz, N. De Marco, T. Huang, S. J. Lee, C. S. Choi, M. Wang, S. Nuryyeva, R. Wang, Y. Zhao, *Adv Mater* **2020**, 32, 1906995.
- [271] S. Zou, Y. Liu, J. Li, C. Liu, R. Feng, F. Jiang, Y. Li, J. Song, H. Zeng, M. Hong, *J Am Chem Soc* **2017**, 139, 11443.
- [272] J.-S. Yao, J. Ge, K.-H. Wang, G. Zhang, B.-S. Zhu, C. Chen, Q. Zhang, Y. Luo, S.-H. Yu, H.-B. Yao, *J Am Chem Soc* **2019**, 141, 2069.
- [273] J.-S. Yao, J. Ge, B.-N. Han, K.-H. Wang, H.-B. Yao, H.-L. Yu, J.-H. Li, B.-S. Zhu, J.-Z. Song, C. Chen, *J Am Chem Soc* **2018**, 140, 3626.
- [274] J. Cao, S. X. Tao, P. A. Bobbert, C. P. Wong, N. Zhao, *Adv Mater* **2018**, 30, 1707350.

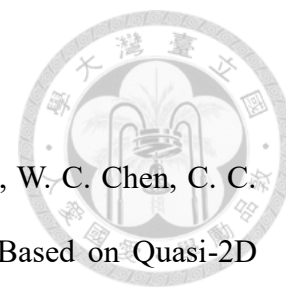
- 
- [275] M. Abdi-Jalebi, Z. Andaji-Garmaroudi, S. Cacovich, C. Stavrakas, B. Philippe, J. M. Richter, M. Alsari, E. P. Booker, E. M. Hutter, A. J. Pearson, *Nature* **2018**, 555, 497.
- [276] J.-N. Yang, Y. Song, J.-S. Yao, K.-H. Wang, J.-J. Wang, B.-S. Zhu, M.-M. Yao, S. U. Rahman, Y.-F. Lan, F.-J. Fan, *J Am Chem Soc* **2020**, 142, 2956.
- [277] M. Abdi-Jalebi, Z. Andaji-Garmaroudi, A. J. Pearson, G. Divitini, S. Cacovich, B. Philippe, H. Rensmo, C. Ducati, R. H. Friend, S. D. Stranks, *Acs Energy Lett* **2018**, 3, 2671.
- [278] S. Zhuang, X. Ma, D. Hu, X. Dong, B. Zhang, *Ceramics International* **2018**, 44, 4685.
- [279] Z. Wang, Z. Luo, C. Zhao, Q. Guo, Y. Wang, F. Wang, X. Bian, A. Alsaedi, T. Hayat, Z. a. Tan, *J. Phys. Chem. C* **2017**, 121, 28132.
- [280] Z. Shi, S. Li, Y. Li, H. Ji, X. Li, D. Wu, T. Xu, Y. Chen, Y. Tian, Y. Zhang, *ACS nano* **2018**, 12, 1462.
- [281] J. Dong, F. Lu, D. Han, J. Wang, Z. Zang, L. Kong, Y. Zhang, X. Ma, J. Zhou, H. Ji, *Angew. Chem.* **2022**, 134, e202210322.
- [282] Y. Jin, Z. K. Wang, S. Yuan, Q. Wang, C. Qin, K. L. Wang, C. Dong, M. Li, Y. Liu, L. S. Liao, *Adv. Funct. Mater.* **2020**, 30, 1908339.
- [283] P. Pang, G. Jin, C. Liang, B. Wang, W. Xiang, D. Zhang, J. Xu, W. Hong, Z. Xiao, L. Wang, *ACS Nano* **2020**, 14, 11420.
- [284] Y. Yan, Q. Zhang, Z. Wang, Q. Du, R. Tang, X. Wang, *Crystals* **2022**, 12, 1286.
- [285] Z. Li, S. Chu, Y. Zhang, W. Chen, J. Chen, Y. Yuan, S. Yang, H. Zhou, T. Chen, Z. Xiao, *Adv. Mater.* **2022**, 2203529.
- [286] J. Chen, J. Wang, X. Xu, J. Li, J. Song, S. Lan, S. Liu, B. Cai, B. Han, J. T. Pecht, *Nat. Photonics* **2020**, 1.
- [287] F. C. Liang, F. C. Jhuang, Y. H. Fang, J. S. Benas, W. C. Chen, Z. L. Yan, W. C. Lin, C. J. Su, Y. Sato, T. Chiba, *Adv. Mater.* **2022**, 2207617.
- [288] A. Mohapatra, M. R. Kar, S. Bhaumik, *Frontiers in Electronic Materials* **2022**, 2, 891983.
- [289] Y. Liu, Y. P. Gong, S. Geng, M. L. Feng, D. Manidaki, Z. Deng, C. C. Stoumpos, P. Canepa, Z. Xiao, W. X. Zhang, *Angew. Chem. Int. Ed.* **2022**, 61, e202208875.
- [290] R. Nie, R. R. Sumukam, S. H. Reddy, M. Banavoth, S. I. Seok, *Energ. Environ. Sci.* **2020**, 13, 2363.

- 
- [291] N. Ito, M. A. Kamarudin, D. Hirotani, Y. Zhang, Q. Shen, Y. Ogomi, S. Iikubo, T. Minemoto, K. Yoshino, S. Hayase, *J. Phys. Chem. Lett.* **2018**, 9, 1682.
- [292] X. Li, X. Gao, X. Zhang, X. Shen, M. Lu, J. Wu, Z. Shi, V. L. Colvin, J. Hu, X. Bai, *Adv. Sci.* **2021**, 8, 2003334.
- [293] Y. Chen, J. Wu, S. Zhang, X. Zhu, B. Zou, R. Zeng, *J. Phys. Chem. Lett.* **2023**, 14, 7108.
- [294] B. J. Moon, S. J. Kim, S. Lee, A. Lee, H. Lee, D. S. Lee, T. W. Kim, S. K. Lee, S. Bae, S. H. Lee, *Adv Mater* **2019**, 31, 1901716.
- [295] X. Zhang, F. Wang, Y. Wang, X. Wu, Q. Ou, S. Zhang, *The Journal of Physical Chemistry Letters* **2023**, 14, 5580.
- [296] Y. Li, T. Gao, Z. He, C. Shen, S. Zhou, M. Li, D. Zhang, Q. Zhang, Y. Fu, X. Mo, *npj Flexible Electronics* **2025**, 9, 32.
- [297] J. H. Jang, S. Li, D. H. Kim, J. Yang, M. K. Choi, *Adv. Electron. Mater.* **2023**, 9, 2201271.
- [298] J. Zhao, L. W. Lo, H. Wan, P. Mao, Z. Yu, C. Wang, *Adv. Mater.* **2021**, 33, 2102095.
- [299] L. Zhao, N. Rolston, K. M. Lee, X. Zhao, M. A. Reyes-Martinez, N. L. Tran, Y. W. Yeh, N. Yao, G. D. Scholes, Y. L. Loo, *Adv. Funct. Mater.* **2018**, 28, 1802060.
- [300] H. Liu, G. Shi, R. Khan, S. Chu, Z. Huang, T. Shi, H. Sun, Y. Li, H. Zhou, P. Xiao, *Adv. Mater.* **2024**, 36, 2309921.
- [301] S. Chu, W. Chen, Z. Fang, X. Xiao, Y. Liu, J. Chen, J. Huang, Z. Xiao, *Nat. Commun.* **2021**, 12, 147.
- [302] S. Chu, Y. Zhang, P. Xiao, W. Chen, R. Tang, Y. Shao, T. Chen, X. Zhang, F. Liu, Z. Xiao, *Adv. Mater.* **2022**, 34, 2108939.
- [303] C. Liu, R. Lin, Y. Wang, H. Gao, P. Wu, H. Luo, X. Zheng, B. Tang, Z. Huang, H. Sun, *Angew. Chem.* **2023**, 62, e202313374.
- [304] B. Yu, F. Tang, Y. Yang, J. Huang, S. Wu, F. Lu, W. Duan, A. Lambertz, K. Ding, Y. Mai, *Adv. Mater.* **2023**, 35, 2202447.
- [305] X. Jiang, S. Qin, L. Meng, G. He, J. Zhang, Y. Wang, Y. Zhu, T. Zou, Y. Gong, Z. Chen, *Nature* **2024**, 635, 860.
- [306] Z. He, R. Yu, Y. Dong, R. Wang, Y. Zhang, Z. a. Tan, *Nat. Commun.* **2025**, 16, 1773.
- [307] Z. Zhang, W. Chen, X. Jiang, J. Cao, H. Yang, H. Chen, F. Yang, Y. Shen, H. Yang, Q. Cheng, *Nat. Energy* **2024**, 9, 592.

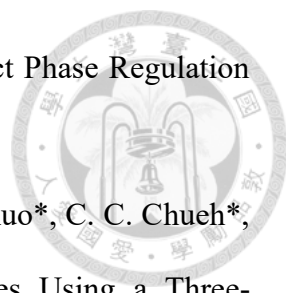
- [308] S. Wu, Y. Yan, J. Yin, K. Jiang, F. Li, Z. Zeng, S.-W. Tsang, A. K.-Y. Jen, *Nat. Energy* **2024**, 1.
- [309] Y. Cho, Z. Sun, G. Li, D. Zhang, S. Yang, T. J. Marks, C. Yang, A. Facchetti, *JACS* **2024**.



## PUBLICATION LIST



1. **C. H. Chen**, Z. Li, Q. Xue\*, Y. A. Su, C. C. Lee, H. L. Yip\*, W. C. Chen, C. C. Chueh\*, “Engineering of Perovskite Light-Emitting Diodes Based on Quasi-2D Perovskites Formed by Diamine Cations”, *Org. Electronics.*, 75, 105400 (2019).
2. C. H. Li, M. Y. Liao, **C. H. Chen**, C. C. Chueh\*, “Recent progress of anion-based 2D perovskites with different halide substitutions”, *J. Mater. Chem. C.* (2020).
3. M. Y. Liao, Y. C. Chiang, **C. H. Chen**, W. C. Chen, C. C. Chueh\*, “Two-Dimensional Cs<sub>2</sub>Pb(SCN)<sub>2</sub>Br<sub>2</sub>-Based Photomemory Devices Showing a Photoinduced Recovery Behavior and an Unusual Fully Optically Driven Memory Behavior”, *ACS Appl. Mater. Inter.*, 12 (32), 36398-36408 (2020).
4. **C. H. Chen**, Y. C. Lin, Y. F. Yang, Y. C. Chiang, Z. Li, H. L. Yip, W. C. Chen\*, C. C. Chueh\*, “Improving the Performance of All-Inorganic Perovskite Light-Emitting Diodes Through Using Polymeric Interlayers with a Pendant Design”, *Mater. Chem. Front.*, 5, 7199-7207 (2021).
5. K. L. Chu<sup>†</sup>, **C. H. Chen**<sup>†</sup>, S. W. Shen, C. Y. Huang, Y. X. Chou, M. Y. Liao, M. L. Tsai, C. I. Wu, C. C. Chueh\*, “A Highly Responsive Hybrid Photodetector Based on All-Inorganic 2D Heterojunction Consisting of Cs<sub>2</sub>Pb(SCN)<sub>2</sub>Br<sub>2</sub> and MoS<sub>2</sub>”, *Chem. Eng. J.*, 130112 (2021).
6. C. H. Liao, **C. H. Chen**, J. Bing, C. Bailey, Y.T. Lin, T.M. Pandit, L. Granados, J. Zheng, S. Tang, B.H. Lin, H. W. Yen, D. R. McCamey, B. J. Kennedy, C. C. Chueh\*, A. W. Y. Ho-Baillie\*, “Inorganic-Cation Pseudohalide 2D Cs<sub>2</sub>Pb(SCN)<sub>2</sub>Br<sub>2</sub> Perovskite Single Crystal”, *Adv. Mater.*, 2104782 (2021).
7. **C. H. Chen**<sup>†</sup>, Y. H. Kuo<sup>†</sup>, Y. K. Lin, I. C. Ni, B. H. Lin, C. I. Wu, H. L. Yip, C. C. Kuo\*, C. C. Chueh\*, “Enhancing the Performance of Quasi-2D Perovskite Light-

- 
- Emitting Diodes Using Natural Cyclic Molecules with Distinct Phase Regulation Behaviors”, *ACS Appl. Mater. Inter.*, 14, 7, 9587–9596 (2022).
8. **C. H. Chen**<sup>†</sup>, C. H. Hsu<sup>†</sup>, I. C. Ni, B. H. Lin, C. I. Wu, C. C. Kuo\*, C. C. Chueh\*, “Regulating the Phase Distribution of Quasi-2D Perovskites Using a Three-Dimensional Cyclic Molecule Toward Improved Light-Emitting Performance”, *Nanoscale*, 14, 17409-17414 (2022).
  9. Y. K. Lin, **C. H. Chen**, Y. Y. Wang, M. H. Yu, J. W. Yang, I. C. Ni, B. H. Lin, I. S. Zhidkov, E. Z. Kurmaev, Y. J. Lu\*, C. C. Chueh\*, “Realizing High Brightness Quasi-2D Perovskite Light-Emitting Diodes with Reduced Efficiency Roll-Off via Multifunctional Interface Engineering”, *Adv. Sci.*, 10, 2302232 (2023).
  10. I. H. Chao, Y. T. Yang, M. H. Yu, **C. H. Chen**, C. H. Liao, B. H. Lin, I. C. Ni, W. C. Chen, A. W. Ho-Baillie, C. C. Chueh\*, “Performance Enhancement of Lead-Free 2D Tin Halide Perovskite Transistors by Surface Passivation and Its Impact on Non-Volatile Photomemory Characteristics”, *Small*, 2207734 (2023).
  11. H. H. Huang, T. A. Yang, L. Y. Su, **C. H. Chen**, Y. T. Chen, D. Ghosh, K. F. Lin, S. Tretiak, C. C. Chueh, W. Nie\*, H. H. Tsai\*, L. I. Wang\*, “Thiophene-Based Polyelectrolyte Boosts High-Performance Quasi-2D Perovskite Solar Cells with Ultralow Energy Loss”, *ACS Mater. Lett.*, 2207734 (2023).
  12. **C. H. Chen**, M. H. Yu, Y. Y. Wang, Y. C. Tseng, I. H. Chao, I. C. Ni, B. H. Lin, Y. J. Lu, C. C. Chueh\*, “Enhancing the Performance of Two-Dimensional Tin-Based Pure Red Perovskite Light-Emitting Diodes through the Synergistic Effect of Natural Antioxidants and Cyclic Molecular Additives”, *Small*, 2307774 (2024).
  13. Y. T. Lai, **C. H. Chen**, M. H. Yu, H. Y. Kuo, I. C. Ni, B. H. Lin, H. Kim, C. C. Kuo, Y. J. Lu, C. C. Chueh\*, “Dual functionality of carbazole-based phosphonic acid

molecular additives realizes efficient hole transport layer-free perovskite light-emitting diodes”, *Chem. Eng. J.*, 158876 (2024)

14. Y. T. Yang, Y. H. Shih, Q. G. Chen, **C. H. Chen**, M. H. Yu, C. H. Nieh, B. H. Lin, W. C. Chen, W. Y. Lee\*, C. C. Chueh\*, “Revealing the Potential of Perovskite Transistors for Dual-Modulated Synaptic Behavior through Heterojunction Design” *ACS Energy Lett.*, 9, 4564 (2024).
15. M. H. Yu, X. Liu, H. W. Yu, S. F. Kao, **C. H. Chen**, Y. C. Tseng, I. C. Ni, B. H. Lin, Y. Wang\*, C. C. Chueh\*, “Impact of self-assembled monolayer structural design on perovskite phase regulation, hole-selective contact, and energy loss in inverted perovskite solar cells” *Nano Energy*, 132, 110405 (2024).
16. C. Liao, R. Tao, G. Wang, W. Duan, J. Bing, C. G. Bailey, T. L. Leung, Z. Li, **C. H. Chen**, L. Granados Caro, Z. Pastuovic, S. Peracchi, R. Drury, A. Xu, C. Brenner, D. R. McCamey, H. T. Nguyen, A. Lambertz, C. C. Chueh, K. Ding, David R. McKenzie, J. Zheng\*, Md Arafat Mahmud\*, A. W. Y. Ho-Baillie\*, “Gas Quenched Alternating Cations in the Interlayer Space Quasi-2D (GA)(MA)<sub>5</sub>Pb<sub>5</sub>I<sub>16</sub> Perovskite for Radiation Tolerant Single Junction and Stable Monolithic Quasi-2D Perovskite-Silicon Tandem Solar Cells”, *ACS Energy Lett.* 9, 5310-5318 (2024).
17. L. Veeramuthu, F. R. Liang, **C. H. Chen**, F. C. Liang, Y. T. Lai, Z. L. Yan, A. Pandiyan, C. T. Tsai, W. C. Chen, J. C. Lin, M. H. Chen, C. C. Chueh\*, C. C. Kuo\*, “Realizing Highly Stable Quasi-2D Blue Perovskite Light-Emitting Diodes Using Energy Cascades Generated by Biomolecule-Derived Plasmonic Nanostructures”, *ACS Appl. Mater. Inter.*, 17, 1782-1791 (2025).
18. D. Choi, D. Shin, C. Li, Y. Liu, A. S. Bati, D. E. Kachman, Y. Yang, J. Li, Y. J. Lee, M. Li, S. Penukula, D. B. Kim, H. Shin, **C. H. Chen**, S. M. Park, K. Koo, C. Liu, A. Maxwell, H. Wan, N. Roiston, E. H. Sargent\*, B. Chen\* “Carboxyl-

functionalized perovskite enables ALD growth of a compact and uniform ion migration barrier”, *Joule*, 9, 3, 101801 (2025).

19. Y. Y. Wang, X. H. Lee, **C. H. Chen**, L. Yuan, Y. T. Lai, T. Y. Peng, J. W. Chen, C. C. Chueh\*, Y. J. Lu\*, “Plasmon-Enhanced Exciton Re-Localization in Quasi-2D Perovskites for Low-Threshold Room-Temperature Plasmonic Lasing”, *Sci. Adv.*, 11, 19 (2025)
20. Y. Liu<sup>†</sup>, C. Li<sup>†</sup>, T. Zhu<sup>†</sup>, **C. H. Chen**<sup>†</sup>, S. G. Choi, J. A. Steele, Y. Chang, C. B. Musgrave, A. Abudulimu, D. Shin, L. Zeng, S. M. Park, X. Li, S. Zeiske, P. Wang, H. Kwon, S. Hu, D. E. Kachman, H. Lu, S-R. Lee, S. Zhumagali, E. Ugur, K. Dolia, S. Tan, W. Ni, S. Kitade, D. Choi, H. Shin, W. A. Goddard, M. G. Bawendi, H. J. Snaith, R. J. Ellingson, S. D. Wolf, B. P. Rand, L. Wang, J.-W. Lee, Z. Song, Y. Yan, B. Chen,\* E. H. Sargent\*, “Field-enhanced hole selectivity for suppressed photo-oxidation in Pb-Sn perovskite solar cells”, *Nature* (2025) (Revision)